SURFACE ACOUSTIC WAVE STREAMING IN A MICROFLUIDIC SYSTEM

Mansuor Mohamed Alghane

A dissertation submitted for the degree of Doctor of Philosophy

Heriot-Watt University
School of Engineering and Physical Sciences

April 2013

This copy of the thesis has been supplied on condition that anyone who consults it is understood to recognise that the copyright rests with its author and that no quotation from the thesis and no information derived from it may be published without the prior written consent of the author or of the University (as may be appropriate).

Abstract

This study focuses on the investigation of interaction mechanism between surface acoustic wave (SAW) and micro-droplets of volumes (1-30µl) by means of experiments and numerical simulations, and reports the achievements on three-dimensional acoustic streaming and mixing dynamics.

Quantitative evidence was provided for the existence of strong nonlinear nature of flow inertia in this SAW-driven flow when the strength of the acoustic force is larger than 0.01 time of surface tension. A new parameter $F_{NA} = \frac{F\lambda}{(\sigma/R_d)}$ was defined to characterise this nature, where F is the acoustic body force, λ the SAW wavelength, σ the surface tension, and R_d the droplet radius. In contrast to the widely used Stokes model of acoustic streaming which generally ignores such a nonlinearity, it was identified that the full Navier-Stokes equation must be applied when $F_{NA} > 0.01$ to avoid errors up to 93 % between the computed streaming velocities and those from experiments as in the nonlinear case. It is suggested that the Stokes model is valid when $F_{NA} < 0.002$. For an F_{NA} ranges between 0.002 and 0.01, the errors were found to be 5% and 20%, respectively. Furthermore, it was demonstrated that the increase of $F_{NA} > 0.45$ induces not only strong nonlinear internal streaming, but also the deformation of droplets.

Effect of SAW excitation frequency on streaming and mixing in the droplets is also investigated in this study. It has been shown that SAW excitation frequency influences the SAW attenuation length, l_{SAW}, and hence the acoustic energy to be absorbed by the droplet. It has been observed that the ratio of droplet radius to SAW attenuation length (R_d / l_{SAW}) plays an important role on SAW streaming. When $R_d / l_{SAW} \leq 1$, fast and efficient mixing process can be achieved, even at the lowest RF power of 0.05 mW supplied. However, when R_d / l_{SAW} exceeds a critical value of 1, weaker acoustic streaming was observed, which leads to a less effective acoustic mixing.

An investigation on the scaling effects in the flow hydrodynamic by SAWs in confined microdroplets between a $LiNbO_3$ substrate and a top glass plate showed that, the ratio of the gap height to SAW attenuation length, (H / l_{SAW}), is an important parameter affecting the streaming flow induced in this confined microdroplet. At a given SAW power and frequency, the results showed that, an increase in H / l_{SAW} results in an increase of streaming velocity; however, if H / l_{SAW} exceeds 0.7, the streaming velocity decreases.

Dedication

IN THE NAME OF ALLAH, THE ENTIRELY MERCIFUL, THE ESPECIALLY MERCIFUL

My Lord, enable me to be grateful for your favour which you have bestowed upon me and to do righteousness of which you approve

To my wonderful parents

Mohamed Alghane, Salima Ibrahim

And lovely wife

Najat Berras Ali

Acknowledgements

I have been very fortunate to receive a great deal of support throughout the course of my research and I wish to express my gratitude for the help given by of my two supervisors, Dr. Richard Fu and Dr. Baixin Chen, I would like to take this opportunity to thank them for their kindness, advice, support, encouragement and friendship in the past exciting and fruitful four years. I would like to thank my lovely mom, Salima Ibrahim for her great support and encouragement during my research work.

I acknowledge support from the Innovative electronic Manufacturing Research Centre (IeMRC) through the EPSRC funded flagship project SMART MICROSYSTEMS (FS/01/02/10). Financial support from the Royal Society-Research Grant (RG090609), Carnegie Trust Funding, Royal Society of Edinburgh, and China-Scotland Higher Education Partnership, Royal Academy of Engineering-Research Exchanges with China and India Awards is also acknowledged.

Finally, I would like thank Dr. Y. Li for his kind help and support during my project; also I would like to express my deep appreciations to both Prof. A. J. Walton and Prof. M. P. Y. Desmulliez for their valuable suggestions and recommendations during my period of research.

ACADEMIC REGISTRY
Research Thesis Submission

Name*:*	Mansuor Mohamed Alghane		
School/PGI:	School of Engineering and Physical Sciences		
Version: *(i.e. First, Resubmission, Final)*	Final	Degree Sought (Award **and** Subject area)	PhD Mechanical Engineering

Declaration

In accordance with the appropriate regulations I hereby submit my thesis and I declare that:

1) the thesis embodies the results of my own work and has been composed by myself
2) where appropriate, I have made acknowledgement of the work of others and have made reference to work carried out in collaboration with other persons
3) the thesis is the correct version of the thesis for submission and is the same version as any electronic versions submitted*.
4) my thesis for the award referred to, deposited in the Heriot-Watt University Library, should be made available for loan or photocopying and be available via the Institutional Repository, subject to such conditions as the Librarian may require
5) I understand that as a student of the University I am required to abide by the Regulations of the University and to conform to its discipline.

* *Please note that it is the responsibility of the candidate to ensure that the correct version of the thesis is submitted.*

Signature of Candidate*:*		Date:	/ 4 / 2013

Submission

Submitted By *(name in capitals):*	MANSUOR MOHAMED ALGHANE
Signature of Individual Submitting:	
Date Submitted:	/ 4 / 2013

For Completion in the Student Service Centre (SSC)

Received in the SSC by *(name in capitals):*			
Method of Submission (handed in to SSC; Posted through internal/external mail):			
E-thesis Submitted **(mandatory for final theses**)			
Signature:		Date:	

Nomenclature and Abbreviations

a	The normal componet of the particle displacement amplitude of the surface wave	m
$\grave{a}$	The tangential componet of the particle displacement amplitude of the surface wave	m
A	Amplitude of surface acoustic wave at the entrance point to the liquid	m
A_c	Clustered starch area	m^2
A_t	Droplet substrate contact area	m^2
b	Width of the solid substrate	μm
c_0	Velocity of compressional waves in fluid	m/s
c_{ijkl}	Elastic coefficients or stiffness tensor	
c	Elastic constant	N/m^2
dV	Infinitesimal volume element	m^3
D	The diffusion coefficient	m^2/s
D_j	Electric displacement	C/m^2
D_a	Degree of arc	degree
dE	Acoustic energy emitted by the Rayleigh wave into the adjacent fluid	W
$d\grave{E}$	Dissipated acoustic energy $d\grave{E}$ by the viscous forces at the adjacent fluid layer	W
d_0	Initial droplet diameter	m
dx	Identified parameter of the centre axis of rotation in the *x* axes direction	m
dy	Identified parameter of the centre axis of rotation in the *y* axes direction	m
d	Interdigitated transducer finger's spacing or width	m
d_r	Confined droplet diameter,	m
E_k	Electrical field strength	J/m
E	The energy transferred per second through the surface element by the Rayleigh wave	W
$\grave{E}$	The shear energy flow in the Rayleigh wave	W
e_{kij}	Piezoelectric tensor	

e	Piezoelectric constant	C/m^2
f	Excitation frequency of surface acoustic wave device	MHz
F_j	Steady force due Reynolds' stress	N/m^3
f_L	Geometric focal length	m
F	Streaming force	N/m^3
F_{NA}	Normalized acoustic force	
F_x	Tangential component of streaming force	N/m^3
F_y	Normal component of streaming force	N/m^3
h_0	Initial droplet height	m
h	Droplet height after acoustic wave application	m
H	Separation gap height	m
H_{cr}	Critical gap height	m
K^2	Electromechanical coupling coefficient	
k	Wave number	1/m
k_R	Wave number of Rayleigh wave	1/m
k_L	Wave number of leaky surface acoustic wave	1/m
k_r	Real component of leaky wave number	1/m
k_i	Imaginary component of leaky wave number	m
Lx	Identified parameter of centre axis of rotation in the *x* axes direction	m
Lz	Identified parameter of centre axis of rotation in the *z* axes direction	m
l_{SAW}	Damping length of the surface acoustic wave	m
m	Mass fraction of mixing species	
m_{max}	Maximum initial mass fraction of dye species	
m_{mean}	Mean mass fraction	
n	Indication to the wave propagation direction	
N	Total number of computation cells	
P	Periodicity of the interdigitated transducers	m
p_0, p_1, p_2	Pressure, where subscripts 0, 1, and 2 refer to the steady (ambient), first-order and second-order terms	Pa
P_D	Radio frequency power applied to the SAW device	W
P_n	Normalized radio frequency power applied to the SAW device	
P_{Dr}	Reference power frequency power applied to the SAW device	W

P	Streaming pressure	Pa
r	Particle radius	m
Re	Reynolds number	
R_d	Droplet radius	m
$\mathrm{Re_l}$	Reynolds number of linearized solution	
$\mathrm{Re_{nl}}$	Reynolds number of nonlinearzed solution	
S	Mechanical strain	
S_{ij}	Symmetrical strain tensor, i, j =1, 2, 3	
T	Mechanical stress	$\mathrm{N/m^2}$
T_{ij}	Symmetrical stress tensor, i, j =1, 2, 3	
u_i	Displacement component along the corresponding Cartesian axes x_i	m
u_1	Longitudinal component of particle displacement of the Rayleigh wave	m
u_3	Transverse component of particle displacement of the Rayleigh wave	m
$\hat{u}_1$	Displacement amplitude of the longitudinal component	m
$\hat{u}_3$	Displacement amplitude of the transverse component	m
$\overline{U_i U_j}$	The mean value of the fluctuation fluid velocities product, i.e., U_i and U_j	$\mathrm{m^2/s^2}$
U	Streaming velocity	m/s
u_x	Longitudinal component of leaky SAW displacement	m
u_y	Transverse component of leaky SAW displacement	m
U_x	Streaming velocity in the *x* axes direction	m/s
U_{xr}	Reference streaming velocity in the *x* axes direction	m/s
U_{xn}	Normalized streaming velocity in the *x* axes direction	
V_R	Propagation velocity of the Rayleigh wave	m/s
V_0	The tangential particle velocity at the surface-liquid interface	m/s
V_L	Leaky surface acoustic wave velocity	
V_i	Localized cell volume of droplet mesh	$\mathrm{m^3}$
V_0	Total droplet volume initially occupied by the dye species	$\mathrm{m^3}$
V_{tot}	Droplet volume	$\mathrm{m^3}$
$\mathrm{v_1}$	First-order or acoustic velocity	m/s
$\mathrm{v_2}$	Second-order or streaming velocity	m/s

W_{SAW}	Width of the surface acoustic wave	m
x_1, x_2, x_3	Cartesian coordinates in the x, y and z axes respectively	
x_i	Cartesian axes, where i =1, 2, 3	
α_L	Absorption coefficient of the Rayleigh wave due to emission of longitudinal waves	1/m
α_s	Absorption coefficient of the Rayleigh wave due to viscous forces	1/m
α	Attenuation constant of leaky surface acoustic wave	
ω	Angular frequency of an applied electrical signal	Rad/sec
δ	The viscous penetration depth	m
ε_{ij}	Permittivity tensor	
ε	Dielectric permittivity	
ϵ	Error parameter	
φ	Electric potential	J
ρ	Solid substrate density	kg/m^3
ρ_f	Fluid density	kg/m^3
ρ_0, ρ_1, ρ_2	Fluid density, where subscripts 0, 1, and 2 refer to the steady (ambient), first order and second order terms	kg/m^3
μ	Fluid shear viscosity	$N{\cdot}s/m^2$
μ_B	Fluid bulk viscosity	$N{\cdot}s/m^2$
λ	Wavelength of the Rayleigh wave	m
λ_f	Wavelenght of longitudinal waves in the fluid	m
Θ	SAW-droplet interaction angle	degree
θ_R	Rayleigh angle	degree
σ_{ij}	Reynolds' stress	N/m^2
σ	Surface tension	N/m
$\langle\ \rangle$	Time-averaging of fast harmonic oscillations of the Rayleigh wave	

2D	Two dimensional
3D	Three dimensional
µTAS	Micro total analysis system
CFD	Computational fluid dynamic
DI	Deionized water

Exp.	Experimental
FE	Finite element
FVM	Finite volume method
FIDTs	Focused interdigitated transducers
FPW	Flexural plate wave
GPL	General public license
IDTs	Interdigitated transducers
LOC	Lab-on-Chip
$LiNbO_3$	Lithium Niobate
LSAW	Leaky surface acoustic wave
MIP	Mixing index parameter
N-S	Navier-Stokes
Num.	Numerical
RF	Radio frequency
SAW	Surface acoustic wave
SSAW	standing surface acoustic wave
PDMS	Poly Dimethyl Siloxan
PDF	Probability distribution function
PZT	Piezoelectric zirconium titanate ceramic plate
VOF	Volume of fluid

Table of Contents

List of Publications

- ***Journal papers:***

1. **Alghane, M.**, Chen, B. X., Fu, Y. Q., Li, Y., Luo, J. K and Walton, A. J., Experimental and numerical investigation of acoustic streaming excited by using a surface acoustic wave device on a 128º YX-LiNbO3 substrate. J. Micromech. Microeng., 2011. **21**: p. 015005. *DOI:10.1088/0960-1317/21/1/015005*
2. **Alghane, M.**, Fu, Y. Q., Chen, B. X., Li, Y., Desmulliez, M. P. Y., and Walton, A. J., *Streaming phenomena in microdroplets induced by Rayleigh surface acoustic wave.* J. Appl. Phys., 2011. **109**: p. 114901. *DOI:10.1063/1.3586040*
3. Brodie, D.S., Fu, Y. Q., Li, Y., **Alghane, M.**, Reuben, R. L. and Walton, A. J. *Shear horizontal surface acoustic wave induced microfluidic flow.* Appl. Phys. Lett., 2011. **99**: p. 153704. *DOI:10.1063/1.3651487*
4. Li, Y., Fu, Y. Q., Brodie, D.S., **Alghane, M.** and Walton, A. J. *Integrated micro-fluidics system using surface acoustic wave (SAW) and electrowetting on dielectrics (EWOD) technology.* Biomicrofluidics, 2012. **6**: p. 012812. *DOI:10.1063/1.3660198*
5. **Alghane, M.**, Fu, Y. Q., Chen, B. X., Li, Y., Desmulliez, M. P. Y., and Walton, A. J., *Scaling effects on flow hydrodynamics of confined microdroplets induced by Rayleigh surface acoustic wave.* Microfluid. Nanofluid., 2012. **13**: p.1-9. *DOI: 10.1007/s10404-012-1010-y*
6. **Alghane, M.**, Fu, Y. Q., Chen, B. X., Li, Y., Desmulliez, M. P. Y., and Walton, A. J., *Frequency effect on streaming phenomenon induced by Rayleigh surface acoustic wave in microdroplets.* J. Appl. Phys., 2012. **112**: p. 084902-12. *DOI: 10.1063/1.4758282*
7. **Alghane, M.**, Chen, B. X., Fu, Y. Q., Li, Y., Desmulliez, M. P. Y., Mohamed, M. I and Walton, A. J., *Nonlinear hydrodynamic effects induced by Rayleigh surface acoustic wave in sessile droplets.* Phys. Rev. E, 2012**. 86**(5): p. 056304. *DOI: 10.1103/PhysRevE.86.056304*
8. **Alghane, M.**, Fu, Y. Q., Chen, B. X., Li, Y., Desmulliez, M. P. Y., and Walton, A. J., *A review of a Rayleigh wave based microfluidic.* (***To be submitted***)

- ***Conference papers:***

1. **Aghane, M.**, Fu, Y. Q. et al, 2Annual Workshop on Institue of Intgrated Sysyems, Feb, 2010, University of edinburgh, Eidniburgh, UK. **(Poster)**
2. **Aghane, M.**, Fu, Y. Q.*, Chen, B. X., Desmulliez, M., Acoustic streaming behavior excited by Rayleigh surface acoustic wave. *1st International conference on fluid problems in process engineering*, 6-8th September 2010, Leeds, UK. **(*Oral & Paper presented*)**
3. **Aghane, M.**, Fu, Y. Q. and Chen, B. X., Surface acoustic wave streaming in microfluidic system. *IMAPS-UK "Making MEMS Work"*, 2010, Edinburgh, UK. **(*Poster*)**
4. **Aghane, M.**, Fu, Y. Q. and Chen, B.X., Finite volume analysis of acoustic wave streaming using various interdigital transducers. *2nd International Conference on Bio-Sensing Technology*, 10-12th October 2011, Amsterdam, the Netherlands, P073. **(Poster)**
5. Li, Y., Fu, Y. Q., Brodie, D.S., **Alghane, M.** and Walton, A. J., *Enhanced micro-droplet splitting, concentration, sensing and ejection by integrating ElectroWetting-On-Dielectrics and Surface Acoustic Wave technologies*. in *Solid-State Sensors, Actuators and Microsystems Conference (TRANSDUCERS), 2011 16th International*. 05-019 Oral Presentation, June 5th to 9th, 2011, Beijing. **(*Paper presented*)** *DOI: 10.1109/TRANSDUCERS.2011.5969406*
6. Y.Q. Fu, J. K. Luo, S. Brodie, **A. Mansuor,** Highly efficient digital microfluidics and Biosensing devices based on ZnO thin films, in 2nd International Conference on Biosensing Technology, Amsterdam, Netherlands, Oct 9th to 12th 2011. **(*Poster*)**
7. Fu, Y.Q., **Alghane, M.,** Luo, J. K., Chen, B.X., Li, Y. and Walton A., Invited paper: Lab-on-chip based on Surface Acoustic Wave devices of piezoelectric ceramic LiNbO3, *International Conference on Electroceramics 2011*, 12-16th December 2011, Sydney, Australia **(*Paper presented*)**

List of Tables

List of Figures

Chapter 1

INTRODUCTION

1.1 General Introduction

Over the past few years, life sciences in parallel with microfluidic technology have shown significant advances and resulted in the establishment of a new field of research known as a micro total analysis system (μTAS) [3]. In a μTAS, the whole laboratory processes of chemical analysis of small amount of fluids are integrated on very small surface of a microfluidic chip, similar to that presented in Fig.1.1 [4]. This process of integration is also known as Lab-on-Chip (LOC) [4-6], which involves shrinking of different microfluidic processes to very small and accurate micro devices and the miniaturisation of chemical and biological systems. There are different considerations for scaling down the size of micro devices; for example, the small volumes of reagents can be efficiently treated in the micro devices. Consequently, the cost of expensive reagents is reduced and less processing energy is needed in the biological and chemical labs [7, 8]. Also, the processing time is reduced and more homogenous reaction conditions can be achieved [5, 9].

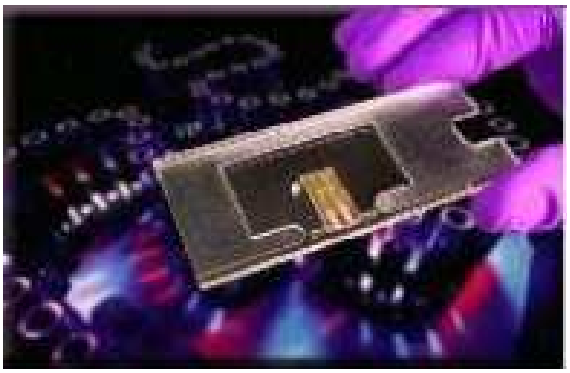

Figure 1.1 Example of biochip for Lab-on-chip [4]

Decrease the volume of fluid in some technical problems associated with microscale volumes. For example, pumping of very small amount of materials (liquids and components) in such microscale dimensions becomes difficult, due to the significant increase in viscous and capillary forces with significant reduction in the dimension of characterised system [10, 11]. Additionally, in chemical and biological micro-devices, moving of fluids in small scale channels like capillaries must be laminar flow due to the small values of Reynolds number [12]. In such microscale systems, effective mixing

by diffusion is difficult and the efficiency is low because it needs large length scales and long duration, which are quite limited in many microfluidic applications, such as biochemical and biological analysis [13, 14], where a fast and efficient mixing process is normally essential. In addition to the above problems, there is no conventional pumping system that can work effectively with small quantities of fluids such as sessile droplets, neither in closed channels nor on free surfaces.

In order to produce microfluidic devices for LOC technology, the above mentioned technical problems must to be addressed. Recently, surface acoustic waves (SAW) have been demonstrated as a novel pumping technique that can be fully integrated in the microfluidic devices without mechanical or moving parts [15]. It is known that when a liquid layer (either in bulk or droplet form) lies in the propagation path of the SAW, the wave energy couples into the liquid medium [16], inducing mixing [17, 18], pumping [19], jetting or atomisation [20, 21] of the microdroplets, depending on the SAW applied power. The main characteristic feature that make the SAW devices an attractive technology for different microfluidic applications is that it can handle both discrete droplets on a free flat surface or continuous flow microchannel with an effective mixing strategy for a fast and homogenous mixing process [22]. Furthermore, it is easily fabricated and integrated into microfluidic systems, which makes it an excellent solution for the portability and miniaturization approaches of the LOC systems.

SAW-driven microfluidics have been classified in the literature [23] according to the geometrical boundaries of the fluid under the SAW application: i.e., SAW-based microdroplets (sessile droplets) and SAW-based microchannels (continuous flow). To the best knowledge of the author, the SAW-fluid coupling mechanism is not yet fully understood and the current studies reported in the literature provide insufficient theories to quantitatively describe the influences of different design parameters (e.g., SAW excitation frequency, etc) on the efficiency of the SAW devices as an actuation technology for microfluidic systems. This is because most of the experimental and theoretical studies were based on two dimensional (2D) observations [24, 25]. Whereas, the streaming flow induced by the SAW-droplet coupling is mainly a three dimensional (3D) phenomena. In order to design an efficient SAW device for driving the LOC systems, the induced flow phenomenon of SAW streaming must be thoroughly understood.

1.2 **Research Objectives**

This thesis focuses on the understanding of the interaction mechanisms between SAWs and microdroplets. To study the hydrodynamics behaviours of the induced streaming phenomena, a 3D numerical model has been developed for this system of SAW-droplet coupling. The 3D model has been applied for a comprehensive and systematic analysis of SAW-induced droplet streaming, with the aim of developing an efficient SAW device for LOC systems. To achieve the objective of this research, the different parameters of SAW system configurations have been investigated by conducting 3D numerical simulations with experimental validations.

1.3 **Thesis Outline**

This thesis has been divided into eight chapters as described below:

Chapter 1: Introduction. This chapter gives a brief introduction background of the present work and provides an overview of the research objectives.

Chapter 2: Wave Generation and Propagation Background. This chapter gives a basic background of an elastic wave generation and propagation followed by a general description of the SAW devices, including the effect of surrounded medium on the characteristic behaviours of SAW propagation.

Chapter 3: Literature Review. This chapter gives a review of the research work that has been done on SAW-based microfluidics, considering both the experimental and theoretical studies, and then introduces the current problems needed to be addressed.

Chapter 4: Streaming Phenomenon. This chapter gives an introduction to the acoustic streaming theory and describes the experimental apparatus, materials and methods used in this study. It provides an overall description of the numerical theory, technique and computational fluid dynamic (CFD) code used in this research. It also explains the physical mechanisms of the different streaming phenomena induced by the interaction between the SAW and liquids.

Chapter 5: Acoustic Streaming and Hydrodynamic Nonlinearity. This chapter reports a systematic experimental and numerical investigation on the role that flow inertia played

in the development of acoustic streaming induced by a Rayleigh SAW in a sessile droplet.

Chapter 6: Influences of Configuration Parameters on Streaming Phenomenon. This chapter presents experimental and numerical results for the effects of characteristic parameters on the performance of the streaming phenomenon of liquid droplets, such as liquid volume, applied power and aperture of the SAW device.

Chapter 7: Frequency Effect on Mixing Performance of Rayleigh SAW. In this chapter, the effects of SAW excitation frequency, on acoustic streaming of ink particles inside microdroplets generated by a SAW have been studied; their affect on the mixing efficiency of the SAW devices has been investigated, using 3D numerical simulations with experimental verification.

Chapter 8: Scaling Effects in SAW Streaming. This chapter reports an experimental and numerical investigation of the scaling affects in the flow hydrodynamics for confined microdroplets induced by surface acoustic waves. The characteristic parameters of the flow hydrodynamics were studied as a function of the separation height, *H*, between the $LiNbO_3$ substrate and a top glass plate, for various droplets volumes and RF powers.

Chapter 9: Conclusions and Future Work. This chapter provides overall concluding remarks and suggestions for the future work.

Contribution to knowledge:

The novel contribution of this study can be briefly summarized as: (1) identified the role of hydrodynamic nonlinearity on the development of SAW acoustic streaming and found a new dimensionless parameter, F_{NA}, the ratio of acoustic force to surface tension that characterises the linear and nonlinear streaming, and the deformation of droplets; (2) enhanced the understanding of the streaming mechanisms including microparticles concentration and mixing process by SAW in microdroplets through the 3D numerical simulations, for which the CFD models were calibrated by Lab experiments.

Chapter 2

WAVE GENERATION AND PROPAGATION BACKGROUND

This chapter provides a basic background and theory of a SAW generation and propagation in an elastic piezoelectric solid, including the effect of surrounded medium type on the characteristic behaviours of SAW propagation.

2.1 **Introduction**

SAW devices have been used since the 1940's [26], for example, in many applications including signal processing, such as filters and oscillators [27]. In addition to this, they have been applied in other areas as sensors [28]. Furthermore, a new aspect has been directed toward the applicability of SAW devices in microfluidic systems [29]. The notion of microfluidics emerged during the 1970's, when the first system of miniaturised gas chromatograph was developed [30], in which the microchannels were fabricated on the surface of a silicon wafer. Later in the 1990's, considerable progress and advances in microfluidic systems have been made towards producing miniaturised devices for many scientific applications, including chemical and biological laboratory processes, such as integrated devices for DNA analysis [31]. These systems were essentially enabling the analysis of small volumes of liquid ranging from the micro to nano litre scale. In this context, the term of LOC emerged, showing the possible application of such microfluidic systems in life sciences [8]. For liquids to be analysed, there are several components required, even for a simple microfluidic system. This includes a pumping device and the structure within which the liquid can travel. Generally, the geometry and diameter of microchannels, through which the liquids or reagents are transported, are in the range of 10 to 500 μm [32]. Typically, these channels are fabricated on the surface of an appropriate substrate material such as quarts, silicon, glass, or a piezoelectric crystal, where in most cases the chip-size is about $1cm^3$ or even less [33, 34]. Currently, due to the progress in production approaches, complicated and reliable chips for chemical and biological applications can be produced [35]. The main advantages of micro devices include the compactness, portability, and lack of moving parts. This allows for the running of massive numbers of experiments with huge data delivery, with less consumption of expensive substances such as chemical and biological materials, and also the possibility of integrating multiple micro-processes on one chip.

For pumping fluids in microfluidic systems, different pumping techniques have been reported in the literature, such as diaphragm displacement, electrohydrodynamic and electro-osmotic micropumps [36]. Generally, such techniques do not allow handling discrete reagents and need the microchannel to be completely filled with fluids to work efficiently. Recently, a novel approach utilising a SAW as an actuation force has been proposed; this can handle continuous or discrete reagents not only in microchannels, but also on the free surfaces [23].

The aim of this thesis is to analyze acoustic streaming induced by the SAW in microfluidics. Therefore, this chapter introduces the basic concepts and theories that are necessary to understand the principle of SAW propagation and its excitation. The influence of a fluid on the substrate surface on the behaviour and mode of an excited SAW is also shown.

2.2 **Bulk Waves in Elastic Solids**

In this section, the wave equation of a non-piezoelectric, homogenous and isotropic elastic solid is derived, using Newton's second law and Hook's law of elastic deformation. The later considers the relation between the mechanical stress, *T*, and strain, *S* of small elastic distortions. Later, to emphasize the mechanical characteristics of piezoelectric solids, the piezoelectricity is introduced into the wave equation, which is an important effect that couples the mechanical waves with the electrical field applied to the piezoelectric substrate [37].

2.2.1 Wave equation in a non-piezoelectric solid

An elastic solid is a material which returns to its original state when the external forces responsible for its deformation are removed, and in which all internal stresses and strains become zero. For an infinitesimal volume element $dV = dx_1\, dx_2\, dx_3$, or a point under distortion within an isotropic homogenous substrate, in the absence of external forces and piezoelectricity, the equation of displacement neglecting gravity can be described using Newton's law by [37]:

$$\rho \frac{\partial^2 u_i}{\partial t^2} = \frac{\partial T_{ij}}{\partial x_j} \tag{2.1}$$

Here, ρ is the mass density of solid substrate, $u_i$is the displacement component along the corresponding Cartesian axes x_i. The exerted forces on an infinitesimal volume *dV*, are those raised from interactions of neighbouring volumes, as described by the symmetrical stress tensor T_{ij} that indicates to nine quantities, corresponding to *i*, *j* =1, 2, 3 [37]. Here, T_{ij} represents the components of the forces per unite area that are exerted by the material on one side of the surface in x_i direction. If $i = j$, T_{ii} describes the stress forces, and if $i \neq j$, T_{ij} describes the shear forces. However, the real distortion of an infinitesimal volume *dV* of the rigid solid body undergoes the displacement can be expressed by a symmetrical strain tensor of S_{ij} [38].

$$\boldsymbol{S_{kl} = \frac{1}{2}\left(\frac{\partial u_k}{\partial x_l} + \frac{\partial u_l}{\partial x_k}\right), (i, j, k, l = 1, 2, 3)} \tag{2.2}$$

Usually, the relationship between the stress and strain of an elastic solid links via the elastic coefficients (or stiffness tensor) c_{ijkl} using Hooke's law of elastic deformation [37-39]:

$$\boldsymbol{T_{ij} = c_{ijkl} S_{kl}} \tag{2.3}$$

Due to the symmetry of tensors S_{ij} and T_{ij}, an interchangeable in the order of either the first two or the last two indices of the stiffness tensor c_{ijkl}, defined in the above equation of Hooke's law, and does not affect the elastic constants [37].

$$\boldsymbol{c_{ijkl} = c_{jikl}} \text{ , and } \boldsymbol{c_{ijkl} = c_{ijlk}}$$

Then, substituting Eq. (2.2) into Eq. (2.3) gives:

$$\boldsymbol{T_{ij} = \frac{1}{2} c_{ijkl} \frac{\partial u_k}{\partial x_l} + \frac{1}{2} c_{ijkl} \frac{\partial u_l}{\partial x_k}} \tag{2.4}$$

Since $c_{ijkl} = c_{ijkl}$ on the right side of above equation, so that it leads to the following three-dimensional version of Hooke's law [39]:

$$\boldsymbol{T_{ij} = c_{ijkl} \frac{\partial u_l}{\partial x_k}} \tag{2.5}$$

The wave equation in a non-piezoelectric solid can be obtained by combining the Newton's second law of motion (Eq. 2.1) and the Hooke's law of elasticity (Eq. 2.5):

$$\rho \frac{\partial^2 u_i}{\partial t^2} = c_{ijkl} \frac{\partial^2 u_l}{\partial x_j \partial x_k} \tag{2.6}$$

2.2.2 Wave equation in a piezoelectric solid

It is known that a piezoelectric effect, is one of existing methods that widely used for the excitation of ultrasonic acoustic waves on a solid crystal [37]. The piezoelectricity physics can be demonstrated by considering a piezoelectric crystal that placed between two parallel metallic plates that act as electrodes, as shown in Fig. 2.1 [40]. If the crystal is not stressed, the centres of positive and negative charges of the crystal atoms are symmetrical (see Fig. 2.1), indicating no polarisation is initiated. However, if an alternating compressive or tensile stress is applied to the opposite faces of the piezoelectric crystal, unsymmetrical distribution of positive and negative charges is induced (i.e., a molecular dipole), where the centres of the both charges becomes non-identical [40]. This process of mechanical distortion, leads to the accumulation of electrical charges on the electrode surfaces and hence to the generation of an electrical potential difference across the electrodes. In this case, the mechanical energy is transformed to an electrical energy. Alternatively, this process of a piezoelectric crystal distortion can be reversed if an electrical potential is applied to the electrodes. This is results in a mechanical distortion of crystal lattice, due to molecular polarization [40]. In this second case, the electrical energy applied to the crystal is transformed into a mechanical distortion. Thus, piezoelectric crystal is a solid material that can be mechanically deformed when an alternating electric field is applied or vice versa.

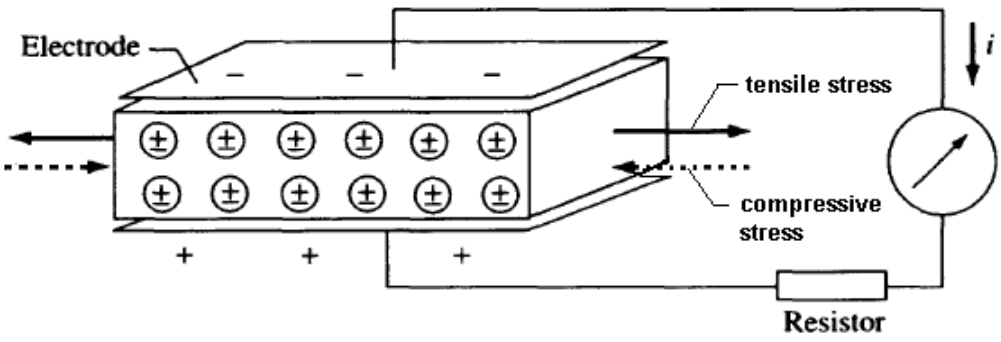

Figure 2.1 Illustration of mechanical energy transformation into an electrical energy [40]

Therefore, piezoelectricity means that, if a stress is applied to a piezoelectric crystal, not only the strain is produced, but also a potential difference between the opposite faces of the piezoelectric solid, is generated. So far, the above equation, (i.e., Eq. (2.6)) of wave motion describes the elastic deformation of isotropic solids in the absence of a piezoelectric effect. Since the interest of this thesis work is the acoustic wave induced by a piezoelectricity, this effect must be introduced in the above equation of motion. Thus, Hooke's law of strain is extended to include an additional term E_k, representing the strength of an electric field. The constitutive equations which can be used to describe the electric displacement D_j for the piezoelectric solids are expressed as [37]:

$$\boldsymbol{T_{ij} = c_{ijkl} S_{kl} - e_{jkl} E_k} \qquad (2.7a)$$

$$\boldsymbol{D_j = e_{jkl} S_{kl} + \varepsilon_{jk} E_k} \qquad (2.7b)$$

here, the strength of electrical field E_k is approximated by a gradient of scalar electrical potential φ as; $E_k = -\frac{\partial \varphi}{\partial x_k}$, where e_{jkl} is the piezoelectric tensor that relates the electrical potential to the equation of elastic wave displacement. The relation between the electric displacement and electric field is linked via the dielectric permittivity tensor, ε_{jk}, measured at constant strain [37]. By using an electrical field approximation in equations 2.7(a) and (b) and substituting the results into the equation of displacement, Eq. (2.1) and into the Poisson's equation;($\frac{\partial D_j}{\partial x_j} = 0$), with the definition of stain tensor, (i.e., Eq. (2.3) and Eq. (2.5)) gives the following equations [37, 39]:

$$\boldsymbol{\rho \frac{\partial^2 u_i}{\partial t^2} - c_{ijkl} \frac{\partial^2 u_l}{\partial x_j \partial x_k} - e_{jkl} \frac{\partial^2 \varphi}{\partial x_j \partial x_k} = 0} \qquad (2.8a)$$

$$\boldsymbol{e_{jkl} \frac{\partial^2 u_l}{\partial x_j \partial x_k} - \varepsilon_{jk} \frac{\partial^2 \varphi}{\partial x_j \partial x_k} = 0} \qquad (2.8b)$$

Generally, these equations describe the motions of different types of bulk wave modes, depending on the properties and the crystal cut of a piezoelectric material used to transform an electric field into a mechanical deformation.

2.3 Rayleigh Surface Acoustic Wave

2.3.1 Introduction

Since the early 1990's, SAW technology has become an interesting area of research [41], especially in the development of microfluidic systems [18]. The propagation mode of SAWs on an isotropic elastic solids was first described theoretically by Lord Rayleigh in 1885, in which he described the energy of acoustic wave was restricted near the free surface of an elastic substrate, thus this type of the wave is often called a Rayleigh wave [42]. In the Rayleigh wave mode shown in Fig. 2.2, the motion of particles in a solid substrate have two components in the sagittal plane of the substrate; a surface-normal component and a surface-tangential component with respect to the wave propagation direction [42]. Mainly, this type of surface acoustic wave is generated on piezoelectric substrates after applying an alternating electric field via a coupling with interdigitated transducers (IDTs) [39], as detailed in the following sections.

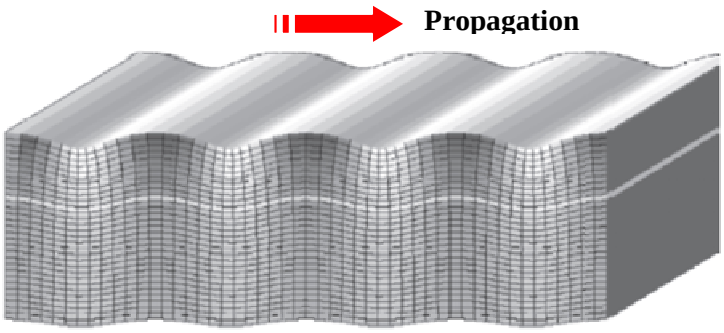

Figure 2.2 A sketch of Rayleigh wave showing its propagation in an elastic solids [43]

2.3.2 Propagation characteristics of Rayleigh wave

The Cartesian coordinate system within an isotropic half-space piezoelectric structure used for the discussion of a surface acoustic wave is illustrated in Fig. 2.3. This acoustic wave is also known as a Rayleigh wave [39], in which the particle displacement of an elastic medium has only two components, one is a longitudinal component, u_1, of the tangential displacement to the SAW propagation, and the other is a transverse component of the vertical displacement, u_3, with no variations in the direction of the x_2 axis.

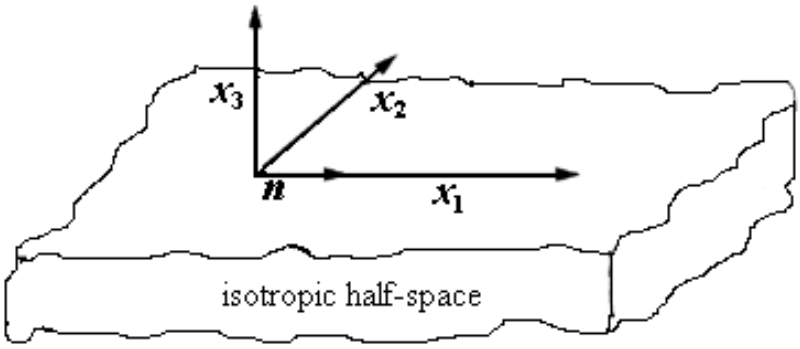

Figure 2.3 Coordinate system for surface waves showing propagation direction, where *n* indicates the wave propagation direction

As shown in Fig. 2.3, the origin of the coordinate system is at the surface of an isotropic solid with the x_3 axis is perpendicular to the free surface. The mechanical stresses at traction-free boundary (x_3= 0) are expressed as [37, 40]:

$$\boldsymbol{T_{13} = T_{23} = T_{33} = 0} \tag{2.9}$$

Thus, the solution of the wave equation, using the constitutive equations (2.8) that satisfies the above boundary condition Eq. (2.9), which describes the displacements of an existing Rayleigh wave induced on an isotropic half-space solid that propagates along the x_1 axis, is given by [37]:

$$\boldsymbol{u_1 = \hat{u}_1 \cos[(kx_1 - \omega t)]}, \quad \text{and} \quad \boldsymbol{u_3 = \hat{u}_3 \sin[(kx_1 - \omega t)]} \tag{2.10}$$

Here, $\hat{u}_1$ and $\hat{u}_3$ are the displacement amplitudes of the longitudinal and transverse components, respectively, ω is the angular frequency of an applied electrical signal, and k is the wave number. The results demonstrated that the motions of wave particles at any solid depth are elliptical, as shown in Fig. 2.4(a). For a typical isotropic material, the amplitudes of wave displacement, $\hat{u}_1$ and $\hat{u}_3$, decay with the depth inside the substrate, which become negligible values in a few wavelengths from the surface [37, 39, 44], as shown in Fig. 2.4(b).

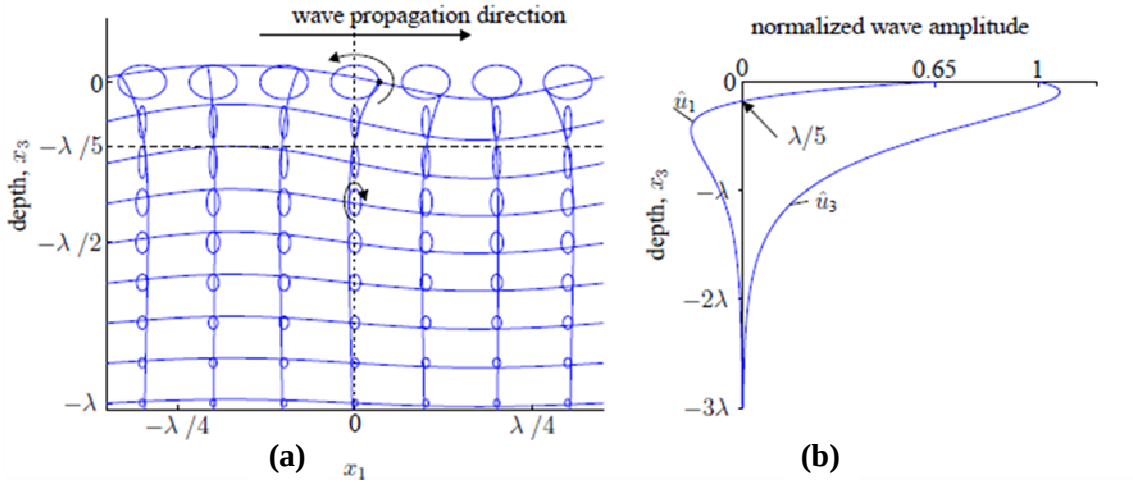

Figure 2.4 Characteristics of a Rayleigh wave in an isotropic half-space elastic solid (e.g., piezoelectric substrate); (a) Displacement field of the wave particles; (b) Decay of displacement amplitudes $\hat{\boldsymbol{u}}_1$ and $\hat{\boldsymbol{u}}_3$ as a function of solid depth [44]

2.3.3 Rayleigh wave excitation

The basic structure of a SAW device consists of an Interdigital Transducer (IDT) and a piezoelectric substrate. An example of a SAW device is shown in Fig. 2.5. It contains interdigitated electrodes of a metallic material like aluminium deposited on the surface of a piezoelectric substrate, such as lithium niobate ($LiNbO_3$) or quartz [27]. These substances convert the electric field into a mechanical stress and vice versa.

A complete surface acoustic wave device consists of two sets of comb-shaped IDTs, one acting as transmitter (electric energy → mechanical energy), which is connected to an excitation source, seen in Fig.2.5, and the other as transducer (mechanical energy → electric energy). However, in many microfluidic applications, only the first set is used. An application of an alternating signal to the IDTs induces a mechanical vibration and periodic deformation, which is defined as a small earthquake wave on the piezoelectric substrate, as shown in Fig. 2.4 (a). This in turn, results in an elastic SAW that propagates away from the transducer with wavefronts parallel to the IDTs, as shown in Fig.2.5. For the special type of wave mode of a SAW being discussed here, the efficiency of a given piezoelectric material in converting the electric field into an associated mechanical wave is typically measured using an electromechanical coupling coefficient, K^2, which is defined in terms of the piezoelectric constant e, elastic constant c and dielectric permittivity ε as $K^2 = \frac{e^2}{\varepsilon c}$ [45]. Also, this characteristic coefficient can be measured experimentally [38]; to be:

$$K^2 = -\frac{2\Delta V}{V_R} \tag{2.11}$$

Here, $|\Delta V|$ denotes the difference in wave velocity of a free (e.g., unperturbed surface) and a shortened surface (i.e., thin high conducting metal film deposited on the surface, between the two set of the device IDTs, shown in Fig. 2.5) of piezoelectric substrate, and V_R is the unperturbed SAW velocity. Usually, the values of K^2 in most piezoelectric materials are small (a few percent) as shown in Table 2.1 for some typical piezoelectric substrates.

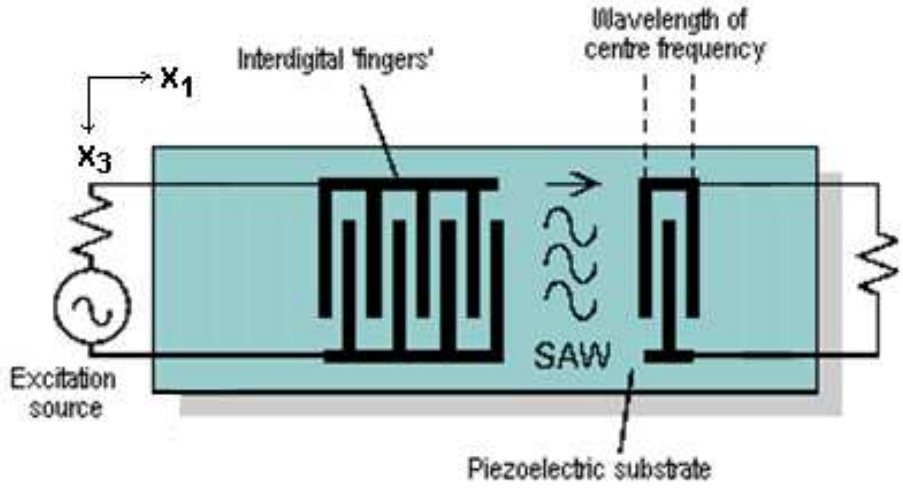

Figure 2.5 Surface acoustic wave device [27]

Table 2.1 Parameters of some typical piezoelectric substrates for SAW devices [40]

Material	**Crystal Cut**	**SAW Axis**	**Velocity, V_R(m/s)**	**K^2(%)**
Quartz	Y	X	4990	1.89
$LiNbO_3$	Y	Z	3158	4.5
$LiNbO_3$	128°	X	3992	5.3

There are different designs for the SAW device electrodes or IDTs according to the purpose of the application. This includes a straight interdigital transducer of a conventional SAW device, and focused interdigital transducer of a focused SAW device, which concentrates the acoustic wave in a single point on the substrate surface [46], as shown in Fig.2.6. For research purposes, the first design of parallel IDTs has been considered in this thesis, for which the SAW devices could be efficiently excited if

the wavelength of a SAW, λ, matches the periodicity, P, of the IDTs (e.g., $\lambda \approx$ P)[40], as sketched in Fig. 2.6(a). This is achieved when the IDTs of the SAW device excited by a design frequency, *f*, defined by the following equation [40, 47]:

$$f = \frac{V_R}{\mathrm{P}} \tag{2.12}$$

where, V_R denotes the propagation velocity of the Rayleigh wave in the substrate, as listed in Table 2.1. Normally, the SAW wavelengths are in a micrometer range, and the wave amplitudes (e.g., the normal displacement of the surface, seen in Fig. 2.4(a)), are in a nanometre range [1, 48].

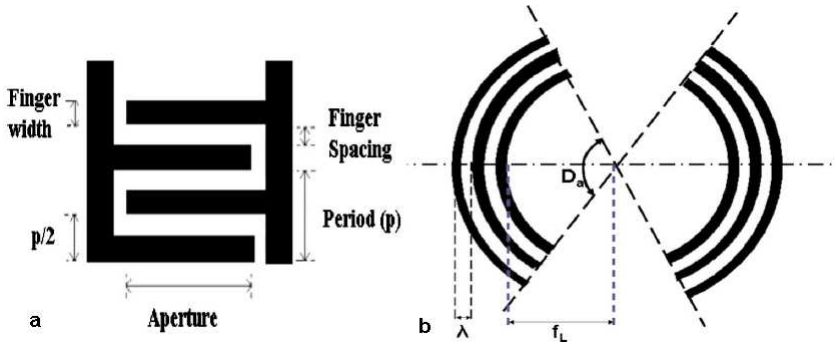

Figure 2.6 Schematic illustration of the IDTs on the substrate surface for; (a) parallel IDTs of a conventional SAW device; (b) curved IDTs of focused SAW device, where D_a is the degree of arc and f_L the geometric focal length [46]

2.4 Raleigh Wave with Liquid Loading

So far, the characteristic behaviours of a Rayleigh surface acoustic wave propagating along a free surface of the piezoelectric elastic crystals have been explored [49]. In this section, a Rayleigh wave propagating on a surface of liquid-loaded piezoelectric crystals is considered, and the basic theoretical ideas are discussed, describing the influences of an adjacent fluid to the solid surface on the characteristics associated with Rayleigh wave propagation.

2.4.1 Attenuation by ambient media

Earlier in this chapter (e.g., Sect. 2.3.2), it was indicated that the elliptical motion of the surface particle in a Rayleigh wave has two components, one is normal to the surface u_3 and the other is tangential u_1. When a liquid medium is loaded on the free surface of the piezoelectric crystal, the normal component couples with a liquid layer, causing

changes in the density of an adjacent fluid layer [50]. This leads to the emission of compressional (longitudinal) waves into the fluid medium. In the same time, the tangential component is coupled to the adjacent fluid via the liquid viscosity μ [50], which leads to frictional losses. However, any matter exposed to the surface of the substrate along the SAW propagation, especially liquids absorbs a certain part of the SAW energy, causing a strong interaction between the liquid and SAW [47]. Both the emission of longitudinal waves and friction losses would contribute to the attenuation of a Rayleigh wave, inducing a new wave mode, know as a Leaky Rayleigh wave [51]. In the following sections, the attenuation of the Rayleigh wave due to the emission of longitudinal compressional waves will be discussed first, followed by the attenuation due to frictional loss.

2.4.1.1 *Attenuation by emission of compressional waves*

As indicated previously, when a liquid layer lying on the free surface of a piezoelectric substrate, the normal component of the particle motion associated with the surface waves couples with the adjacent liquid, resulting in an emission of longitudinal waves into the liquid, as illustrated in Fig. 2.7(a). Because the velocity V_f of longitudinal sound waves in the liquid is less than that of a Rayleigh wave in solids, V_R, these waves will be radiated into the fluid at an angle θ, known as Rayleigh angle θ_R [50]:

$$\sin\theta_R = \frac{V_f}{V_R} = \frac{\lambda_f}{\lambda} < 1 \tag{2.13}$$

Where, λ_f is the wavelength of longitudinal waves in the fluid and λ the wavelength of a Rayleigh wave or SAW, as shown in Fig. 2.7(a). The value of Rayleigh angle θ_R, is about 23º, for 128º YX-$LiNbO_3$ substrate [52]. The portions of acoustic energy leaked into the adjacent fluid and the attenuation of the associated Rayleigh wave were given in details by Dransfeld and Salzmann [50]. For a surface layer element with a thickness of λ and a solid substrate of width b, as shown in Fig. 2.7 (b), the energy E transferred per second through the surface element by the Rayleigh wave can be expresed as [50]:

$$E = \lambda b 2\pi^2 \rho V_R^3 (a/\lambda)^2 = \frac{2\pi^2 b \rho V_R^3 a^2}{\lambda} \tag{2.14}$$

where, ρ is the desnsity of the solid substrate and a is the amplitude of the Rayleigh wave using the normal componet of the particle displacement [50]. As both the amplitude of the longitudinal wave in the adjacent fluid layer and the amplitude of the Rayleigh wave at the substrate surface are similar, the acoustic energy dE emitted by the substrate surface into the adjacent fluid is expressed as [50]:

$$\boldsymbol{dE = 2\pi^2(b\,dx)\rho_f V_f^3(a/\lambda_f)^2 = 2\pi^2(b\,dx)\rho_f V_f V_R^2(a/\lambda)^2} \quad (2.15)$$

Here, ρ_f is the fluid density. The emission of an acoustic energy into the fluid medium results in an energy loss of the Rayleigh wave with an absorption coefficient α_L, which was estimated to be [50]:

$$\boldsymbol{\alpha_L = (1/E)\,dE/dx = \rho_f V_f/\rho V_R \lambda} \quad (2.16)$$

Typically, the amplitude of the Leaky (damped) Rayleigh wave attenuates to 1/e of its initial value over a distance of a few wavelengths from its coupling with the fluid [50].

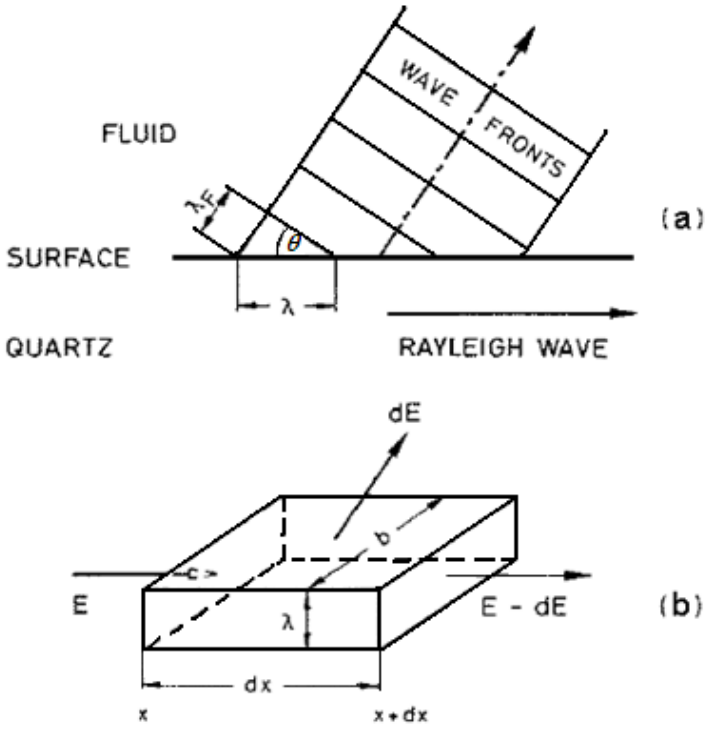

Figure 2.7 An illustration of (a) Rayleigh wave attenuation by radiating longitudinal waves from the substrate into the adjacent liquid at an angle $\boldsymbol{\theta}$ of $\boldsymbol{\theta_R}$; (b) an element of the solid surface showing the leakage of Rayleigh wave energy into the fluid [50].

2.4.1.2 *Attenuation by viscous friction*

The energy loss due to the coupling of the tangential component of the surface particles of associated Rayleigh wave into the adjacent liquid layer was studied in detail by Dransfeld and Salzmann [50], using the same surface element shown in Fig. 2.7(b). If $\dot{a}$ is the tangential componet of the particle displacement amplitude of the surface wave, the dissipated acoustic energy, $d\dot{E}$ by viscous forces at the adjacent fluid layer to the surface area $b\ dx$ of the substrate element (see Fig. 2.7(b)) can be expressed as [50]:

$$d\dot{E} = \frac{1}{2}(\mu/\delta)V_0^2\ b dx \tag{2.17}$$

Here, V_0 is the tangential particle velocity at the surface-liquid interface, and μ is the fluid viscosity. The term δ is the decay length for the adjacent liquid velocity due to the viscous coupling of the shear wave component to the adjacent fluid (i.e., a measure of effective thickness of the boundary layer driven by the shear wave) [50],

$$\delta = 2\pi(2\mu/\rho_f\ \omega)^{1/2} \tag{2.18}$$

From Eq. (2.14) using $\dot{a} = V_0/\omega$, the shear energy flow in the Rayleigh wave along the substrate surface can be given as [50]:

$$\dot{E} = \frac{1}{2} b\rho V_R V_0^2 \lambda \tag{2.19}$$

Therefore, the corresponding energy loss of the Rayleigh wave due to the presence of frictional viscous forces can be described by the absorption coefficient α_s, which is estimated to be [50]:

$$\alpha_s = \left(1/\dot{E}\right) d\dot{E}/dx = \frac{(\rho_f \mu \omega^3/2)^{1/2}}{4\pi^2 \rho V_R^2} \tag{2.20}$$

Typically, the contribution of the viscous losses in the attenuation of the Rayleigh wave is negligible in comparison with the contribution of the longitudinal waves, i.e., $\alpha_s \ll \alpha_L$ [50, 53].

2.5 **Internal Streaming**

So far, it has been shown that when a liquid layer (e.g., liquid droplet shown in Fig. 2.8) lies on the free surface of the SAW device, the Rayleigh wave establishes an emission of longitudinal pressure waves upon its arrival at the boundary between the solid (substrate) and the liquid. Due to the mismatch in the sound velocities between the solid and the liquid medium, these waves were diffracted into the liquid by an angle known as a Rayleigh angle θ_R, as shown in Fig. 2.8. In addition to this, the emission of longitudinal waves into the fluid results in the attenuation and damping of the Rayleigh wave within a few wavelengths underneath the liquid, which changes its mode into a Leaky SAW (LSAW) [52], as seen in Fig.2.8. This interaction between the fluid and the SAW results in the body force acting on the fluid volume, known as the acoustic streaming force [54]. These forces are referred to the action of Reynolds' stress of the fluctuating flow due to sound wave propagation into the liquid medium, which can be expressed as [55, 56]:

$$\boldsymbol{\sigma_{ij} = \rho_f \overline{U_i U_J}} \tag{2.21}$$

where, the symbols of i and j = 1, 2, 3 are the fluctuating components of the flow velocity, U, in the three coordinates x, y and z, respectively, while the upper bar indicates the mean value of these velocities products [55]. The spatial gradient of the Reynolds' stress due to velocity fluctuations results in a steady force F_j acting in the body of fluid medium within the propagation distance, which can be written as :

$$\boldsymbol{F_j = -\sum_{i=1}^{3} \frac{\partial \overline{\rho_f U_i U_J}}{\partial x_i}} \tag{2.22}$$

These forces can induce an internal circulation into the liquid droplet, known as acoustic streaming [29, 57], if the acoustic power is high enough (see Fig. 2.8 for more details).

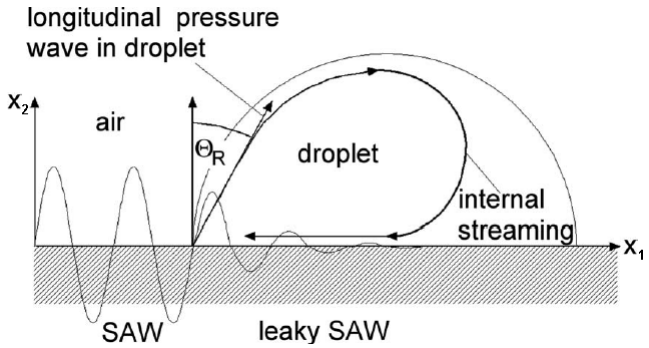

Figure 2.8 Sketch of SAW stream acting on liquid droplet [58]

Furthermore, an increase in the applied power can cause movement of the droplet in the SAW propagation direction, depending on the droplet volume and substrate surface treatment [17]. Moreover, if the intensity of SAW power is increased further, the droplet will be atomised [21]. According to Uchida et al. [59], these SAW induced longitudinal waves are significantly influenced by the viscosity of the liquid, and their attenuations are much higher than those excited by any conventional ultrasonic resonator. The transformation from a SAW into a LSAW depends on the viscosity and density of the fluid loaded on the substrate surface. An analytical formula for the streaming force of a LSAW has been derived based on Nyborg's theory of acoustic streaming [54]. Both experimental and theoretical studies showed that the SAW streaming force is strong enough to induce internal streaming inside the droplets or eject small liquid particles from liquid layers in contact with the SAW. It has been concluded that SAW streaming depends on the frequency, power and aperture of the SAW in addition to substrate surface, fluid volume and viscosity [60-62].

2.6 **Summary**

In this chapter, some basic background of the concepts and the theories that are necessary for understanding the principle of the SAW generation, propagation and excitation using the piezoelectric materials, were introduced. The influence of liquids loading on the characteristic behaviours and mode of an excited SAW is also shown.

Chapter 3

LITERATURE REVIEW

This chapter gives a review of the research work that has been achieved on surface acoustic waves based microfluidics; focussing on the relevant studies that have been previously conducted using SAW in the different LOC applications. This is divided into two main section; experimental studies and numerical studies.

3.1 Experimental Study of SAW-Based Microfluidics

Recently, there have been many approaches utilising the streaming phenomenon of SAW liquids coupling in numerous engineering applications for digital microfluidics [49]. In the following sections, a review on SAW technology and their current microfluidic applications is presented.

3.1.1 SAW for acoustic mixing

Mixing of reagents inside small liquid volumes is an essential process in many chemical and biological applications. However, this is a difficult task due to the small dimensions of fluids being considered, especially when sessile droplets are used [22]. In this context, SAW-induced streaming (see Fig. 2.8) can be utilised to overcome such microfluidic limitations. The experimental work of Wixforth (see Fig. 3.1) [16] showed that a small amount of fluorescent dye spot deposited on the substrate surface just before a 50 nl water droplet was placed on top of it, was quickly dissolved and distributed into the whole droplet volume after applying the SAW; this is due to the internal acoustic streaming induced inside the droplet. Figure 3.1 shows two snapshots of this mixing process, which were taken half a second apart[16]. As can be seen from Fig. 3.1, the induced acoustic streaming can be used to mix the dye particles inside the droplet effectively, a phenomenon which is a good indication towards the possibility of dissolving chemical species in small droplets using the SAW technique [16].

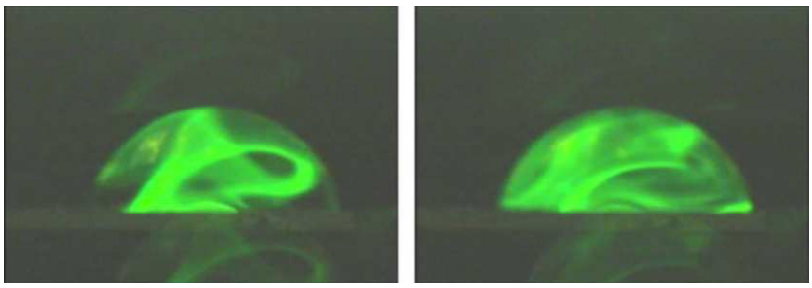

Figure 3.1 Snapshots of SAW-induced internal streaming in a 50 nl droplet, showing the dissolving process of a dye spot deposited on a SAW device surface [16]

Kulkarni et al.[63] has introduced a new approach for chemical synthesis on small scale droplets (of about 40 nl), utilising the surface of a piezoelectric substrate as a reactor and the SAW as an actuation technique and energy source at high applied powers, as shown in Fig. 3.2. In general, the authors have demonstrated a new approach for enhancing chemical reactions in droplets volumes utilising SAW energy, where fast reactions and clean chemical products can be achieved.

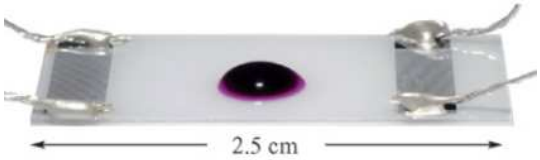

Figure 3.2 Photo of a ~ 40 nl droplet on the surface of SAW device that was used during a chemical reaction experiment [63]

The SAW induced mixing works not only in an open geometry like sessile droplets, but also in closed fluid geometries. For example, Frommelt et al. [64] reported that after applying a SAW, the fluorescent beads in a water droplet (~ 0.35 µl) confined by a gap space (~ 240 µm) between a top glass slide and a substrate surface, were effectively mixed in a short time period in comparison with the time that the pure diffusion would take. Figure 3.3 shows experimental images of mixing snapshots taken at a certain time after applying the SAW power. As can be seen from the images, the frequency modulation plays an essential role in the characteristic behaviours of a SAW induced mixing. Maezawa et al. [65] has expressed a similar view, where he demonstrated that the sweep in the driving frequency resulted in changes in the flow profiles, showing an improvement in the mixing performance and time in which a SAW was coupled to the fluid through the bottom of a cell cavity, as shown in Fig. 3.4.

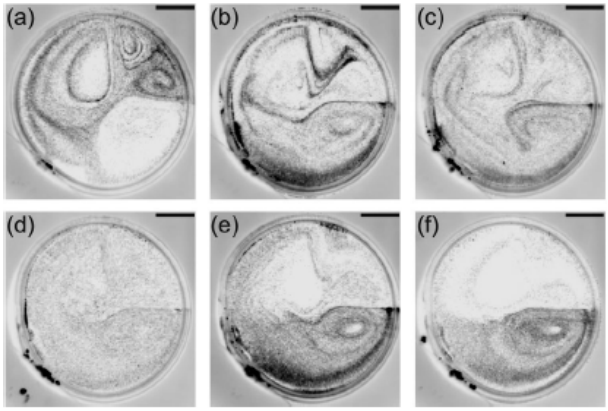

Figure 3.3 Top view series images of the mixing experiments of beads in a confined water droplet taken about 105 s after applying the SAW power, using an 128º Y-cut $LiNbO_3$ piezoelectric substrate for different modulation frequencies; The SAW device was operated at a constant power in (a), and (b)-(f) modulated at frequencies 0.042, 0.083, 0.17, 0.34, and 0.68 Hz, respectively [64]

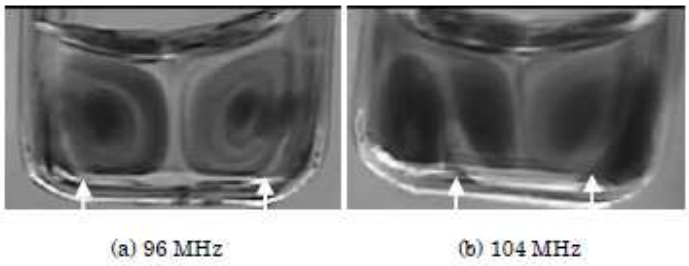

Figure 3.4 Fluid streaming induced by an IDT fitted at the bottom of the cell, the solid white arrows indicate to the source points, where the higher driving frequency is, the smaller distance between the two sources [65]

According to Frommelt et al. [64] and Maezawa et al. [65], the modulation of signal frequency contributes to the chaotic advection, which in turn results in mixing of the system in an effective manner. Recently, the work of Shilton et al. [22] provides evidence of such chaotic advection in the SAW system by comparing the flow trajectories of fluorescence particles inside microfluidic wells (see Fig. 3.5(a)) with other new trajectories over the time, as shown in Fig. 3.5(b). Their results showed that the strength of chaotic advection was increased with an increase in the SAW applied power, and hence the mixing performance of SAW induced streaming. This was attributed to the increase in streaming velocity of the particles that resulted in an intensification of the disturbances in the fluid [22]. In addition to this, it was observed that the viscosity of the fluid also influences the strength of a chaotic advection, which is decreased for an increased fluid viscosity. This increase in the fluid viscosity suppresses the flow velocity that gives rise to the disturbances in the fluid, which are necessary for the a chaotic advection to induce effective acoustic mixing [22].

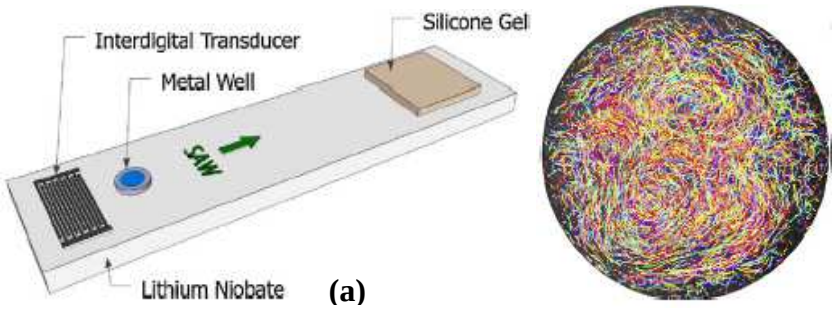

Figure 3.5 (a) Schematic illustration of experimental setup; (b) Tracked trajectories of fluorescence particles in a microfluidic well induced after SAW-fluid coupling [22]

Furthermore, SAW induced mixing in closed channels have also been demonstrated [58, 66]. Sritharan et al. [58] has investigated the mixing performance of SAW-induced streaming in a simple Y-shaped microchannel, where the IDT of the SAW device was fitted underneath the channel and near the Y-junction, as depicted in Fig. 3.6 (a). The channel was fabricated using Poly Dimethyl Siloxan (PDMS) with a height of 75 μm and a width of 100 μm. The channel contains two water inlets, with one of them containing fluorescent beads, as shown in Fig. 3.6 (a) and (b). Figure 3.6 (c) shows that before applying the SAW power, the flow in the microchannel was completely laminar, where the separation line between the two fluids can be easily distinguished. Whereas, coupling of a SAW with the fluids through the bottom of the channel induced effective mixing in the channel flows, as shown in Fig. 3.6 (d). The detailed results of the evaluated mixing efficiency suggested that a higher SAW amplitude is, the more efficient mixing was achieved with decreasing distance from the channel entries [58].

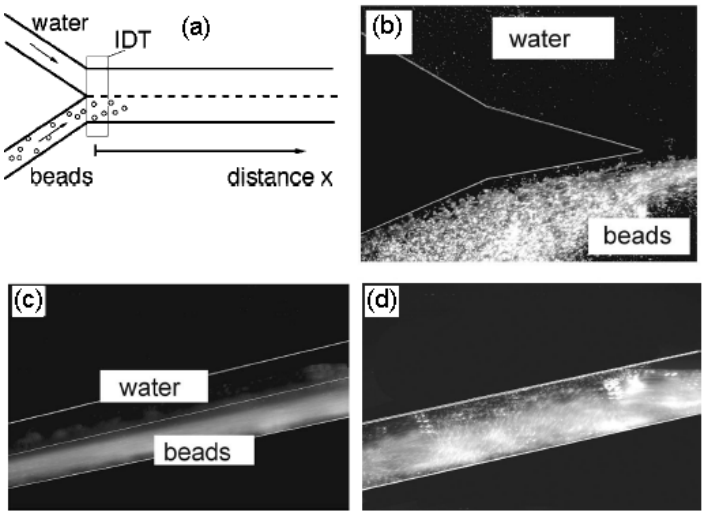

Figure 3.6 Sketch and illustration of a microchannel used in the investigation of SAW induced mixing; (a) Sketch showing the setup used during experiment; (b) Image

showing the distribution of the fluorescence bead at Y-junction; (c) Image of the channel flow when the SAW was not operated; (d) Image of the channel flow with SAW excited from underneath the channel [58]

More recently, Zeng et al. [67] also reported an investigation of SAW induced mixing in a Y-type microchannel. In his study, the launched SAW coupled transversally to the flowing fluid into the bonded PDMS microchannel, using focused IDTs, as shown in Fig. 3.7 (a). The dimensions of the fabricated microchannel were 240 μm in width and 85 μm in height, and the microchannel was bonded to the top surface of a $LiNbO_3$ piezoelectric substrate. Deionized (DI) water and fluorescent dye solution were injected inside the microchannel during the experiments. It was observed that when a SAW was excited, the fluorescent dyes were quickly mixed with the water inside the channel. It can be easily observed from the images of Figs. 3.7 (b) and (c) that the fluids were homogenously mixed in the presence of a SAW. The mixing performance was characterised through measurement of the variations in the intensity of florescence dye that extracted from the images of mixing process at a specific region, as shown in Figs. 3.7 (c)-(e). The normalized dye concentrations were obtained by comparing the obtained fluorescent intensities with the peak intensity of an original dye [67]. These profiles in Figs. 3.7 (d) and (e) indicate that a nearly uniform distribution of fluorescent dye was observed across the width of the channel after the SAW was launched, showing the effectiveness of the proposed technique in mixing these two fluids.

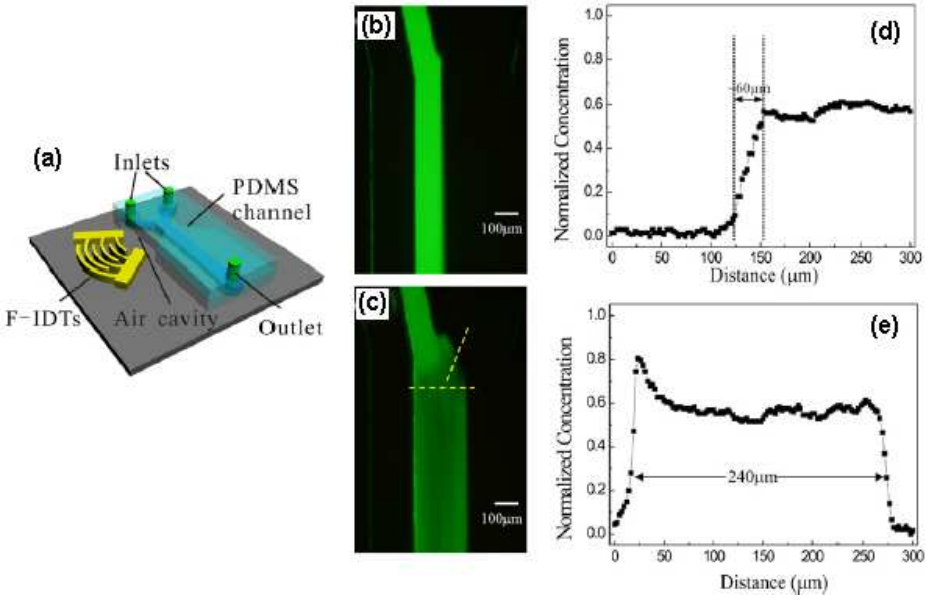

Figure 3.7 Characteristics of SAW-induce mixing in a Y-type PDMS microchannel; (a) Illustration showing the position of F-IDTs with the bonded microchannel; (b) No mixing was induced without a SAW ; (c) Mixing observed after the SAW was excited;

(d) and (e) Normalized concentration of fluorescent particles measured along the width of channel for no-SAW and SAW cases, respectively [67]

3.1.2 SAW for particles concentration

A study by Li et al. [68] revealed that the phenomenon of SAW induced streaming can also be used to concentrate microparticles distributed in a liquid droplet. It has been demonstrated that asymmetric positioning of the droplets in the SAW propagation path (see Fig. 3.8(a)), or making a diagonal cut in the substrate (see Fig. 3.8 (b)), results in an asymmetric distribution of a SAW radiated across the substrate surface and coupled to the liquid, which is in turn induces an azimuthal flow circulation in the droplet [68]. Monitoring of the fluorescent particles and live yeast cells inside the liquid droplets after applying the SAW power showed that the induced flow circulation causes migration of particles or cells towards the centre of the droplet and clustering at its base within time period ranging from two to twenty seconds, depending on particles type, size, and applied power to the SAW device (see Fig. 3.9). The concentration time was decreased with an increase of the applied power, due to increased an inward radial force of shear gradient that drives the particles towards the droplet centre [68]. A study by Shilton et al. [69] reported that the internal flow circulation was enhanced when the excited SAW on a 128º YX-$LiNbO_3$ substrate was focused through using curved IDT patterns (see Fig. 2.6(b)), which is attributed to the increased wave amplitude. Consequently, a concentration of fluorescent particles suspended in a 5 μl water droplet was achieved quickly in a shorter time than that of the straight IDTs.

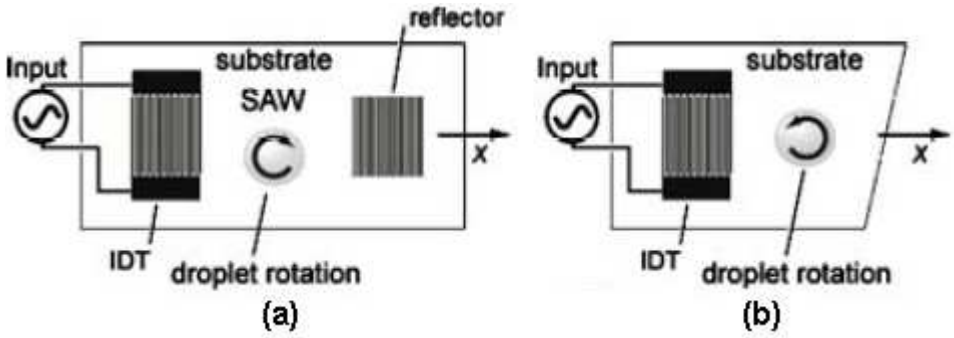

Figure 3.8 Schematic illustration for breaking the symmetry of SAW propagation; (a) A droplet positioned asymmetrically in the SAW propagation path; (b) Piezoelectric substrate with a diagonal cut[68]

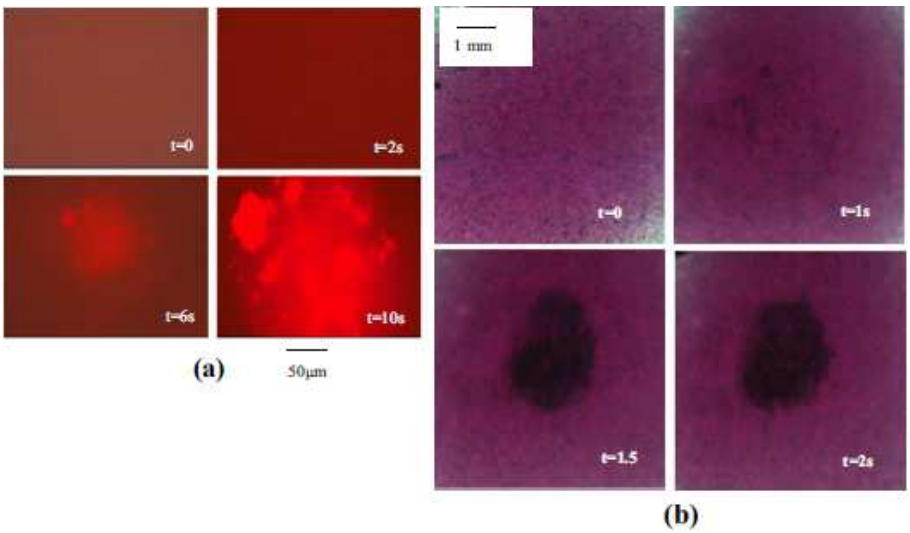

Figure 3.9 Snapshots showing the concentration process in a 5µl liquid droplets, using a SAW device of 128º YX-$LiNbO_3$ substrate with straight fingers pattern of a 1200 µm aperture and ~ 8.6 MHz signal frequency at an RF power of 330 mW; (a) Images showing accumulation sequence of fluorescent particles at the droplet centre of 1µm in diameter ; (b) of live yeast cells that quickly concentrated at the centre of the droplet, in 2 s [68]

So far, many studies have been reported utilising SAW-induced streaming for particle concentration [15, 24, 70-72]. For example, Wilson et al. [72] has demonstrated that it is possible to concentrate blood cells into small samples of diluted blood using SAW together with a phononic structure. Figure 3.10 shows the rapid concentration of the blood cells in a 10 μl droplet within a short time, which was dependent on the SAW frequency and power [72].

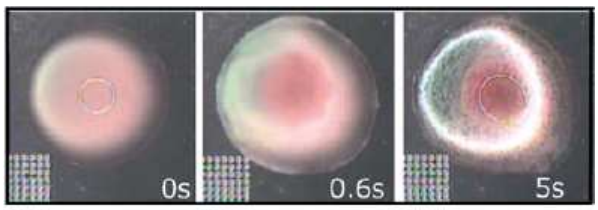

Figure 3.10 Sequence images of blood cell concentration using a diluted blood sample of a 10 μl droplet volume, based on 128º YX-$LiNbO_3$ SAW device with a straight IDTs aperture of 1 mm at power of 10^3 mW, with phononic crystal structures [72]

3.1.3 SAW for particle focusing and sorting

Recent advances in biological studies have drawn attention of many researchers to develop an effective, compact, and non-destructive actuation system that can treat particle and cells individually for Lab-on-Chip technology. Shi et al. [73] proposed a novel method for focusing microparticles in microfluidic channels utilizing a standing surface acoustic wave (SSAW). SSAW can be launched by using a SAW device with

pairs of IDTs that are aligned on either sides of the microchannel, as shown by the schematic illustration of device in Fig. 3.11(a). The interaction of two excited waves from both the IDTs results in the generation of a standing wave, which in turn induces a periodic distribution of pressure nodes and anti-nodes in the fluid medium inside the microchannel [73]. Thus, the induced acoustic radiation forces by a fluctuating pressure cause the suspended particles in the fluid to move towards the pressure nodes or anti-nodes, depending on its density and fluid property [73]. However, if the channel width is designed to have only one pressure node, the particles will be focused in the centre of channel, as shown in Fig. 3.11(a). Using a PDMS microchannel measuring 50 μm wide and 1.3 cm long bonded to the surface of a 128º YX-$LiNbO_3$ SAW device, polystyrene particles of 1.9 μm in diameter were focused in the channel centre after the SSAW interacted with the fluid [74], and the subsequent tracking images showed that the trapped particles were distributed uniformly across the channel width, as demonstrated in Fig. 3.11(b).

Shi et al. [75, 76] also found that the SSAW device was capable of separating particles of similar density in a microfluidic channel based on its size, where the particles were aligned separately into the channel, as shown in Fig. 3.12. This is because the acoustic radiation force exerted on a particle is proportional to its volume (r^3), whereas the viscous force is only proportional to the particle radius (r) [75]. The particles with larger volumes will move towards the pressure nodes in the microchannel faster than the smaller particles. Therefore, the particles in the microfluidic channel can be separated based on size, as shown in Fig. 3.12.

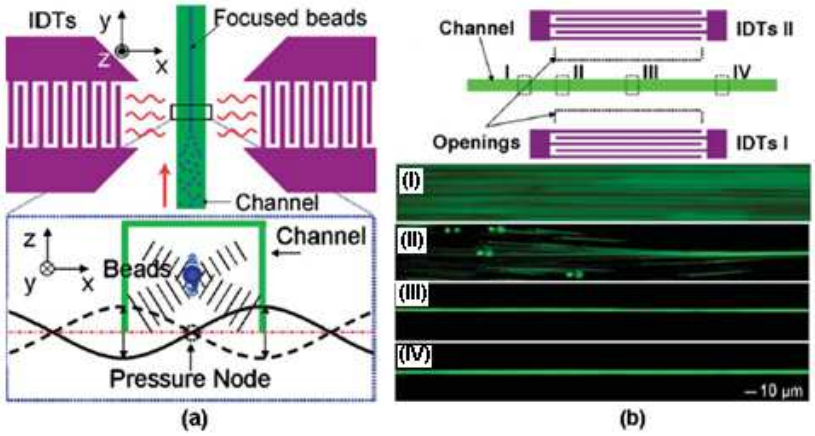

Figure 3.11 (a) Schematic illustration of a SSAW device inducing particle focusing with demonstration showing its working mechanism; (b) Focusing of polystyrene beads in the centre of a PDMS microchannel, which was monitored at different position [73]

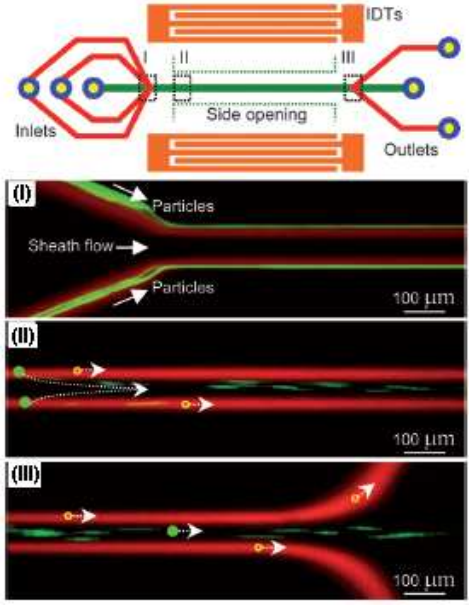

Figure 3.12 The top sketch indicates the monitored sections (I-III) of particles separation in a PDMS channel measuring 150 μm width and 80 µm height bonded on a 128º YX-$LiNbO_3$ piezoelectric substrate; the bottom image shows the fluorescent images at the sections (I-III), where the green colour indicates polystyrene beads of 4.17 µm in diameter and red colour indicates the 0.87 μm beads, where the beads were separated in ~360 ms [75]

Meng et al. [77] demonstrated that the position of particles within the microfluidic channels can be changed by a phase-shifting between the two input signals of opposite IDTs, which results in changes in the position of pressure nodes of the SSAW. Accordingly, the acoustic radiation forces exerted on these particles will be changed also [77]. Therefore, the particles will move to a new position, depending on a phase deviation. Similar work has been reported by [78] and [79].

3.1.4 SAW for fluid pumping

As discussed before, a SAW-fluid interaction at relatively small acoustic powers induces acoustic streaming within small droplets, a phenomenon which can be used to mix different chemical or biological species. However, if the applied SAW power is increased to some extent, the streaming phenomenon can cause a deformation to the droplet free-surface, which eventually leads to the movement of the droplet into the direction of SAW propagation, if the substrate surface is chemically t pre-treated (e.g., hydrophobic surfaces). Wixforth [16] reported an experimental work in which a water droplet was placed on the surface of a piezoelectric substrate against the propagation direction of an intensive pulsed SAW, i.e., coming from the left side in Fig. 2.20. Once the SAW interacts with the droplet, an internal acoustic streaming was observed inside

the droplet, which causes the droplet deformation and droplet shooting, as depicted in Fig. 3.13.

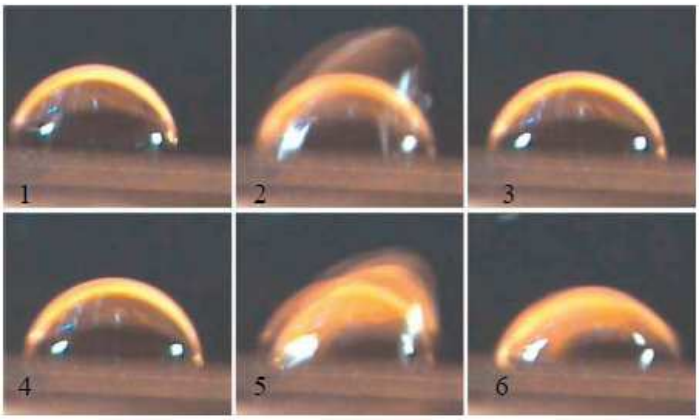

Figure 3.13 Deformation and pumping of a 50 nl water droplet on the surface of a $LiNbO_3$ SAW device. In pictures 2 and 5, the droplet is under an intensive pulsed SAW. In pictures 3 and 6 the droplet returns to its original shape after the SAW is turned off [16]

Figure 3.14 depicts snapshots of series of images taken during the experiments, showing the programmable movement of three droplets on the surface of a microfluidic chip that contains multi-programmable IDTs. Three droplets were moved individually on this chip using a SAW-induced streaming. The author reported that after the droplets were merged, acoustic streaming within the new droplet led to a faster chemical reaction than that of the normal diffusion process [16].

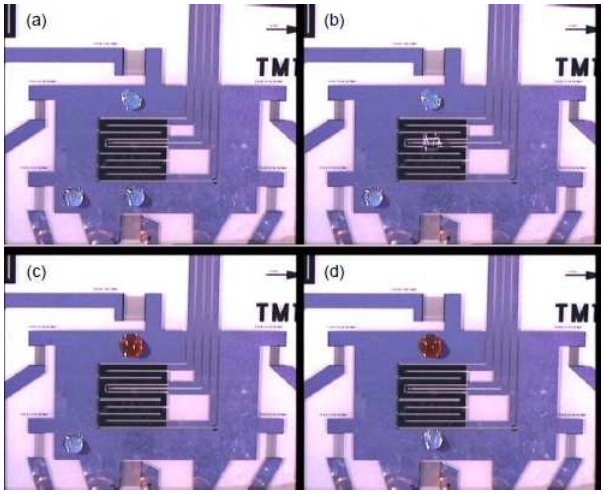

Figure 3.14 Snapshots of a SAW-driven microfluidic process for three droplets of ~ 100 nl in volume each; (a) initial state; (b)-(d) a series of images presents the movement of droplets and the occurrence of a chemical reaction (e.g., colour change) after the droplets were merged [16]

Beyssen et al. [80] experimentally studied the motion of different types of liquid droplets, ranging from 2 to 20 μl in volume on the surface of a 128º YX-$LiNbO_3$ piezoelectric substrate. An IDT of a 5 mm aperture and an excitation frequency of ~ 40 MHz were used for experiments. Results showed that the fluid viscosity strongly influences the pumping speed of droplets. The speed of a water droplet decreased from 40 mm/s to 2 mm/s when a mixture of water/glycerol was used instead of water. Tracking of the droplet motion using a high-speed camera revealed a periodic vibration/pumping phenomenon of droplets during their motion, as shown in Fig. 3.15. Du et al. [17] has conducted an experimental study investigating SAW-induced streaming and actuation (pumping) of liquid droplets. Results demonstrated that both the droplet size and applied voltage have significant influences on the pumping speed of droplets, which was increased with an increase in the signal voltage, as demonstrated in Fig. 3.16. It can be shown that the droplets with smaller volumes moved at a speed faster than those of larger volumes, and a maximum velocity of ~140 mm/s for a 1 μl water droplet at an applied signal of 40 V. However, when the surface of a piezoelectric substrate was not hydrophobically treated, a signal voltage of up to a 45 V was not enough to cause the droplets to move on this chip, and only droplet deformation was observed. In contrast, significant pumping can be realised easily after the substrate surface was treated with Octadecyltrichlorosilane [17, 19, 81].

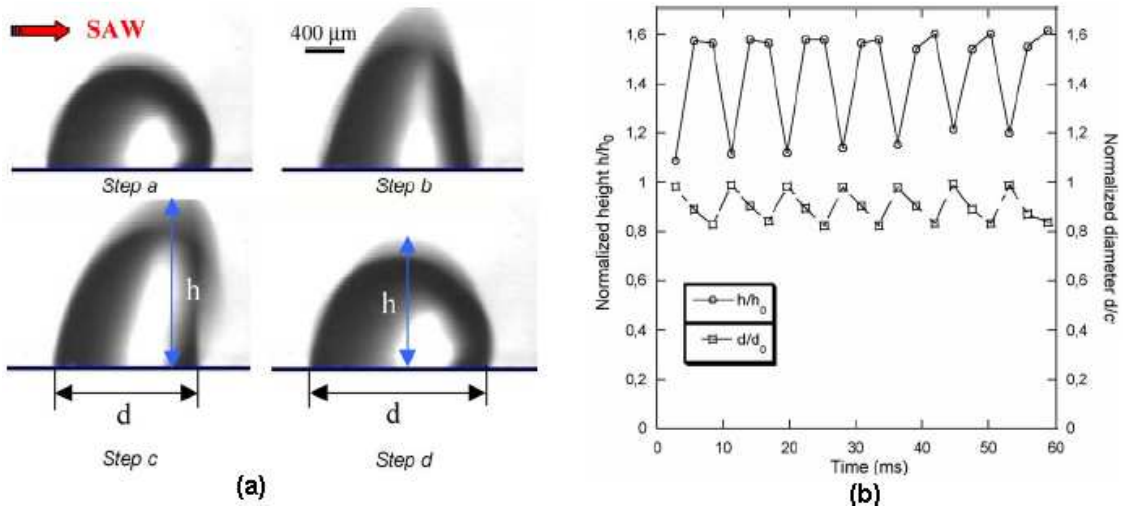

Figure 3.15 Periodical distortion of a 2 μl water droplet; (a) Subsequence images taken at time steps 0, 0.0028, 0.0056 and 0.0084 s, respectively using a high-speed camera; (b) Evaluated changes in droplet height h_0 and d_0 [80]

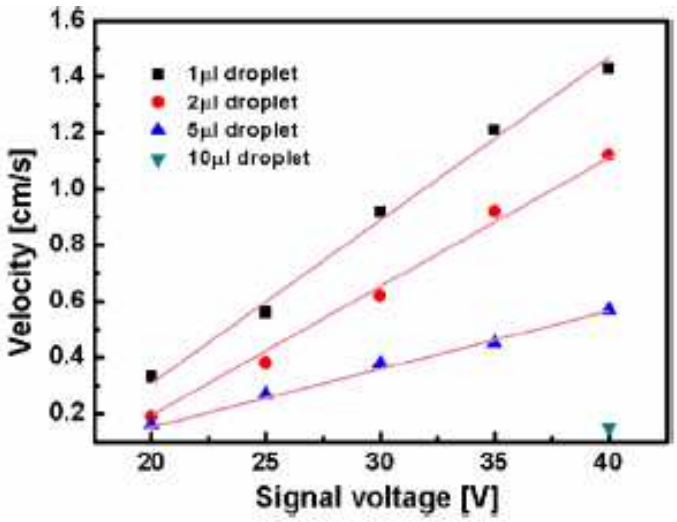

Figure 3.16 Sliding velocity of water droplets as a function of applied voltage for a $LiNbO_3$ treated with Octadecyltrichlorosilane [17]

SAW technology has also been demonstrated to pump fluids in closed microfluidic systems. Renaudin et al. [61] reported the squeezing of 1.5μl water droplets through a gap of 300 µm in height between a top plate and a $LiNbO_3$ piezoelectric substrate, as sketched in Fig. 3.17(a). When a hydrophobic guided layer was used, the droplet was moved faster in a straight trajectory. Otherwise, the droplets moved in a wavy trajectory on a hydrophilic area, as shown in Fig. 3.17(b).

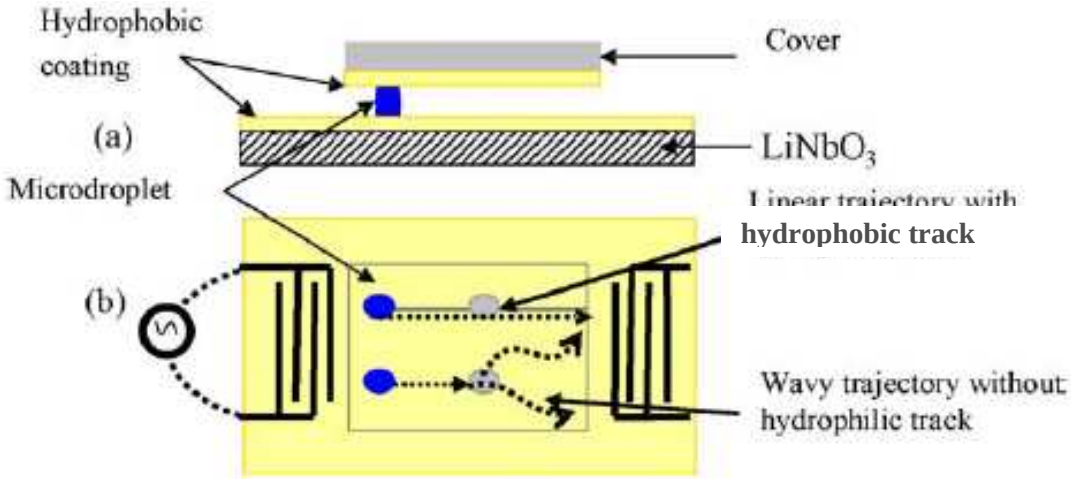

Figure 3.17 Sketch of a SAW-driven guided droplet system; (a) Side view; (b) Top view[61]

Girardo et al. [82] also reported SAW-induced pumping for fluids in a closed microchannel. PDMS microfluidic channels of lateral dimensions between 210 and 520 μm are deposited on a $LiNbO_3$ substrate, which was aligned along the propagation path

of a SAW, as shown in Figs. 3.18 (a) and (b). A water droplet of ~ 2 µl was placed at the opposite end to the IDTs (see Fig. 3.18 (c)). When an RF signal was applied to the SAW device, the droplet was extracted into the channel towards the other channel end due to atomisation and condensation of water drops within the microchannel. During the experiments, the speed of forced water into the microchannel reached up to 2.6 mm/s, as shown in Figs. 3.18 (d)-(f). Although a high power up to 1 W was needed to induce an efficient pumping, a SAW-driven fluid extraction demonstrated an attractive method for withdrawing fluids in LOC systems of biological applications. Similar work has been reported by Cecchini et al. [83], where a counter-flow of fluid into a PDMS micro-channel was induced by a SAW.

More recently, Masini et al. [84] demonstrated that the SAW-induced counter-flow mechanism is capable of withdrawing fluids in a complex web of microfluidic channels. Figure 3.19 shows geometrical configuration of a PDMS microfluidic network that was mounted onto a $LiNbO_3$ SAW chip. As can be seen, multiple IDTs were patterned onto the chip for a programmable fluid driving. The widths of the channels ranged from 200 to 300 μm, with a width/height ration of 10:1. The results showed that a water droplet of about 0.5 μl was successfully extracted into the network, and the speed of droplet in each microfluidic path is dependent on the power applied to the active IDTs and the distance between them and the droplet [84].

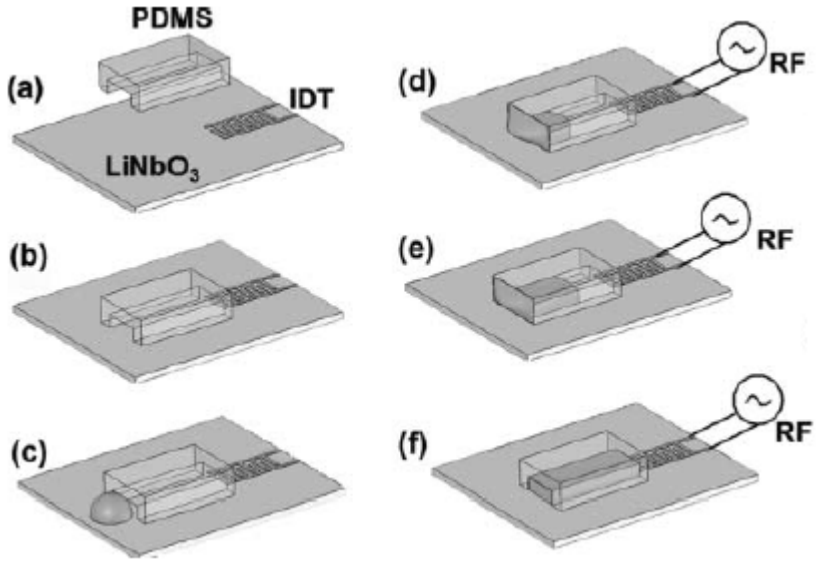

Figure 3.18 Experimental configuration of SAW-induced pumping in a microchannel; (a)-(b) demonstrating the placement of the PDMS channel on a $LiNbO_3$ substrate, and a 2 μl water droplet; (d)-(e) Withdrawing of the droplet after applying the electric signal [82]

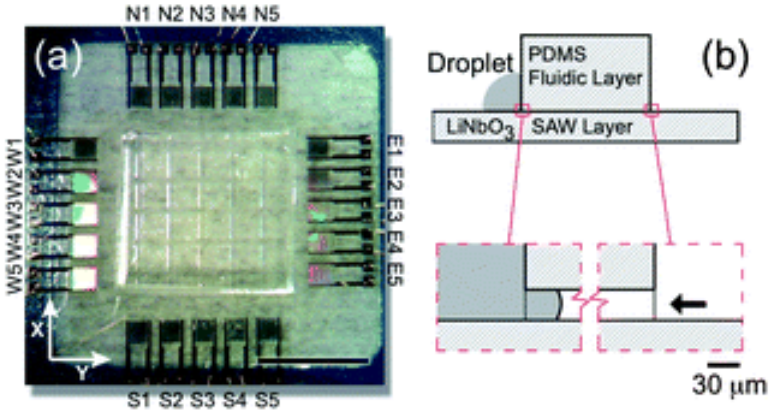

Figure 3.19 (a) Top view image showing the whole microfluidic chip that contains multi IDT's; (b) Side view sketch showing the water droplet placed at the channel entrance [84]

3.1.5 SAW for fluid jetting and atomization

More than twenty years ago, Shiokawa et al. [52, 85, 86] reported a jetting phenomenon of a liquid layer coupled with a SAW. When the applied power to the SAW device exceeded a certain peak value, discrete particles were ejected from the liquid layer at an ejection angle equivalent to a Rayleigh angle θ_R, forming jet streams [85], as shown in Fig. 3.20 (a). The wave was excited using a classical straight IDT design, which was patterned on a 128º YX-$LiNbO_3$ substrate with an aperture of 2 mm, using an excitation frequency of 50 MHz. Bennes et al. [87] found that the jetting phenomenon is strongly dependent on the hydrophobic nature of a substrate surface. On a hydrophobic surface, narrow bands of water jet were observed. In contrast, multi water jets with an increased number of unidirectional droplets were observed for a hydrophilic surface, as seen in Fig. 3.20 (b) and (c).

More recently, research by Tan et al. [20] suggested a new approach for a SAW-induced jetting phenomenon utilising a couple of opposite focused IDTs (FIDTs), similar to what has been sketched in Fig. 2.6 (b). The FIDTs were fabricated on a 128º YX-$LiNbO_3$ piezoelectric substrate with a wavelength of ~ 200 μm. The radiation of surface acoustic waves at Rayleigh angles from both sides into a water droplet placed on the IDT's focal point resulted in a deformation of water droplet, which was elongated vertically forming a coherent cylindrical liquid beam, as shown in Fig. 3.21 (a). Near to the finishing of jetting process, the elongated jet suffered from the classical Rayleigh-Plateau instability and breaking up of small droplets. Depending on the liquid volume, properties and SAW wavelength, when the acoustic power was increased above a

certain threshold value, break-up of small droplets from the tip of the liquid column were observed [20], as shown in Fig. 3.21 (b). However, at low applied powers, which were smaller than the threshold value, only droplet vibration was observed with an amplitude height dependent on the SAW power and surface tension. Due to increased demand of droplet generation technology, the direct jetting capability of the SAW devices could find many innovated applications in inkjet printers or other biological analysis, etc.

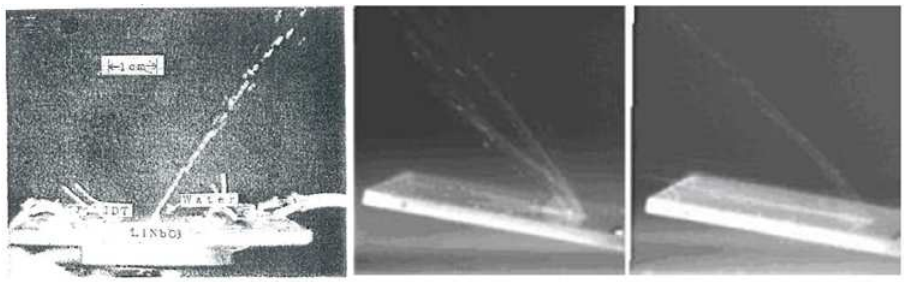

Figure 3.20 (a) Image of jet streams that formed during experiment by a SAW from the water layer on a hydrophobic surface of a 128° YX-$LiNbO_3$ piezoelectric substrate [85]; (b) Jet without surface treatment (hydrophilic), and (c) for a hydrophobically treated surface, in which the water jet is more directional than that without treatment [87]

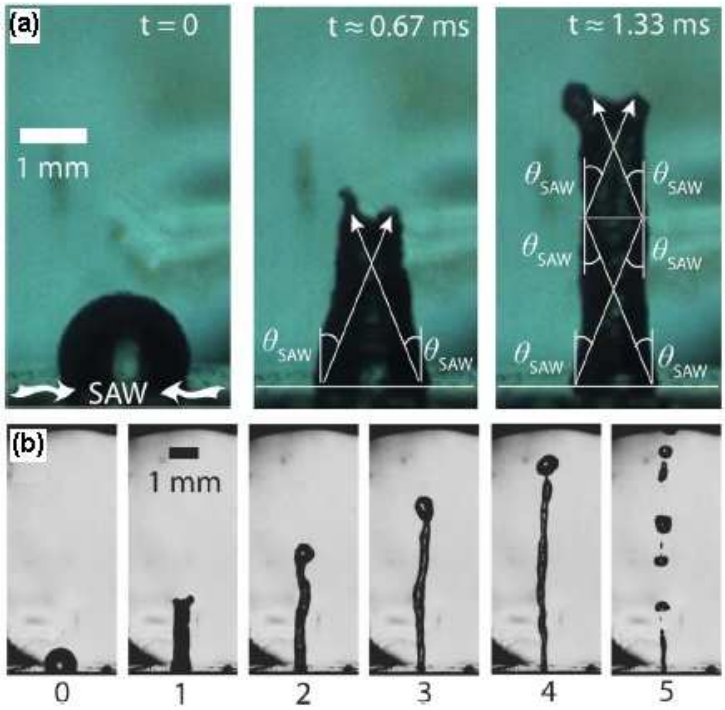

Figure 3.21 Jetting phenomenon of a water droplet initiated by focused SAW, using a 128° YX-$LiNbO_3$ piezoelectric substrate; (a) Subsequent images showing the early stages of the jet initiation for water droplet placed at the focal point of focused IDT's; (b) Images showing the process of jet breakup and droplets formation by increasing of the applied power above a certain threshold value, which enables the acoustic and inertial forces to overcome the interfacial forces of droplet surface tension[20]

Furthermore, atomization is another microfluidic process, which was reported utilizing a SAW technology. A SAW atomiser was proposed for the first time in the early 1990's by Kurosawa et al. [88]. At a relatively high input power, for a thin liquid film of about 10 μm in height was coupled with a Rayleigh wave, the displacement velocities of the vibrating surface was transferred to the liquid layer, inducing capillary waves at the free surface of thin film, as shown in Fig. 3.22 (a). When the intensity of Rayleigh wave is high enough, a fine mist of liquid particles was observed, as seen in Fig. 3.22 (b). This is due to a strong destabilisation of liquid interface, which leads to the atomisation of the thin film [88]. The measured atomisation rate was about 0.1 ml/min at an applied power of a 2.5 W and an excitation frequency of ~ 10 MHz, using a 128º YX-$LiNbO_3$ SAW device with an IDT aperture of a 10 mm. Chano et al. [1] demonstrated that the atomisation characteristics, such as the mist direction and height, were dependent on the SAW input power.

More recently, SAW atomisation using high frequencies (e.g., ranging from 50 to 95 MHz) were reported by Ju et al.[89] indicating that the minimum input power required for the atomisation process as influenced by the excitation frequency of a SAW device. For example, the minimum atomization power was about 4 W for a frequency of 50 MHz, while it was about 24 W for 95 MHz. Similarly, the atomisation speed was also influenced by the SAW frequency. Furthermore, the results showed that there is a considerable drop in the mean measured diameter of atomised droplets with the increase of frequency, where the estimated diameters of nebulised droplets were about 5.7 μm and 2.7 μm at 50 MHz and 95 MHz, respectively [89].

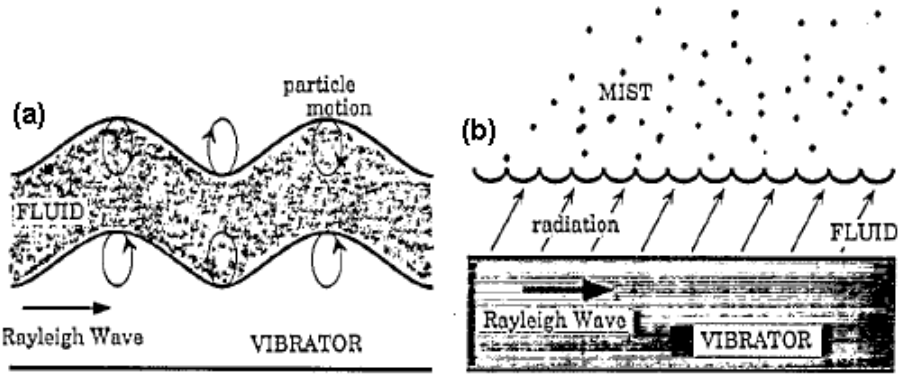

Figure 3.22 Schematic illustration of atomization principle; (a) Oscillation effect of a Rayleigh wave motion on an adjacent fluid layer, which was vacillated accordingly; (b) Atomization of adjacent liquid film by a strong destabilization of capillary wave, showing the mist formation [88]

In many cases, the SAW atomisers have provided a simple and fast technique for the atomisation processes over a range of engineering and scientific applications. For instance, Alvarez et al. [90] have used this technique for the generation a polymer nanoparticles, which were spatially ordered in regular patterns onto the chip surface by SAW-induced atomisation. During the experiments, a droplet of polymer solution was loaded on the surface of a 127.68º YX-$LiNbO_3$ piezoelectric substrate, on which straight aluminium IDTs were deposited, as shown in Fig. 3.23 (a). When an input power was sufficiently high, the radiated SAW translated the droplet into its propagation path (Fig. 3.23 (b)), leading to the formation of a thin film fluid layer, about 10 μm thick, as seen in Fig. 3.23 (c). High surface acceleration (about 10^7 m/s^2) inside the liquid layer by a propagated Rayleigh wave contributes to strong destabilisation of the film interface, leading to atomisation of the thin film. Finally, the thin film was atomised, leaving behind spot patterns of polymer particles with a spatial periodicity depending on the SAW wavelength [90], as seen in Fig. 3.23 (d). The sequences of droplet evaporation and polymer pattern formation can be observed in Figs. 3.23 (e)-(h). Research by Friend et al.[91] has achieved a similar result of polymer patterning, utilising this technique. More recently, Qi et al. [92] has reported the extraction of liquid, protein molecules, and yeast cells utilising the SAW atomiser, describing it as a promising technique for the applications of drug delivery and medical diagnostics.

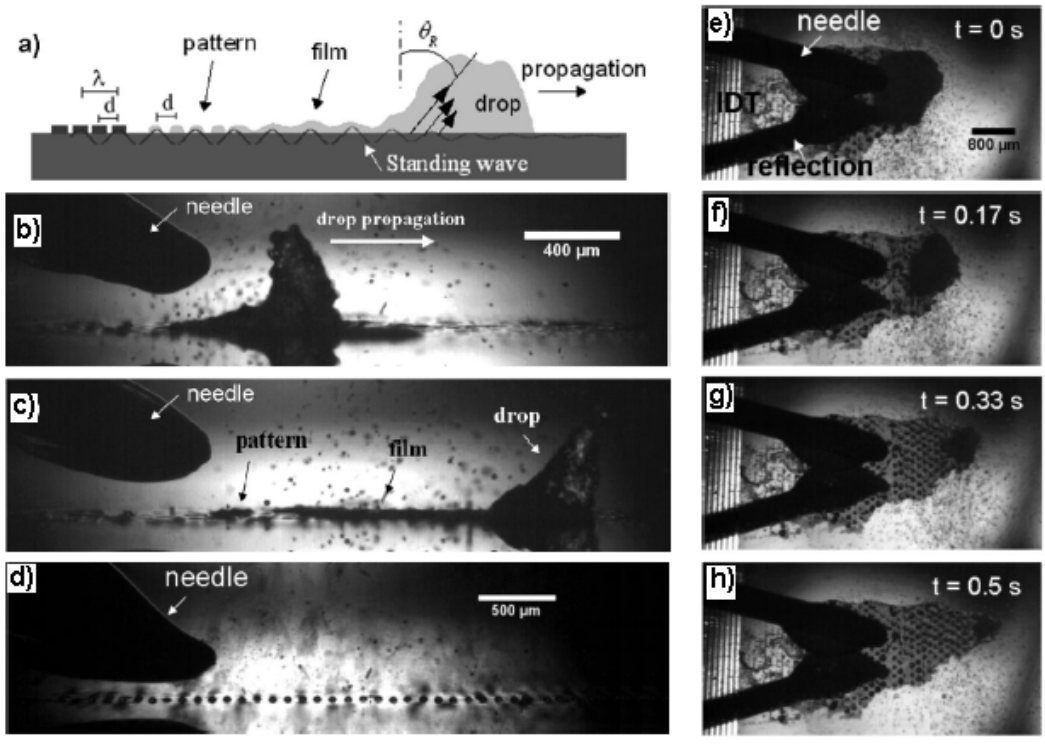

Figure 3.23 (a) Schematic illustration of SAW atomizer; (b)-(c) Side view images using a high speed camera showing a droplet translation, distortion, thin film formation

and atomization;(d) Side view of formulated polymer patterns using a 20 MHz excitation frequency; (e)-(f) Sequent images from top view showing the depiction of a thin film atomisation and polymer particles patterning. The needle in images was used to deliver the polymer solution onto the substrate surface but was not touching it [90]

3.2 **Numerical Analysis of SAW-Liquid Interaction**

Recent experimental studies have demonstrated that the SAW induced streaming can be used for mixing, pumping, jetting and atomization of microfluidics, besides focusing, patterning and sorting of microparticle [23, 49, 93]. However, an efficient utilisation of these phenomena requires a full understanding of the hydrodynamic behaviours and mechanisms in these SAW microfluidic systems. Computational modelling is one of the methods that can be used for an in-depth analysis of the streaming phenomena induced by the SAWs.

3.2.1 Streaming phenomena

To date, many attempts have been made to model the streaming phenomenon of a SAW-fluid interaction investigating the characteristic behaviours of fluid dynamics. Köster and Antil et al. [94-96] have provided a mathematical model for the case of fluid movement in microchannels placed on top of a piezoelectric biochip. Generally, the model approach was based on the coupling of piezoelectric and microfluidic equations through two sets of governing equations, following a perturbation expansion method presented in Eqs. (3.1). This enabled the containment of the two different time scales, the sound field (nanoseconds) and streaming field (milliseconds) [54]. The first set of equations, i.e., Eqs. (3.2), governs the sound field, and the second set, i.e., Eqs. (3.3), governs the acoustic streaming. [94].

$$\boldsymbol{p} = \boldsymbol{p_0} + \boldsymbol{p_1} + \boldsymbol{p_2} + \cdots \qquad (\mathbf{3.1a})$$

$$\boldsymbol{\rho} = \boldsymbol{\rho_0} + \boldsymbol{\rho_1} + \boldsymbol{\rho_2} + \cdots \qquad (3.1b)$$

$$\mathbf{v} = \mathbf{v_1} + \mathbf{v_2} + \cdots \qquad (3.1c)$$

Where p, ρ and v denote the pressure, density, and velocity, respectively, while the subscripts 0, 1, and 2 refer to the steady (ambient), first-order and second-order terms, respectively. Based on the first-order approximation [54, 97-100], which treats the

coupled acoustic wave into fluid as a first-order perturbation, the developed governing equations of wave propagation were stated as:

$$\frac{\partial \rho_{f,1}}{\partial t} + \rho_{f,0}(\nabla . \mathbf{v_1}) = \mathbf{0} \qquad (\mathbf{3.2}a)$$

$$\rho_{f,0}\frac{\partial \mathbf{v_1}}{\partial t} = -\nabla p_1 + \mu\nabla^2\mathbf{v_1} + \left(\mu_B + \frac{\mu}{3}\right)\nabla\nabla\cdot\mathbf{v_1} \qquad (3.2b)$$

$$p_1 = c_0^2\rho_{f,1} \quad , \quad \mathbf{v_1} = \frac{\partial u}{\partial t} \qquad (3.2c)$$

Where, v_1 is the acoustic wave velocity, $u = (u_1, u_2, u_3)$ the mechanical displacements of a Rayleigh wave using Eqs. (2.8), p_1 is the acoustic wave pressure, c_0 is the velocity of compressional waves in the fluid, and ρ_f, μ, μ_B are the density, shear viscosity, and bulk viscosity of the fluid, respectively. Following the assumption of Nyborg and others [54, 97-100], which treated the acoustic streaming of ultrasonic waves as a second-order effect, the governing equations of induced streaming flow involving second-order terms were given as:

$$\rho_{f,0}(\nabla\cdot\mathbf{v_2}) + \langle\nabla\cdot\left(\rho_{f,1}\mathbf{v_1}\right)\rangle = \mathbf{0} \qquad (\mathbf{3.3a})$$

$$\langle\rho_{f,1}\frac{\partial \mathbf{v_1}}{\partial t}\rangle + \rho_{f,0}\langle(\mathbf{v_1}\cdot\nabla)\mathbf{v_1}\rangle = -\nabla p_2 + \mu\nabla^2\mathbf{v_2} + \left(\mu_\mathbf{B} + \frac{\mu}{3}\right)\nabla\nabla\cdot\mathbf{v_2} \qquad (3.3b)$$

where, v_2 is the streaming velocity, and the brackets $\langle\,.\,\rangle$ in the above system stand for a time-averaging of fast harmonic oscillations of the Rayleigh wave that interrupted the steady-state flow, $\langle a\rangle = 1/T\int_{t_0}^{t_0+T} a\,dt$ [94]. This set of equations, i.e., Eqs. 3.3 (a) and (c) describe the acoustic streaming as a stationary compressible flow problem (e.g., Stokes system). These equation were solved numerically in 2D using finite element (FE) method for a water filled microchannel based on a 128° YX-$LiNbO_3$ SAW device [94]. Figure 3.24 shows a comparison between the flow patterns of the experimental fluorescence images and that obtained from the numerical computation at an excitation frequency of 100 MHz. As can be seen from Fig. 3.24, results for both experiment and simulation are not in good agreement, where the simulation showed a single vortex, whereas double vortices were produced in experiments. In the studies by Tan et al. [34, 101] for SAW streaming phenomena, a similar approach has been used for the case of acoustic streaming induced in a rectangular groove type microchannel patterned through

the propagation path of Rayleigh wave onto a 128º YX-$LiNbO_3$ SAW device. However, it should be clearly noted that the above approach is only applicable for a creeping flow, where the flow inertia is negligible [95].

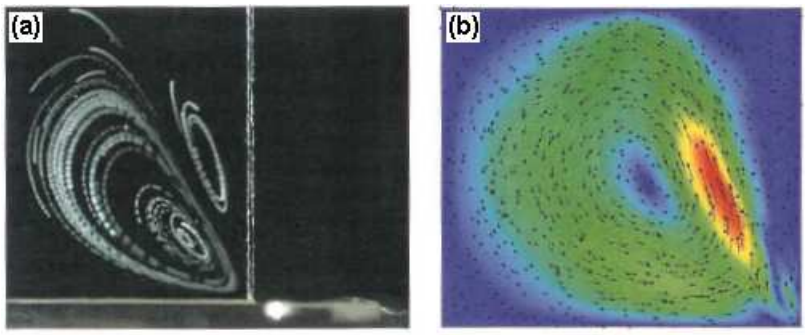

Figure 3.24 Comparison for streaming results between an experimental data (a) and numerical simulations (b), based on 2D computations of water loaded a 128º YX-$LiNbO_3$ piezoelectric substrate at an excitation frequency of 100 MHz [94]

More recently, Frommelt et al. [25] presented a new approach for determining the acoustic streaming pattern that was induced by a SAW in a confined droplet between a top glass slide and substrate surface, using finite element (FE) numerical method. According to this study, the streaming phenomenon of a SAW-fluid coupling can be modelled using the stationary Stocks equation, i.e., Eq. 3.4 of an incompressible flow, where $\nabla \cdot U = 0$. The SAW streaming was assumed driven by an external body force, F, which was generated in the fluid by SAW coupling [54].

$$-\boldsymbol{\nabla P} + \boldsymbol{\mu \nabla^2 U} + \boldsymbol{F} = \mathbf{0} \tag{3.4}$$

In this equation, U represents the acoustic streaming velocity, and P is the streaming pressure. According to Nyborg's theory of acoustic streaming [54], radiation of a high frequency ultrasound beam into fluids gives rise to steady body forces into the fluid volume. This body force acts on a long-time scale of flow, leading to a steady state fluidic flow, known as acoustic streaming. In Frommelt's study, the body force was calculated by developing a ray-tracing algorithm with the aid of experimental readings. Frommelt's study shows that the huge effort of using conventional finite element method, (e.g., Eqs. (3.2) and (3.4)) for SAW streaming simulation can be decreased, where good agreement between the experimental and numerical results was obtained, as depicted in Fig. 3.25. A similar approach has been reported in a study of SAW-induced microchannel flow by Schindler et al. [102]. However, it should be emphasised here

that the above model also assumes that the inertia effects of a streaming flow are small and can be ignored [25, 64].

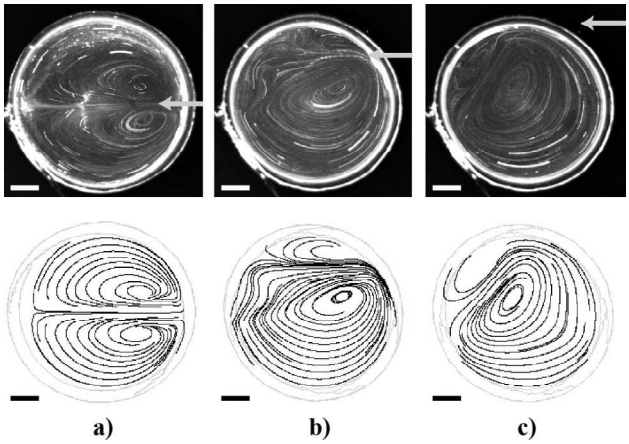

Figure 3.25 SAW streaming patterns in different SAW positions (depicted by narrows): (a) Centre, (b) Side and (c) Outer part. The upper pictures represent the particles trajectory and the bottom pictures represent ray-tracing stream simulation [25]

Further to the previous attempts, Sankaranarayanan et al.[48, 103] has developed a coupled field fluid-structure interaction finite element model to investigate acoustic streaming that is induced by a SAW on a fluid layer loaded SAW device. The fluid flow was modelled using the transient incompressible Navier-Stokes equations. For coupling proposes at the fluid-solid interface (e.g., between the piezoelectric substrate and fluid layer), displacements and stresses have been assumed to be of equilibrium conditions, (i.e., $v_2 = v_1 = \frac{\partial u}{\partial t}$) where the surface displacement of the piezoelectric material, u was obtained by solving the equations of a Rayleigh wave motion, i.e., Eqs. (2.8) simultaneously. Figure 3.26 shows an example of a streaming pattern that is formed in a fluid domain of water, due to a SAW-fluid interaction.

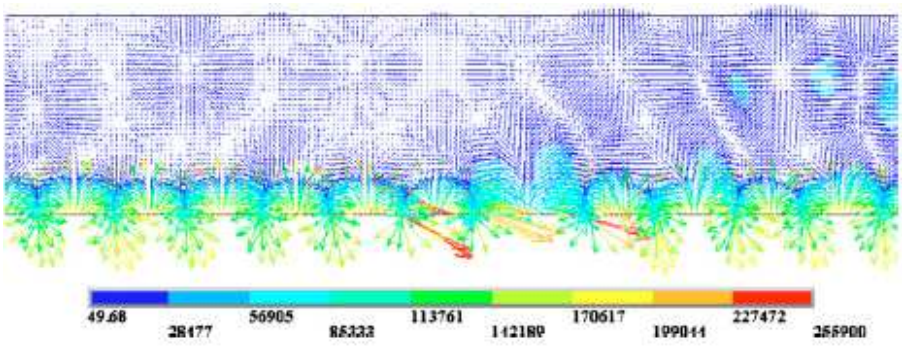

Figure 3.26 Numerical streaming patterns generated in water on a YZ-$LiNbO_3$ SAW device, at an excitation frequency of 100 MHz and an applied voltage of 10 V; The calculated velocities are in μm/s [103]

3.2.2 Droplet deformation

It has been shown earlier in this chapter (Sect. 3.1) that an increase in the applied RF power above certain levels for the case of SAW-driven droplets, pumping, jetting and atomization of the droplets could be induced. Understanding the physics behind these phenomena using experimental measurements is extremely challenging because of the difficulties in capturing the temporal, fine and complex dynamic behaviours of droplets at high SAW frequencies [104]. Consequently, attention has been drawn towards the theoretical investigations using numerical techniques. For example, Schindler et al. [105] and Köster [95] studied a SAW-driven sessile droplets confined between the liquid/air interface and the substrate surface in order to understand the physical mechanisms lying behind the deformation of a droplet's free surface. This explained the internal fluidic flow by the surface acoustic wave, such as that presented in Fig. 3.15(a). However, having a droplet deformed at its free surface along with its internal streaming has added more complexity to the problem, because of the involvement of two phase systems (e.g., water/air interface).

Schindler et al. [105] presented a finite element algorithm for computing the flows of the free surface of a stationary droplet driven by arbitrary SAW body forces. It should be noted here that Schindler's algorithm was designed based on a certain fluidic assumptions. For example, the fluidic flow should be an incompressible steady state flow, and the inertial effect must be negligible (i.e., Eq. 3.4). Besides, a fixed SAW body force was assumed, and its real distribution into the fluid domain was ignored. Nevertheless, Schindler's algorithm was capable of capturing the apparent free-surface deformation by a SAW, and the simulation results matched the experimental results presented by Wixforth et al.[16] (i.e., Fig. 3.13), as seen in Fig. 3.27(a). Schindler's work suggested that a free-surface deformation was due to the contribution of a large acoustic pressure, regardless of the weak viscose forces. The problem was solved numerically in two steps: (1) solving the previously prescribed microfluidic problem (e.g., stationary droplet domain), by using the Stocks equation, i.e., Eq. (3.4), and assuming a slip boundary condition at the droplet free-surface, (2) using these flow results to solve a geometric equation, which is a consecutive update of the droplet domain. Accordingly, the droplet free-surface boundary located by the finite elements (i.e., Fig. 3.27(b)), moves by the applied fluidic stresses behind its surface, and then the surface adjusts its curvature to balance the normal stresses on it by its tenacity to minimize its free energy.

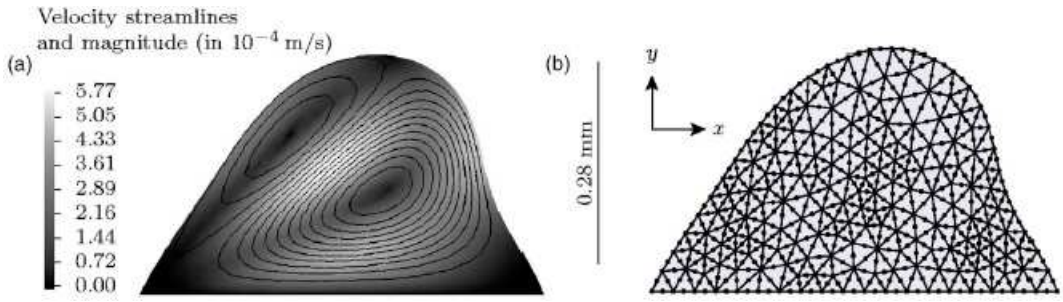

Figure 3.27 Numerical calculations of the droplet deformation and acoustic streaming by a SAW; (a) streaming velocity and flow patterns; (b) FE computational grid [105]

Köster [106] extended the perturbation expansion model of compressible Stokes system, i.e., Eqs.(3.3) for fixed geometries, in order to compute the free capillary motions at the droplet interface induced by a SAW. The Köster technique for capturing the free-surface deformation was based on an arbitrary Lagrangian Eulerian approach, in which the droplet domain follows the fluid motion [107]. Although the Köster's model was not able to capture or predict the initiation of capillary waves at the droplet free-surface, it was able to predict the deformed droplet shape induced by the surface acoustic wave, which matched the experimental results of the SAW-induced droplet distortion, as shown in Fig. 3.28.

More recently, the work from Tan et al. [104] provided a clear insight into the capillary wave dynamics in a two dimensional analysis, through the incorporation of additional analytical equations together with the above perturbation fluidic model, supported with experimental measurements. Their results suggested that at a low power regime, the capillary wave amplitude and frequency are comparable to that of the Rayleigh wave at the substrate surface. However, the amplitude of the free-surface displacement is much higher than that of the substrate surface, inducing a low vibration frequency.

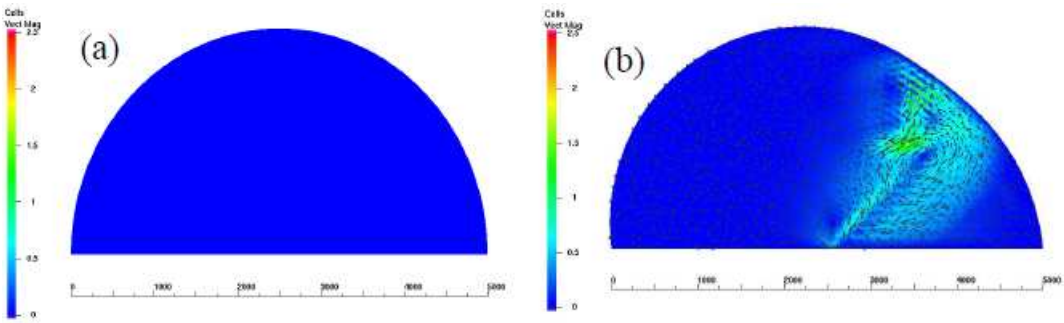

Figure 3.28 Finite element numerical results of SAW-induced streaming for the free boundary domains (sessile droplets); (a) and (b) the droplet shape before and after the SAW turned on in, respectively. [106].

3.3 Software for SAW Steaming Simulation

In the following, overviews for different available computational fluid dynamic (CFD) softwares which were potentially proposed for a SAW simulation are summarised.

3.3.1 Commercial codes

3.3.1.1 *ANSYS CFX*

ANSYS CFX software is flexible and general purpose CFD package that is used in academic and industrial environments for different levels of engineering simulations using finite element analysis. It offers a lot of physical models that can be applied for wide range of engineering applications [108].

3.3.1.2 *ANSYS FLUENT®*

FLUENT is a powerful ANSYS CFD packages for complex flow regimes from an incompressible subsonic flow to highly compressible hypersonic flow. It is provided with multi choice solvers for a wide range of engineering applications with the ability of using flexible, deformable and moving meshes. Moreover, it has the function that enables the user to define, added and implement of new model [109].

3.3.1.3 *ANSYS Multiphysics*

ANSYS Multiphysics represents a comprehensive CFD software for coupling different applied physics like structures, thermal, fluid dynamics and electromagnetic simulation, all in a single engineering package [110].

3.3.1.4 *FLOW-3D*

FLOW-3D software specialises in transient fluid dynamic and micro-fluidic flow for confined and free surface flow in two and three dimensions, but is also able to handle steady state problems [111].

3.3.1.5 *COMSOL Multiphysics*

COMSOL Multiphysics is easy-to-use software package. This package has already predefined many of common physical problems. In COMSOL, the user can choose one of these predefined problems and combine it with another one according to his defined problem or he can implement his own partial differential equation and combine them with other predefined physical equations. The user can also couple and define any

number of partial differential equations as he needs. Moreover, in COMSOL Multiphysics, the interface with any CAD package is possible. The most sophisticated modelling in COMSOL Multiphysics is the modelling of Microelectromechanical Systems, which are usually a Multiphysics problem [112].

3.3.2 Free codes

This section contains the codes that are in public domain, which are available under General public license (GPL) or under similar licenses.

3.3.2.1 *MFIX Code*

MFIX Code is a general purpose computer FORTRAN code based for finite volume methods. This code has been developed to describe hydrodynamics, heat transfer and chemical reaction. In general, it is a multiphase 3D flow code with interphase exchange. This code is provided with full documentation, starting from the theory and numerical guides to run available tutorials [113].

3.3.2.2 *OpenFVM*

OpenFVM code is one of the GPL computational fluid dynamic solvers. This code is developed for 3D flow simulation on complex geometry by using finite element method. It is capable to built unstructured meshes for arbitrary shapes and is able to solve non isothermal multiphase equations. However, this code is still in its first steps towards the developing process and there is no more information about its features, and it does not come with any documentation [114].

3.3.2.3 *Elmer*

Elmer is an open CFD source code for Multiphysics problems. It uses finite element methods for solving the partial differential equations. The source code is written in FOTRTRAN 90, C and C++ programming languages. In Elmer, the user is able to modify the predefined solvers or develop a new solver according to the user demand. Elmer comes with a number of predefined models for fluid dynamics and coupled physics. However, Elmer is not restricted with this predefined coupling models because it can be coupled with other different physics [115].

3.3.2.4 *OpenFOAM*

OpenFOAM is an open source CFD software for the simulation of different physical and engineering applications, starting from fluid dynamics with heat transfer, chemical reactions and turbulent flow for single or multiphase flows to solid dynamics and electromagnetic. The source codes in OpenFOAM are written in C++ programming language. For the solution of partial differential equations, the finite volume numerical method is developed. OpenFOAM can be used as any typical CFD code because it contains a lot of predefined solvers for the different flow cases. It provides C++ libraries that can be used in different models and it can be used as a 2D or 3D solver according to the neediness of the user. In OpenFOAM different discretization schemes can be used. Moreover, it provides structured and unstructured grids with uniform and non-uniform meshing. However, OpenFOAM is not like any another GPL software because its utility and library are fully accessible and extendable. OpenFOAM is provided with full documentation for both the users and programmers [116].

3.3.2.5 *OOFEM*

OOFEM code is a free finite element CFD software released under GPL. This code is suitable for transient incompressible flow and it provides semi implicit algorithm. However, it can be used for the simulation of a two-phase flow in 2D for free and closed surface flows. It provides volume of fluid (VOF) based on an interface tracking algorithm. This code is provided with online documentation [117].

3.3.3 Software selection

In brief, according to the list of commercial codes, COMSOL Multiphysics is the best one because as it was mentioned before the user also has the option of choosing different models from the Multiphysics menu of the code and defining the interdependencies himself. The user can specify his/her own partial differential equations, and couple them with other equations and physics. On the other hand, OpenFOAM is the best one from the free code list, and it is based on FVM and is written using C++. OpenFOAM code is fully open for the development and changes with complete accessibility to the source code, which allows the user to implement new partial differential equations for further extension and improvement of available solvers. This code is provided free with full documentation and a free discussion group on line for any bugs occurring during the use of code. The other important thing is that the code

provides a huge list of physical libraries that can be used without adding any coding or even needs some small modification to meet the user demands. OpenFOAM can be used for Multiphysics applications with different grid structures. Besides, in OpenFOAM, code solvers can run in parallel simultaneously on several distributed processors of cluster systems, with applicability of mapping the course mesh results onto the fine mesh. These features all contribute to improve the running time of huge mesh cases, and help to move towards fast research progression. The use of commercial codes is restricted by its blocked design, which limits the accessibility of the source codes and existing libraries, and high licensing costs, while free OpenFOAM code is completely extendable even in its C++ library. This lack in the freedom of research work using commercial codes, could contribute to the delay in the researcher progress. Therefore, in this research work, OpenFOAM code has been chosen to be used in the modelling development of a SAW-fluid interaction.

3.4 **Summary**

In recent years, SAW devices and their microfluidic applications have drawn the attention of many researchers extensively. The basic principles of the SAW, such as the wave propagation, generation and its characteristic behaviours in solids and fluids, have been introduced in this chapter. The acoustic streaming induced by the SAW in coupled fluids is an important phenomenon with wide potential applications, especially when the SAW device as a miniaturised and compact actuation part in MEMS devices for LOC systems. Although the acoustic streaming phenomenon and its related microfluidic studies have shown extensive progress in recent years, there is still much in-depth work to be done and SAW induced fluidic behaviours to be explored, which could enhance the understanding of this actuation mechanism. Currently, to the best of the author's knowledge, almost all the available experimental and numerical studies were generally based on a two dimensional analysis. An efficient utilization of the different streaming phenomena needs the hydrodynamics to be understood in three dimensions. For example, the detail of a SAW-fluid coupling problem is still under consideration and the three dimensional streaming phenomenon of SAW-driven sessile droplets has not been truly understood. Also the inertial effects of flow hydrodynamics have been widely ignored in literature, without clear justification. Therefore, this research work focuses on the investigation of SAW streaming behaviour and wave/fluid coupling, using both the experimental and numerical methods. This systematic study gives more in-depth

insight into the flow hydrodynamics generated by the SAW, which could significantly help in designing efficient SAW parameters, towards system optimisation.

Chapter 4

STREAMING PHENOMENON

In this chapter the numerical and experimental methodologies developed to investigate the acoustic streaming motion generated by a SAW in microdroplets are introduced. The numerical results are validated through a comparison with an experimental data of similar set up. The different streaming phenomena induced by a SAW into the liquid droplets were explained using experimental observations and 3D numerical simulations.

4.1 Introduction

As shown in Fig. 4.1, SAW can be launched by applying an alternating electric field to the IDT, which then propagates along the interface between the solid surface and gas (air), and changes its mode to leaky SAW when it reaches a boundary between the solid and liquids. As discussed in Chapter 2, this leaky SAW produces a longitudinal wave that attenuates within a few micrometers depending on the liquid density and substrate material property, which in turn establishes an effective body (streaming) force acting into the fluid medium [86]. The longitudinal waves propagate into the fluid with the Rayleigh angle Θ_R [118], as shown in Fig. 4.1. The generated body force can create significant acoustic streaming in the liquid and facilitate liquid mixing, stirring, vibrating, pumping, ejection and atomization [119].

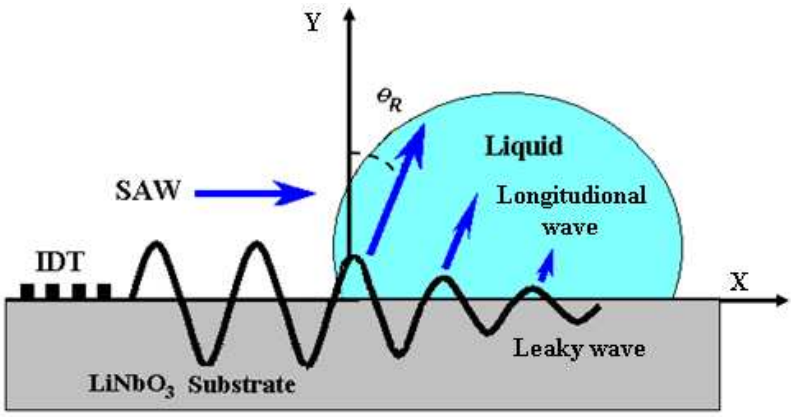

Figure 4.1 Illustration of SAW propagation into droplet

Acoustic streaming is known as an inherent fluid motion due to acoustic energy attenuation of intensive ultrasound waves propagating through a fluid medium. This

phenomenon was first studied by Lord Rayleigh [120] then followed by Nyborg [54, 97] and Westervelt [121]. These authors calculated the flow motion due to ultrasound propagation via the momentum equation of steady incompressible laminar flow driven by an external body force F:

$$\boldsymbol{\rho_f(U \cdot \nabla)U = F - \nabla P + \mu \nabla^2 U} \tag{4.1}$$

where U is the acoustic streaming velocity, P the pressure, ρ_f and μ are the fluid density and dynamic viscosity, respectively, F is the acoustic body or streaming force term due to ultrasound propagation, and the left side of Eq. (4.1) represents the hydrodynamic nonlinear term.

Currently, most studies of SAW streaming are based on Nyborg's assumption [54, 97]. He claimed that the acoustic streaming is a second-order effect and streaming velocity is a second-order quantity. Therefore, the hydrodynamic nonlinear term i.e., $\rho_f(U \cdot \nabla)U$ in the above equation is a fourth-order quantity, which can be easily ignored. Later, Lighthill [55, 56] argued that ignoring the hydrodynamic nonlinear term should be dependent on its numerical value, but not on its mathematical order. He pointed out that the second- order approximation for acoustic streaming is only valid for very slow fluid motion, i.e., creeping motion of Reynolds number, Re smaller than one [56]. Kamakura and Mitome [74, 122] showed that the hydrodynamic nonlinear term played a major role in the generation of acoustic streaming, especially for a strong focused ultrasound beam. However, during the studies of SAW streaming, the hydrodynamic nonlinear term has been frequently neglected or ignored even at very high SAW powers and the so-called linearised momentum equation used, (i.e., Eq.(3.4)) [25, 34, 41, 46, 48, 105, 123, 124].

SAW acoustic streaming in a microdroplet is a 3D phenomenon, whereas currently SAW acoustic streaming numerical modelling is normally performed in a 2D mode, largely due to the complication in developing a 3D model for the a nonlinear body force term of the SAW-fluid coupling [25, 64]. Hence, a few of studies have been extended into three dimensions for SAW microdroplet streaming [70]. To fully understand the effects of the SAW streaming mechanism, it is important to be able to model the mechanism in 3D in order to design efficient microfluidic SAW devices for microfluidic application.

This chapter presents the numerical model and experimental methodology developed in this study for the investigations of SAW-based microfluidics in a 3D, and focuses on the physical mechanism of the different streaming phenomena induced by SAWs in the microdroplets, such as a particle concentration in a water droplet using asymmetrical SAW position.

4.2 **Experimental Details**

4.2.1 Experimental apparatus and signal measurement

The SAW devices were fabricated on 128^{o} YX- black $LiNbO_3$ substrates by sputtering 200 nm thick Aluminium to form the IDTs. The surface of the $LiNbO_3$ wafers is hydrophilic with a water contact angle of about 35^{o} as can be observed in Fig. 4.2(a). In this study, a spin-coated CYTOP® (Asahi Glass Co., Ltd., Tokyo., Japan) layer was prepared to make the surface hydrophobic and increase the contact angle from about 35^{o} to 110^{o}, as shown in Fig. 4.2 (b). The details of the SAW device fabrication have been documented [17]. The finger width of the IDT electrodes determines the resonant frequency of the SAW device[125]. In this study, an IDT with a finger width of 16 μm was used, and an IDT aperture of 2,000 μm. The fundamental frequency, f of the SAW device was measured using an HP 8752A Network Analyzer, as shown in Fig. 4.3. Using a network analyzer, the excitation frequency of the SAW device was swept over arrange of signal frequencies, until the corresponding resonant frequency of the SAW device was measured from the reflected signals. This is found in this study to be 62 ± 0.5 MHz, as indicated in Fig. 4.4.

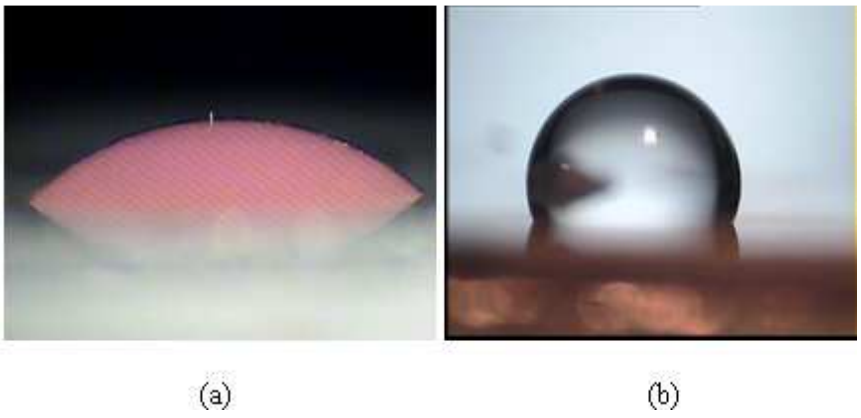

Figure 4.2 Water droplets on $LiNbO_3$ (a) untreated surface (b) hydrophobic surface treated with CYTOP.

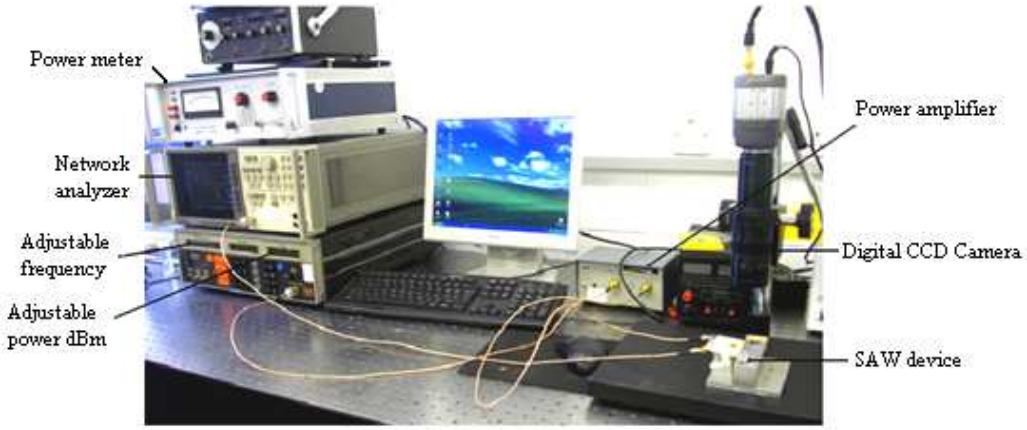

Figure 4.3 Photograph of the experimental apparatus used for of SAW induced streaming experiments.

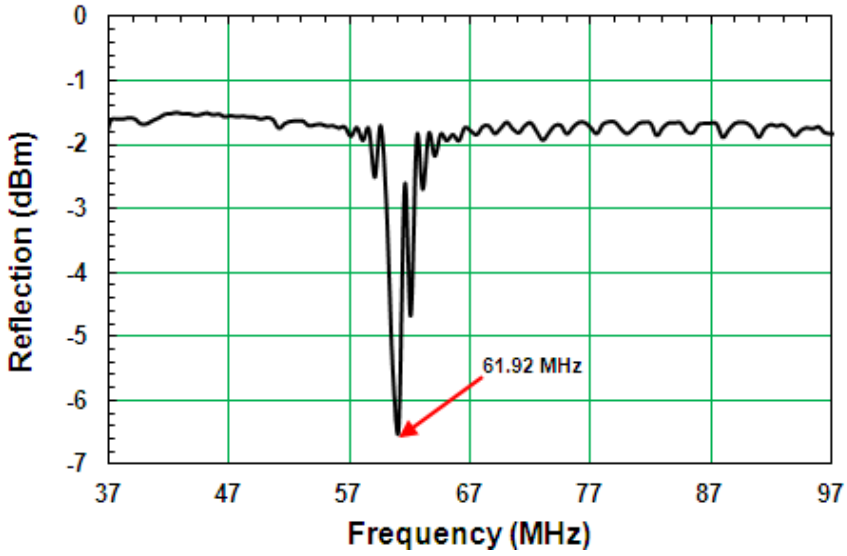

Figure 4.4 The reflection signal of a 128° YX- black $LiNbO_3$ SAW device with IDTs periodicity of 64 μm, measured using a network analyzer; the red arrow indicates to the peak resonant frequency of the SAW device

To agitate the liquid droplets, the SAW was generated on the surface by applying an RF signal to the IDTs using a standard signal generator MI 2019A, which was amplified by an MI TF2175 RF power amplifier. The exact output reading P_D applied to the SAW device from the power amplifier was measured as a function of variable input powers, P_{in} of the signal generator at a moderate range of excitation frequencies, ranging from 20 to 100 MHz, as presented in Fig. 4.5. This reading of the power amplifier was calibrated using a Racal 9104 RF power metre. For flow behaviours, the resulted flow patterns within the liquid droplet were captured using a standard digital CCD camera, as illustrated in Fig. 4.3.

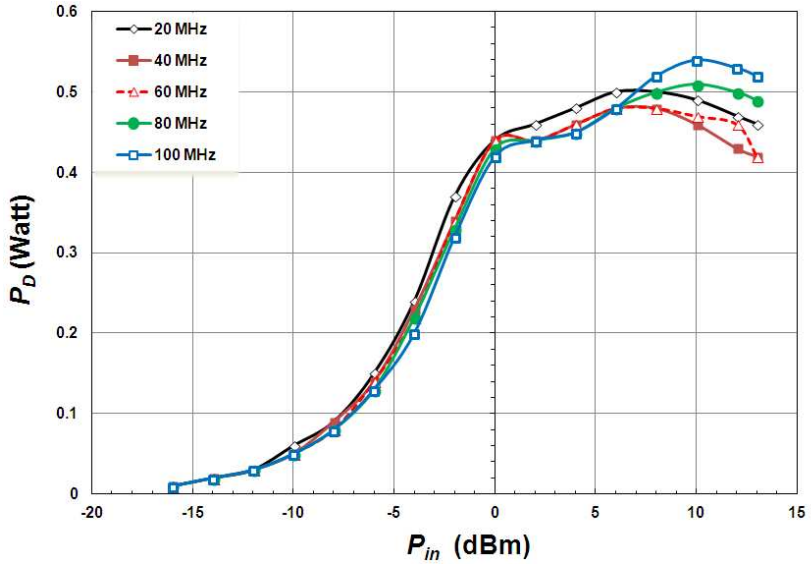

Figure 4.5 Output reading of an MI TF2175 RF power amplifier measured using a Racal 9104 RF power metre for a moderate range on input power and excitation frequencies, using a 128^{o} YX- black $LiNbO_3$ SAW device.

4.2.2 Streaming velocity measurement

4.2.2.1 *Experimental setup*

A high speed tracking technique was used for the visualisation and investigation of the flow behaviours induced by SAWs in the water microdroplets (2.5 to 30 μl), as shown in Fig. 4.1. The droplets were loaded at the centre of the SAW propagation path by using a micro-volume Kit micropipette. For high speed videos recording, a high speed camera (Kodak Motion Corder Analyzer with 600 frames per second) was placed above the SAW device, directly above the test droplet, as shown in Fig. 4.6. In order to measure the time variation of a SAW streaming velocity, polystyrene particles with average diameters of 6 μm were placed inside the water droplets, which were illuminated using a source of AmScope 150 W Haloids Light Microscope Illuminator, and their motion was recorded (see Fig. 4.6). The specific gravity of the polystyrene particles is 1.05. Using the video records, it was observed during the experiment that when the SAW power was turned off, the tracer particles were suspended inside the droplets and no motions were induced. This suggests that the polystyrene particle used in this study does not subject to the relative motion of the flow inside the droplets, if the acoustic power is turned on. Thus, these particles were treated as passive tracers that

move with the same streaming velocity and follow the stream paths of fluid flow, in a similar manner to that assumed in [25, 64]; see also footnote [1].

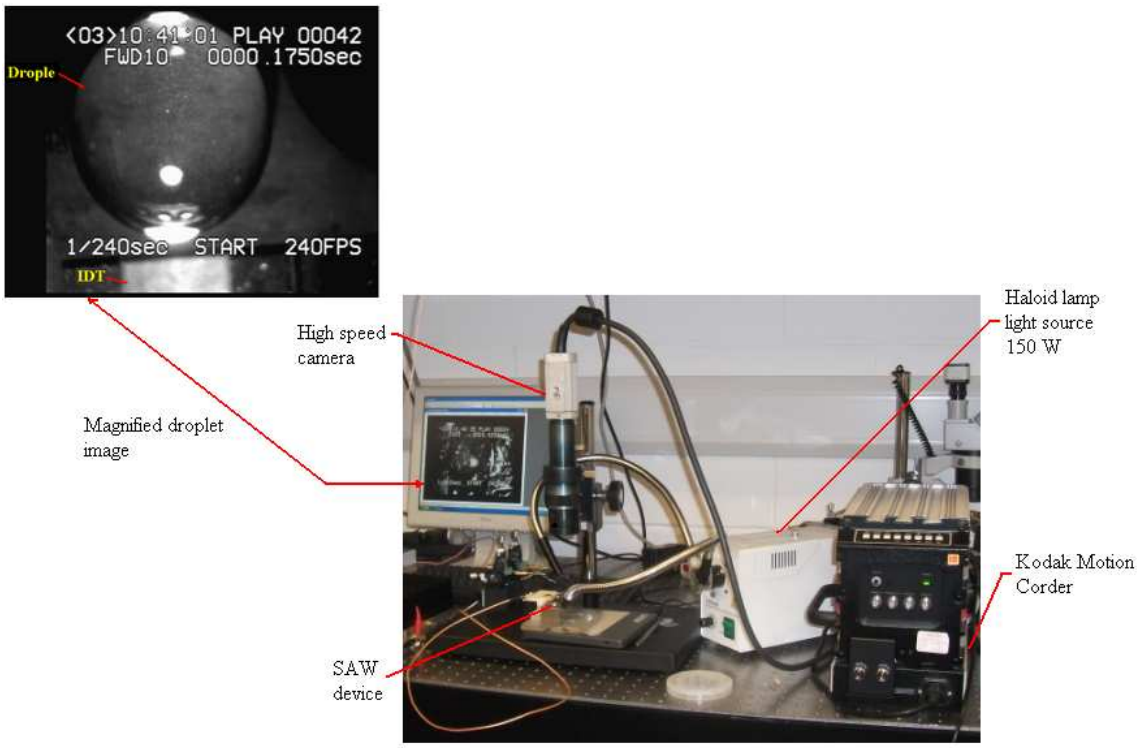

Figure 4.6 Photograph showing a high speed camera experimental setup of a streaming velocity measurement.

4.2.2.2 *Measurement procedure*

During the measurement of streaming flow, the high speed camera used in this study was adjusted to a 240 frame per second with a resolution of 480 × 720 pixels. For magnification, a Cosmicar lens was used, which provides 0.7 to 22 magnifications. The measurement of streaming velocity was initiated after the SAW power was turned on and the streaming flow of tracer particles was diminished, as shown in Fig. 4.7(a). Then, the zoom and height of the High Speed Camera located directly above the droplet were adjusted to achieve high quality images of the streaming particles within the focal region (i.e., the specified area at the top centre of the droplet), as illustrated in Fig. 4.7(b)-(d). After locating the tracer particles in the foal region, the SAW power was turned off. After the desired power of the signal generator was adjusted, the SAW power, P_D was turned on and the initiated streaming flow in the droplet was allowed to reach a steady-state. Numerical results of this study suggested that the streaming flow

[1] See EPAPS document no E-PRLATAO-100-082802 for the experimental methods for the dual-jet flow patterns and other operation modes. For more information on EPAPS, see http://www.aip.org/pubservs/epaps.html.

reaches a steady-state in 1~2 s, depending on the applied power and liquid volume. Thus, after ~ 10 s the High Speed Camera was triggered to catch the images of the streaming flow, as shown in Fig. 4.8(a).

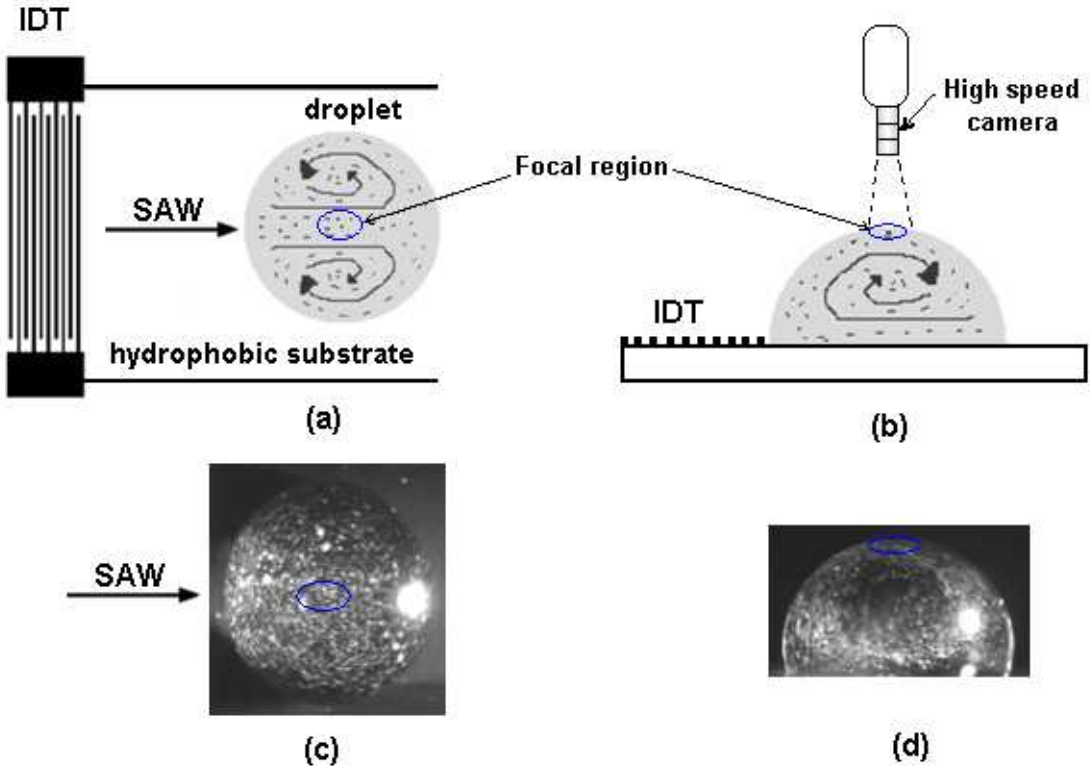

Figure 4.7 (a) and (b) schematic illustration of a water droplet with seeded particles on the SAW device, showing the focal region of High Speed Camera from top and side view respectively; (c) and (d) captured images of droplet from top and side views during the experiment.

In order to measure the streaming velocity of the tracer particles at the top centre of droplets, a single pair streaming images was captured at different time periods, using a high speed camera, such as in Figs. 4.8 (a) and (b). Using a reference scale i.e., width of the device IDT, the distance Δx that particle travelled during the time period Δt within focal region can be estimated, where x denotes the particle position, as shown in Fig. 4.8(c). Thus, the streaming velocities were calculated from processed images using $U = \frac{\Delta x}{\Delta t}$, where the precision of measurement using direct particle tracking is 0.06 mm ± 0.04 mm. However, to avoid large random errors in velocity measurements, 15 image pairs were taken in 10 s duration. Then, an average streaming velocity of a tracer particle was calculated, using these image pairs. The standard deviation in streaming velocity from an average value for the 15 mage pairs was estimated to be between ~ ± 2 % and ± 50 %, depending on the SAW applied power. This is attributed to an increased

blurring image of the tracer particle at higher powers i.e., 16 mW, besides the uncertainty in the position and number of the tracer particles in focal region, see Fig. 4.8 (c)

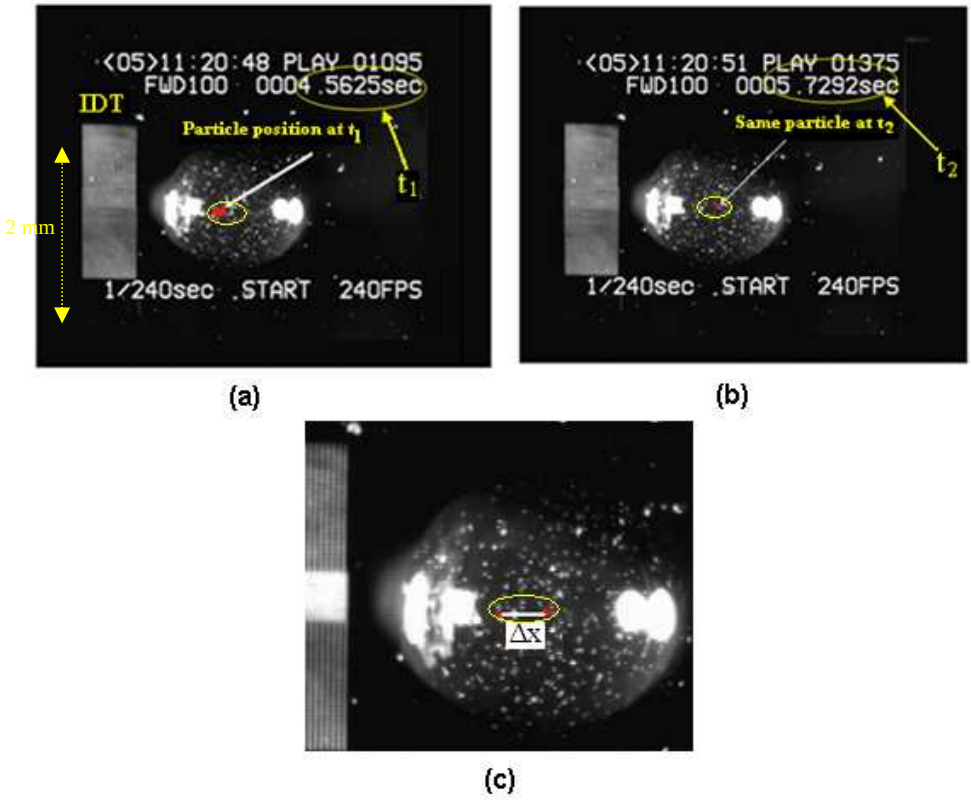

Figure 4.8 An experimental snapshots using high speed camera showing the particle trajectory.

4.3 **Modeling Details**

4.3.1 Governing equations

4.3.1.1 *Acoustic streaming*

The generated streaming motion due to SAW energy attenuation in the liquid droplet is assumed to be governed by the continuity equation, Eq.(4.2a) and the full laminar incompressible Navier-Stokes equation (i.e., momentum equation), Eq. (4.2b) that is driven by an effective SAW body (or streaming) force F [122, 126]:

$$\boldsymbol{\nabla \cdot U = 0} \tag{4.2a}$$

$$\boldsymbol{\frac{\partial \rho_f U}{\partial t} + \rho_f (U \cdot \nabla) U = -\nabla P + \mu \nabla^2 U + F} \tag{4.2b}$$

The governing equation of the acoustic streaming force has been derived by Nyborg [54], for an incompressible fluid, which is given by the following equation:

$$-\boldsymbol{F} = \boldsymbol{\rho_f}\langle(\mathbf{v_1}\cdot\boldsymbol{\nabla})\mathbf{v_1} + \mathbf{v_1}(\boldsymbol{\nabla}\cdot\mathbf{v_1})\rangle \tag{4.3}$$

where v_1 represents the velocity of Rayleigh wave in the fluid, and the brackets $\langle\cdot\rangle$ indicate the time averaged (mean) value [54, 97]. Therefore, the nonlinear acoustic streaming force F can be calculated, once the wave velocity is known.

4.3.1.2 *Leaky Rayleigh waves*

As indicated earlier (see Section 2.4.1), the SAW changes its mode to a leaky SAW once it interacts with the liquid volume. This leaky SAW establishes a longitudinal wave within the liquid medium and propagates with a Rayleigh angle $\Theta_{R,}$ as depicted in Fig.4.1. Considering the surface displacements to be independent on the z coordinate [127], the leaky SAW displacements are considered; (u_x, u_y), which can be expressed by [52]:

$$\boldsymbol{u_x} = \boldsymbol{A\,exp(j\omega t)\cdot exp(-jk_L x)\cdot exp(-\alpha k_L y)} \tag{4.4a}$$

$$\boldsymbol{u_y} = \boldsymbol{-j\alpha A\,exp(j\omega t)\cdot exp(-jk_L x)\cdot exp(-\alpha k_L y)} \tag{4.4b}$$

Here,α represents the attenuation constant,

$$\boldsymbol{\alpha^2} = \mathbf{1} - \left(\frac{\boldsymbol{V_L}}{\boldsymbol{V_f}}\right)^{\mathbf{2}} \tag{4.5}$$

and V_L and V_f are the Leaky SAW velocity and the sound velocity in the liquid, respectively. A is equivalent to the SAW wave amplitude at the entrance point to the liquid and the angular frequency $\omega = 2\pi f$. The SAW number $k_R = (2\pi/\lambda)$ is a real number, where λ is the wave length, and the leaky SAW number $(k_L = k_r + jk_i)$ is a complex number with the imaginary part representing the SAW energy dissipation within the liquid medium [48]. The leaky SAW number (k_L) can be obtained be extending the method of Campbell and Jones [86, 127, 128] to the solid-liquid structures assuming both stress and displacement to be continuous boundary condition at y = 0 ,(see Table 4.1), and V_f =1 500 m/s.

Table 4.1 Leaky SAW parameters calculated based on Campbell and Jones [46, 123]

Crystal Orientation	**Rayleigh SAW Velocity ($m\ s^{-1}$) V_R**	**Water loaded leaky SAW velocity V_L**	**Leaky SAW wave number (m^{-1}) k_i**	**Attenuation Coefficient α_1**
128° YX-$LiNbO_3$	3994	3931+j68.1	-2768	2.47

4.3.1.3 ***Streaming force***

If the wave displacements (u_x, u_y) are replaced by the first-order wave velocities using $v_j = \partial u_j/\partial t$ and substituting these values into equation (4.3), the two components of streaming force are given, for an incompressible fluid, by [86]:

$$\boldsymbol{F_x = -\rho_f\left(1+\alpha_1^2\right)A^2\omega^2 k_i \cdot exp2(k_i x + \alpha_1 k_i y)} \qquad (4.6a)$$

$$\boldsymbol{F_y = -\rho_f\left(1+\alpha_1^2\right)A^2\omega^2 k_i \alpha_1 \cdot exp2(k_i x + \alpha_1 k_i y)} \qquad (4.6a)$$

where $\alpha = j\alpha_1$. The total SAW streaming force F can be calculated by $F = \sqrt{F_x^2 + F_y^2}$ [86] , which is then given by Eq. (4.7). The force direction in the fluid is similar as the Rayleigh angle θ_R [41](i.e., Eq. (2.13)) of the longitudinal wave radiation into the fluid (see Fig. 4.1).

$$\boldsymbol{F = -\rho_f\left(1+\alpha_1^2\right)^{3/2}A^2\omega^2 k_i \cdot exp2(k_i x + \alpha_1 k_i y)} \qquad (4.7)$$

The SAW force F acts in the main fluid volume as a body force, but the exponential decay of the leaky SAW limits the influence of this force within the fluid volume. This leads to a complete diminishing within a few microns from the interaction point between the SAW and a liquid droplet. Therefore, substituting equations (4.6a) and (4.6b) into equation (4.2b) and numerically solving Eqs. (4.2a) (4.2b) with suitable boundary conditions can be used to predict acoustic streaming patterns induced by SAW.

4.3.1.4 *Boundary conditions and solution method*

In this study, the case setup is based on a $LiNbO_3$ SAW device with a wavelength of 64 µm and a resonant frequency of 62 MHz was used in the experiments, which was indicated earlier in this chapter. Water droplets with different volume ranges were loaded on the central and asymmetric positions on the SAW propagating path, as shown in Figs. 3.9 (a) and (b).

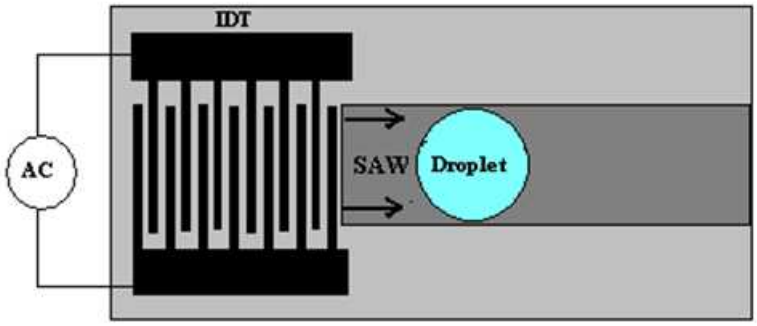

(a)

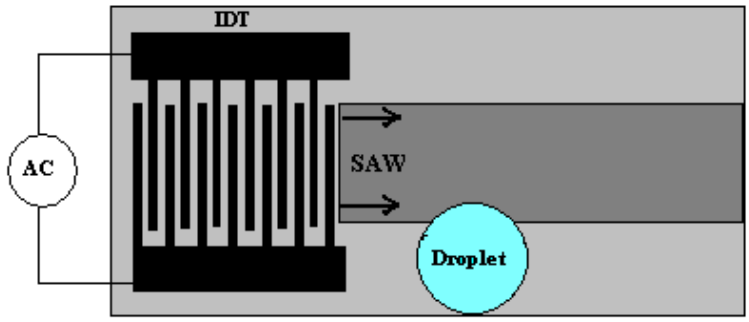

(b)

Figure 4.9 (a) Illustration of a droplet positioned symmetrically on surface of a SAW device; (b) asymmetric positioning of water droplet on the SAW device.

In all the streaming tests in this study, the RF powers for SAW streaming were low and no apparent deformation in the droplet's shape was observed during the experiment. Therefore, the fluid can be assumed to form its equilibrium shape, and the small free surface instability due to SAW microdroplet interaction was ignored in the simulation, and the droplet was assumed to be confined within a stress-free boundary. A slip boundary condition is assumed at the gas/liquid interface boundary and non-slip boundary condition is assumed at the substrate (liquid-surface contact area). The droplet domain in this numerical model was built using a curvilinear grid structure with grid number of 90 × 45 × 90 in x, y and z direction, receptively, as shown in Fig. 4.10. For droplets loaded on the substrate surface in this study, experimental measurements of droplets contact angles showed that the standard deviation in the contact angle from an

average estimated value of 90º to be ± 20º, depending on the surface energy of the substrate surface (i.e., hydrophobic nature of the substrate surface) .Thus, the droplet was assumed to form a hemispherical shape (contact angle of 90º), and small deviations from the actual three phase contact angle were ignored (see Fig. 4.10). The governing equations of a SAW streaming; the continuity equation (4.2a), the momentum equation (4.2b) and streaming force equation (4.7), were implemented and programmed in the OpenFOAM-1.6 CFD code (OpenCFD LTD), which has been chosen as a basis for the development of SAW streaming model (see Section 3.3.3). These equations were solved over the entire droplet domain in three dimensions using a finite volume numerical method (FVM) [129, 130]. A linear upwind differencing scheme [121] was used for the discretization of the nonlinear convective term in Eq. (4.2b).

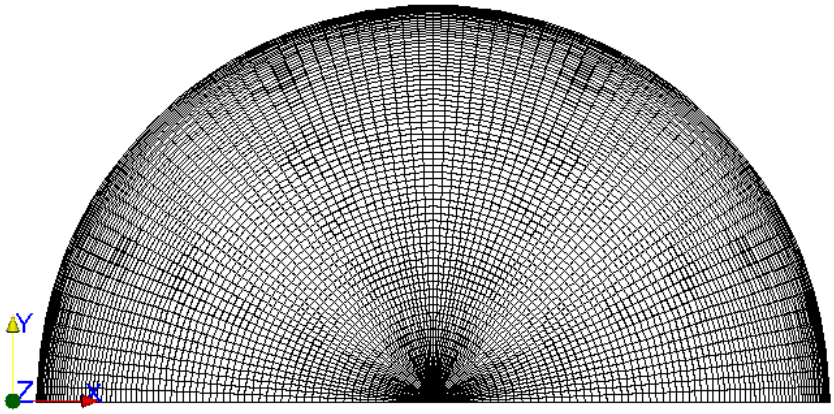

Figure 4.10 Computational curvilinear grid meshing of sessile droplet from side view

4.3.1.5 *Measurement of SAW amplitude*

The exact magnitude of the SAW amplitude at the entrance point, *A*, is required for calculating the SAW streaming force *F* and solving the Navier-Stokes equation. Therefore, the numerically calculated relationship between time and streaming velocity was used to correlate with the experimentally measured data, and then the SAW amplitudes at different RF powers were estimated to have a good match of streaming velocities from both experiments (see Figs. 4.11 and 4.12).

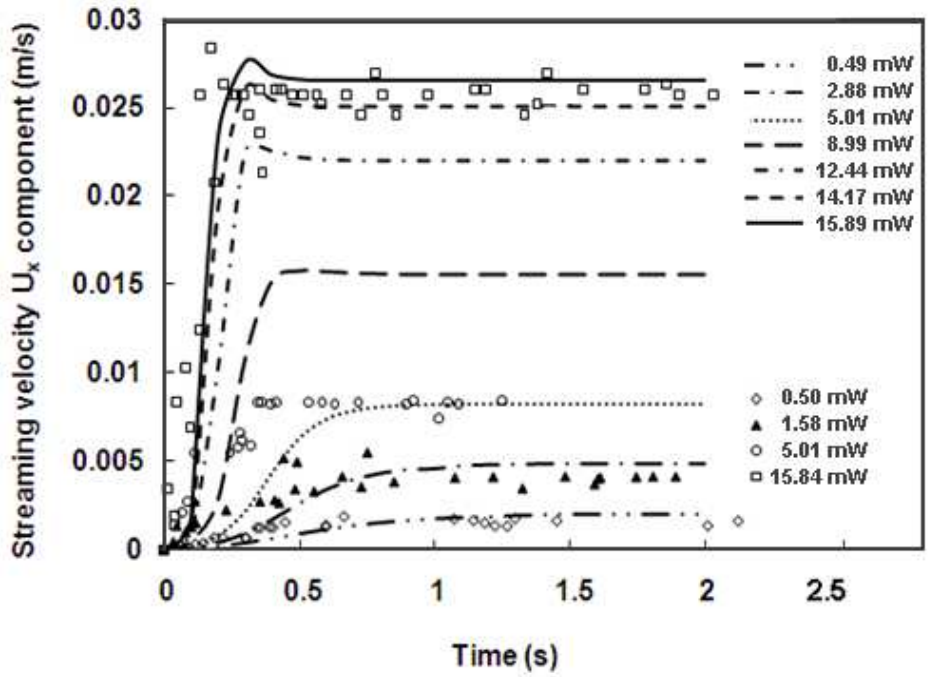

Figure 4.11 Streaming velocity at top centre of 30 μl droplet positioned symmetry within a SAW propagation direction at f = 62 MHz (SAW device has an aperture of 2 mm); Solid lines represent numerical results at different RF powers; the markers denote experimentally measured data.

Figure 4.12 shows the variation of the normalised wave amplitude by the wavelength of a Rayleigh wave as a function of applied RF power to the SAW device. Both, the current study results and the experimental measurements available in [1, 2], show that the normalised wave amplitude exhibit similar values at different excitation frequencies. The wave amplitude A, which is a parameter directly related to the RF power, is illustrated in Fig. 4.12. The normalised SAW amplitude A/λ was identified by the following an empirical correlation that fits most of the results:

$$\frac{\boldsymbol{A}}{\boldsymbol{\lambda}} = \mathbf{8.15}\times\mathbf{10}^{-\mathbf{6}}\boldsymbol{P}_{\boldsymbol{D}}^{\mathbf{0.225}} + \mathbf{5}\times\mathbf{10}^{-\mathbf{6}}\,\boldsymbol{P}_{\boldsymbol{D}}^{\mathbf{0.8}} \tag{4.8}$$

where P_D is the radio frequency (RF) power applied to the SAW device in Watts, and λ is the SAW wavelength. This relationship was used to predict the exact value of the wave amplitude in order to calculate the SAW streaming force. Among the range of the RF power applied in this study (i.e., P_D < 5 $V_{p\text{-}p}$), using this correlation showed that the standard deviation in the wave amplitude from the extrapolated data are ≤ ± 8%. This is the range of RF power in this study. This correlation was extended to a higher power range that available in [1, 2] (i.e., P_D ≥ 5 $V_{p\text{-}p}$) for further studies. In spite of the

increased deviation in the wave amplitude from the experimental measurements [1, 2], the both results are generally in the same trends.

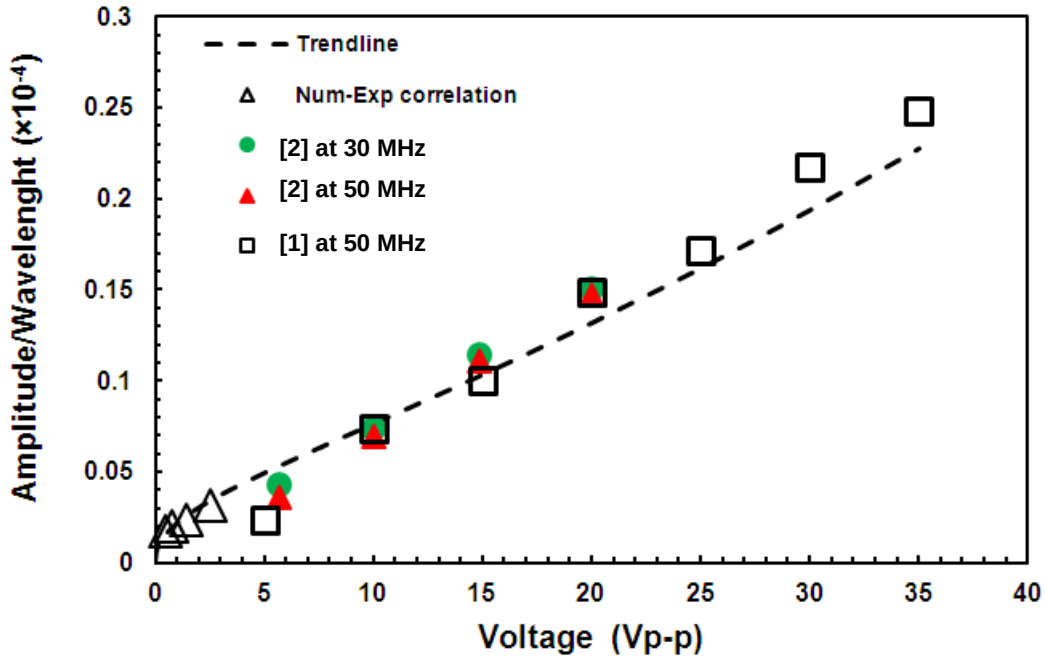

Figure 4.12 Effect of driving RF power on the normalised SAW amplitude, A / λ at the interaction point. From this study, a Numerical-Experimental correlation results were presented, where a 30µl droplet positioned symmetry within SAW propagation on a 128º YX-$LiNbO_3$ SAW device at 62 MHz. Along with the experimental measurements of SAW amplitude available in the literature [1, 2]

4.4 Results and Discussions

4.4.1 Symmetric SAW streaming-mixing effect

Droplets with a volume of 30 μl were loaded on the central axis of the path taken by a SAW propagating during this experiment, as depicted in Fig. 4.9(a). Figure 4.11 compares experimental and numerical results of streaming velocities at different RF powers measured at the centre of the top surface of the droplet in the x direction, as illustrated in Fig. 4.8. These results show that the streaming velocity approaches a constant value within a time period less than 1 s, as the viscous resistance prevents any further increase in flow velocity [56]. The velocities from experiments and the simulations have similar values when the flow reaches a steady state, but these are less similar during the starting period due to the complicated interaction between the polystyrene solid particles and liquid. Figure 4.12 shows numerical results of the normalised steady-state streaming velocity in the x direction, $U_{xn} = U_x/U_{xr}$, with the

corresponding normalized power $P_n = P_D / P_{Dr}$, where U_x represents a streaming velocity at the RF power P_D, and U_{xr} represents reference streaming velocity at the reference power P_{Dr} (the highest power in this series of experiments). In general, it can be observed that the calculated and measured streaming velocities are in good agreement. The error bars represent the standard deviation in streaming velocity from average values measured during experiment.

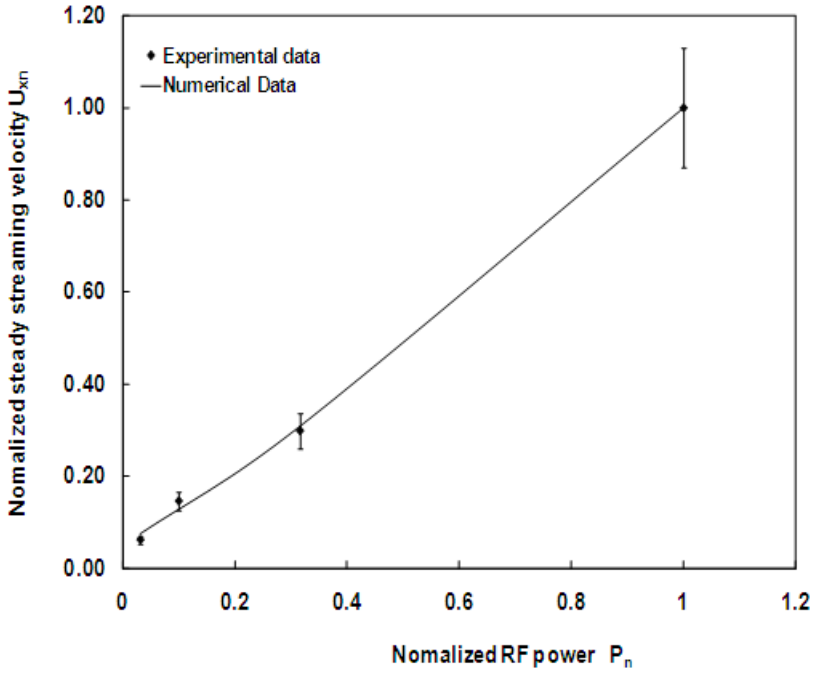

Figure 4.13 Flow normalized streaming velocity as a function of normalised RF power for a 30 μl droplet size using a 128° YX-$LiNbO_3$ SAW device (IDT with 60 fingers).

Figure 4.14 shows the simulated streamlines of the SAW streaming with 3D circular flow patterns for a 30 μl water droplet at an RF power of 15.89 mW. The simulation results show that the highest value of streaming velocity is located at the interaction area between the droplet and SAW because a higher momentum is delivered near the substrate surface (SAW-droplet interaction area), where the source of SAW force is more intense. This momentum source at the SAW-droplet interaction area establishes a flow field that drives the flow with a Rayleigh angle, resulting in a continuous flow within the droplet. Indeed, experimental observation using a high-speed camera revealed that the particles inside the droplet started to move from the bottom to the centre of the top surface of the droplet after SAW application, and this phenomenon of flow development has been predicted by current model numerical simulation results presented in Fig. 4.15.

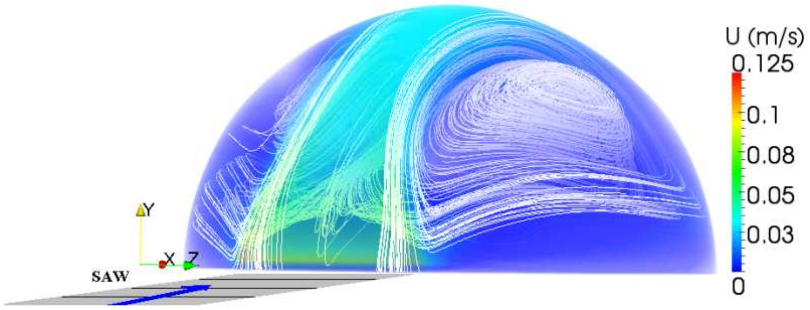

(a)

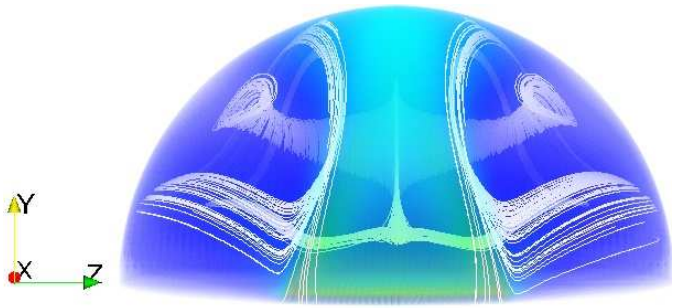

(b)

Figure 4.14 Numerical 3D illustration showing the droplet SAW interaction leading to 3D complex flow patterns due to SAW energy attenuation and Reynolds stresses formation which in turn produces an effective steady force acting in the fluid body (30 μl droplet at an RF power of 15.89 mW); (a) tilted view, (b) direct view focusing through droplet centre

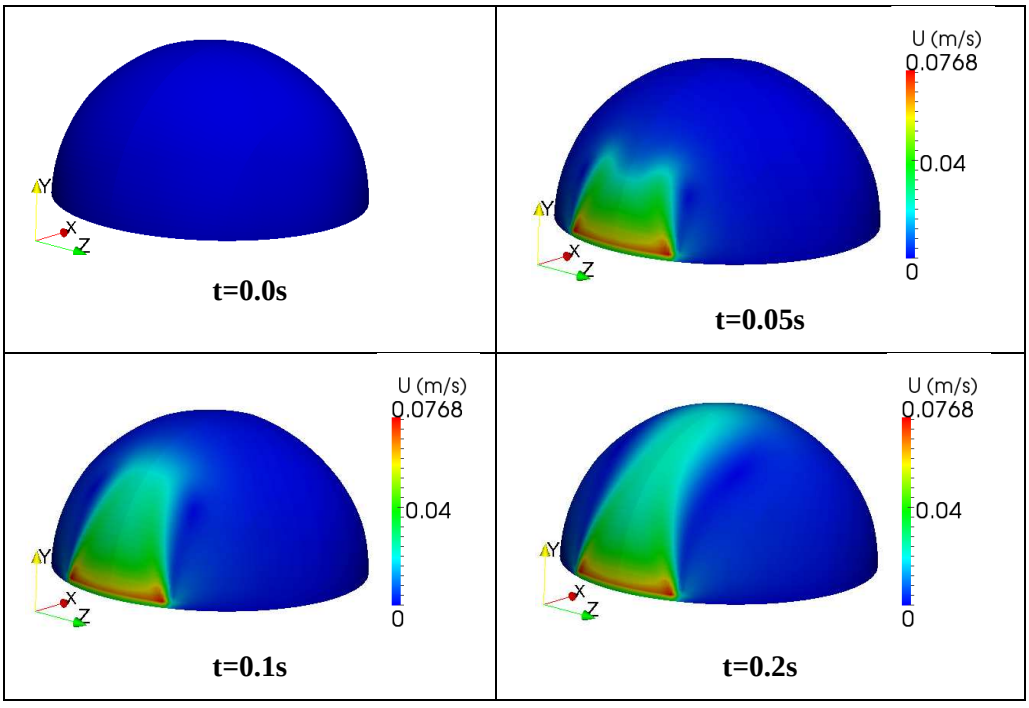

Figure 4.15 Numerical results showing the progress of flow field after applying the RF power and SAW propagation (30 μl droplet at an RF power of 2.75 mW)

When the moving liquid reaches the droplet boundary, the interaction between the liquid and the solid boundary induces a reverse flow at both sides of the droplet and the bottom liquid-solid boundary. When this reverse flow goes back towards the IDTs, the driving flow due to a SAW force drives the reverse flows upwards to the top of the droplet. Eventually, the interaction between the reverse flow and the SAW driving flow produces a double vortex flow pattern that reaches a steady state within a few seconds, depending on the applied RF power, droplet size and fluid viscosity, as shown in Fig. 4.14. The interaction between the two flows contributes to a decrease in the streaming velocity, especially at a high RF power (i.e., high wave amplitude), where the progression flow is accelerated to a higher velocity and then decelerated to a steady velocity afterwards as can be observed by the velocity profiles in Fig. 4.11. Figure 4.14(b) shows a streaming vortex centre line is generated inside the liquid droplet. Figures 4.16(a) and (b) indicate that increasing the SAW force results in an increase of the streaming velocity and a change in the position of the vortex central line. The same phenomenon has been confirmed by experimental observations.

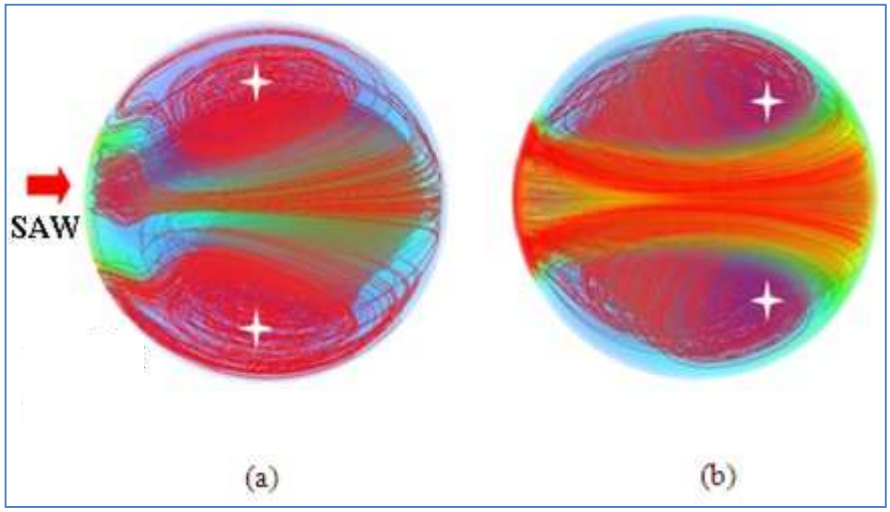

Figure 4.16 SAW numerical streaming patterns for 30 μl droplet at different SAW forces. The streaming velocity increases from zero (sky blue) to higher velocity (light red); (a) RF power of 2.75 mW; (b) RF power of 46.56 mW. The white stars indicate the circulation centres

The streaming patterns obtained from solving the continuity equation, Eq. (4.2a) and the Navier-Stokes equation, Eq. (4.2b) and those from the captured trajectory pictures of 6µl polystyrene particles were compared at the same SAW setup and droplet size. Figure 4.17 shows good agreement has been obtained from different elevations. These figures present comprehensive views of SAW streaming patterns within microdroplet-

positioned centre on the SAW propagation direction, and the driving flow and reverse flow are clearly visible.

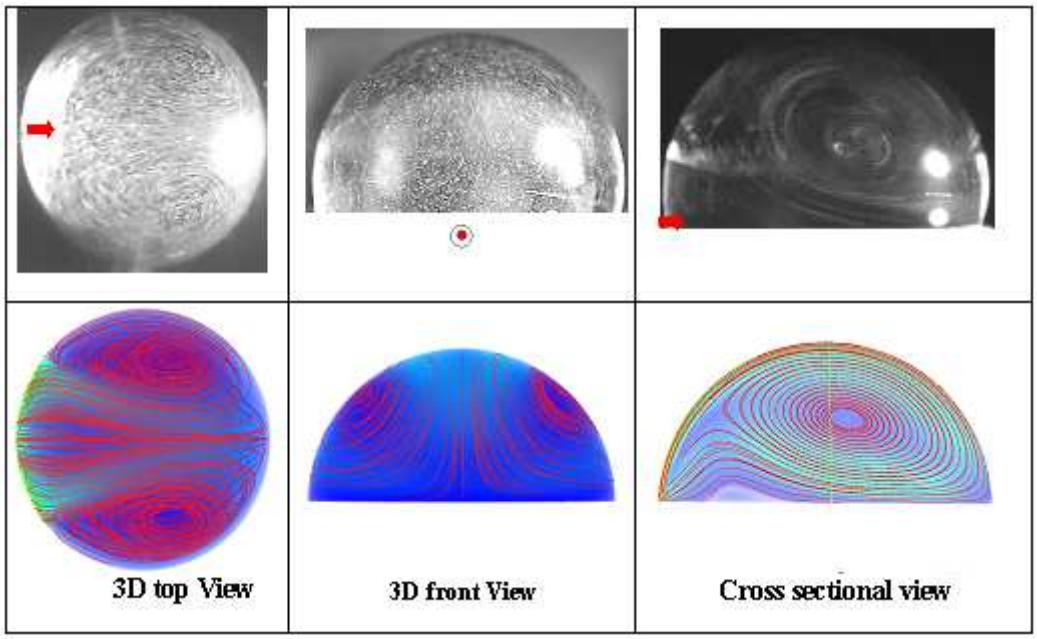

Figure 4.17 Comparison of experimental and numerical modeling for a 30 μl droplet positioned at the centre with the SAW propagation direction; the upper row shows pictures of particles trajectories; the bottom row shows the corresponding streaming patterns from numerical simulations. The red arrow indicates the SAW propagation direction.

4.4.2 Concentration of particles using asymmetric SAW streaming

It has been well documented that an acoustic radiation force can cause microparticles to migrate towards the pressure nodes, or antinodes, depending on their mechanical properties, and that particles can also be fractionised (according to their size and density), and thus concentrated and/or separated within the liquid [68, 69, 131, 132]. A simple method to concentrate the particles within a droplet is to use an asymmetric distribution of SAW radiation along the width of the droplet as shown in Fig. 4.9(b), and this has been well documented in [70]. Figure 4.18 shows the captured images of the starch particle concentration process within a 30 μl droplet at an input RF power of 79.34 mW. The induced flow circulation in the droplet due to acoustic streaming rapidly establishes a circulation pattern, and particles clustering near the droplet centre in the form of conical shape as can be observed in Fig.4.18.

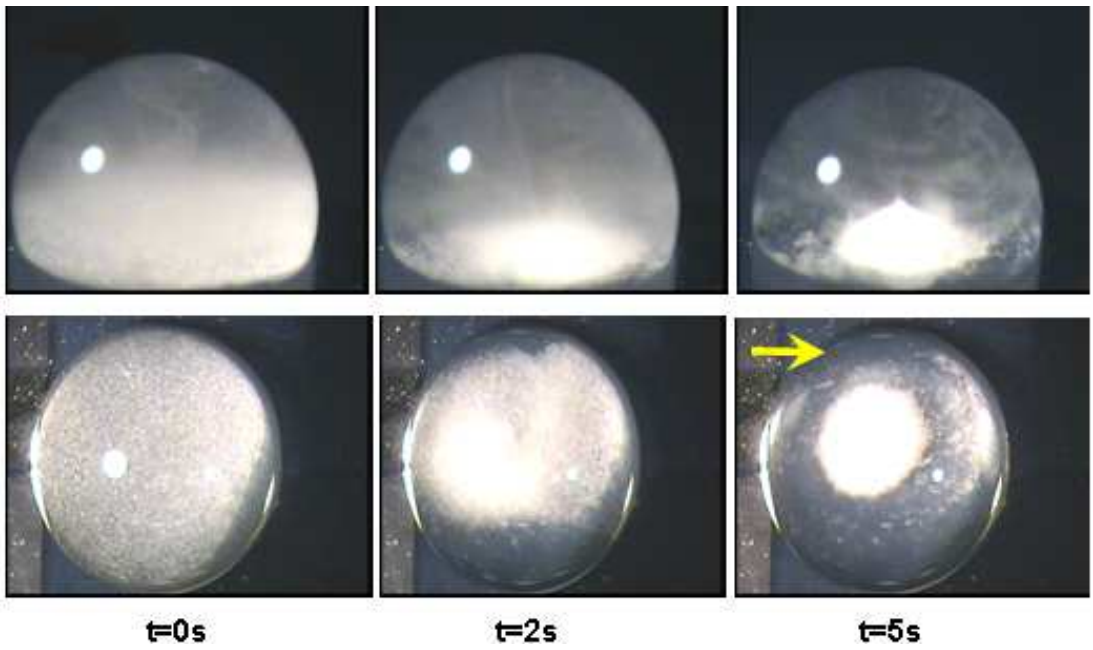

Figure 4.18 Captured video images illustrating the rapid concentration process for a 30µl water droplet with starch particles at an RF power of 79.43 mW, frequency 62 MHz and SAW width 2 mm; the first row shows a side view of the droplet, while the second row shows a top view of the starch being concentrated. The yellow arrow indicates the SAW propagation direction

Raghavan et al. [70] reported that the flow phenomenon within liquid droplets due to the asymmetric positioning of SAW is similar to that obtained by the flow field between stationary and rotating disks, which is known as Batchelor flow [133]. From the side view of the movies, the fluid was observed to be pushed upward just above the SAW propagation area which results in the primary azimuthal rotation within the droplet periphery, where the same flow feature has been reported in [70]. This flow phenomenon can be seen clearly in Fig. 4.19(a), which gives a numerical illustration of three dimension velocity vectors on the droplet surface. Figure 4.19(b) depicts the corresponding experimental snapshot of such flow phenomena. After applying the SAW power, the starch particles are quickly follow the azimuthal fluid flow within the droplet, which agree well with the numerical results presented in Fig. 4.19(a). Therefore, the starch particles follow the flow field in a helical manner around the surface periphery of the droplet to the upper position from the droplet bottom. The numerical results show that the streaming velocity of the flow field at upper levels is much higher than the lower one, as shown in Fig.4.20.

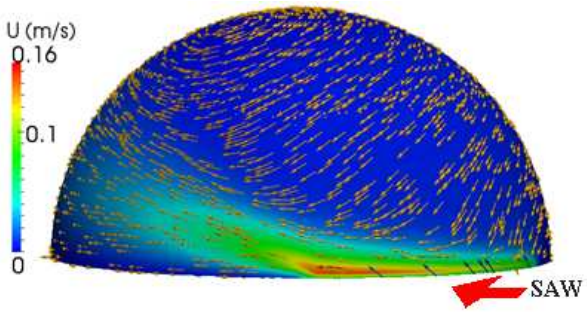

(a)

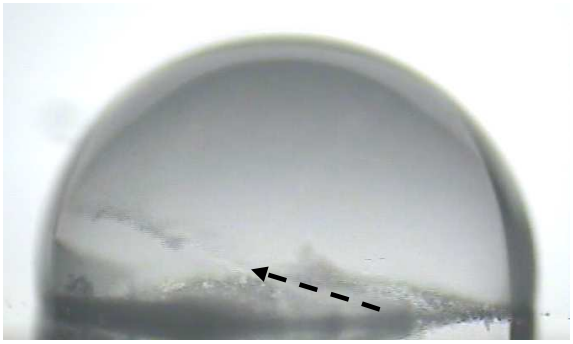

(b)

Figure 4.19 (a) Illustration of numerical result of streaming velocities for a 30 μl droplet at the RF power of 24.39 mW; the vectors indicate the flow circulation direction at the droplet surface. (b) Side view snapshot of a corresponding experiment shows particles trajectories after SAW application, as indicated by the black arrow

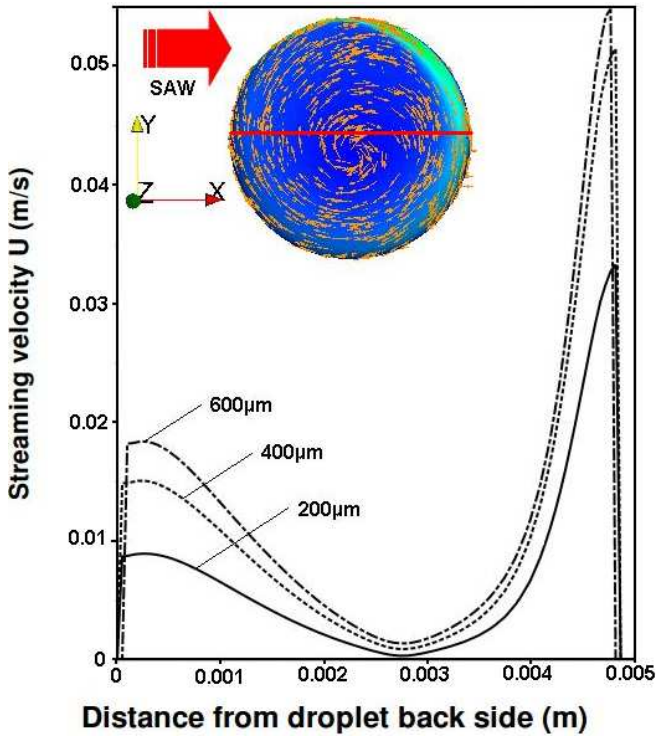

Figure 4.20 Streaming velocity distributions across the centre of a 30 μl droplet at the RF power of 46.56 mW. These curves represent numerical results along with x-axis as depicted by the red line through the droplet centre for different heights from the substrate surface (droplet-surface contact area)

During the experiment, it has been noted that particles were directed downwards, i.e., towards the substrate surface near the SAW interaction area, where they move closer to the half rear of the droplet and are then forced upwards again when they reach the SAW interaction area. Figures 4.19(a) and 4.20, shows the numerical simulation results for the flow phenomenon, where the streaming velocities at the back side (e.g., away from SAW source) of the droplet are smaller than the front (e.g., near the SAW) for a given horizontal cross section. Velocity vectors in Fig. 4.19(a) shows how the flow is directed down near the SAW propagation area before it is forced upward again along the droplet periphery, which is in consistent with the experimental observations (see Fig. 4.20(b)).

The streaming velocity at the droplet bottom is zero due to surface friction, as shown in Fig. 4.20. Consequently, the primary azimuthal rotation flow around the droplet periphery produces a secondary bulk circulation flow [134-137], as illustrated in Figs. 4.21(a) and (b). This secondary circulation flow exists due to the net inward radial velocity field close to the bottom of the droplet, which gives rise to a swirl like flow at the bottom of the droplet. Therefore, the fluid close to the droplet bottom moves toward the centre stagnation point and takes the starch particles along with it. This swirling along the bottom of the droplet can be easily seen in Figs. 4.21(c) and (d). As a result of mass conservation (continuity), the flow swirls back upward towards the top of the droplet (secondary circulation flow), as illustrated in Fig. 4.21(b).

The experimental results show that starch particles are clustered closely to the SAW propagation area, as shown in the rightmost panel of the second row in Fig. 4.18, and this is attributed to a higher inward radial velocity on the right bottom side of the droplet (opposite side to the SAW-droplet propagation area) than the left bottom side of the droplet (the SAW-droplet propagation area). This is illustrated by the numerical simulation results of radial velocity component in Fig. 4.22. The negative radial velocity component in the left side of Fig. 4.22 represents inward radial velocity towards the central stagnation point, while the positive radial velocity represents the outward velocity (away from centre line). In the right-hand side, the positive velocity represents inward velocity, while the negative one represents the outward velocity. Figure 4.22 shows that the radial inward velocity component near the bottom of the droplet is larger than that in the upper regions, which explains the existence of a strong swirl motion at the bottom of the droplet during the measurements, as depicted by the numerical results in Fig. 4.21(d).

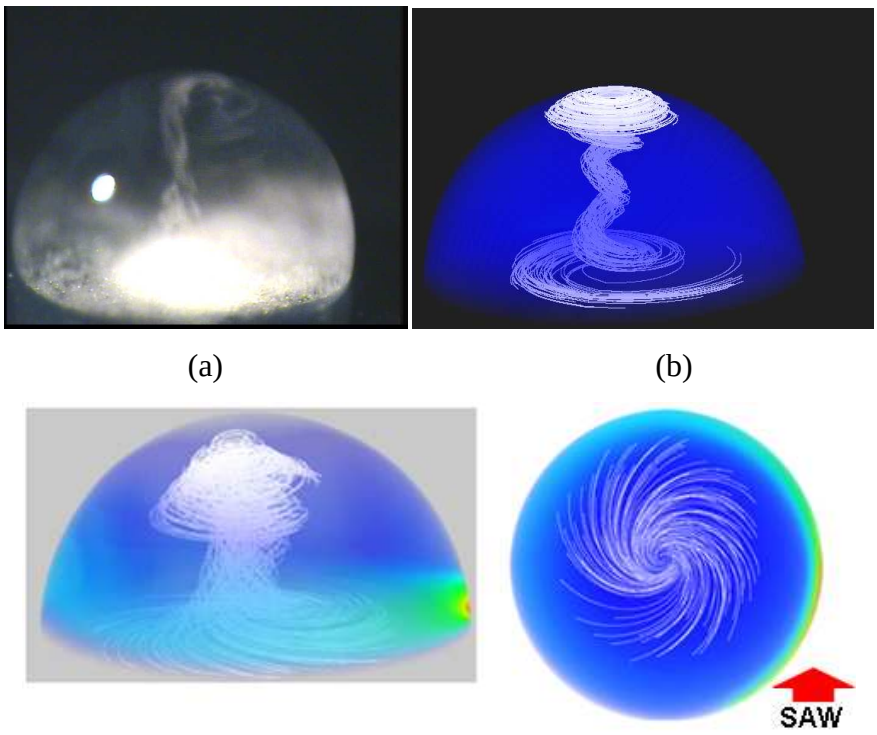

Figure 4.21 Experimental and numerical illustrations of a secondary recirculation for a 10 μl water droplet ; (a) the captured video image during the concentration process of starch particles at the RF power of 79.43 mW; (b) the corresponding numerical streaming patterns focusing through the droplet volume; (c) streaming patterns illustrates the column of secondary and the swirl motion; (d) a cross-sectional plan view seen from the bottom of the droplet, which illustrates the swirling motion towards the centre of rotation.

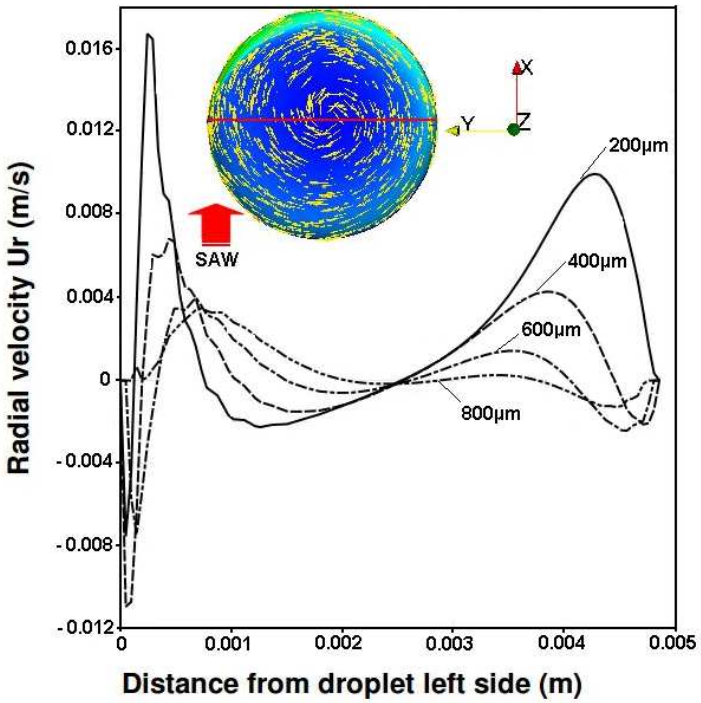

Figure 4.22 Radial streaming velocity components from numerical results at different heights from the droplet bottom for a 30 μl droplet at an RF power of 79.43 mW.

Even though the flow swirls upward through a secondary circulation central column of flow, the starch particles cluster at the centre of the column, in a conical shape, as shown in Fig.4.18. Raghavan et al. [70] found that if the streaming velocity U is low enough near the stagnation area, the particles will be concentrated near the stagnation area due to the sedimentation force. Numerical results in Fig. 4.20 clearly show that the streaming velocity near the stagnation point at substrate surface is smaller than in other regions. However, the experimental measurement also shows that the tip height of the clustered starch particles is ~ 850 μm in the case of 79.43 mW RF power. The numerical simulation results for the equivalent RF power case showed that the tip height corresponds to the numerical height in which the radial velocity becomes zero near the droplet centre, as depicted in Fig. 4.22, at cross sectional height 800 μm.

The required time for the particles to accumulate in a conical shape has been recorded for different RF powers. In this study, the concentration time is defined as the time needed for the clustered particles to accumulate and form the final steady state (i.e., when the area A_c occupied by the clustered particles on the substrate surface changes by less than 5 % in 30 s duration) conical shape starting from the initial application of the RF power. Figure 4.23 shows the effect of the RF power on the starch particle concentration time within the water droplets for a moderate range of droplet sizes. This shows that the concentration time decreases with increasing RF power, which is attributed to the increase in the inward radial velocity (Ur), near the bottom of the droplets. This results in a stronger swirl motion near the bottom of the droplet, which collects the particles within the droplet. Figure 4.24 shows results from numerical simulations of the radial streaming velocities 200 μm above the bottom of a 30 μl droplet for different RF powers. The figure clearly shows that radial streaming velocity increases with increasing the RF power; a factor which directly influences the wave amplitude (A). Above a certain RF power, the central streaming velocities are so high that the particles cease to be concentrated and flow away with streams towards the droplet top through the central column, as depicted in Fig. 4.21(a).

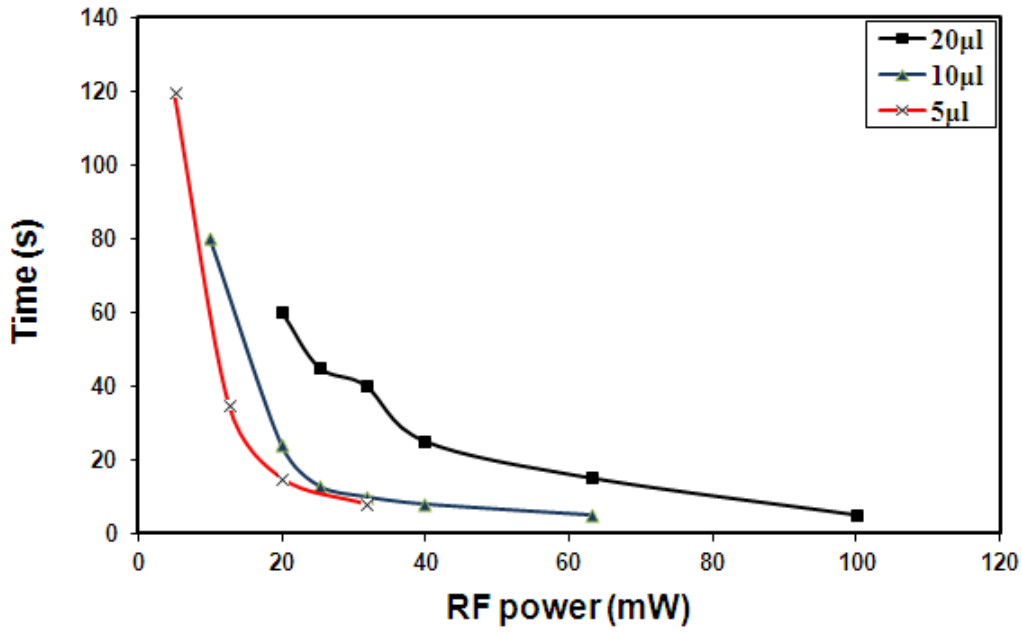

Figure 4.23 Effect of RF power and droplet size on the particle concentration time (time for particle accumulation to change from its initial to the final steady state for moderate range of droplet size)

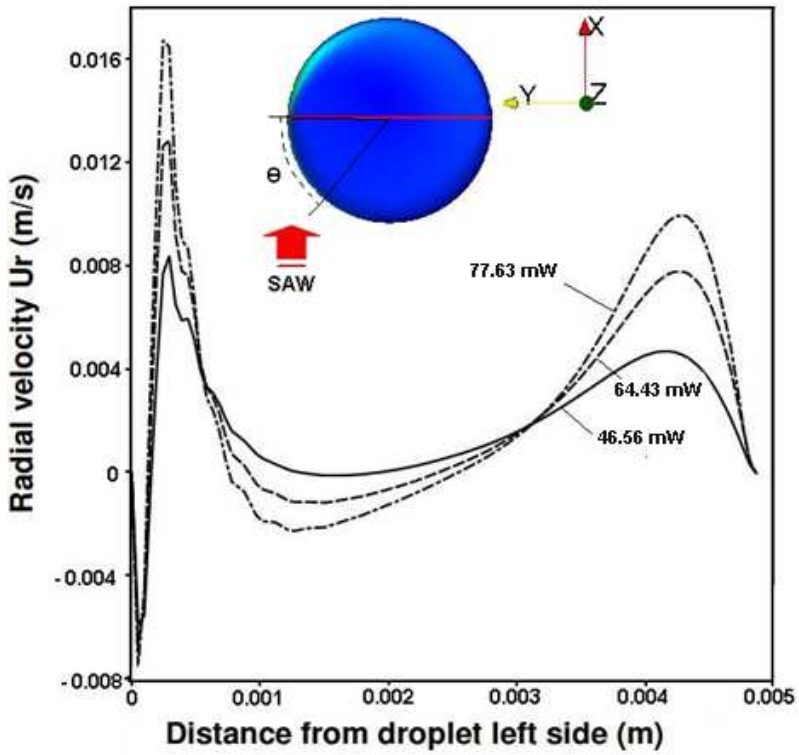

Figure 4.24 Radial streaming velocities from numerical results at 200 μm height from the droplet bottom for 30 μl droplet at different RF powers

To investigate the effect of a droplet's asymmetric position in the SAW propagation direction, numerical simulations have been carried out at different SAW interaction angles, as indicated by the droplet illustration in Fig. 4.24. The results show that the

suitable interaction angles of SAW with the liquid droplet should be in the range $22.5^{o} \leq \Theta \leq 90^{o}$, in order to achieve larger inward radial velocity and shorter concentration times. For interaction angles $>110^{o}$, the circulation flow pattern becomes a double vortex circulation pattern, similar to that shown in Fig. 4.16, and the range $90^{o} \leq \Theta \leq 110^{o}$ could be named as transition zone between circulation flow pattern and double vortex flow pattern. Therefore, the concentration effect is dependent on a SAW input power as well as the droplet position.

The simulation and experimental results show that there is a range of RF power within which the concentration of starch particles can be achieved, as shown in Fig. 4.25. This can be described by four regions according to the RF power and concentration time. The lower region in Fig. 4.25 (zone 1) represents the region within which there is no bulk circulation for the flow field. The SAW force is not zero, but it is balanced by the pressure term in Eq. (4.2b), which represents hydrostatic solution [55, 56]. The adjacent zone to the particle concentration curve (zone2) represents the region within which a weak bulk circulation occurs, but it is not large enough to drive the particles towards the circulation centre. The lower threshold RF power for the particles to be concentrated lies directly above the upper limit of zone 2. Thus, for particle concentration, an efficient inward radial velocity must be obtained, and that can be achieved within zone 3. The concentration is enhanced with increasing applied RF power up to a critical value (the upper limit of zone3). Above this the redispersion of the particles becomes dominant (zone 4). This is attributed to the increase in the streaming velocity near the stagnation point which in turn starts to overcome the sedimentation force and drives the particles away from the concentration cone through the central column as illustrated in Figs. 4.21(a) and (b). The droplet size as well as the magnitude of the RF power sets the upper limit threshold (i.e., the highest power that can be applied to achieve the particle process), as can be observed in Fig. 4.23. This value can be seen to increase with larger droplet sizes, which is due to lower streaming velocities for bigger droplets at the same RF power, i.e., higher power is required for larger droplets to achieve the same concentration time. In a similar manner to the concentration upper threshold RF power, the lower threshold RF power is also affected by the droplet size.

Figure 4.26 show the area concentration ratio A_c / A_t (i.e., the ratio between the clustered starch area A_c and the droplet substrate contact area A_t viewed from the top) as a function of the RF power and droplet size. Lower ratios are obtained at higher RF

power, which is attributed to the corresponding increase in streaming velocity. This in turn produces higher inward radial velocity that drives more particles towards the stagnation point and results in a smaller concentration area. Streaming with low inward radial velocities (weak swirl motion) results in larger concentration area, and low concentration ratios.

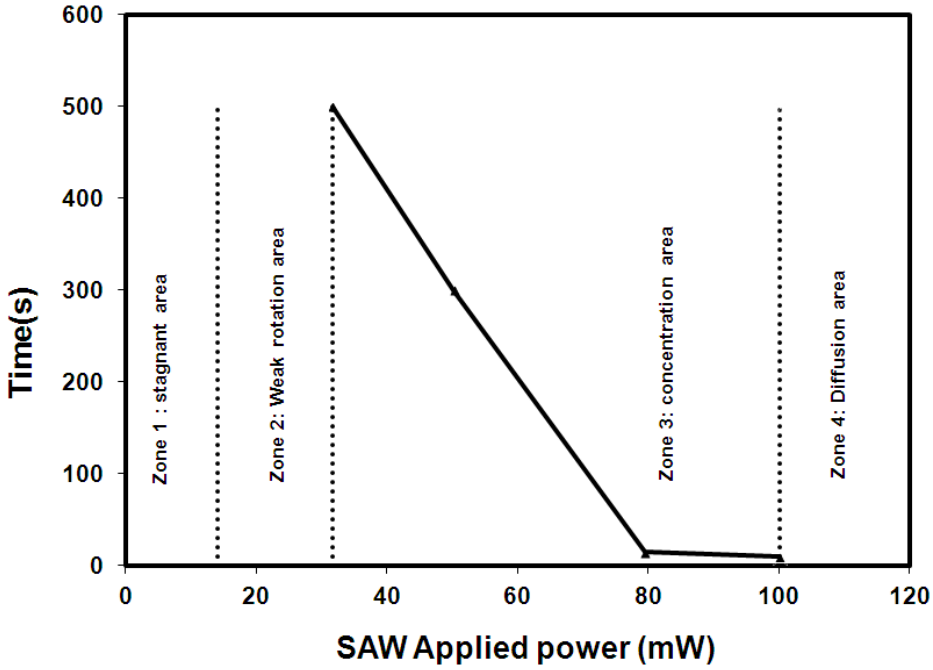

Figure 4.25 Experimental time-RF power concentration curve for a 30 μl droplet size in asymmetric position with a SAW device at 62 MHz.

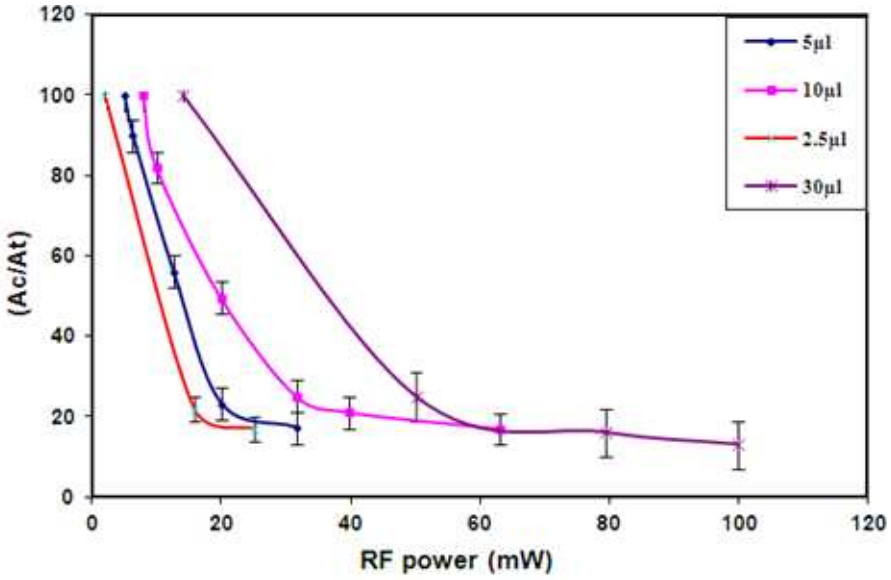

Figure 4.26 The area concentration ratio A_c / A_t (the ratio between the concentrated starch area A_c and the whole droplet area A_t viewed from top) as a function of the droplet size and RF power

4.5 **Summary**

In this chapter surface acoustic waves generated by 128^{o} YX- black $LiNbO_3$ SAW devices have been characterised for microfluidic mixing and concentrating particles, and a 3D numerical model of SAW acoustic streaming in microfluidic applications has been developed. A SAW acoustic streaming model has been calibrated using experimental results, which predicted the SAW streaming phenomena for different experimental setups. The concentration of suspended particles within a droplet can be obtained when the droplet is located asymmetrically on the SAW propagation direction. The applied RF power, droplet size and droplet position have been identified as factors affecting the concentration process, with the concentration rate being enhanced with increased applied RF power until a critical value is reached above which the dispersion of the particles becomes dominant. The magnitude of the critical values is also influenced by the droplet size. The 3D model which has been developed captures the physics behind the mechanism of suspended particles concentration by placing the SAW-driven microdroplet in an asymmetric position.

Chapter 5

ACOUSTIC STREAMING AND HYDRODYNAMIC NONLINEARITY

Since the numerical model of a SAW-induced streaming field was developed using the full nonlinear Navier-Stokes equation (i.e., Eq. (4.2b)), and its results were verified and compared with the corresponding experimental data, where good agreement between the two results is obtained (discussed in Chapter 4). This chapter investigates the effect of hydrodynamic nonlinearity on the development of acoustic streaming induced by a Rayleigh SAW, and discusses its significance on the generation of a streaming field, using both the experiments and 3D computations.

5.1 **Introduction**

As introduced in Chapter 4 (Sect. 4.1), many studies have been done to provide numerical solutions for the SAW-driven microfluidics, most studies of the SAW-driven fluids used the acoustic body force approach based on the Stokes model of Nyborg's theory [54]. For instance, Franke et al. [93] reported that the nonlinearity (inertial) effects arising from a SAW propagation in a fluid medium were nearly negligible and the Stokes model, i.e., Eq. (3.4) is applicable, due to the small geometries of droplets.

However, only a few studies have been reported on the effects of hydrodynamics nonlinearity in acoustic streaming [74, 138, 139], and even these studies were limited to ultrasonic standing waves, rather than SAW. For example, Lighthill [55, 56] discussed the effects of hydrodynamic nonlinearity on acoustic streaming of standing wave generated by a cylindrical resonator in an unbounded fluid medium, and concluded that the nonlinearity effects of fluid inertia were significant in all noticeable acoustic streaming examples. Nevertheless, the nonlinear term of flow inertia in the SAW studies was normally ignored [104], even for very high SAW powers up to 6×10^4 μW [46, 48, 103, 123]. To the best of author's knowledge, in this chapter, a systematic experimental and numerical investigation concerning the effects of the hydrodynamic nonlinearity on the SAW-driven fluids is presented for the first time.

5.2 **Methods**

5.2.1 Experimental

The IDT of a SAW device used in this investigation has a wavelength of λ = 64 μm and a fundamental frequency $f \approx$ 60 MHz. Water droplets (1-30 μl) were loaded symmetrically with the SAW propagation path (see Fig. 4.7 (a)), using a micropipette. For the measurements of the streaming velocities, the same experimental setup presented in Chapter 4 was used (see Section 4.2.2).

5.2.2 Modeling Details

The induced flow streaming in the liquid droplet was assumed to be governed by the continuity and laminar incompressible 3D Navier-Stokes equations, i.e., Eqs. 4.2(a) and (b), respectively that driven by an external acoustic body force F [122]. The numerical method and boundary conditions used in this study was presented in Sect. 4.3.1.4.

In this numerical analysis, RF powers were applied in range of $P_D \leq$ 16 mW, to keep the droplet in its original shape without inducing significant distortion. Consequently, stress-free boundary conditions can be applied at the droplet/air interface. The preliminary results and calibration of our code have been reported in Chapter 4. Only for the analysis of linearised hydrodynamic model, the nonlinear term, $\rho_f(U \cdot \nabla)U$ in Eq. 4.2(b) was ignored, which gives a transient version of the Stokes model, Eq. (3.4). In this study, all the numerical cases were run to a steady state, and these results are discussed in the following sections.

5.3 **Results and Discussions**

5.3.1 Dimensionless parameters

The main parameters that govern the system of SAW-driven droplets are those of the flow field of the droplet hydrodynamics, and those of the sound field that generates either a flow inside the droplets or distortion of droplets shape. The hydrodynamics parameters include the streaming velocity U (m/s), the fluid viscosity ν (m^2/s), and the droplet radius R_d (m), as characterised by the Reynolds number $\mathrm{Re} = UR_d/\nu$. Another parameter is the surface tension σ (N/m), a force that plays significant role against the SAW force to retain the original shape of the droplet. The characteristic parameters of the sound field; are the SAW wave amplitude A (m), Eq. (4.8), the SAW wavelength,

λ (m) that measures the propagation depth of SAW into the droplet fluid [53]. These two parameters are involved in Eq. (4.7) of the acoustic body force F (N/m^3).

In this study, it has been found from both the experimental and numerical simulation results, that the driving SAW characteristics can be described by a dimensionless parameter of normalised acoustic force F_{NA}, as defined by:

$$\boldsymbol{F_{\mathrm{NA}} = \frac{F\lambda}{\sigma/R_d}} \tag{5.1}$$

The proposed parameter of F_{NA} represents the ratio of the acoustic force (e.g., measured at a point where the SAW enters the droplet) per unit area, $F\lambda$, to the surface tension per unit length, σ / R_d. The new dimensionless parameter of the F_{NA} proposed in this study can be used to describe not only the characteristics of the acoustic wave field, but also the hydrodynamics of the SAW-driven droplets including the deformation mechanism. These two dimensionless parameters, i.e., F_{NA} and Re, are used in the analysis and discussion of hydrodynamics of droplets induced by a Rayleigh SAW in this chapter.

5.3.2 Influences of fluid inertia on streaming phenomena

5.3.2.1 *Reynolds number*

Effects of hydrodynamic nonlinearity on the streaming phenomenon are discussed in terms of the steady-state Re of an induced internal flow dynamics by a SAW-droplet coupling, using a moderate range of the normalized acoustic force, F_{NA} (i.e., Eq. (5.1)), as shown in Fig. 5.1. As can be seen in Figs. 5.1(a) and (b) by the relationship between the Reynolds number and F_{NA} parameter in log-log scale, when $F_{\mathrm{NA}} \leq 0.002$ ($P_D \leq 1$ μW), the results from the Stokes model, Eq. (3.4), and the full N-S model, Eq. (4.2b) give very good agreement in comparison with experimental measurements. This is based on an error analysis using defined deviation of $\epsilon = \left|1 - \frac{\mathrm{Re_l}}{\mathrm{Re_{nl}}}\right| \leq 5.0\text{x}10^{-2}$, where $\mathrm{Re_l}$ and $\mathrm{Re_{nl}}$ are the Reynolds number of linearised and non-linearized cases, respectively. This means that the linearization assumption is valid only for the simulation of acoustic streaming at very low SAW powers of the microwatts range. This validation can also be identified by the associated Reynolds number with Re < 1, if and only if, the droplets size is small enough, such as for the droplet volumes of 1.0 or 2.5 μl used in this study, as illustrated in Figs. 5.1(a) and (b) respectively. It should be

noted that the condition of Re < 1 that has been imposed in most studies of employing the linear assumption [104], is not applicable for larger droplet volumes, such as 5 or 10 μl in this study.

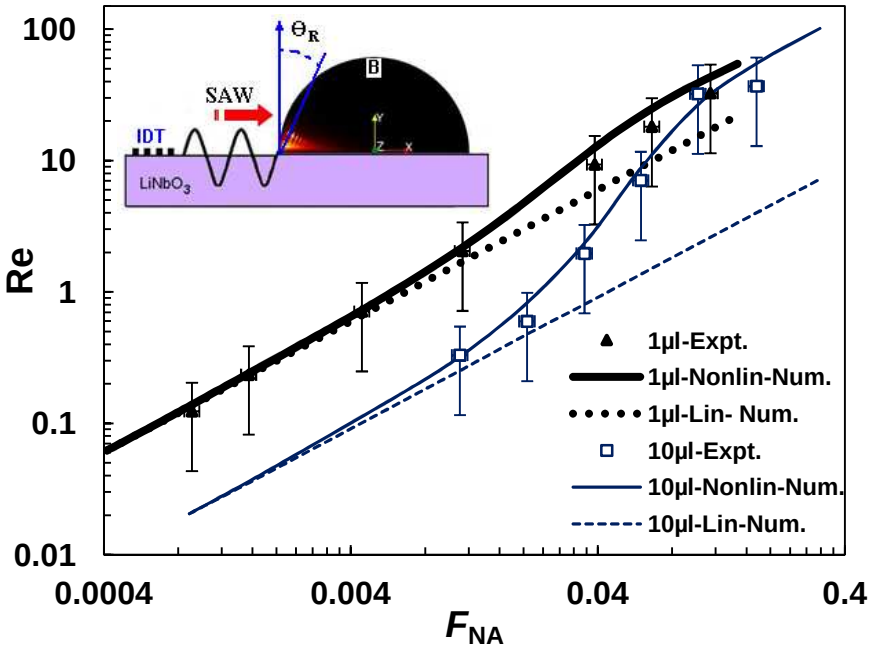

(a)

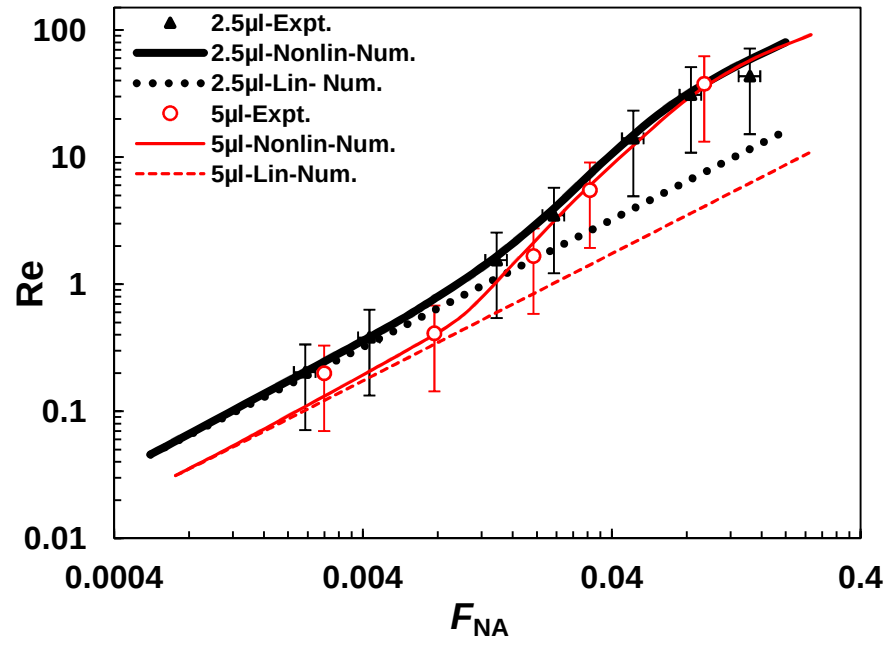

(b)

Figure 5.1 Effects of hydrodynamic nonlinearity in the relationship between the steady state Reynolds numbers, Re and F_{NA}, using 128° YX-$LiNbO_3$ SAW device with 0.5 mm aperture excited by a frequency of 60.4 MHz; (a) results for 1 and 10 μl droplets; and (b) results for 2.5 and 5 μl droplets. Solid and broken lines represent the nonlinear and linear numerical results, respectively. The markers denote the experimental data

The results in Fig. 5.1 show that the flow inertia does appear, and becomes negligible only at a condition of Re <<1. However, when the SAW power increases, $F_{\mathrm{NA}} \geq 0.01$ (or $P_D \geq 20\ \mu$W), the difference between the Stokes model results and the experimental data becomes significant, and can be as high as 90%, especially for the larger droplets. Meanwhile, this difference is only about 10% for the N-S model, as shown in Figs. 5.1(a) and (b). This closer agreement of the N-S model results with experimental data is due to the contribution of flow inertia, where the increase in the F_{NA} (or SAW power) enhances the role of the hydrodynamic nonlinearity term in the nonlinear N-S model, in Eq. 4.2(b); which becomes too large to be ignored.

Additionally, in the nonlinear region, it is clearly visible from the experimental and the nonlinear N-S modeling results in Figs. 5.1(a) and (b) that the differences in the value of Re for the two droplets sizes decrease gradually with an increase of the acoustic power, and becomes considerably smaller as long as $F_{\mathrm{NA}} > 0.05$. In contrast, the Stokes model results show a fixed difference in the value of Re with variation in the drops volumes for the whole range of F_{NA} values, a situation not confirmed by the experimental data.

5.3.2.2 *Flow development and streaming velocity*

In order to identify the role of the nonlinear term in SAW acoustic streaming, the transient streaming velocities of the N-S model presented in Fig. 4.11 for a 30 μl droplet, and those of the Stokes model were examined in Fig. 5.2(a) by comparing both simulation and experimental results. Results show that the droplet internal flow has been accelerated quickly to a steady velocity within one second, with higher F_{NA} of a 0.419. Increasing of F_{NA} (or RF power) reduces this initial time due to the increase in the SAW momentum delivered to the fluid. As shown in Fig. 5.2(a), the values of streaming velocities from the nonlinear N-S model are in good agreement with the experimental data. On the other hand, the Stokes model results are one order of magnitude less than those from experiments. Furthermore, the discrepancy between the steady state experimental and numerical results for F_{NA} of 0.248 is 87.4%, and becomes 92.5% for F_{NA} of 0.419, when flow inertia (hydrodynamic nonlinearity) is ignored. Conversely this discrepancy is only 0.47% and 1.37%, respectively, when the hydrodynamics nonlinearity is taken into account. Also, at a steady state stage, the deviation of the velocity for the two power cases is ~16 mm/s, both from the experimental and nonlinear numerical results using the N-S model, compared with only ~0.846 mm/s in the linear case, i.e., using Stokes model.

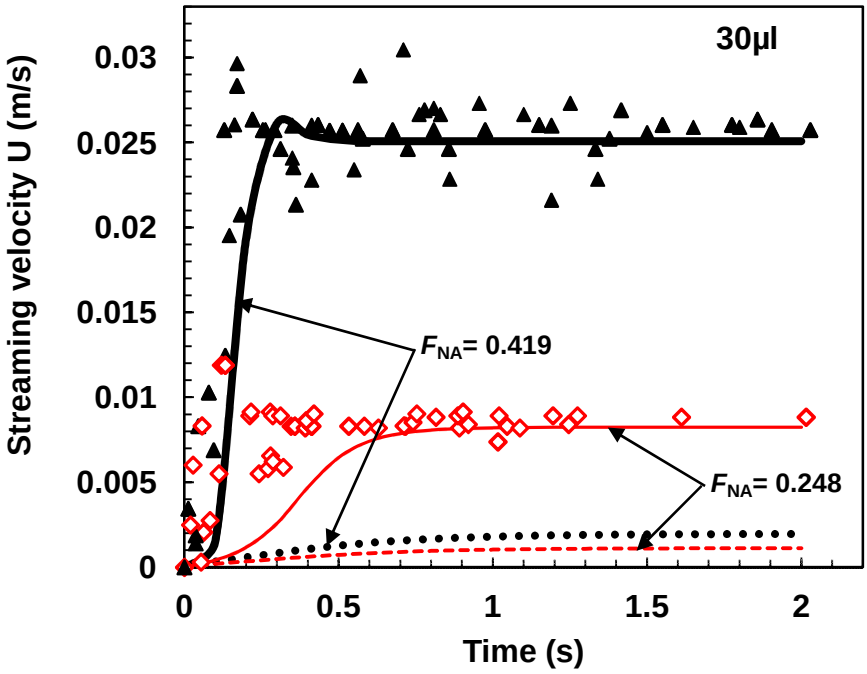

(a)

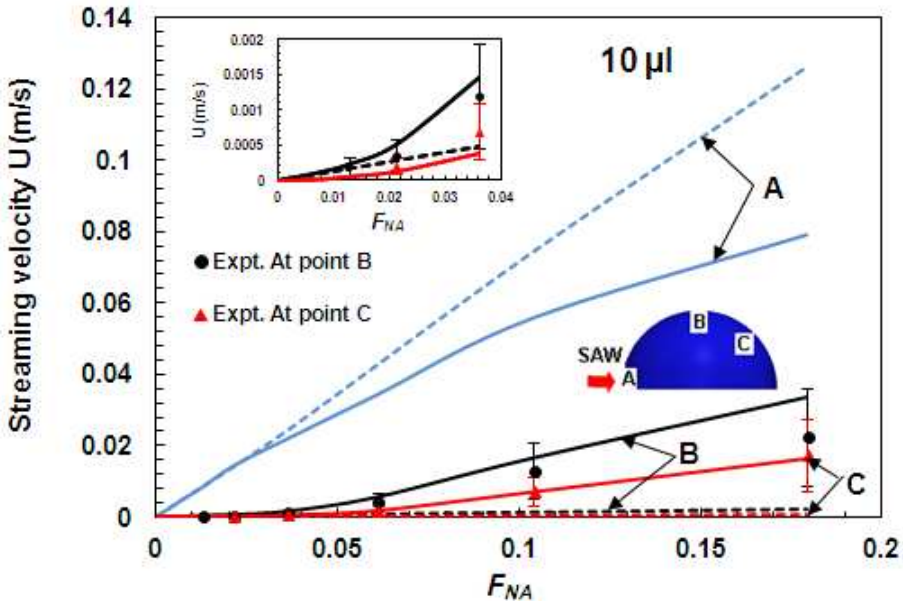

(b)

Figure 5.2 Hydrodynamic nonlinearity effects on; (a) the transient streaming velocity of a 30 µl droplet measured at point B, using 128° YX-$LiNbO_3$ SAW device with 62 MHz frequency, 2 mm aperture at different $\boldsymbol{F_{NA}}$; (b) the streaming velocity as a function of $\boldsymbol{F_{NA}}$ for a 10 μl droplet using a 0.5 mm aperture SAW device driven at 60.4 MHz. Solid and broken lines represent the nonlinear and linear numerical results, respectively. The markers are the experimental measurements

Figure 5.2(b) shows both experimental and simulations results of the streaming velocity as a function of F_{NA} for a 10 μl droplet at three observation points; i.e., point *A* is close to the SAW source, point *B* at the top centre of the droplet, and point *C* far away from

the SAW source. However, due to the difficulties and challenges with capturing the flow field near the SAW source during the experiments, only the numerical results are presented for point *A*. It can be observed once again that the importance of the fluid-hydrodynamics nonlinearity becomes more significant with the increase of the SAW power, due to the increase of the streaming velocity, where the inertial forces become dominant. The linear approximation using the Stokes model results in a higher streaming velocity near the SAW source (point *A*) and a much lower reading at regions away from the SAW source (*B* and *C*).

The role of the nonlinear term on the droplet-acoustic streaming can be further illustrated by taking the case of a 20 μl droplet and examining the velocity distribution in three dimensions. The velocity distribution was measured along two axes through the droplet, i.e., the vertical y axis shown in Fig. 5.3(a), and the horizontal z axis at a height of 1200 μm from the bottom of the droplet shown in Fig. 5.3(b). Figure 5.3(a) shows that at an early stage (i.e., t = 0.1 s), both the nonlinear and linear approximations have similar velocity profiles. However, as the flow develops, the differences between the two profiles become significant. This is also true for the velocity profiles along the horizontal z axis, as can be observed in Fig. 5.3(b). Fig. 5.3(a) shows that the value of the steady-state streaming velocity using the Stokes model is less than that using the N-S model by about 93% at the top of droplet, and about 60% less at the centre of the droplet, as shown in Fig. 5.3(b). These results clearly show the consequences of ignoring the hydrodynamic nonlinearity of flow inertia in the predictions of SAW acoustic streaming, from both qualitative and quantitative points of view.

5.3.2.3 ***Flow patterns of acoustic streaming***

For qualitative illustration, the simulated flow patterns inside the droplet from the two models are presented in Fig. 5.4, i.e., the Stokes and the N-S model. The top row in Fig. 5.4 shows that the butterfly flow pattern rotates around one elliptical axis of rotation through the droplet centre when the N-S model is applied, which have been verified by experimental observations [62, 140]. In contrast, when the Stokes model is used for the simulations, the flow pattern only rotates around the double vertical axis with two small vortices near the SAW source, as shown in the lower row in Fig. 5.4, which does not agree with the experimental observations.

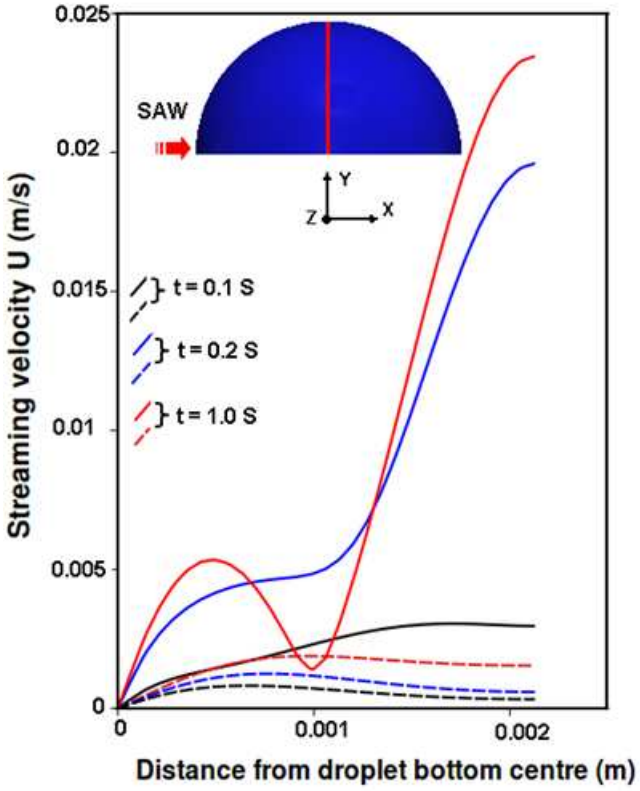

(a)

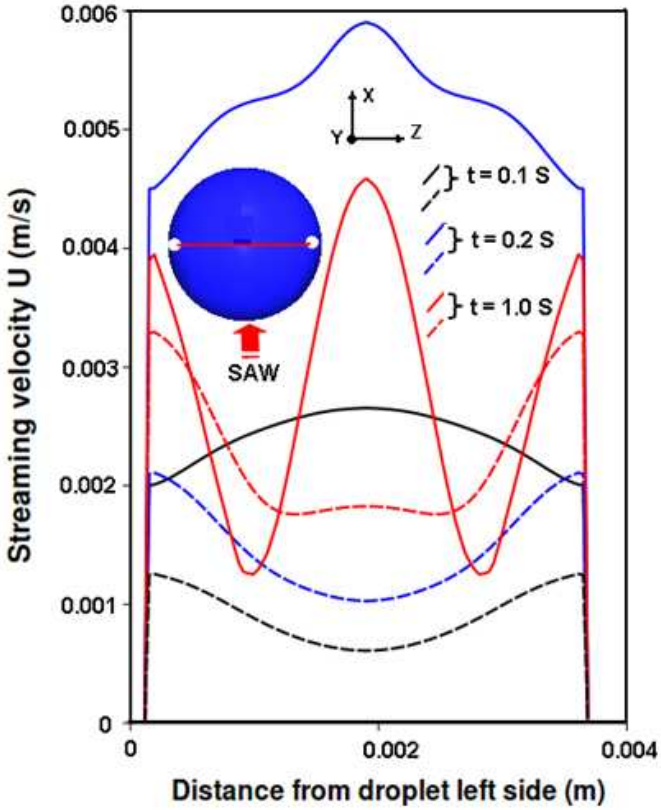

(b)

Figure 5.3 Simulated streaming velocity profiles for a 20 μl droplet, using SAW device with 2.5 mm aperture, 62 MHz frequency and $\boldsymbol{F_{NA}}$ of 0.366; (a) along the y axis ;(b) along the z axis at a 1,200 μm height from the droplet bottom. Solid and broken lines represent the nonlinear and linear cases, respectively

The precise identification of the acoustic streaming patterns is required when designing efficient Lab-on-Chip SAW-mixing devices with a minimal applied RF power. For instance, applying the Stokes model (ignoring the non-linear term) to model SAW-mixing of bio-particles inside a relatively larger droplets (such as 20 μl simulated in this study) will predict that a very large power is needed to get the uniform butterfly flow pattern with efficient flow rotation, as shown in the first row of Fig. 5.4. Such a large recommended power is not necessary as evidenced by experiments carried out from this paper. It is also well-known that the application of high acoustic powers would cause significant acoustic heating effects, which would be detrimental to the biosensing process or could potentially destroy temperature sensitive biological samples [141, 142].

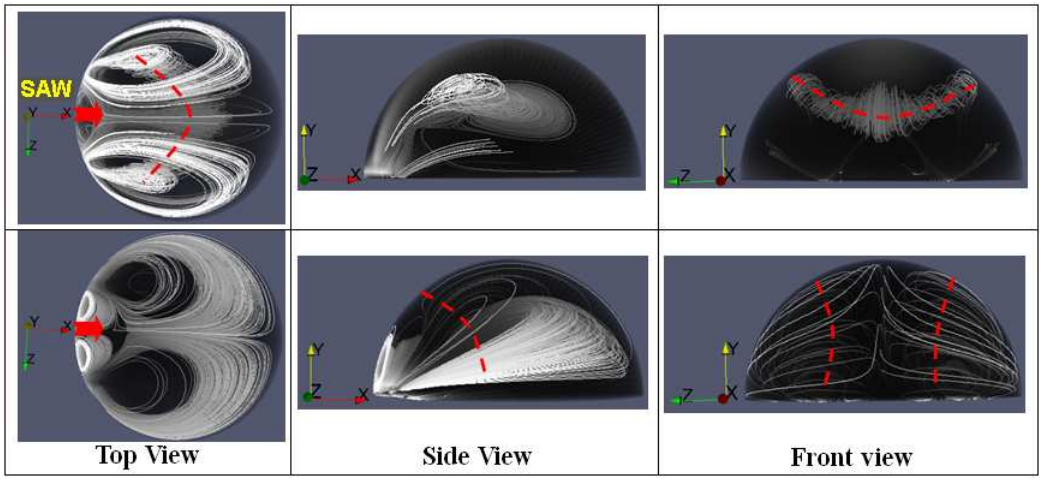

Figure 5.4 Simulated streaming patterns for 20 μl droplet, using SAW device with 2.5 mm aperture, 62 MHz frequency and $\boldsymbol{F_{NA}}$ of 0.366. The upper and lower row represents the nonlinear and linear cases, respectively. Broken lines represents axis of rotation

5.3.3 Droplet Deformation

Additionally, it is demonstrated here that the new F_{NA} parameter can also be employed to identify the induced droplets deformation by SAW. The detailed experimental measurements of the droplet height ratio h / h_0 as a function of the F_{NA}, seen in Fig. 5.5, show that the droplet deformation with a significant change in its height h from initial height h_0 can be clearly predicted at $F_{NA} > 0.45$. Although the detailed mechanism of SAW-induced droplet deformation is beyond the scope of this study, the author would like to give a brief explanation. As it has been suggested earlier, the acoustic power emitted by the SAW into the droplets is dominated by the balance between the SAW acoustic force and surface tension force, as characterized by the values of the F_{NA}.

When the F_{NA} > 0.45, SAW-droplet coupling induces hydrodynamic forces and pressure [105, 143], which cannot be balanced by surface tension, and thus results in droplet distortion into an asymmetrical shape, as shown in Fig. 5.5.

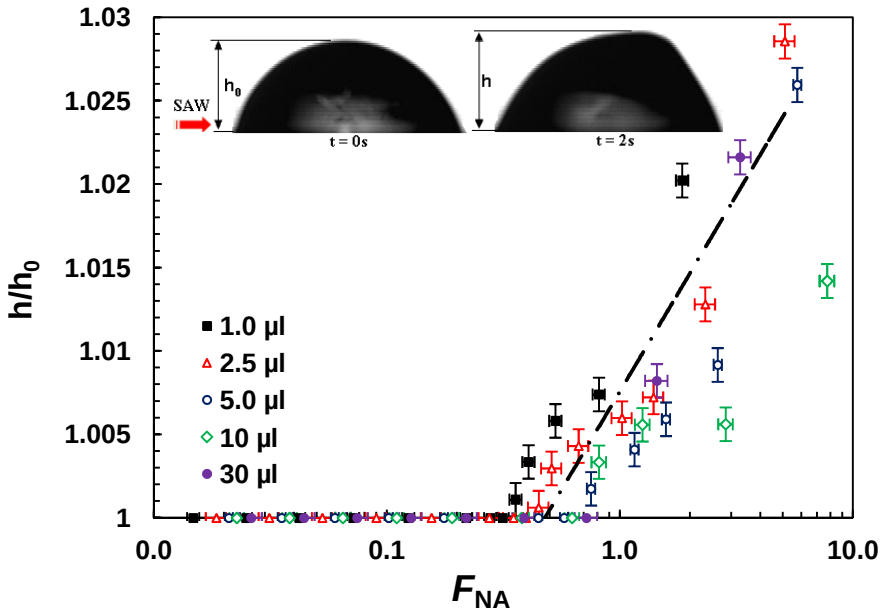

Figure 5.5 Normalized droplet height as a function of the normalized driving force (F_{NA}), for different droplet volumes, using 128º YX-$LiNbO_3$ SAW devices with 0.5 mm aperture excited by a frequency of 60.4 MHz; dashed line stands for trendline

5.4 Summary

In summary, by introducing a new dimensionless acoustic force parameter F_{NA} in the current analysis for the SAW-induced acoustic streaming inside the droplets (1-30 μl), this study was able for the first time to present qualitative and quantitative comparisons between the experimental data and numerical simulation results. This provides strong evidence of the existence of significant hydrodynamics nonlinearity in this system, over a range of the values of F_{NA}. Therefore, the flow within droplets has been classified into three flow regimes or modes: (1) viscous dominant mode, when the $F_{NA} \leq 0.002$, where the widely reported Stokes model of Nyborg's theory [54] is applicable; (2) inertia dominant mode, when the $F_{NA} \geq 0.01$, where the full 3D N-S equations must be applied in order not to cause large error in streaming velocity predictions, which could be as large as ~93% ; (3) droplet deformation or movement mode, with a threshold $F_{NA} \approx 0.45$, above which the droplet deforms. In brief, it is demonstrated that the hydrodynamic nonlinearity plays a significant role in most noticeable SAW acoustic streaming of droplets actuation (e.g., Re $\geq$1).

Chapter 6

INFLUENCES OF CONFIGURATION PARAMETERS ON STREAMING PHENOMENON

This chapter reports the numerical simulation and experimental characterisation of 3D acoustic streaming behavior of a liquid droplet subjected to a Rayleigh surface acoustic wave. The streaming behavior into the droplet was studied in depth as a function of radio-frequency (RF) power, aperture of the interdigitated transducer, and the volume of the liquid droplet.

6.1 **Introduction**

As explained in Chapter 3, if a liquid droplet lies in the path of a SAW, the wave creates a significant acoustic streaming in the liquid that facilitates mixing, stirring, vibrating, pumping, ejection and atomization [81, 144-148]. However, to the best of the author's knowledge, few studies have reported the variations of the 3D SAW streaming patterns within the liquid droplets as a function of the RF powers, droplet sizes and SAW aperture widths as well as their effects on flow velocity, liquid agitation and mixing efficiency [70, 148]. Understanding the influence of these parameters on the flow streaming will allow for efficient design and control of SAW mixing/pumping for microfluidic applications. This chapter provides a systematic analysis of the SAW streaming in a microdroplet based on both experimental characterisation and 3D numerical simulation of the hydrodynamic flow patterns within the droplet.

6.2 **Experimental**

The experimental setup and measurement methods applied in this study were presented in Chapter 4 (i.e., Sec. 4.2). The RF power applied to the IDTs was only restricted to inducing acoustic streaming within the liquid droplets by ensuring that neither droplet deformation nor movement was induced.

6.3 **Modeling Details**

As indicated in Chapter 2, an OpenFOAM-1.6 CFD code (OpenCFD Ltd) was used for the development of the SAW liquid coupling model [140]. The governing equations of

the streaming model, computational techniques and the boundary conditions were presented in Chapter 4 (i.e., Sec. 4.3).

6.4 **Results and Discussions**

6.4.1 Acoustic streaming vs. power

With a 30 μl water droplet loaded symmetrically on the SAW propagation path, the SAW-fluid coupling provides a source of momentum at the SAW-droplet interaction area that drives the fluid with a Rayleigh angle, resulting in a continuous flow within the droplet. When the moving liquid reaches the droplet boundary, the interaction between the liquid and solid boundary induces a reverse flow on both sides of the droplet and the bottom liquid-solid boundary as shown in Figs. 6.1(a)-(f). When this reverse flow goes back towards the IDTs, the flow due to the SAW force drives the reverse flows upwards to the top of the droplet, as can be observed in Figs. 6.1(g) and (h). Eventually, the interaction between the reverse flow and the SAW driving flow produces a double vortex (butterfly) flow pattern as shown in Fig. 6.1. The vortex reaches a steady state within seconds, depending on the applied RF power, droplet size and fluid viscosity.

The usage of a high speed camera for the creation of Figs. 6.1(a)-(g) has provided a thorough understanding of the 3D liquid streaming patterns inside the liquid droplet, which is difficult to observe with the naked eye, even from different angles. There is a clear vortex central line (axis of rotation), where the flow velocity is minimal, as can be observed in Fig. 6.1(f). Figure 6.2 presents the simulation results of a range RF powers (0.5 to ~16 mW) for a 30 μl droplet using a 2 mm wide IDT, and it can be observed that increasing power modifies the position of the axis of rotation. The location of the central axis of rotation at the droplet surface and its path through the droplet centre (centre line) have been tracked and characterised, as illustrated in Fig. 6.2. The path and position of this central line and the distances between the double vortices will indicate the shear velocity gradients and nature of the streaming patterns, thus showing the mixing efficiency. Hence these positions and the streaming velocity have been measured in the next sections as functions of RF power, SAW aperture and droplet volumes.

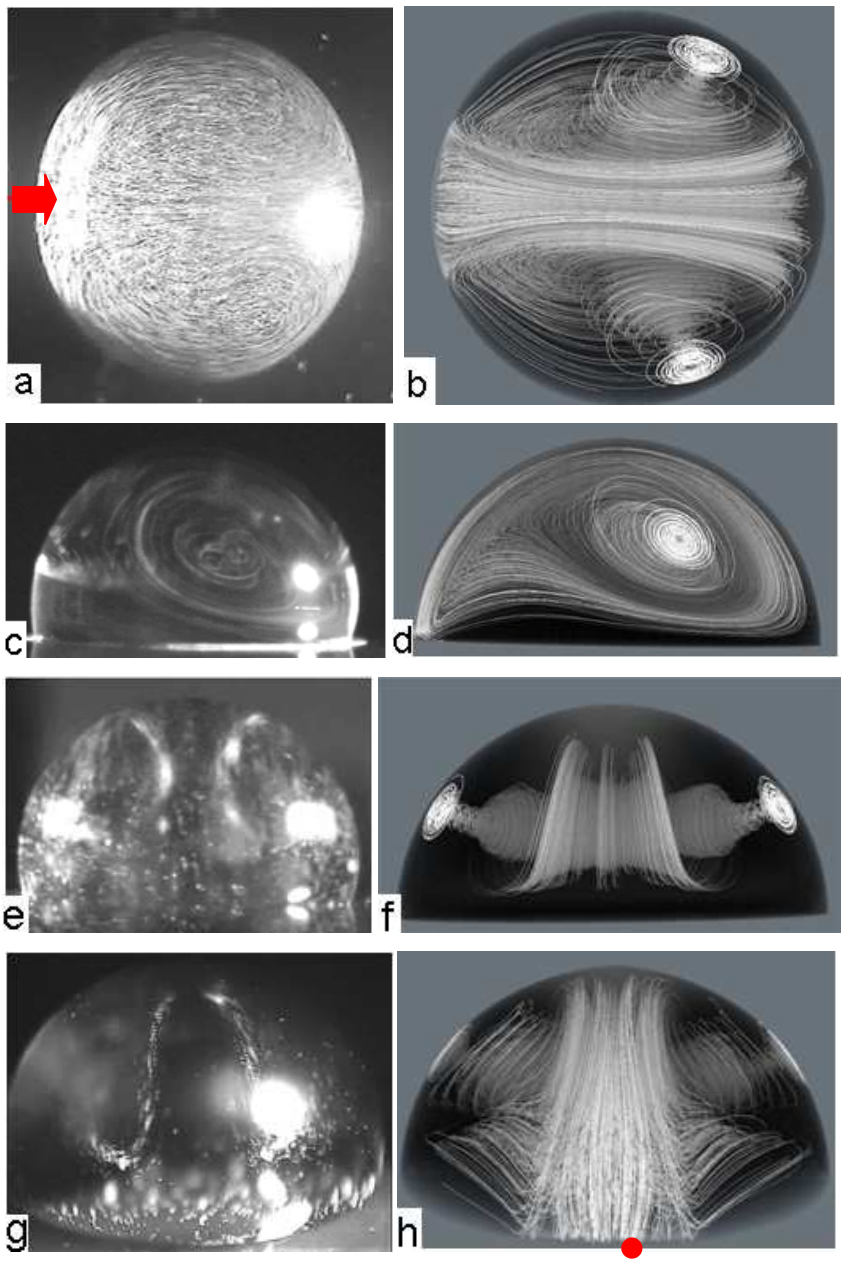

Figure 6.1 SAW streaming patterns for a 30 μl droplet from top (a) and (b), side (c) and (d), front (e) and (f), and back view (g) and (h) using a 128º YX-$LiNbO_3$ SAW device (60 IDT fingers, 2 mm aperture and 50 mW RF power). The left column photos of 6 μm polystyrene particles trajectories, while the right column represents the corresponding simulated streaming patterns. The red arrow in the first row indicates to the SAW propagation direction

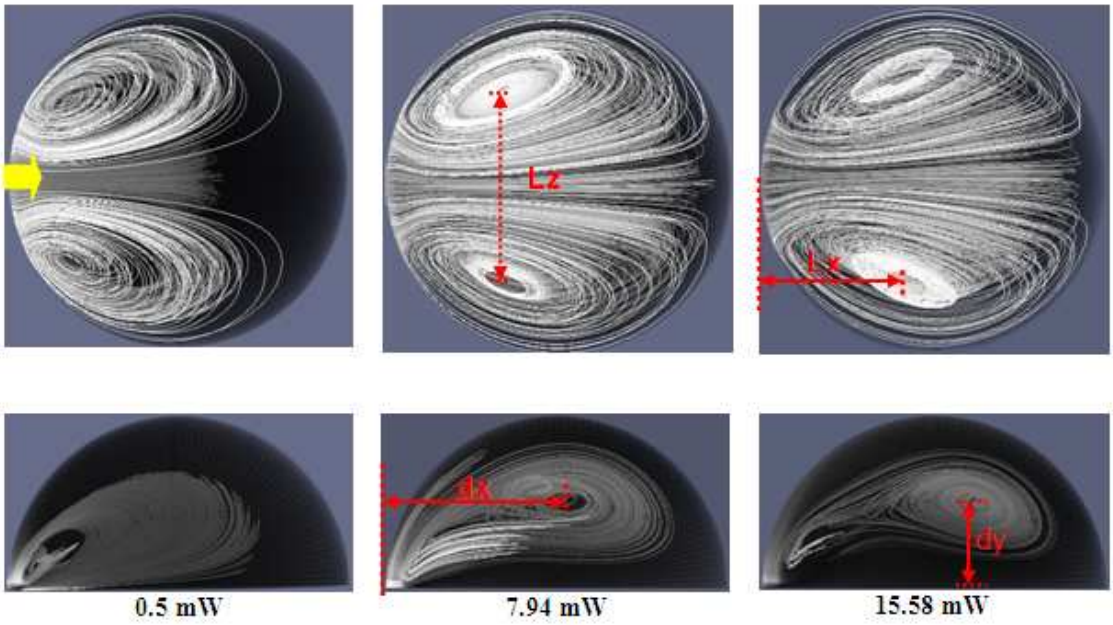

Figure 6.2 Numerical results showing the changes in the position of the axis of rotation with the increase in the RF power for a 30 μl droplet using 2 mm wide IDT. The upper row focuses on the droplet top surface, where the centre of the double vortex can be easily seen; the lower row shows the side view focusing through the droplet centre (middle position with the droplet volume), where the position of the axis of rotation at the middle of the droplet volume is clearly indicated. The parameters Lx and Lz indicate to the positions of the centre of double vortex, while dx and dy indicate the positions of the central axis of rotation through the droplet centre

Figure 6.3 presents the changes in the positions of the central axis as a function of different RF powers, derived using the simulation results shown in Fig. 6.2. As the RF power increases, the double vortices at the droplet top surface move towards the front of the droplet. This movement can be attributed to an increase in the momentum delivered to the fluid, as identified by the parameter Lx in Figs. 6.2 and 6.3. As the centres of the double vortices move forward, the distance between the double vortices, Lz, is also increases in a similar manner to Lx. It can be observed that the central line positions into the droplet centre, dx and dy, did not change significantly with increasing the RF power up to a critical value of RF power. The range within which a weak bulk circulation occurs near the SAW fluid interaction area (e.g., near the IDT), as shown in the first column of Fig. 6.2. However, a further increase in the RF power provides a SAW force that is large enough to overcome the high viscous resistance of the bulk liquid and move the centre of rotation further towards the droplet front. Figure 6.3 shows that the central axis of rotation is pushed towards the droplet front, as can be observed in the second row of Fig. 6.2. The same phenomenon has also been observed in the values of Lx and Lz, but this is not strong as the parameters dx and dy, perhaps

due to the restricted space within the 3D shape of the droplet and its outer surface as the double vortex movement is restricted by the droplet outer surface.

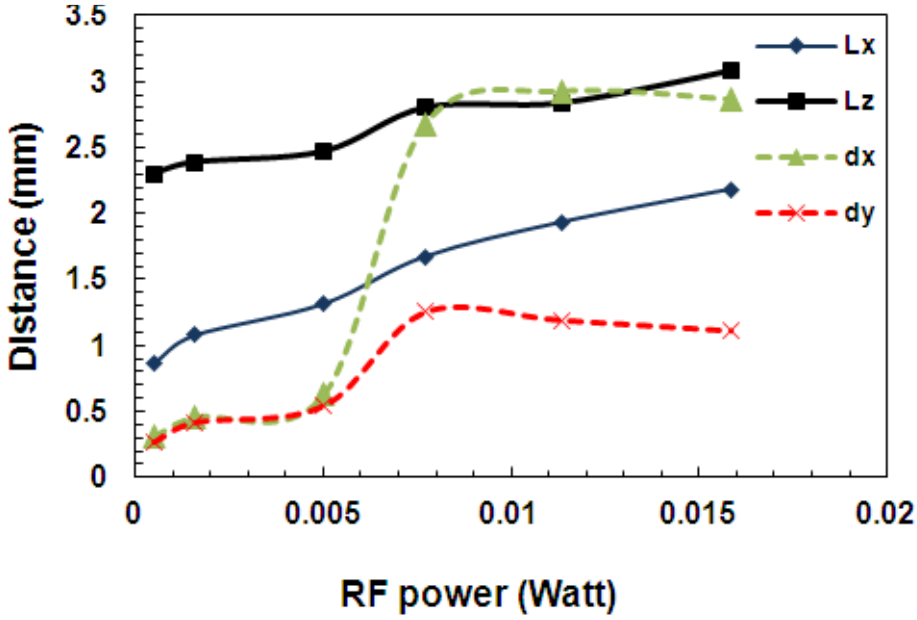

Figure 6.3 Numerical results representing the changes in the parameters of the central axis of rotation with the RF power for a 30 μl droplet using 2 mm IDT width and excitation frequency of 60 MHz.

Figure 6.4 presents the vector field distribution of the streaming velocity through the centre of a 30 μl droplet as a function of the RF power, which directly affects the wave amplitude, A as presented by Eq. (4.8). Negative values of the velocity represent backward streaming towards the SAW device. Figure 6.4 clearly reveals that the streaming velocities near the droplet bottom are smaller than those in the upper regions, near the droplet surface, due to the surface friction at the substrate surface where the SAW is attenuated (e.g., away from the interaction point). A lower velocity is also observed near the centre of circulation, as can be observed in Figs. 6.1(c)-(d), and 6.4. Figure 6.4 also shows that the streaming velocity increases with the RF power (e.g., SAW amplitude) as a result of increased momentum force delivered to the fluid within the SAW-droplet interaction area.

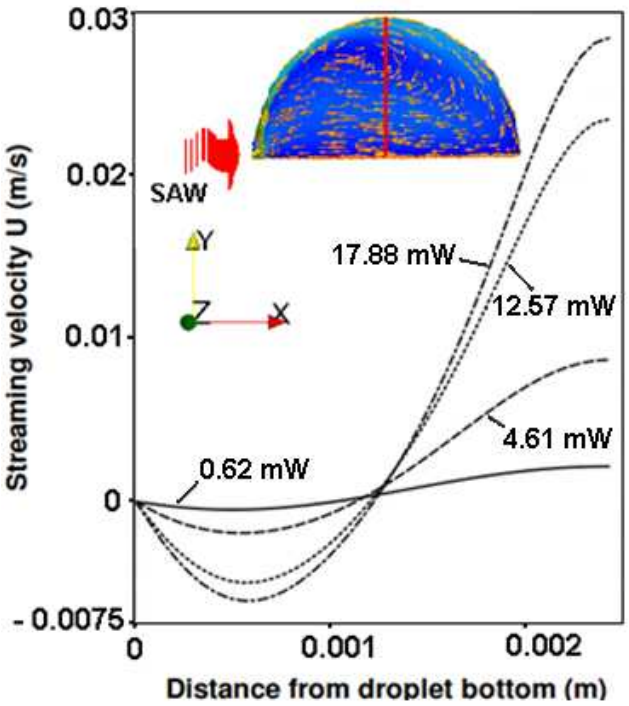

Figure 6.4 Simulated vector field streaming velocity distribution for a 30 μl at its centre along with the y axis depicted by the solid red line through the droplet centre. Different RF powers (e.g., SAW amplitudes) have been computed for the 128^{o} YX- black $LiNbO_3$ SAW device with 60 MHz with 60 pairs of IDTs and a 2 mm SAW aperture.

6.4.2 Streaming vs. SAW aperture

Figure 6.5 shows the butterfly-shape streaming patterns and the location of the axis of rotation for a 30 μl droplet for a range of different SAW apertures and an RF power of 15.85 mW. It can be observed these do not show a dramatic change in the streaming patterns for the different SAW apertures. The detailed results in Figs. 6.5 and 6.6 show that the previously defined axis of rotation parameters, Lx, Lz, dx and dy increase slightly with the IDT aperture up to a critical value, above which they decrease. This critical value of the IDT aperture is estimated to be about half of the droplet radius. Figure 6.5 also shows that the curvature of the central axis of rotation reduces as the RF power is increased.

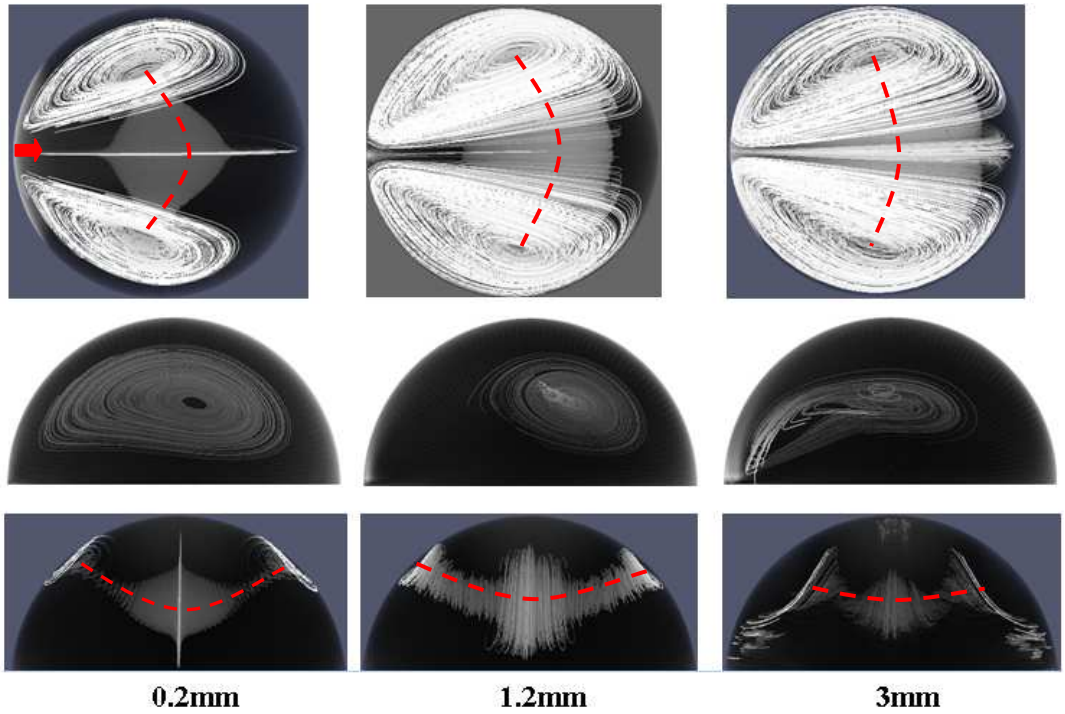

Figure 6.5 Numerical results showing the changes in the axis of rotation position for a 30 µl droplet excited by different IDT apertures with an RF power of 15.85 mW. The first row shows a top view of the double vorticity; the second row shows the side view focusing through the droplet centre, and the third row views the droplet centre from the front. The yellow arrow in the first row indicates the SAW direction and the dot red line represents the axis of rotation

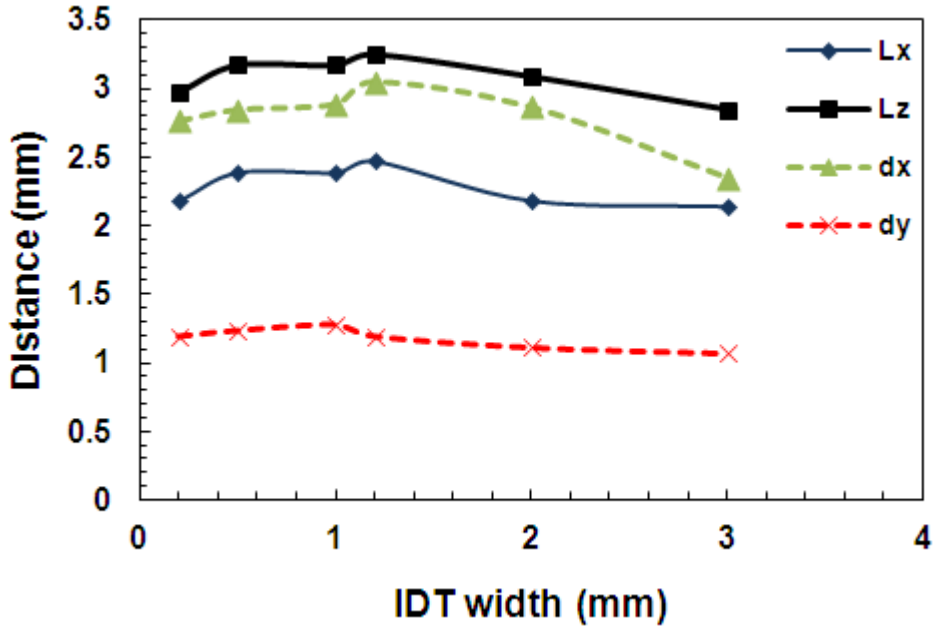

Figure 6.6 Numerical results presenting the axis of rotation parameters as a function of the IDTs aperture value for a 30 μl droplet with 15.85 mW and 60 MHz excitation frequency

Experiments have also been performed to investigate the effects of the width of the SAW aperture on the streaming velocities for a range of SAW apertures and droplet sizes. Figure 6.7 shows that increasing the SAW aperture results in a higher streaming velocity until a critical SAW aperture size is reached, which is also dependent on the droplet size. The simulation results show a similar trend to those observed experimentally. In general, both results are in good agreement with slight deviation at higher powers; this is attributed to the inaccuracy in capturing the fast speed of the polystyrene particles at high RF powers.

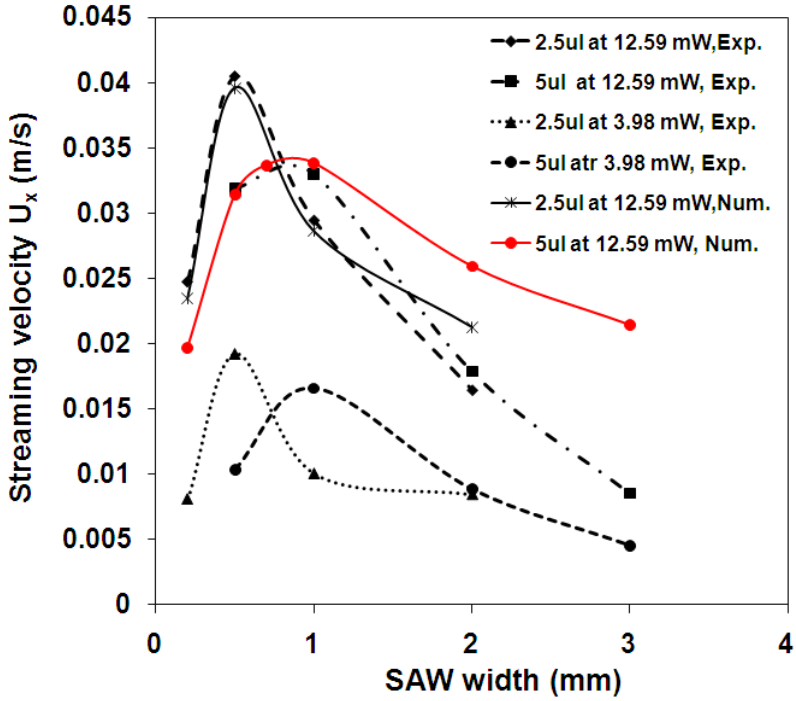

Figure 6.7 Comparison of experimental and numerical results of the x-component streaming velocity measured at the top centre of the droplets at different RF powers using a 128º YX-$LiNbO_3$ SAW device with a range of SAW apertures (60 MHz and pairs of IDTs with 30 fingers) for 2.5, and 5 μl droplet sizes

The experimental results presented in Fig. 6.7 show measurements at the top centre of the microdroplets. Although it would be possible to make further measurements in other positions, 3D SAW streaming patterns and detailed streaming velocities at any point for the whole droplets at the different SAW apertures can be more readily obtained using simulation. Figures 6.8(a)-(c) show the simulated velocity distribution in a 30 µl droplet for different sections through the droplet domain for a range of the SAW apertures. This shows the streaming velocity is enhanced as the SAW aperture increases up to a peak value (see Fig. 6.7), above which the streaming velocity decreases. This can be attributed to an increase in the radial component of the streaming velocity U_z,

near the SAW source, as shown in Fig. 6.8(d). The positive values of U_z in the left hand side of Fig. 6.8(d) indicates the inward radial velocity towards the droplet centre, whereas on the right hand side, the negative values indicate an inward radial velocity towards the droplet centre. The increase in U_z on both sides of the droplet results in a decrease in the streaming velocity near the SAW source as can be observed in Fig. 6.8(a). Thus, the momentum delivered to drive the fluid upward is decreased, which explains the trends shown in Figs. 6.5-6.7. However, these critical values of the SAW aperture for the change in streaming velocities are also affected by the droplet size as indicated by the experimental and numerical results presented in Fig. 6.7. Both the experimental and numerical results show that the maximum streaming/mixing velocity is achieved when the ratio of SAW aperture to droplet radius, (W_{SAW}/R_d) is about 0.5.

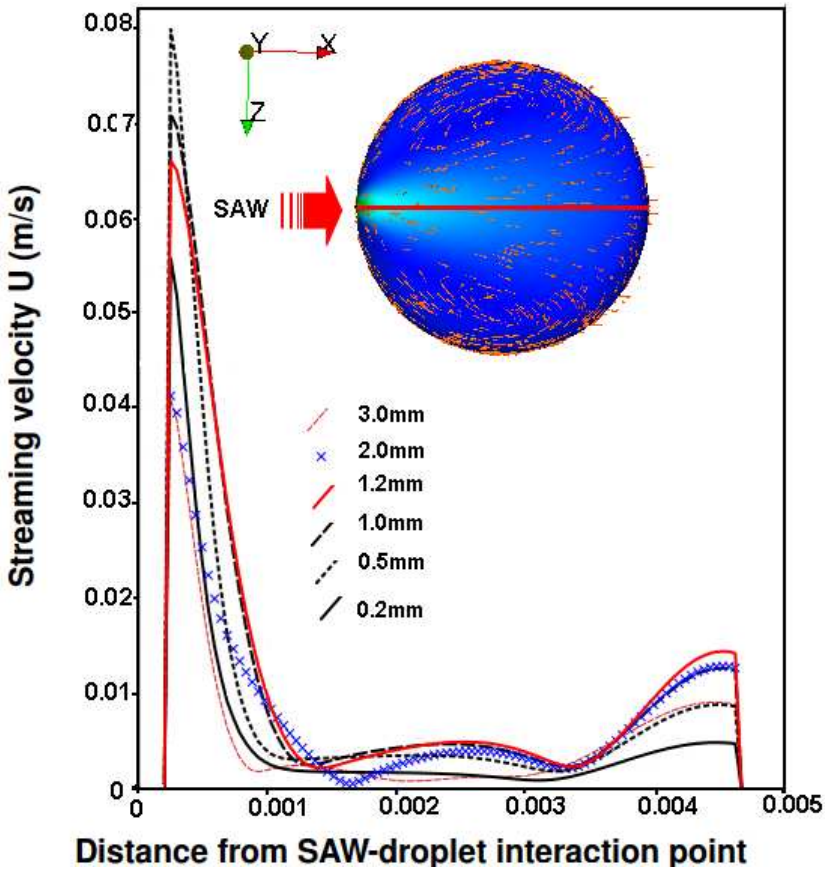

(a)

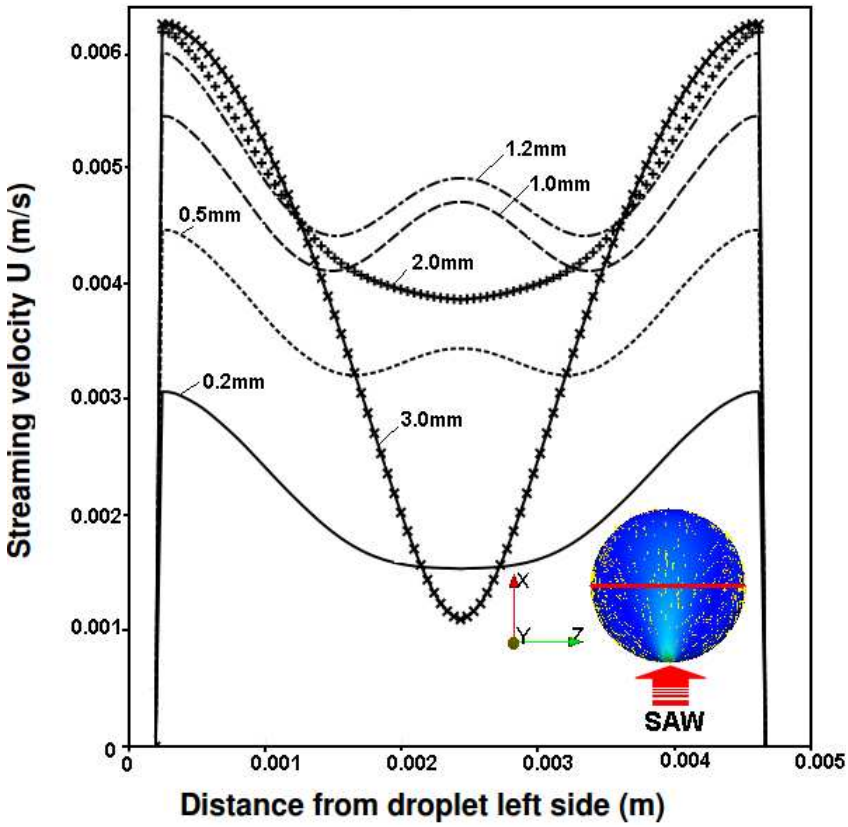
Streaming velocity U (m/s)
0.006
0.005
0.004
0.003
0.002
0.001
0
1.2mm
1.0mm
0.5mm
2.0mm
0.2mm
3.0mm
X
Y
Z
SAW
0
0.001
0.002
0.003
0.004
0.005
Distance from droplet left side (m)

(b)

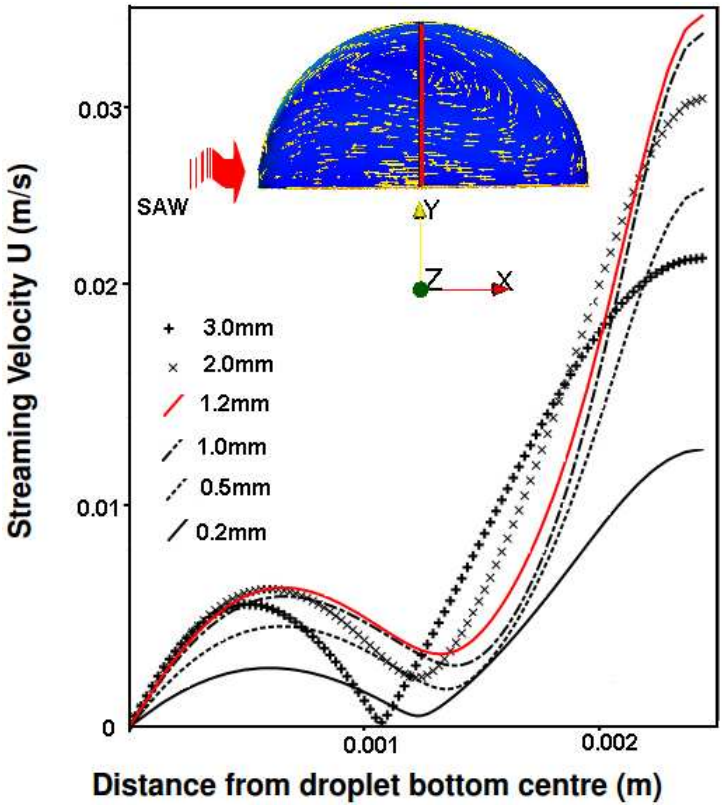
Streaming Velocity U (m/s)
0.03
0.02
0.01
0
SAW
Y
Z
X
3.0mm
2.0mm
1.2mm
1.0mm
0.5mm
0.2mm
0.001
0.002
Distance from droplet bottom centre (m)

(c)

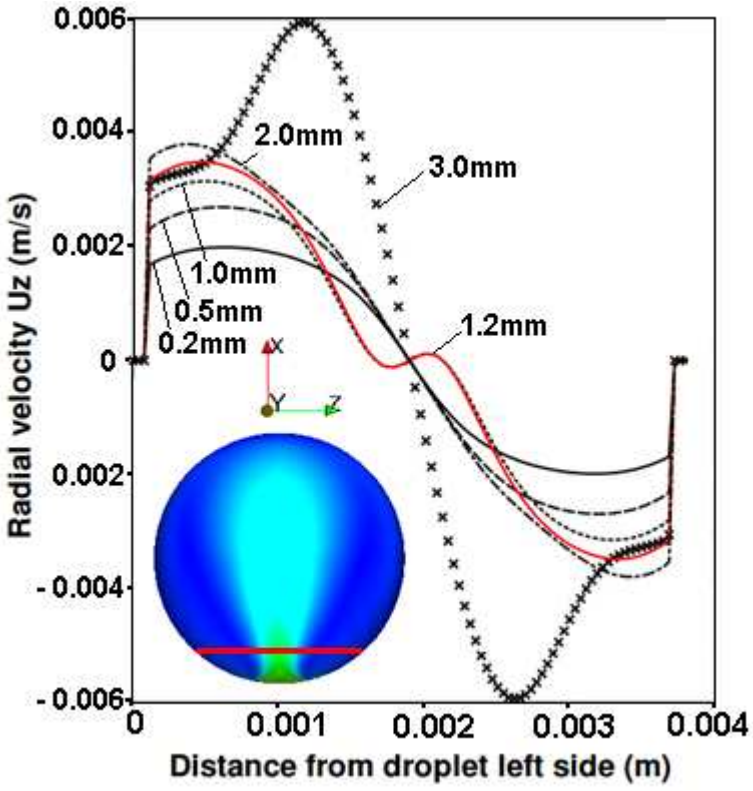

(d)

Figure 6.8 Numerical simulations of the streaming velocity as a function of SAW apertures for a 30 µl droplet excited using 12.59 mW RF; (a) and (b) scalar values of streaming velocity measured at a height of 1,000 μm from the droplet bottom in the SAW direction and droplet diameter as indicated by the solid red line in the droplet illustrations; (c) scalar values of streaming velocity measured at the droplet centre through its height; (d) vector values of radial streaming velocity components measured at 1,000 μm height from the droplet bottom and 800 μm from the SAW-droplet interaction area as depicted by the red line through the droplet illustration

6.4.3 Streaming patterns vs. droplet volume

Figure 6.9 shows the 3D streaming patterns for a range of droplet sizes with a fixed RF power of 15.85 mW and a SAW aperture of 0.5 mm. The butterfly streaming pattern does not change much with volume, and the elliptical shape of the central axis of rotation remains nearly constant for all droplet volumes, as can be observed from the dotted lines in Fig. 6.9. However, the detailed measurements of the parameters defining the location of the axis of rotation in Fig. 6.10 show some dramatic increases as the droplet's volume is increased, which is predictable. Figure 6.11 also shows the changes of the central line parameter ratio as a function of droplet radius. The results indicate that the central-line parameters through the droplet centre, (dx/R_d) and (dy/R_d) are nearly constant ~ 1.15 and 0.52, respectively. Figure 6.11 shows slight differences of less than 12% and 10% for the central line parameter ratios (Lx/R_d) and (Lz/R_d),

respectively, as the size of the droplet changes. Therefore, the central line parameters ratios can be reasonably assumed constant over a moderate range of droplet volumes.

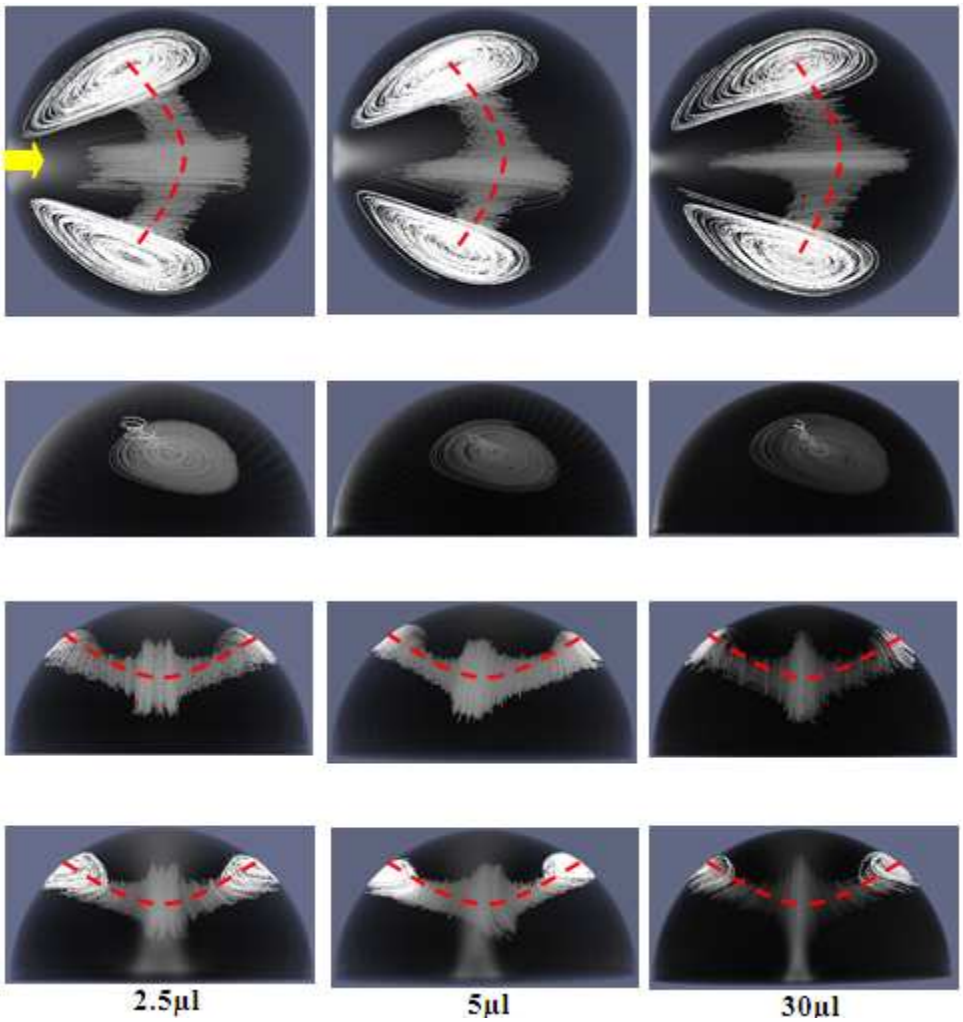

Figure 6.9 Numerical results showing the changes in the centre line (axis of rotation) position for different droplets sizes at RF power 15.85 mW. The first row represents the two vortices as seen from the top; the second represents the side view through the droplet centre; the third represents the droplet centre from droplet front (away from the IDTs); the fourth focuses into the droplet centre as seen at the back of the droplet (near the IDTs). The yellow arrow in the first row indicates to the SAW direction and the dot red line represents the central line of circulation.

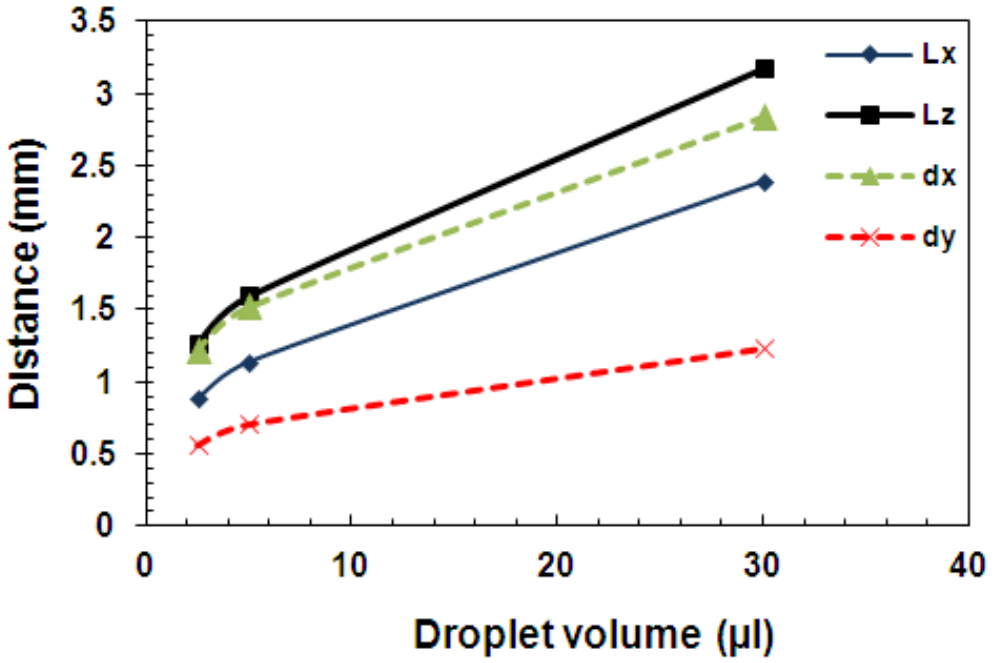

Figure 6.10 Numerical results represent the changes in the parameters of the axis of rotation with the droplet volume using 0.5 mm IDT width and 15.85 mW RF power

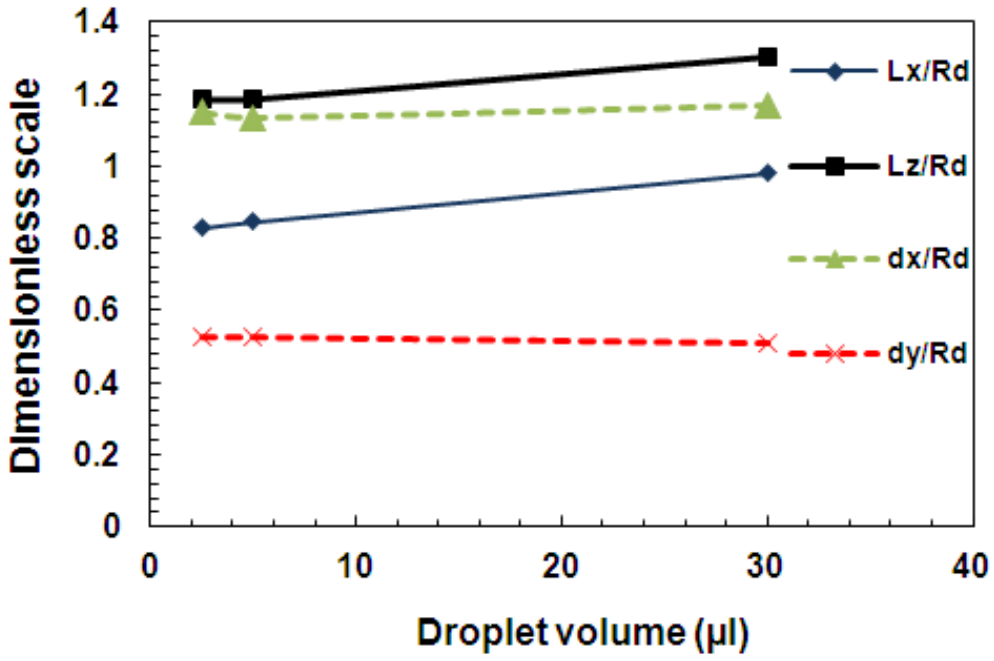

Figure 6.11 Dimensionless numerical values of the axis of rotation position as a function the droplet volume for a 0.5 mm IDT width and 15.85 mW RF power

6.5 **Summary**

Experimental and numerical studies of SAW acoustic streaming within a microdroplet have been conducted to investigate the effects of parameters such as droplet size, RF power, and SAW aperture. It has been shown that a higher RF power and a decreased droplet size result in an increase in the SAW streaming velocity. The spatial position of the central-line of rotation (axis of rotation) is directly affected by the droplet volume, RF power and the SAW device aperture. The dimensionless parameter values of the central line position as a function of droplet volume remain nearly constant with a percentage increment of not more than 12% at the droplet surface and 10% through the centre as the droplet volume increases. The SAW aperture has been identified as the main factor influencing the mixing (streaming) velocities, which increase with the SAW aperture up to a critical value, above which a decrease in velocity is observed. The magnitude of the velocity is determined by the droplet size with a maximum mixing velocity when the ratio of the SAW aperture to droplet radius is 0.5.

Chapter 7

FREQUENCY EEFECT ON MIXING PERFORMANCE OF A RAYLEIGH SAW

In this chapter, a streaming phenomenon of ink particles inside a water microdroplet generated by a surface acoustic wave (SAW) has been studied numerically using a finite volume numerical method. These results have been verified using experimental measurements. Effects of SAW excitation frequency, droplet volume and radio-frequency (RF) power were investigated.

7.1 Introduction

As explained before, when liquid (either in bulk or droplet form) lies in the propagation path of the SAW emitted by the IDT, it attenuates and changes its mode to a Leaky Surface Acoustic Wave (LSAW) upon its arrival at the boundary between solid (substrate) and liquid, due to acoustic velocity mismatch between the solid and the liquid medium [149]. This leakage of the SAW inside the droplet leads to the generation of longitudinal pressure waves that propagates at a Rayleigh angle into the fluid [118]. Although it is well known that the leakage of acoustic energy into the fluid medium is responsible for the SAW streaming phenomena, and the wavelength of the Rayleigh wave λ (as a part of the absorption coefficient, α_L., i.e., Eq. 2.16) determines the portion of acoustic energy absorbed by the fluid, few studies have been conducted concerning the effects of wavelength (or excitation frequency) on SAW acoustic streaming [20]. For example, Tan et al. [101, 150, 151] reported that when the width of a grooved microchannel fabricated on the substrate surface was increased beyond an acoustic wavelength, the induced fluid flow in the microchannel by SAW excitation changed from an axially symmetric laminar flow to a vortical mixing flow, and became more chaotic with further increases in the channel width. However, there was no report on a systematic study of its mixing performance. Maezawa et al. [65] reported that modulation of the frequencies of a SAW device improved mixing efficiency of liquids contained inside a liquid cell driven by a SAW, but there was no discussion of the effect of cell volume on the mixing performance. Strobl et al. [18] studied SAW-driven flow inside microdroplets, and experimental observations showed that a laminar flow within

a 5 µl droplet was disturbed by switching the device frequency between 114 and 340 MHz, which resulted in effective mixing for dye particles placed in water droplet.

Clearly, apart from applied SAW power that plays an important role in SAW induced mixing, the excitation frequency applied to the SAW devices represents another key parameter for enhancing the streaming phenomenon and mixing performance. Nevertheless, current literature does not provide sufficient information to quantitatively describe the influence of excitation frequency on the efficiency of mixing in SAW-based microdroplet systems. This chapter investigates the effects of different flow parameters, including SAW excitation frequency, droplet volume and applied power, using a 3D systematic simulation with experimental verification. The results provide good guidance for the selection of an optimal excitation frequency for an effective mixing device, with a minimized applied SAW power for reducing acoustic heating.

7.2 **Numerical Analysis**

7.2.1 Computational experiment setup

For the simulations, water droplets with volumes of 2.5, 5.0, 7.5 and 10 µl, were positioned on the SAW propagation path, as schematically illustrated in Fig. 4.9(a) and excited using 128º YX-$LiNbO_3$ SAW devices with an IDT aperture of 500 µm. Given a uniform finger spacing and SAW width, [47] the resonant frequency for each design IDT layout can be calculated by $f = V_R/\lambda = V_R/4d$, where V_R =3992 m/s [152], where d is the IDT finger spacing or width. In this study wavelengths ranging from 32 to 1,061 μm were used.

7.2.2 Streaming model

In order to simulate the internal fluid flow of acoustic streaming for SAW-droplet coupling, the continuity equation Eq. (4.2a) and the Navier-Stokes equation (momentum equation) Eq. (4.2b) were used for the laminar incompressible flow driven by an external SAW body or streaming force (see Sect. 4.3). The verification and preliminary results of this model have been reported previously [62, 140].

7.2.3 Mixing model

In order to evaluate the mixing performance of SAW-induced streaming in microdroplets, the conservation equation of mixing species was used [129]:

$$\frac{\partial \boldsymbol{m}}{\partial \boldsymbol{t}} + \boldsymbol{U} \cdot \boldsymbol{\nabla m} = \boldsymbol{D\nabla^2 m} \tag{7.1}$$

where U represents the acoustic streaming velocity, m denotes the mass fraction of mixing species (such as dye particles in this study), which is defined as the ratio of the mass of the mixing species in a given volume to the total mass of the mixture contained in the same volume. The diffusion coefficient D (diffusivity of dye in water in our case) was assumed to be 1×10^{-20} m^2/s, and the viscosity of the dye/water solution was estimated the same as that of pure water [8]. Thus, the mass fraction function (or colour indicator) for an incompressible fluid can be given as:

$$\boldsymbol{m} = \text{(Volume occupied by dye species) / (total volume of the mixture)} \tag{7.2}$$

The values of the mass fraction m in Eq. (7.2) should be $0 \leq m \leq 1$, where, zero corresponds to water with no dye, and a value of 1 corresponds to a volume that consists only of the dye species. Any values between 0 and 1 represent a mixture of water and dye species. By calculating the distributed values of the mass fraction, m, inside the droplet, it is possible to evaluate the mixing performance of SAW-driven microdrops.

7.2.4 Boundary conditions and solution

The maximum RF power applied to the SAW device was limited to 0.5 mW, a value which is large enough to induce efficient acoustic streaming, but without any induced droplets deformation or pumping [62, 140]. In this case, the water droplet can be considered as a hemispherical body, as depicted in Fig. 7.1. The droplet domain was constructed using a curvilinear mesh with a grid resolution depending on the SAW wavelength, to ensure the capture of any high energy dissipation [149]. For the flow model, a non-slip boundary condition was assumed at the droplet/substrate interface, while a stress free boundary condition was applied at the interface of the droplet and air. For the mixing model, zero gradient mass fractions were assumed at all the droplet boundaries. In order to visualise the whole mixing process inside the microdroplets and to evaluate the mixing performance of the SAW devices for different design parameters, the water droplets were initially (at time t = 0 s) assumed to have dissolvable dye particles on the droplet base with a 70 μm height from its base and with a mass fraction of m = 1 (the red colour base as shown in Fig. 7.1).

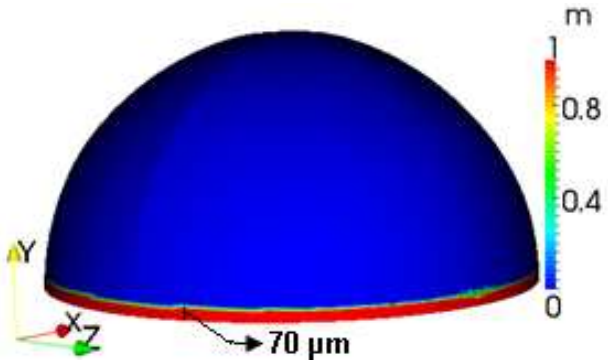

Figure 7.1 Illustration showing the initial mass fraction used in this study with a value of m = 1.0 (dyed water) at the droplet base for a 70 μm height from its base in the y direction, and value of 0.0 elsewhere (pure water)

7.2.5 Mixing index

In order to quantify the mixing performance of such dye within the water droplet under the excitation of SAW, a mixing index parameter *(MIP*) has been used, which can be determined from the analysis of mass fraction intensity extracted from the simulation results:

$$\boldsymbol{MIP} = \frac{\sum_{i=1}^{N} \boldsymbol{V_i m_i}}{\boldsymbol{V_0 m_{max}}} \qquad (\mathbf{7.3})$$

where N is the total number of computation cells in the droplet mesh, V_i is the localised cell volume, V_0 is the total droplet volume initially occupied by the dye species (m=1.0), as shown in Fig. 7.1, m_{max} is the maximum initial mass fraction of dye species (set to 1 in this study). Here, the value of *MIP* varies between 0 (unmixed) and 1 (complete mixed). Eq. (7.3) represents the percentage of the initial dye particles at the bottom of the droplet (i.e., seen Fig. 7.1) that have been propelled by the internal acoustic streaming into the pure water, or driven away from the bottom of the droplet after a SAW excitation. Thus, the defined mixing index parameter, *MIP*, can be used as a measure for describing mixing performance across the different simulated regimes.

7.3 **Experimental**

For experimental verification, the SAW devices were fabricated on a 128^o YX- black $LiNbO_3$ substrates by sputtering 200 nm thick aluminium to form the IDTs, with an IDT

aperture of 500 μm. The details of the SAW device fabrication have been documented elsewhere [17]. The surface of the $LiNbO_3$ wafers is hydrophilic with a water contact angle of about 35^o as can be observed. In this study, a spin-coated CYTOP® (Asahi Glass Co., Ltd., Tokyo., Japan) layer was also prepared to make the surface hydrophobic. Experimental instruments and measurement method were presented in Chapter 4 (i.e., see Sec. 4.2). Water droplets with volumes ranging from 2.5 to 10 μl were loaded at the centre of the SAW propagation path by using a Micro-Volume Kit micropipette, similar to that illustrated in Fig. 4.9(a). In addition to droplet volume and SAW wavelength, the effect of a moderate range of applied RF powers from 0.05 to 0.5 mW, were evaluated. These were selected to ensure that the droplet would not be dramatically deformed but sufficient energy would be available to induce internal streaming and mixing inside the droplets. In order to determine the streaming velocity, polystyrene particles with average diameters of 6 μm were placed inside the water droplets and their motion was recorded using a high speed camera (Kodak Motion Corder Analyzer - 600 frames per second). In order to experimentally visualise the whole mixing process inside the microdroplets and to evaluate the mixing performance of the SAW devices for different design parameters, dried particles of food dye were initially placed underneath the droplets (at time t = 0 s), and their mixing process inside the droplets after the SAW power was tracked.

7.4 **Comparison and Discussion**

7.4.1 Acoustic mixing process

The characteristic mixing process of SAW-induced microdroplets mixing will be discussed first. Figure 7.2 presents sequential images of the simulated mixing process of the dye in a 5 μl droplet. Here, an RF power of 0.5 mW was applied to the SAW device, and an excitation frequency of f = 39.92 MHz (corresponding wavelength, λ = 100 μm) was used. The first column (a) in Fig. 7.2 shows 3D volume images of the changes of dye concentration with the time period after the SAW excitation. After applying an RF power to the IDTs of the SAW device, a SAW was launched and coupled with the water droplet. Its energy is radiated into the droplet at a Rayleigh angle, inducing an effective acoustic momentum (body force) that decays exponentially away from the SAW interaction region. This momentum source at the SAW-droplet interaction region establishes a flow field that drives the fluid upwards at a Rayleigh angle, resulting in build-up of a progressive flow within the droplet, as seen in the left

hand column of Fig. 7.2, after 0.03 s. It can be observed that in Fig. 7.2 (column (a)), the streaming velocities are the highest near the SAW source, especially during the early stages of flow development.

Simultaneously, the generated flow in the droplet induces advection for the dye particles at the bottom of the droplet towards the top of the droplet at the same Rayleigh angle of longitudinal pressure wave. This is clearly observed in the early stage images presented in column (a) of Fig. 7.2. The flow is guided by the curved droplet/air interface back down towards the droplet base where it is then directed back towards the SAW excitation source along the base of the droplet. When this reverse flow reaches the region near the SAW source, the SAW drives the reverse flow upwards again, causing an advection for more dye particles that travels away from the droplet bottom into the droplet volume. Finally, after a few seconds, the developed flow reaches a steady stage of the double vortex (butterfly) flow patterns [14], as shown by the velocity vectors in the latest stages of column (a) (time = 7 s) in Fig. 7.2. This steady flow pattern is dependent on the excitation frequency, the applied SAW power, the droplet size and the fluid properties [48, 62, 140].

For further analysis, the mass fraction data were divided into two groups; with the first group covering the mass fraction range of 0-0.5 and the second one from 0.5 to 1.0. The second column (b) in Fig. 7.2 shows the simulated contours of mass fraction ranging from 0 to 0.5 using 3D clips (e.g., 3D droplet volume images with cutting planes along the y and z axis showing half of the hemispherical body). These results show that the dye particles follow the fluid flow in similar patterns with an increasing dye mixing volume inside the whole droplet. The dye mixing volume increases continually as the dye is fed from the dye particles at the droplet bottom, through streaming-induced advection. This advection of the dye particles results in a decrease in the volume of the high concentration zone ($m \geq 0.5$) with the development of a streaming flow, as shown in the third column (c) of Fig. 7.2 that covers a higher mass fraction range of 0.5-1.0. Also, it can be observed from Fig. 7.2(c) that the quantity of dye particles driven from the droplet base decreases with the duration of streaming flow. Eventually, the concentration of the dye particles that dissolved in the water droplet reaches a steady state value and the solution nearly becomes homogeneous.

Figure 7.3 shows that the simulation results are identical to our experimental observations as well as those from literature [18, 93]. For comparison, dried particles of food dye were deposited underneath a 5µl water droplet before applying RF power. Figure 7.3 depicts four snapshots of such mixing experiments of SAW-induced streaming. After applying the RF power, the dye is quickly mixed in the droplet in a few seconds. As can be observed from the snapshots of the dye mixing in droplet, the coupled SAW from the bottom of the droplet induces acoustic streaming that leads to advection for the food dye particles at the bottom of the droplet (blue colour) towards the top of the droplet at the Rayleigh angle of longitudinal pressure wave, as indicated by the black dashed arrow in Fig. 7.3 at a time of 1 s, which agrees well with the results presented in Fig. 7.2 at the same duration time. Finally, the dissolving process of the dye particles reaches a steady state distribution inside the droplet volume, as can been seen from both the numerical and experimental observations presented in Figs. (7.2) and (7.3), respectively, at a duration of 7 s.

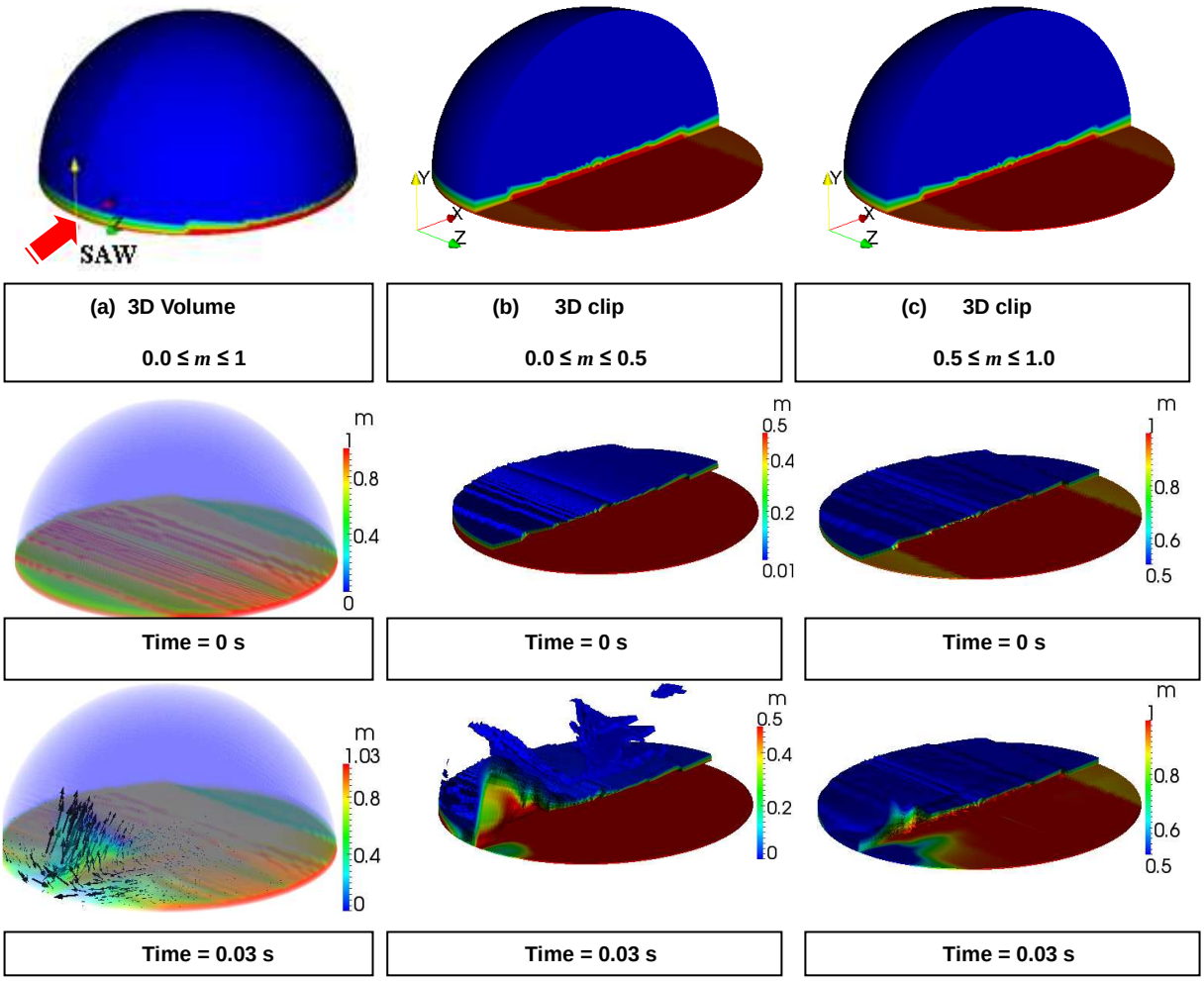

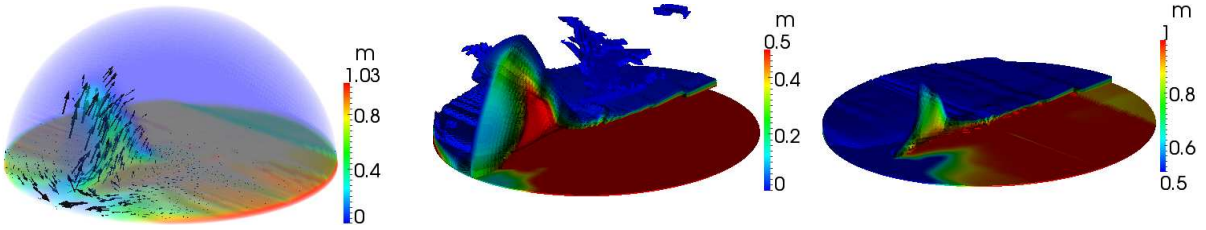

Time = 0.05 s | Time = 0.05 s | Time = 0.05 s

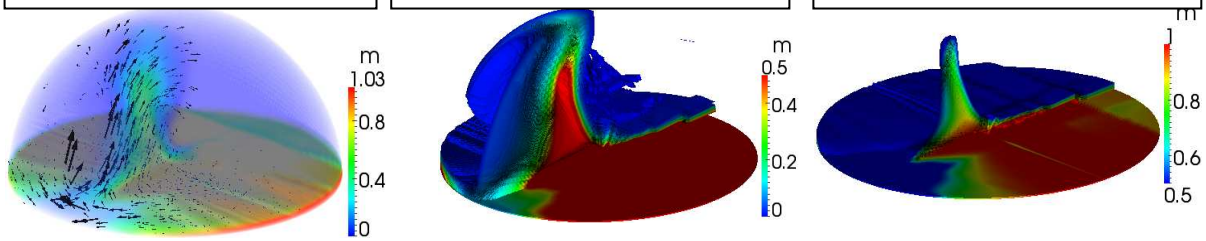

Time = 0.1 s | Time = 0.1 s | Time = 0.1 s

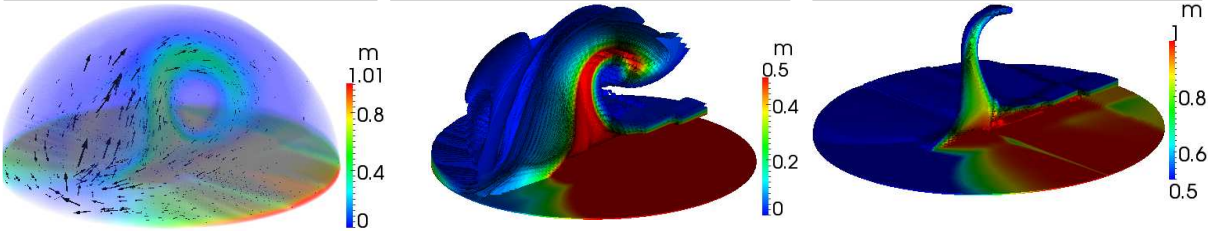

Time = 0.3 s | Time = 0.3 s | Time = 0.3 s

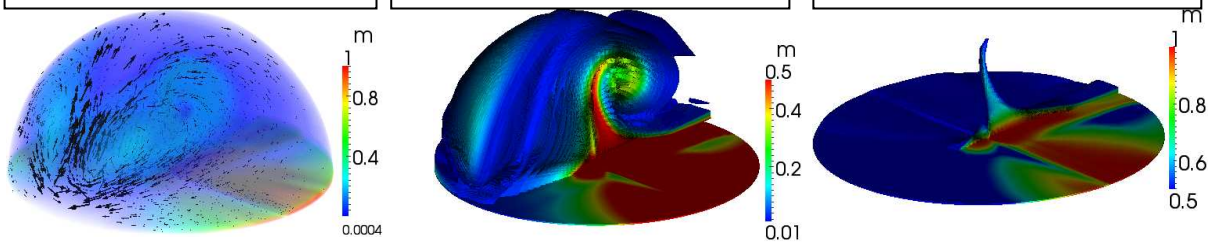

Time = 1.0 s | Time = 1.0 s | Time = 1.0 s

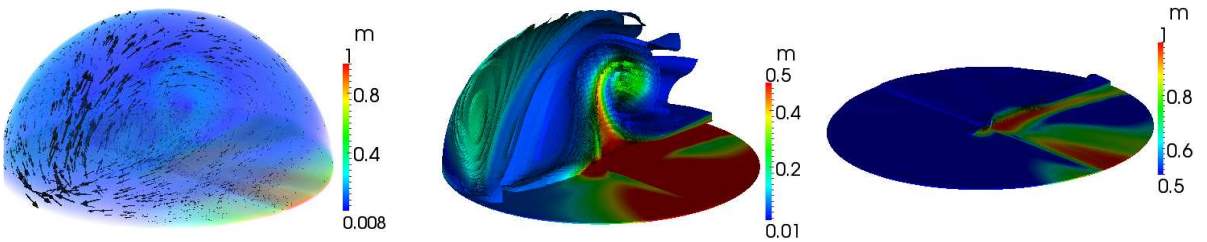

Time = 1.5 s | Time = 1.5 s | Time = 1.5 s

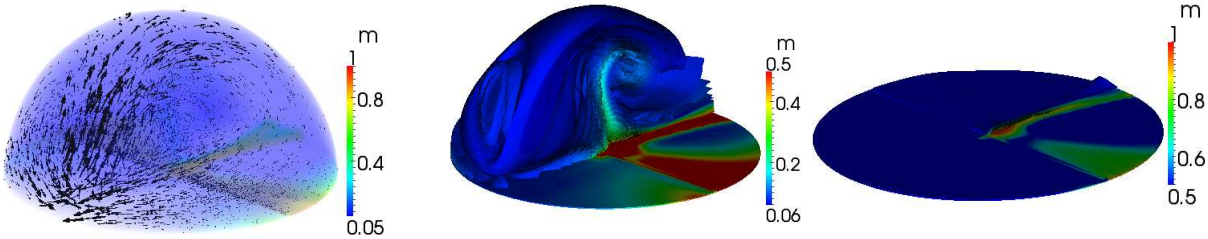

Time = 3.0 s | Time = 3.0 s | Time = 3.0 s

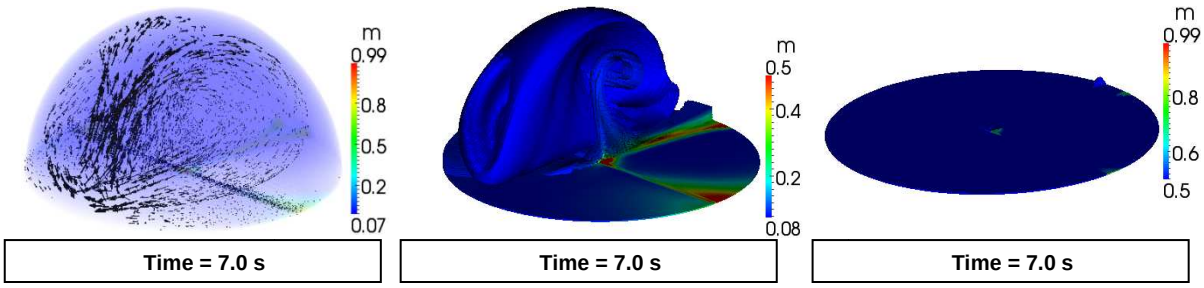

Figure 7.2 Three dimensional images of the simulated mixing process for a 5 μl water droplet, using 128 º YX-LiNbO3 SAW devices with 0.5 mm SAW aperture and excited by a frequency of 39.92 MHz at an RF power of 0.5 mW. The first row shows different illustrations of the droplet at different views and mass fraction ranges; Column (a): the mixing process in 3D volume images using mass fraction range $0.0 \leq m \leq 1$, and the black arrows indicate the velocity vectors of the flow field; Column (b): 3D images of the mixing process looking through the droplet by cutting slices into it, as shown in the first row, using smaller range of mass fraction $0.0 \leq \text{m} \leq 0.5$; column (c) similar to column (b) but covers the largest mass fraction range of $0.5 \leq m \leq 0.1$.

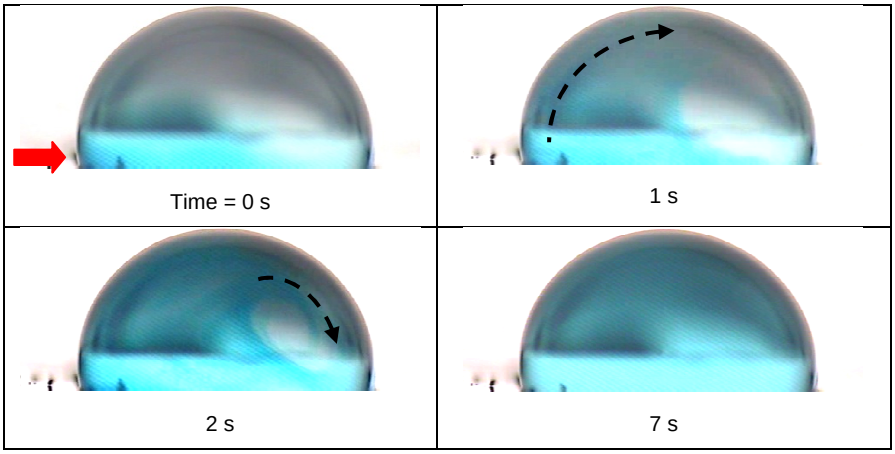

Figure 7.3 Side view snapshots of SAW-induced internal streaming in a 5 µl water droplet, where dried particles of food dye were placed underneath the droplets. After the SAW excitation, the dye colour quickly fills the whole droplet volume. The black arrow with dash line shows the fluid flow inside the droplet and the red arrow indicates the direction of the SAW propagation.

7.4.2 Mixing efficiency versus SAW excitation frequency

The relationship between the mixing efficiency and excitation frequency (or wavelength) was studied and the values of the mixing index parameter *MIP* were investigated as functions of droplet volume, wavelength and RF power. Figure 7.4(a) shows the derived mixing efficiency as a function of a dimensionless ratio between the droplet radius, R_d, and the estimated attenuation length of a Rayleigh wave, l_{SAW} [149, 153] , i.e., R_d / l_{SAW}. In this case, a 5 μl water droplet was used, and a 500 μm aperture

SAW device was excited with an applied RF power of 0.5 mW. This damping length, l_{SAW}, of the SAW can be estimated using [50, 53, 153]:

$$\boldsymbol{l_{SAW} = 1/\alpha_L = \frac{\rho_f V_f}{\rho V_R \lambda}} \tag{7.4}$$

Where, V_f is the velocity of longitudinal waves in the fluid, V_R the velocity of Rayleigh wave in solids, λ the wavelength of a Rayleigh wave, ρ_f and ρ is the density of the fluid and substrate material, respectively. In order to derive more information about the effectiveness of SAW-induced convective mixing, the relationship between *MIP* and R_d / l_{SAW} was studied for different ranges of mass fraction. As can be observed in Fig. 7.4(a), the *MIP* profile that covers the whole range of mass fraction ($m \leq 1.0$) shows only minimal variation with R_d / l_{SAW} and gives little insight into the effectiveness of the value of R_d / l_{SAW} on the mixing efficiency of SAW devices. Comparing these results with other mass fraction ranges in Fig. 7.4(a), the trends for both the profiles for $m \leq 0.1$ and $m \leq 0.5$ are similar and show clearly that there is a critical value of $R_d / l_{SAW} = 0.92$, beyond which there is a considerable decrease in the mixing efficiency (e.g., reducing l_{SAW} as an increase in the excitation frequency or a decrease in wavelength). With the acoustic energy loss being the dominant mechanism for the generation of acoustic streaming, coupled with minimal acoustic heating resulting from the low RF power and fluid viscosity [55, 141], this flow phenomenon can only be explained by the acoustic energy that is absorbed by the liquid layer. Based on the results presented in Fig. 7.4(a), the *MIP* profile has more sensitivity to the variation of the R_d / l_{SAW} ratio when the mass fraction of $m \leq 0.1$ (a value that corresponds to mean mass fraction, $m_{mean} = 0.1$). Hence, the mass fraction range of $m \leq m_{mean}$ was used in this study to quantify the SAW mixing efficiency, where m_{mean} is the mass fraction of homogenous mixing, which can be calculated by the ratio of initial dye volume to total droplet volume and the maximum initial mass fraction, $m_{mean} = m_{max} V_0 / V_{tot}$.

Figure 7.4(b) presents the simulated steady state (the time after which there is no changes in the dye concentration) results of 3D clip images, showing the effect of R_d / l_{SAW} ratio on the dye homogeneity (or mixing efficiency). From the image of first column (corresponding to $R_d / l_{SAW} = 0.92$), the droplet mixture is shown to be extremely homogeneous and the dye particles are distributed uniformly across the whole droplet volume, with a mass fraction value of $m \approx 0.1$ everywhere inside the droplet. In

contrast, when the R_d / l_{SAW} ratio is larger than one, such as 1.43 in Fig. 7.4(b), an inhomogeneous mixture is obtained with less dye particles transported into the droplet volume, due to the weakness of acoustic streaming flow, which can be seen from the results of $m \leq 0.1$ shown in Fig. 7.4(a). This flow becomes much slower with further increases in the R_d / l_{SAW} ratio. For example, a value of 3.35 in Fig. 7.4(b) resulted in larger area of the dye particles that clustered at the droplet bottom, with high concentrations (e.g., $m \geq 0.5$). This can also be verified by mixing efficiency shown in Fig. 7.4(a) for the curve of $m \geq 0.5$. When the value of R_d / l_{SAW} exceeds unity, the percentage of the droplet volume that contains a high concentration of dye particles significantly increases, and reaches up to 60% with further increases in R_d / l_{SAW}, indicated by the case of $m > 0.5$, show in Fig. 7.4(a). This clearly shows that the SAW mixing becomes poorer at high frequencies.

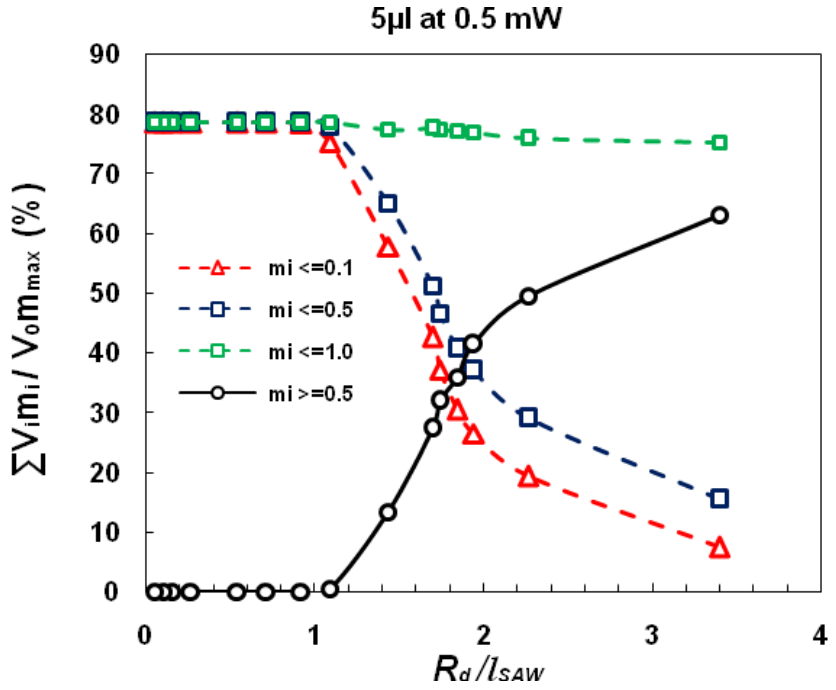

(a)

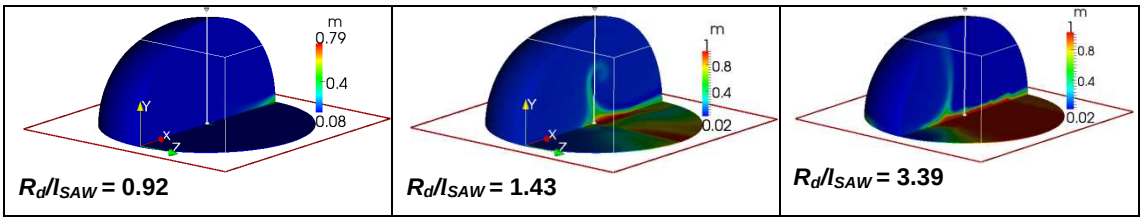

(b)

Figure 7.4 Normalised mixing intensity results for a 5 μl droplet, using 500 µm aperture SAW device at a RF power of 0.5mW, and with an initial mass dye particles concentration of m =1 for a 70 μm high layer from the droplet base and m = 0 elsewhere (pure water); (a) deviation in the steady state mixing intensity as a function of R_d / l_{SAW}

for different mass fraction ratios (b) 3D captured clips of the droplet showing the effect of R_d / l_{SAW} ratio on mixing efficiency

Figure 7.5 presents the *MIP* as a function of R_d / l_{SAW} ratio at three different RF powers (0.05, 0.15 and 0.50 mW) using a 2.5 μl droplet with an initial dye concentration similar to that shown in Fig. 7.1. Generally, the relationship for each power in Fig. 7.5 shows a similar trend to that of 5 μl droplet in Fig. 7.4(a) for equal mass fraction range of $m \leq$ 0.1. This indicates that the mechanism of the dye mass transported by a bulk liquid circulation of SAW excitation is similar. However, beyond a critical R_d / l_{SAW} ratio which is dependent upon RF power, further increase in this ratio results in a considerable decrease in the mixing efficiency. The results show that, the critical ratio of R_d / l_{SAW} decreases from 0.86 at an RF power of 0.5 mW to about 0.6, when a lower RF power of 0.05 mW is applied to the SAW device. This could be the result of less acoustic energy being absorbed by the water droplet with the same fluid inertia, causing a slow streaming flow, and thus a less mixing efficiency [62]. It is also interesting to note from the results that when the R_d / l_{SAW} ratios are much smaller than one, a mixing efficiency of 100% can be obtained even with a small value of SAW powers of 0.05 mW. This reveals that if the condition of mean critical ratio of $R_d / l_{SAW} \leq 1.0$ has been reached, the devices with a lower frequency could induce efficient mixing, even with low SAW powers.

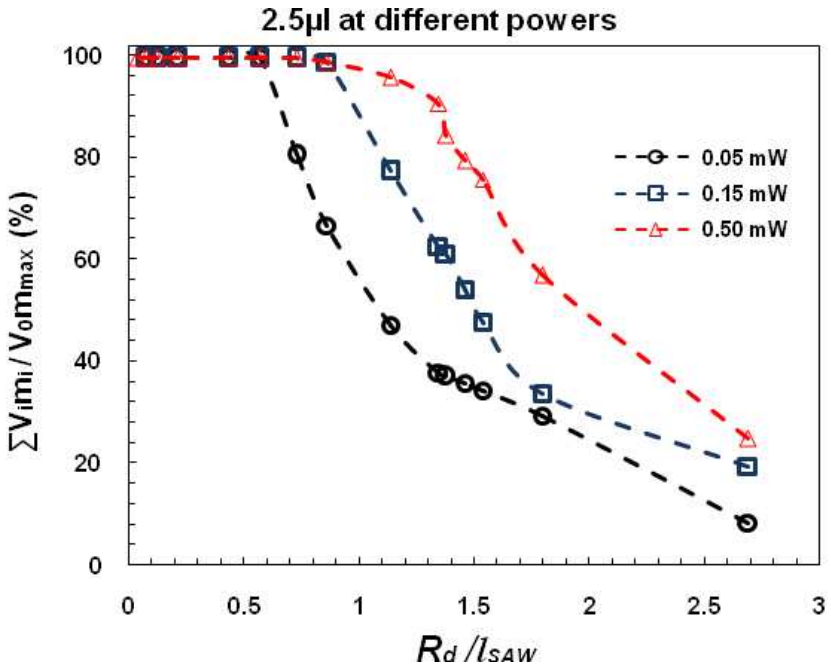

Figure 7.5 Variation of mixing efficiency for 2.5 μl droplets as a function of R_d / l_{SAW} for different RF power, using 500 μm apertures SAW devices.

In order to further clarify the role of the R_d / l_{SAW} ratio (e.g., acoustic wavelength or frequency) in the SAW-droplet based mixing system, a probability distribution function (PDF) of the dye particles concentration, *m*, was calculated at three different R_d / l_{SAW} ratios for two droplets of 2.5 and 5.0 μl, and at a duration time of steady state mixing (no variation in the dye concentration in droplets with further increase in duration time). The PDFs were obtained through calculating the total mixture (e.g., dye/water) volume contained in the droplet,V_i for a set of mass fraction groups, m_i, which were further normalized by the total volume of the droplet V_{tot}. The mass fractions were classified into 10 groups ranging from 0 to 1.0, in order to distinguish and quantify the mixing performance for each R_d / l_{SAW} ratio, as shown in Fig. 7.6, using a log-scale.

Figure 7.6(a) shows that for a 2.5 μl droplet, the value of PDF initially is about 10% (with mass fraction of one). Under SAW excitation, the dye particles distribute across the volume of water droplet and reach a steady state distribution in a few seconds. However, the mixing behavior depends strongly on the value of the R_d / l_{SAW} ratio. For the ratios smaller than a mean value of 1.0, such as R_d /l_{SAW} =0.43 presented in Fig. 7.6(a), the histogram of PDF has only one component at a mass fraction of m_i = 0.1, indicating a homogeneous mixture, and effective SAW-induced mixing. In contrast, for larger R_d /l_{SAW} ratios, such as 1.37 and 2.47 presented in Fig. 7.6 (a), non-uniform distributions of the dye particles inside the water droplet are obtained. With further increases in the R_d / l_{SAW} ratio above one, clustering of high concentration dye particles of $m \geq 0.5$ at the droplet bottom is observed, as shown in Fig. 7.4(b), indicating that mixing is inefficient. In general, the data in Fig. 7.6(b) for a 5 μl water droplet show similar behaviours to those in Fig. 7.6(a) where good mixing is achieved when the R_d / l_{SAW} ratios are less than 1.0.

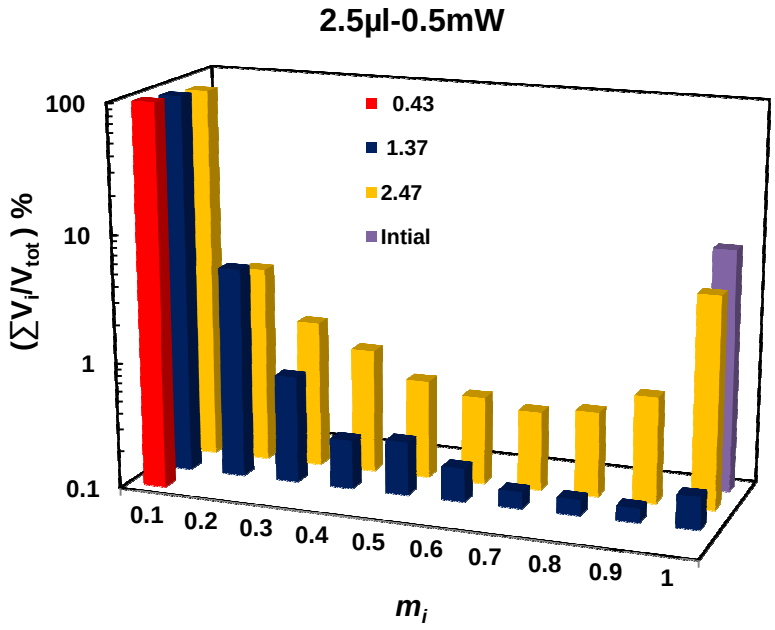

(a)

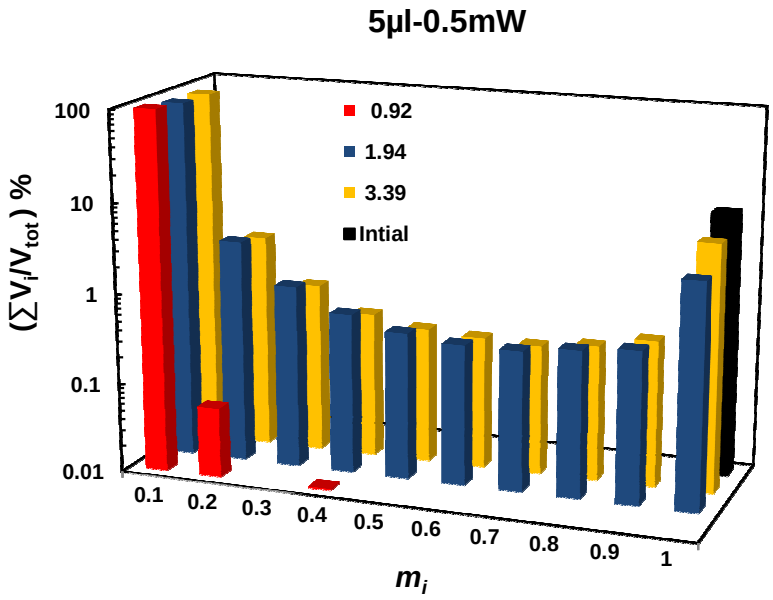

(b)

Figure 7.6 Probability distribution function (PDF) quantifying the distributions of the dye particles for different R_d / l_{SAW} ratios at 0.5 mW RF power; (a) for a 2.5 μl droplet; (b) for a 5 μl droplet. The probability values of the histogram were obtained through normalising the total mixing volume by a total droplet volume

However, results show that the SAW-induced mixing within a small droplet is more homogeneous than that of larger volumes with the same R_d / l_{SAW} ratios. Figure 7.7 shows the variation of the *MIP* as a function of droplet radius R_d at an RF power of 0.5

mW with an R_d / l_{SAW} ratio of ~1.1. As can be seen clearly, an increase in the droplet radius (or size) results in a decrease in the mixing efficiency. This can be explained by the increase of liquid inertia for a larger droplet, resulting in a slower streaming velocity (e.g., measured at the top centre of droplets) as shown in Fig. 7.7. This has been verified based on both simulations and experimental observations using a high speed camera (Kodak Motion Corder Analyzer - 600 frames per second).

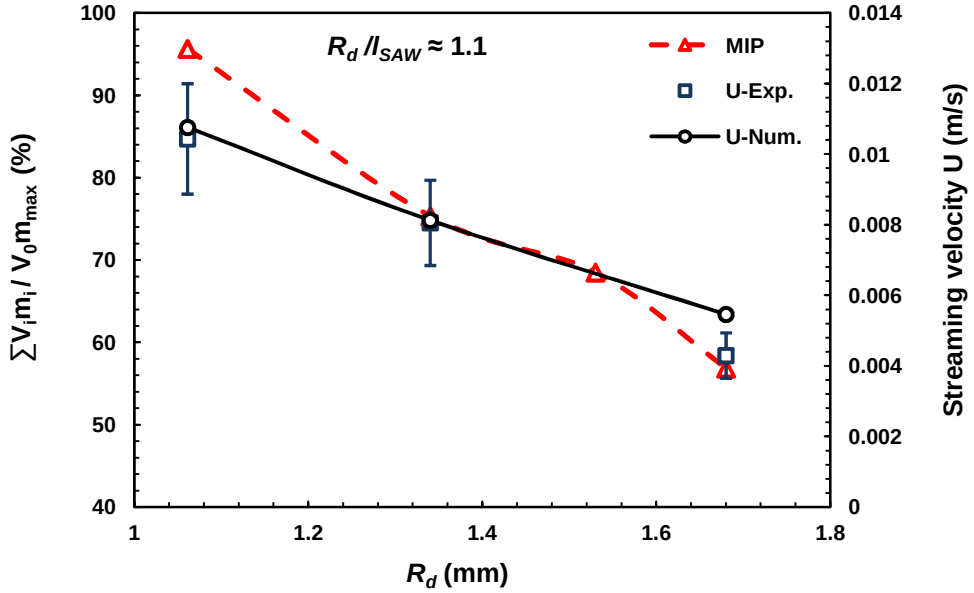

Figure 7.7 Variation of mixing efficiency, and streaming velocity (both from experiment and simulation) as a function of droplets radius, using 500 μm apertures SAW devices with $R_d / l_{SAW} \approx 1.1$ and 0.5 mW RF power

Effects of the R_d / l_{SAW} ratios on variations of *MIP* as a function of time were also investigated for different droplet volumes and RF powers. Figures 7.8(a) and (b) show the development of dye particles mixing inside water droplets of 2.5 and 5.0 μl volumes, respectively, with an applied SAW power of 0.5 mW. After an RF power is applied to the SAW device, a non-zero *MIP* value is obtained, which increases gradually and finally approaches a steady-state value, depending on the SAW power, excitation frequency and droplet volume. As clearly shown in Figs. 7.8(a) and (b), the mixing rate and efficiency are determined by the values of R_d / l_{SAW} ratios (or SAW frequencies). Fast mixing processes are obtained when the R_d / l_{SAW} ratios are smaller than one. In contrast, when R_d / l_{SAW} ratios are larger than one, lower mixing rates and efficiencies are induced, as shown in Figs. 7.8(a) and (b). For instance, from data in Fig. 7.8(b), the values of mixing rate and mixing efficiency for the R_d / l_{SAW} ratio of 0.54 are

~ 48 s^{-1} and ~ 79 %, respectively, whereas these are only ~18 s^{-1} and ~37 % for an R_d / l_{SAW} ratio of 1.74. From the profiles in Figs. 7.8(a) and (b), the mixing efficiencies for the R_d / l_{SAW} ratios less than unity are similar for the same droplet volumes and are about 100 % for of 2.5 μl and 80 % for of 5 μl droplet, even though the mixing rate was different for the different ratios. These results confirm that SAW-driven convective mixing is inefficient when the $R_d / l_{SAW} >> 1.0$.

Figure 7.8(c) shows the variation of the *MIP* as a function of time for three different applied RF powers of 0.05, 0.15 and 0.5 mW for a 2.5 μl droplet with the R_d / l_{SAW} ratio fixed at 0.56. This shows that the mixing rate is enhanced and mixing time is reduced with an increase in the RF power. For example, the mixing duration is only 4 s at an RF power of 0.5 mW, while it is 61 s at 0.05 mW. Nevertheless, the steady-state value of mixing efficiency is not influenced significantly by the applied RF power, whereas the results presented in Figs. 7.8(a) and (b) clearly show that the mixing efficiency changes significantly with the R_d / l_{SAW} ratio (e.g., SAW excitation frequency).

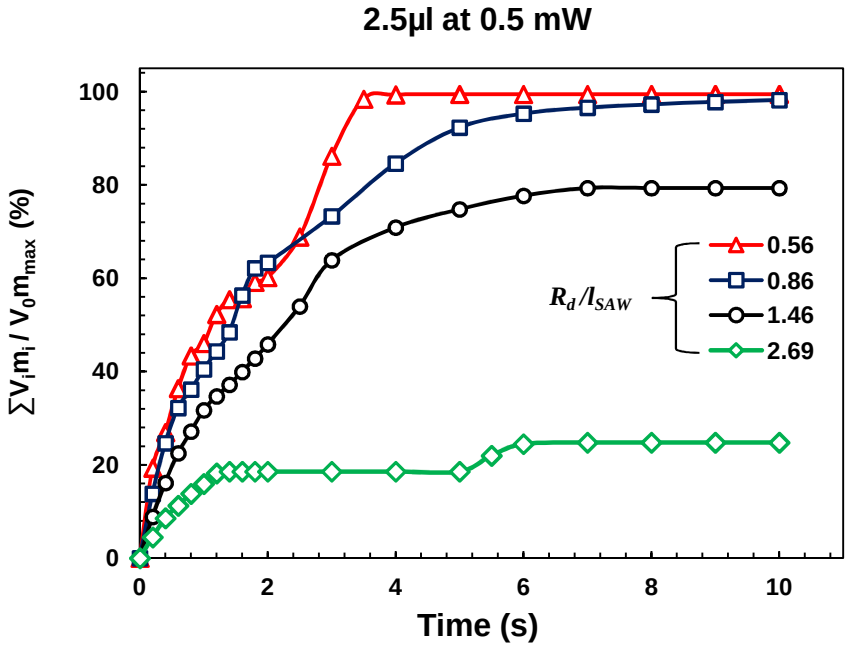

(a)

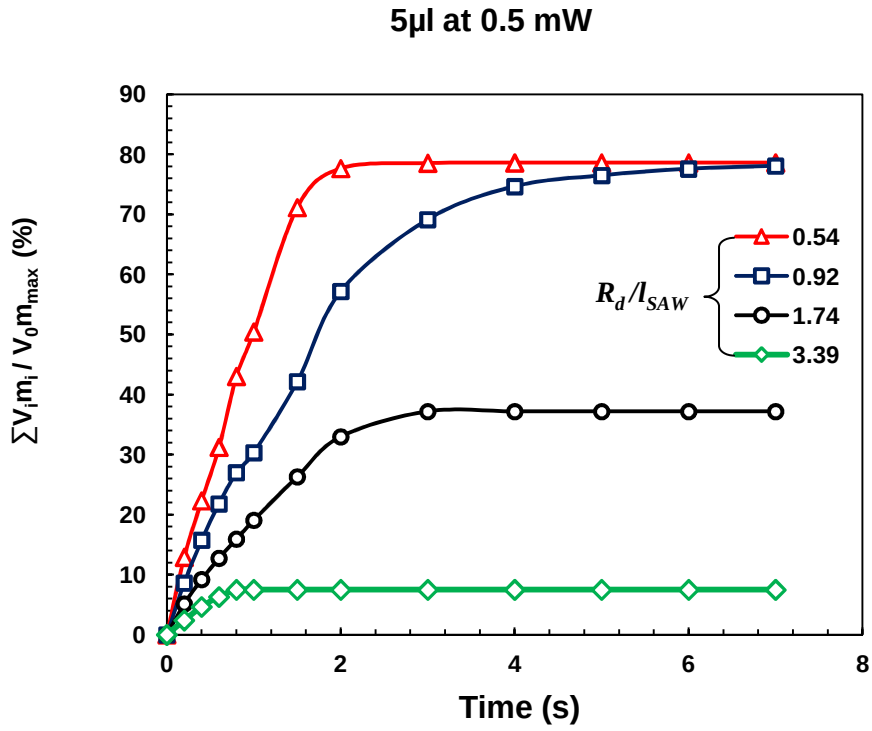

(b)

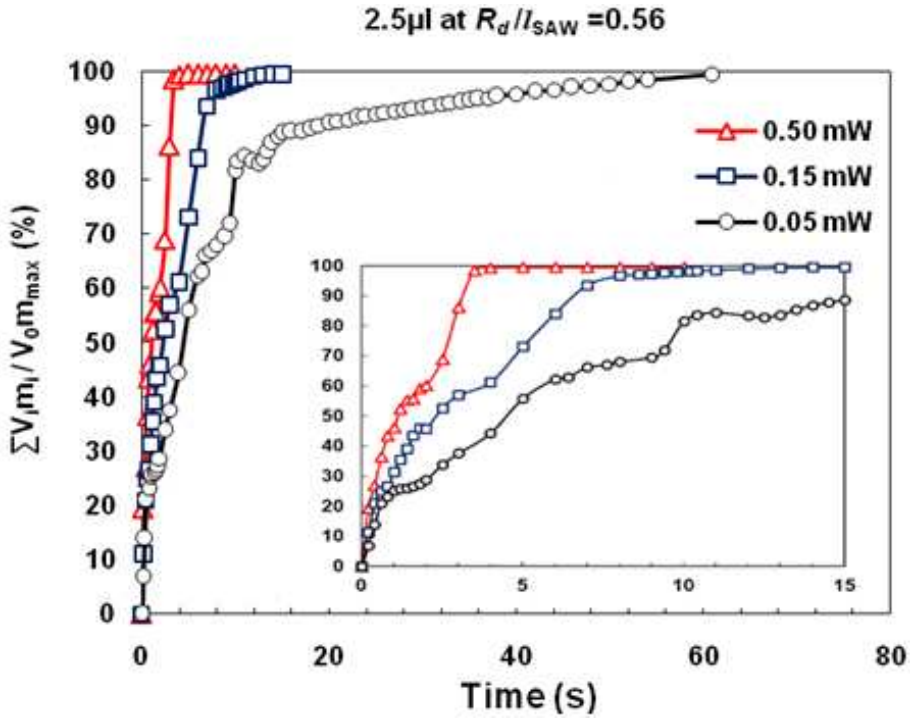

(c)

Figure 7.8 Mixing efficiency (*MIP* % for m_{men}) as a function of time for (a) 2.5 μl water droplets - RF power of 0.5 mW (b) 5 μl water droplets - RF power of 0.5 mW, (c) of 2.5 μl water droplets at R_d / l_{SAW} = 0.56 for different RF powers of 0.015, 0.05 and 0.5 mW.

7.4.3 Acoustic streaming versus SAW wavelength

The effects of a droplet volume and applied power on the streaming flow have been reported [62]. In this section, acoustic streaming phenomena and flow patterns were investigated for different R_d / l_{SAW} ratios. Figures 7.9(a) and (b) present the distribution of simulated streaming velocities for a 2.5 μl water droplet with different R_d / l_{SAW} ratios, measured along the z and y axis of the droplet. Clearly, a decrease in the R_d / l_{SAW} ratio results in an enhancement in the streaming velocities. When the R_d / l_{SAW} ratio is less than one, higher velocity gradients are observed inside the droplet, whereas smaller gradients are seen for R_d / l_{SAW} ratios larger than one, indicating a weakness of flow circulation by SAW excitation. These results support those in Figs. 7.4 and 7.5, i.e., with the higher the velocity gradient in the droplet, the better the mixing process, due to a stronger streaming-driven convection being produced. Therefore, the larger the shear velocity gradients across the droplet axis, the faster the convective velocities that transport the dye particles into the bulk droplet, resulting in a more efficient mixing process.

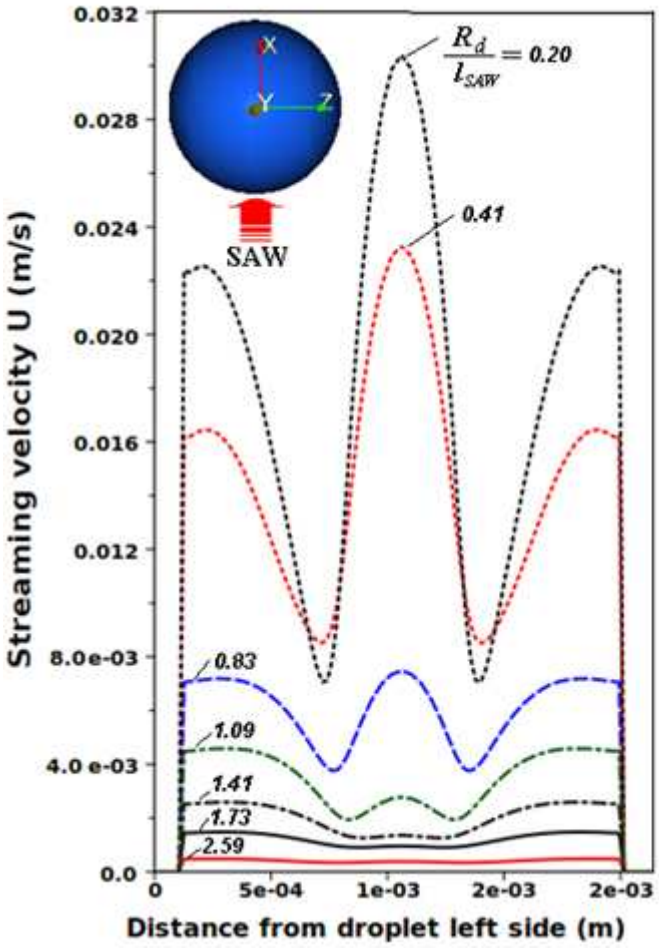

(a)

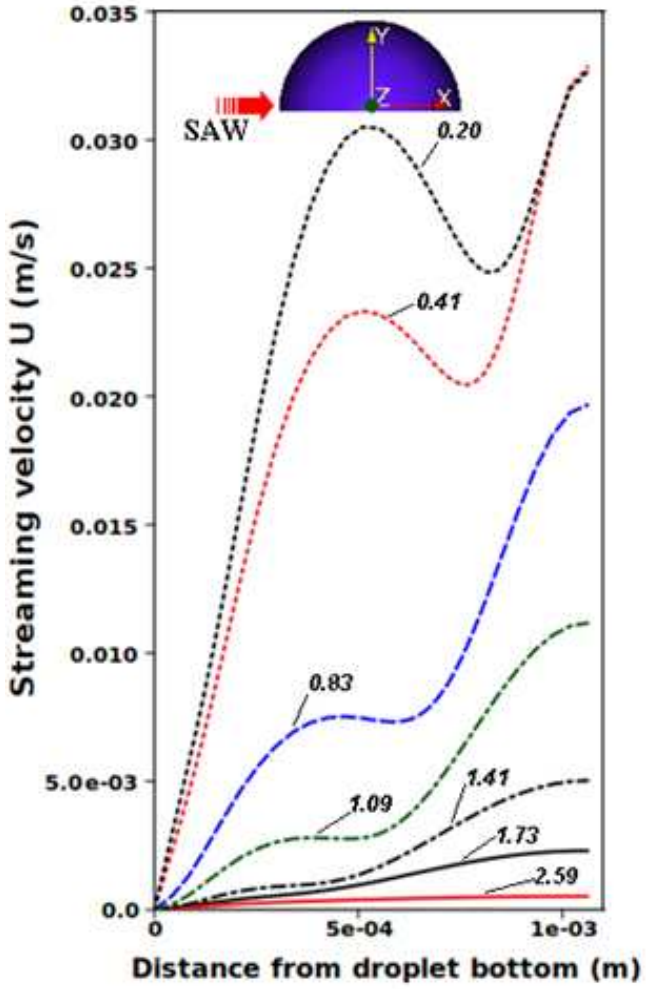

(b)

Figure 7.9 Simulated streaming velocity profiles measured along two different axes into a 2.5 μl droplet for a range of R_d / l_{SAW} ratios, using 500 μm aperture SAW device with an RF power of 0.5 mW; (a) measured along the z axis at 500 μm height from the droplet bottom; (b) radial distribution measured along the y axis at the droplet centre

To clarify the physics behind the effects of the R_d / l_{SAW} ratio, the characteristic flow parameters of a 5.0 μl droplet with an applied power of 0.5 mW were calculated, and the results are listed in Table 7.1. This shows that although the streaming force is enhanced, the increase in the excitation frequency (or decrease in wavelength) offsets the increase of streaming velocity (measured at the top centre of droplet). These conflicting mechanisms can be attributed to the decrease in the SAW attenuation length, l_{SAW} [50, 149], due to the increase in the excitation frequency, which causes the SAW acoustic energy to be strongly absorbed by the liquid, and hence the higher rate of energy dissipation. Consequently, the more rapid the acoustic energy dissipation, the smaller the energy to be reach the droplet top free surface, which in turn results in a slower flow circulation due to a large fluid inertia, and less effective mixing.

Table 7.1 Characteristic flow parameters for numerical simulation of 5.0 μl droplet at RF power 0.5 mW.

Wavelength λ (µm)	**Excitation frequency f (MHz) Eq. (2.12)**	**R_d/l_{SAW} $l_{SAW,}$ Eq. (7.4)**	**SAW amplitude A (A°) Eq. (4.8)**	**Streaming force, F (Nm^{-3}) $\times 10^3$ Eq.(4.7)**	**Streaming velocity U (ms^{-1})**	***MIP* % Eq.(7.3)**
200	19.96	0.543743	2.971	14.524	0.032573	78.61178
117.888	33.862	0.922474	1.752	24.641	0.021347	78.42174
100	39.92	1.087486	1.485	29.012	0.016342	75.35968
75.7857	52.6748	1.434949	1.125	38.288	0.008128	57.87846
58.944	67.7274	1.844947	0.875	49.282	0.00312	30.50193
32	124.75	3.398393	0.4755	90.778	0.00027	7.487235

Figure 7.10 shows the simulated distribution profiles of SAW streaming force along the propagation path of the longitudinal wave starting from the SAW interaction point (near SAW source) towards the top centre of a 5.0 μl water droplet and for different R_d / l_{SAW} ratios, using a 500 μm aperture SAW device at an applied RF power of 0.5 mW. Figure 7.10 shows that the streaming forces decrease with the distance from the interaction region of SAW, which indicates damping of the wave. Comparing results for the different R_d /l_{SAW} ratios, the value of streaming force at the interaction region (near the SAW source) is enhanced by increasing the ratio of R_d / l_{SAW}. Nevertheless, the momentum of acoustic energy (streaming force) that is transferred away from the SAW interaction region decreases significantly with an increase in the R_d / l_{SAW} ratio, especially when the R_d / l_{SAW} ratio is larger than one. This is attributed to an increase in attenuation rate with increasing SAW excitation frequency as listed in Table 7.1.

Figure 7.11 presents the simulation results of the flow streaming patterns induced by SAW excitation in a 2.5 μl droplet with an applied RF power of a 0.5 mW for a range of R_d / l_{SAW} ratios. These results show that the flow patterns are strongly affected by the frequency, especially for a high excitation frequency, or the R_d / l_{SAW} ratios larger than unity. Therefore, the streaming patterns can be classified into two groups based upon the shape of the flow axis of rotation. The first group is associated with the ratio of $R_d / l_{SAW} \leq 1.0$ and the regular butterfly patterns are observed, where the fluid flow rotates

about one elliptical axis of rotation through the droplet centre in a similar manner to those shown in the first and second column in Fig. 7.11. In the second group, when the ratio of $R_d / l_{SAW} >> 1.0$, such as 1.41 and 2.93, an irregular (weak) streaming pattern results, where the fluid flow rotates about two individual axes of rotation, as shown in the third and forth column in Fig. 7.11. When the regular butterfly patterns are induced by the SAW with a ratio of $R_d / l_{SAW} \leq 1.0$, the strong interaction between the driving flow and back flow contributes to the mixing efficiency. This is confirmed by results of different mixing index parameters presented in Figs. (7.4) to (7.7) showing an effective mixing and better homogeneity for the solution mixture. In contrast, an ineffective mixing were induced for an $R_d / l_{SAW} >> 1.0$, where the longitudinal pressure wave arriving at the droplet free surface is strongly attenuated thus resulting in a weak acoustic streaming force. This demonstrates that the streaming velocity, flow profiles and mixing efficiency all are influenced by the SAW excitation frequency.

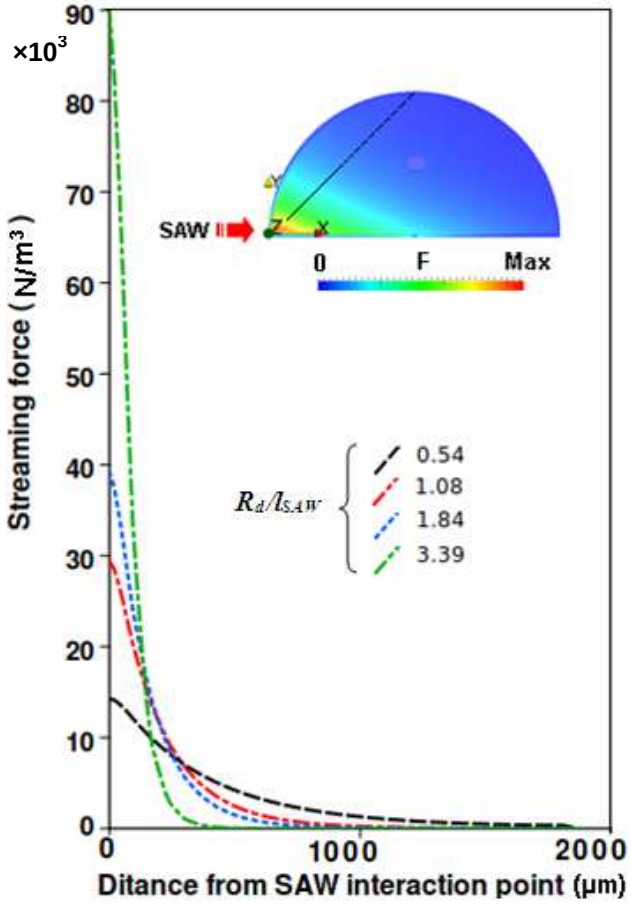

Figure 7.10 Measurements of acoustic streaming force at SAW interaction point and along the propagation direction of the longitudinal wave towards the top centre of 5.0 μl droplet, and for R_d / l_{SAW} ratios; the black line in the droplet show the measuring path of acoustic streaming force

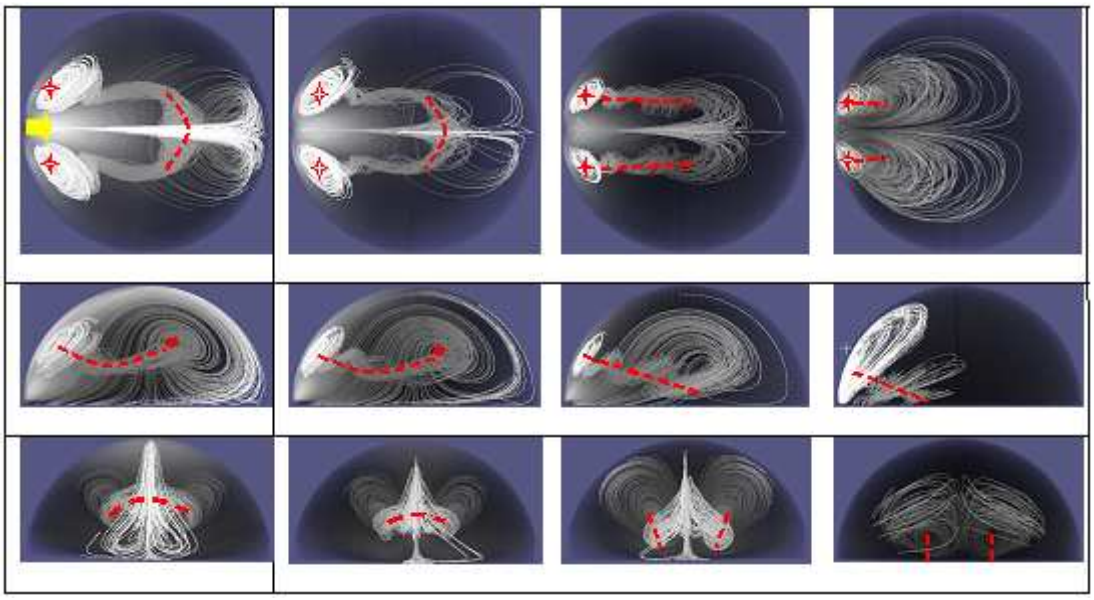

0.83 **1.09** **1.41** **2.93**

Figure 7.11 Simulated results showing the changes in the streaming patterns with R_d / l_{SAW} ratio, and for 2.5 μl droplet using 0.5 mm aperture SAW device and 0.5 mW RF power. The first row shows a top view of the double vorticity; the second row shows the side view focusing through the droplet centre, and the third row views the droplet from the front. The yellow arrow indicates the SAW direction and the red broken lines the axis of rotation.

7.5 **Summary**

In summary, a SAW-driven mixing process of the dye particles inside microdroplets has been simulated numerically and verified experimentally, in order to investigate the effect of SAW excitation frequency (or wavelength) in the flow streaming and mixing process for a range of droplet volumes and RF powers. It has been shown that a higher RF power and a decreased droplet size results in an increase in the streaming velocity and mixing efficiency, whereas a higher excitation frequency can result in less effective mixing with a slower mixing rate, due to weakness of streaming flow. The SAW attenuation length, l_{SAW}, (a factor directly related to the SAW excitation frequency and wavelength) has been identified as a parameter indicating the efficiency of SAW-inducing convective mixing. A fast and effective mixing process results until l_{SAW} reaches a critical value, beyond which a significant decrease in streaming velocity and mixing efficiency is observed. The magnitude of streaming velocity, mixing rate and efficiency were determined by the droplet size to be a highest when the ratio of the droplet radius to SAW attenuation length R_d / l_{SAW} $\leq$ 1.0, even at small SAW powers,

such as 0.05 mW. In contrast, inhomogeneous mixtures with slower mixing rates were obtained when $R_d / l_{SAW} >> 1.0$, due to the higher attenuation rate of acoustic energy and minimisation of energy reaching the droplet free surface. As a high power results in a significant heating effect, this mean critical ratio, i.e., ($R_d / l_{SAW} \leq 1$) can be used as a guideline in the SAW device design for microfluidic applications that include temperature sensitive biological samples inside the microdroplet [141, 142].

Chapter 8

SCALLING EFFECTS IN SAW STREAMING

This chapter reports an experimental and numerical investigation on the scaling effects in the flow hydrodynamics for confined microdroplets induced by a Rayleigh surface acoustic wave. The characteristic parameters of the flow hydrodynamics were studied as a function of the separation height, *H*, between the $LiNbO_3$ substrate and a top glass plate, for various droplets volumes and radio-frequency (RF) powers.

8.1 **Introduction**

Although SAW-induced streaming has been studied extensively in digital microfluidics [16, 62], fewer studies have been reported for SAW microfluidics in confined spaces or microchannels [151]. In some recent work [34, 150, 151], a top-open microchannel was fabricated on the substrate surface of a $LiNbO_3$ SAW device using laser micromachining. These studies showed that the changes in the SAW excitation frequencies switch the flow pattern from uniform (parallel) to mixing (vortical) flow, depending on the ratio of wavelength to microchannel width. Gu et al. [154] studied the performance of a non-contact linear motor driven by a SAW through a thin liquid layer on which the slider was suspended. The motor was contained within a top-open glass cell located at the SAW device surface. Results showed that the velocity of the slider is proportional to the power applied to the SAW device, and is also dependant on the thickness of the liquid layer.

For semi-closed microfluidic systems, Shiokawa et al. [52] reported that placing a guide plate on the top of a liquid layer is an effective method to control the flow of the liquid in the propagation path of a SAW, but the flow velocities were slower than that of liquid without a top plate, due to the resultant shear gradient induced at the surface of the top plate. A similar experimental set up has also been used in many SAW-mixing studies [25, 64], and results showed that the flow patterns in the droplets with a top plate enhanced the mixing efficiency of the contained micro-particles.

For closed microchannels, Schmid et al. [153] observed that the scattering of SAW energy which was leaked through a liquid layer into the upper glass slide generated an

acoustic power, which was able to drive and pump biological substances in a rectangular Polydimethylsioxane (PDMS) microchannel located on the glass slide. SAW-induced streaming has been reported to be one of the more efficient techniques to enhance mixing efficiency in a continuous microchannel flow [67, 142].

Microchannel design (i.e., shape and geometry) has also been reported to influence the flow characteristics inside the microchannels [11]. For example, microchannel height has been reported to have significant influences on the characteristic flow parameters of streaming phenomena induced by a flexural plate wave (FPW) [155-157]. Min-Chien and Tzong-Shyng [158] showed that, within a microchannel with a height < 100 μm, the induced shear stress from the side walls causes a significant effect on the streaming velocity profiles. Guo et al. [159] theoretically studied the acoustic streaming generated by a lead zirconium titanate (PZT) piezoelectric ceramic plate attached to the bottom of micro-machined silicon microchannel. Their results showed that acoustic streaming velocity was dependent not only on the acoustic power, but also on the channel height, and a maximum streaming velocity was increased from 0.16 to 0.2 m/s by increasing the channel height from 0.5 to 1 mm.

Clearly all these studies exhibit apparent significant scaling effects of height on the streaming flow induced by acoustic waves in confined microdroplets or microchannels. However, it should be noted that most studies of height effects induced by SAW streaming were based on the microdroplet or open microchannels with no top-plate. So far, to the best of author's knowledge, there have been no systematic studies of the height scaling effect on SAW streaming in a confined microdroplet. Clearly, a simple but an efficient method is needed to evaluate this scaling effect in confined microfluidics. In this chapter experimental and numerical investigations for the height scaling effects on the characteristic flow hydrodynamics were carried out for confined microdroplets actuated with a SAW technology.

8.2 Experimental and Numerical Details

The configuration of the experimental setup includes a glass slide and a $LiNbO_3$ substrate, the latter of which generates the SAW. The slide and substrate are separated by a distance H and a water microdroplet placed between them, as shown in Fig. 8.1. The microfluidic experiments were carried out using a 128º YX-$LiNbO_3$ SAW devices

with an aperture of 1.5 mm, a finger width of 16 μm and a wavelength of 64 μm. The measured excitation frequency of the SAW device is ~ 60 MHz. In this study, a CYTOP®(Asahi Glass Co., Ltd., Tokyo Japan) layer was spin-coated on both the top glass slide and $LiNbO_3$ SAW substrate surface to make the surfaces hydrophobic, as hydrophilic surface have been reported to suppress the streaming velocity [52, 86]. The space between the top glass plate and substrate, defined in this study as the gap height *H*, were set to 65, 102, 271, 548 and 1,113 μm by using specially designed spacers, as illustrated in Figs. 8.1 and 8.2(a). The droplet volumes were adjusted in order to maintain a constant droplet diameter of either ~ 2.2 or ~ 3 mm. In order to determine the streaming velocity, polystyrene particles with average diameters of 6 μm were placed inside the water droplets and their motions were recorded using a high speed camera (Kodak Motion Corder Analyzer - 600 frames per second), as demonstrated in Fig. 8.1.

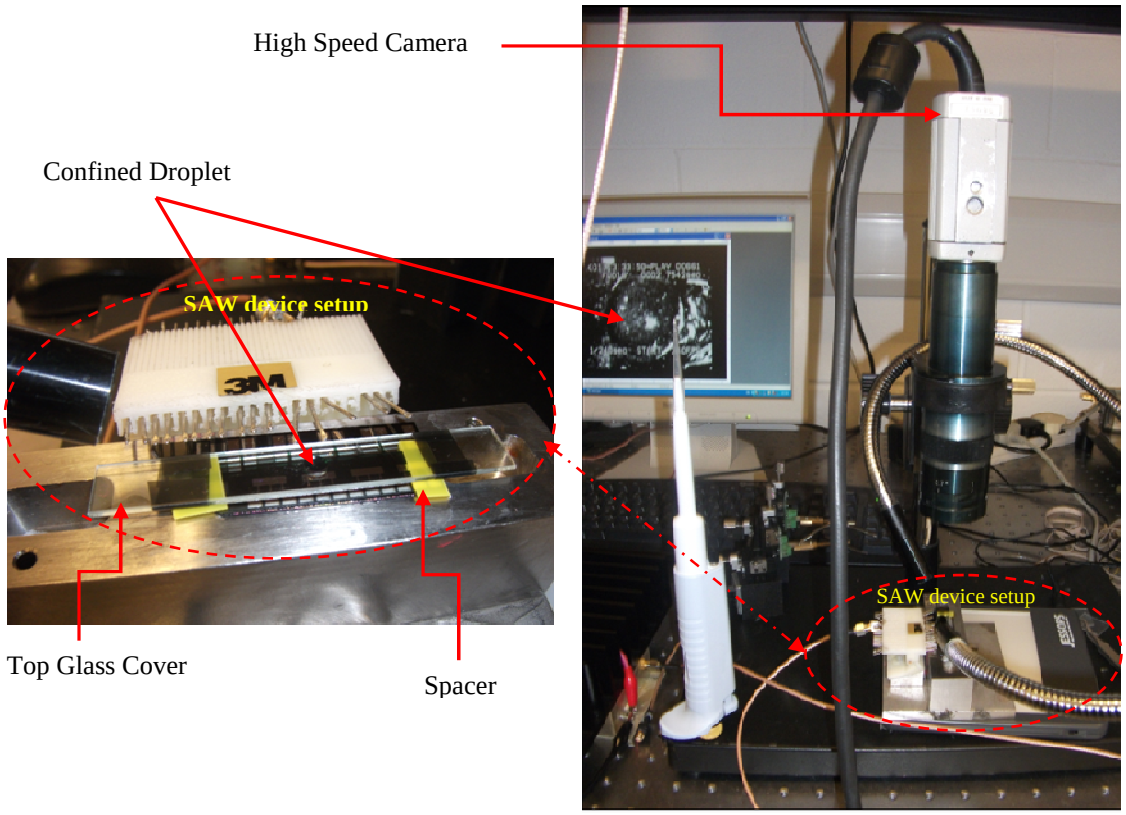

Figure 8.1 Photograph of an experimental setup used for height effect measurements

For the flow hydrodynamic simulations, the laminar incompressible Navier-Stokes equation of SAW-liquid coupling [140], driven by an external body force, *F* (i.e., see Sect. 4.3), was solved numerically in three-dimension using a finite volume numerical method [129]. The meshing of the confined droplet domain was built using a curvilinear grid structure with a grid size of 50 x 25 x 50 cell nodes, in x, y and z axis, respectively.

As can be observed from Fig. 8.2(c), the interface curvature of the droplet is small and can be reasonably approximated by a straight line with a wetting angle of ~ 90º. Hence in the simulation, the droplet contact angle at the solid surface was assumed to be 90º and the small deviation from the actual contact angle was ignored. In all the experimental tests of this study, no significant deformation at the droplet/air interface was observed due to the low SAW power used during the streaming process, therefore, a slip (or stress free) boundary condition on the droplet/air interface, and a non-slip boundary condition on the droplet/solid surface (glass slide and substrate surface) were assumed, as indicated in Fig. 8.2. The streaming simulations were carried out using a SAW device with an excitation frequency of 60 MHz. As mentioned above, the droplet volumes were set by fixing the droplet diameter at 2 mm with gap heights of 50, 100, 250, 333, 400, 500, 600, 750 and 1,000 μm. RF powers ranging from 0.5 to 50 mW were applied in the simulations.

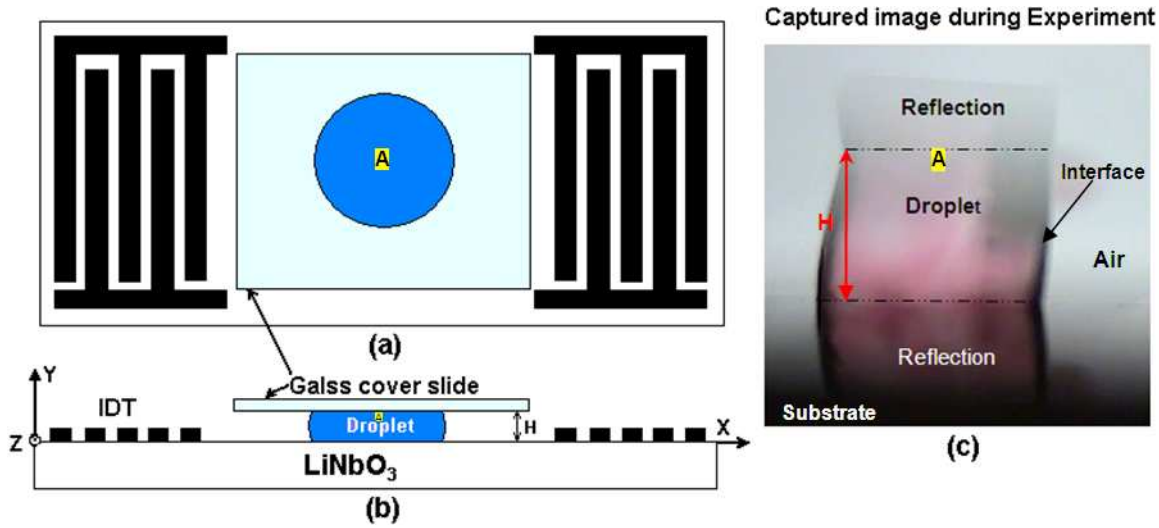

Figure 8.2 Schematic illustration of experimental and numerical setups; (a) Top view; (b) Cross sectional view; (c) Captured Cross-section image of 4 μl droplet from side view during the experiment with a gap height (H) of 1,113 μm

8.3 Results and Discussions

8.3.1 Streaming velocity versus RF power and gap height

Variations of the streaming velocity as a function of the RF power and gap height were studied both experimentally and theoretically. From the results, the streaming velocity is dependent not only on the RF power and liquid volume (or droplet diameter, d_r), but also on the separation between the top plate and substrate (or gap height, H). Figure 8.3 shows the experimental results of the streaming velocities measured at the top centre of

the droplets (point *A* as shown in Fig. 8.2) as a function of the RF powers for different droplet volumes and gap heights. These results show that the streaming velocity increases with increase of the RF power, because at high powers, a higher acoustic pressure or momentum will be delivered to the liquid layer due to the increased SAW amplitude. A linear relationship between the streaming velocity and RF power is observed for smaller gap heights such as of 271 and 102 μm in Fig. 8.3. This linearity is reasonable because of higher shear gradient of flow at the solid wall (e.g., top plate) with such small gap heights [74]. This, in turn results in a slower flow motion in the droplet when Reynolds number values approach unity. In this study, the droplet diameter d_r is used as a length scale in the calculation of Reynolds number. With such a small value of Reynolds number or creeping flow, inertial effects (hydrodynamics nonlinearity) do not play a significant role in comparison with the viscous effects [56]. In contrast, a nonlinear variation of streaming velocity with the RF power is obtained for a larger gap height of 548 μm. High speed camera observations revealed that the speed of polystyrene beads inside the droplets was only 0.9 mm/s for a small gap height of a 271 μm, whereas it was a 4.6 mm/s with larger gap height of a 548 μm, at the same RF power of ~ 0.03 W. Results in Fig. 8.4 clearly show the influence of gap height on the SAW streaming flow.

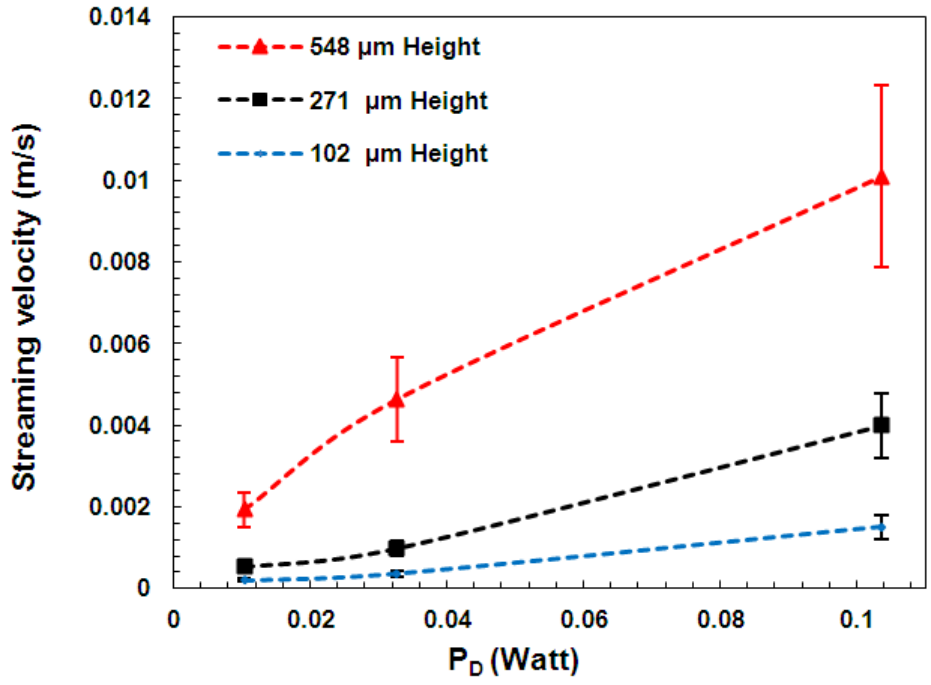

Figure 8.3 Experimental measurements of maximum streaming velocity as a function of RF power for a ~3 mm droplet diameter and different gap heights, using a 128° YX-$LiNbO_3$ SAW device with a 1.5 mm aperture excited by a frequency of 60 MHz

Figure 8.4 shows the variation of streaming velocity data measured at point A, as shown in Fig. 8.2, as a function of gap height, *H*, for droplets with nominal diameters of ~2.2 and ~3 mm, and SAW excitation powers of 0.01, 0.03 and 0.1 W. From results of a ~3 mm droplet diameter shown in Fig. 8.4(a), the streaming velocity is suppressed as the gap height decreases, due to the increase in shear force gradient. Generally, the variation of streaming velocities with the gap height is nearly linear due to the lower value of inertial forces in comparison with viscous forces at lower velocities.

In general, the data in Fig. 8.4(b) for a droplet with a diameter of ~ 2.2 mm shows a similar phenomenon to those in Fig. 8.4(a) where the streaming velocity is enhanced as the gap height increases. However, beyond a critical gap height of ~ 550 μm, any further increase in the separation results in a decrease in the streaming velocity. As the acoustic energy loss is the only mechanism for the generation of acoustic streaming, and acoustic heating is also minimal at small applied power and fluid viscosity [141, 142], this flow phenomenon can only be explained by the acoustic energy that was leaked into the liquid layer, a phenomenon which will be explained in detail in Sect. 8.3.2.

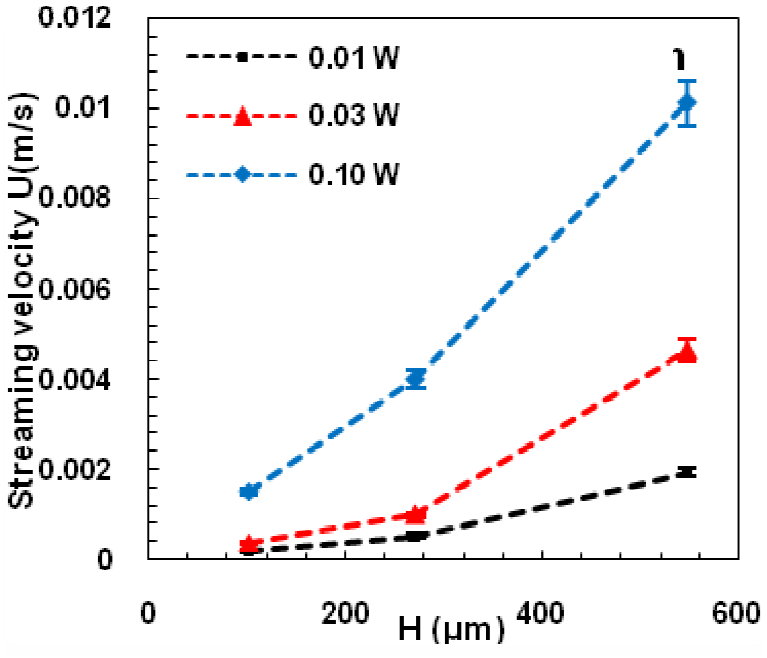

(a)

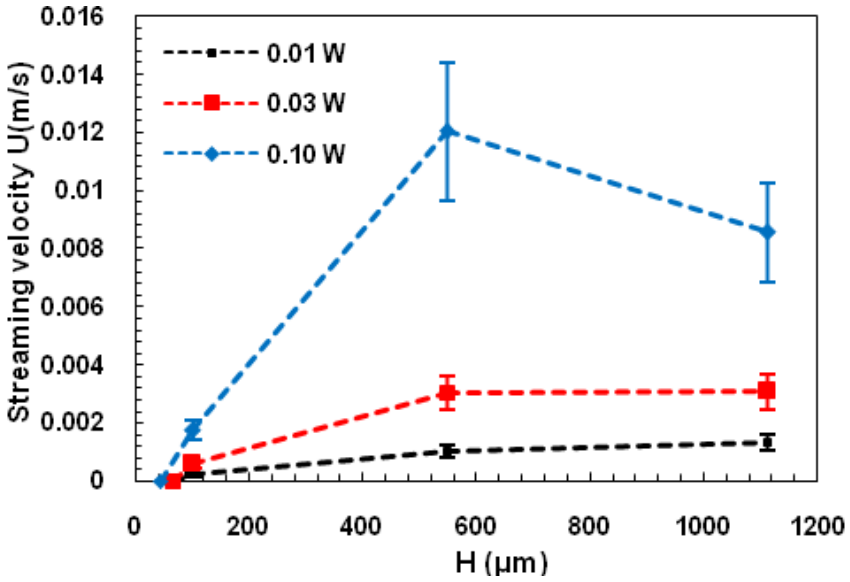

(b)

Figure 8.4 Experimental results of streaming velocity at the top of a droplet as a function of gap height for different RF power levels using 128º YX-$LiNbO_3$ SAW device with a 1.5 mm aperture excited by a frequency of a 60 MHz; (a) Droplet diameter of 3.0 mm; (b) Droplet diameter of 2.2 mm

Figure 8.5 shows numerical simulations of the detailed flow characteristics at various RF powers and gap heights. These results show that the streaming velocity (measured at point *A* in Fig. 8.2) increases with the gap height until reaching a critical value for the gap height, H_{cr}, of 500 μm, above which the streaming velocity decreases. Considering the uncertainty associated with the experimental measurements, the critical value obtained from the simulation agrees well with the critical gap height of ~ 550 μm obtained from the experimental measurements. However, when H is < 500 μm, the streaming velocity decreases as the gap height decreases, which could be attributed to the increase in the dragging forces at the top and bottom solid boundaries (e.g., top glass plate) [11]. With further reduction in the gap height to 50 μm, the simulated streaming velocity almost approaches zero, especially with RF powers < 0.05 W.

Indeed, our observations using a high speed camera showed that when the gap height was reduced to ~ 65 µm, the velocity of polystyrene particles in the droplets was almost zero, and the liquid inside the droplet did not show any apparent flow patterns over the range of RF power used in this study**,** as can be observed in Fig. 8.4(b). In general, the experimental results in Fig. 8.4 are in good agreement with those obtained from the numerical simulations shown in Fig. 8.5.

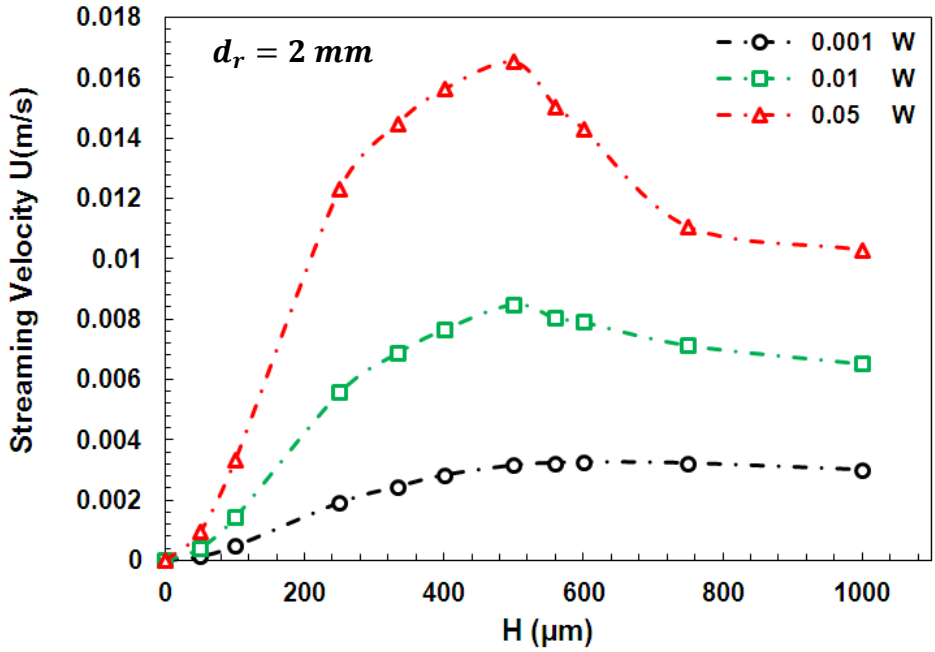

Figure 8.5 Numerical results showing the maximum streaming velocity at the top centre of the droplet as a function of gap height for a 2mm droplet diameter and different RF power levels, using a 128º YX-$LiNbO_3$ SAW device with an excitation frequency of 60 MHz.

8.3.2 Physical mechanism

In order to explain the observed flow phenomena at various gap heights, the mechanism of SAW acoustic streaming and the SAW attenuation in the liquid layer should include a consideration of flow parameters, such as Reynolds number. As explained in Chapter 2, the emission of this compressional (longitudinal) waves leads to an attenuation of SAW, within an absorption coefficient of α_L, i.e., Eq. (2.16), which damps exponentially within an attenuation length of l_{SAW}, causing a change in its mode to a Leaky SAW (LSAW) [86], as show in Fig. 8.6(a). This damping length, l_{SAW}, of the SAW can be estimated using Eq. (7.4).

In this study, a wavelength of λ = 64 μm and an excitation frequency of f = 60 MHz were used, and the liquid (water) density is taken as ρ_f = 1,000 kg/m^3. The density of the SAW device substrate (128º YX-$LiNbO_3$ material) is 4,630 kg/m^3 [152]. The calculated velocity of the SAW, V_R, is 3,840 m/s, based on $V_R = f\lambda$ [47], and the sound velocity in the fluid, V_f, is 1,500 m/s. It should be noted that the parallel component of the particle motion of a Rayleigh SAW at substrate surface leads to frictional losses, which can be calculated using the viscosity of liquid layer, μ, using Eq. (2.20). The calculation based on Eqs. (2.16) and (2.20) shows that $\alpha_s \ll \alpha_L$. Therefore, in

comparison with the contribution of longitudinal wave, the attenuation due to viscous losses can be neglected in this study, [86].

Thus, the SAW attenuation length in this study was calculated using Eq. (7.4) with a value of $l_{SAW} \approx 750\ \mu$m, i.e., a length required for the acoustic energy to be completed absorbed by the droplet liquid. The leakage of acoustic energy by SAW into the liquid droplet results in a net body force, *F*, (force per unit volume) [41, 48], which can be calculated using Eq. (4.7).

Both the experimental and numerical results show that, when the gap height is less than ~ 500 µm, the streaming velocity is enhanced with increasing gap height. In this regime, the acoustic energy absorbed by the liquid layer due to the emission of longitudinal waves induces an acoustic streaming flow. If these waves propagate through a liquid layer of gap heights less than its damping length, a part of the longitudinal waves will be refracted from the liquid layer into the upper glass slide, which means that less energy will be coupled into the liquid layer. Indeed, the distribution profile of streaming force presented in Fig. 8.6(b) shows that the portion of acoustic momentum delivered to the liquid by the SAW per unit area (i.e., area under curve) at small gap heights such as 100 μm is smaller than that of larger heights. Therefore, with a smaller gap, less energy will be delivered from the SAW. Also the corresponding increase in the wall shear resistance from the top plate will contribute to a decrease in the streaming velocity. Therefore, any increase in the gap height will enhance the SAW momentum, and hence the streaming velocity.

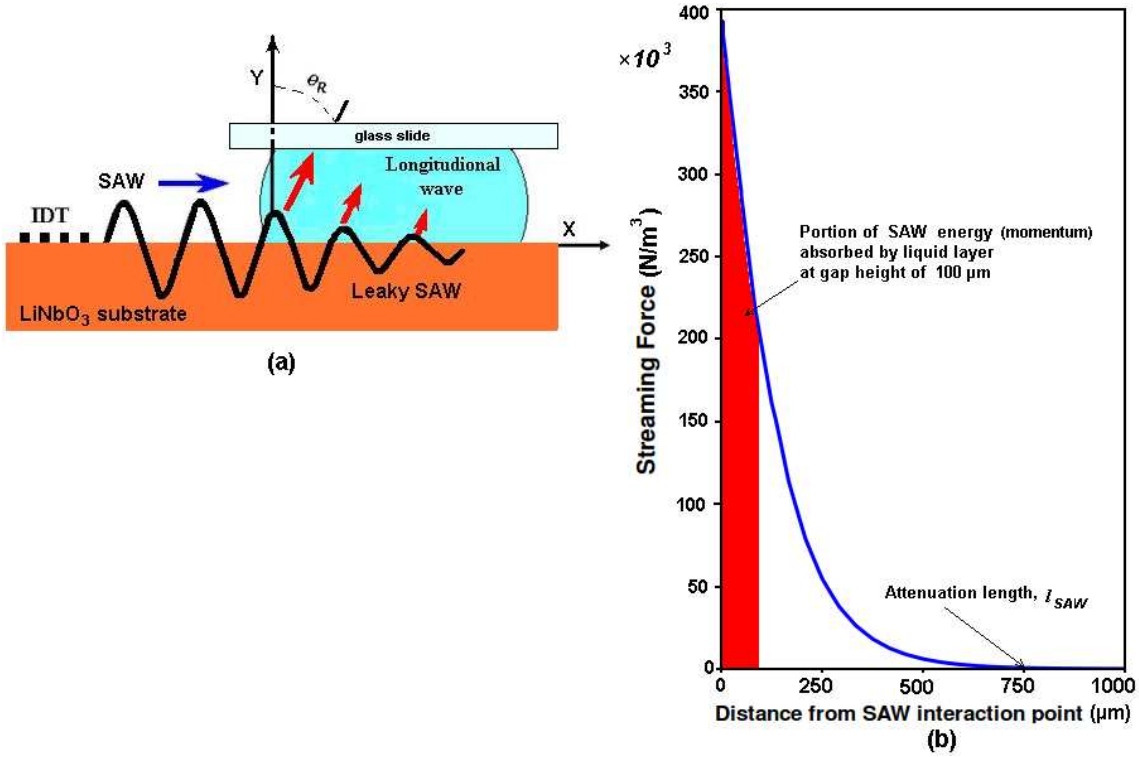

Figure 8.6 Leaky SAW induces body (streaming) force; (a) illustration shows attenuation of leaky SAW by liquid coupling and the propagation direction of an induced longitudinal wave; (b) calculated streaming force at SAW interaction point and along the propagation direction of the longitudinal wave towards the *upper glass slide*

However, it has been shown earlier in this chapter that if the gap height is increased beyond a critical value of ~ 500 μm, the streaming velocity will drop gradually, as shown in Figs. 8.4 and 8.5. This reduction in the value of streaming velocity with gap heights larger than ~ 500 μm can also be explained from Fig. 8.6(b). An increase in the gap height beyond a 500 μm will induce a negligible increase in the SAW momentum delivered to the fluid, where the most of the acoustic momentum is already coupled into the fluid. On the other hand, there is a large increase in the mass inertia of the droplet volume with increased gap height, which could explain the decrease of the streaming velocities as the gap heights larger than ~ 500 μm.

Figure 8.7 shows simulation results of Reynolds number (using the value of the streaming velocity at point A, shown in Fig. 8.2) as a function of the normalised gap height, H/l_{SAW} for a range of acoustic powers (the droplet diameter is 2 mm). This reveals that if the gap height, H, exceeds a critical percent of the attenuation length of the Rayleigh SAW, l_{SAW}, which has been identified as$(H/l_{SAW}) \approx 0.7$, the Reynolds number decreases dramatically with further increases in the gap height, especially at excitation RF powers larger than 1 mW, which corresponds to a critical gap height of

500 μm, in which the amplitude of the LSAW nearly attenuates to ~ 1/e, as shown by the value of streaming force in Fig. 8.6(b).

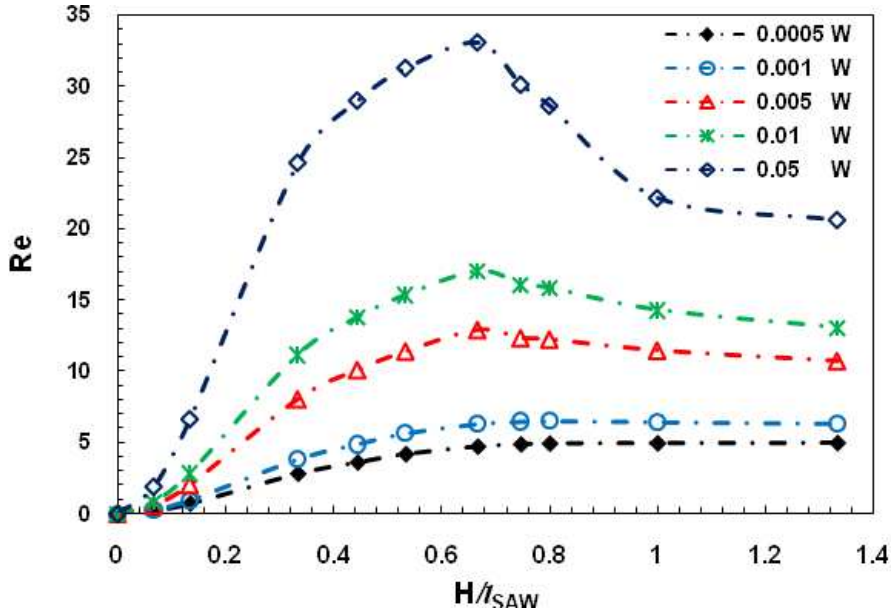

Figure 8.7 Numerical results of Reynolds number as a function of normalized gap height for 2 mm droplet diameter excited by a range of RF powers using a 128º YX-$LiNbO_3$ SAW device with 1.5 mm aperture and excitation frequency of a 60 MHz

For smaller gap heights, as the dimensionless gap height ratio, $H/l_{SAW} < 0.067$ (equivalent to $H < 50$ μm), the momentum of the SAW produces a slower flow motion (with Re ≤ 1) even at the highest RF power of 0.05 W in this study (see Fig. 8.7). From experiments, the motion of polystyrene particles becomes undetectable for gap heights < 100 μm, and the polystyrene particles quickly adhered to the substrate surface due to the large shear gradients generated near the solid surfaces at small gap heights [11], as shown in Fig. 8.7. During the experiments with gap height of 65 μm, there was no apparent streaming effect or motion of the polystyrene particles even when the applied RF power was increased up to 20 W. However, these higher powers induce a significant heating effect, causing the severe evaporation of the liquid, as shown in Fig. 8.8. Weilin et al. [160] have also reported a similar significant increase in the viscous friction in the case of liquid flows in trapezoidal silicon microchannel when the channel height was changed from 111 to 28 μm.

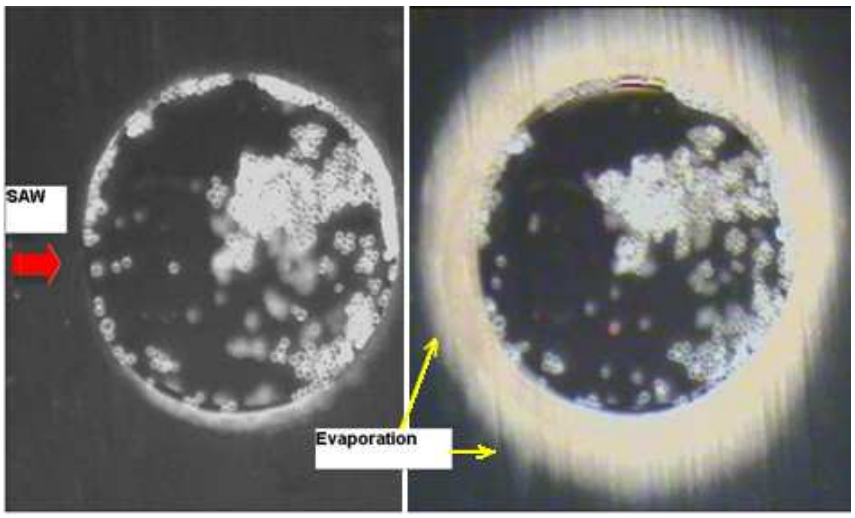

(a) (b)

Figure 8.8 Experimental captured images of a droplet located on a 128º YX-$LiNbO_3$ substrate in line with a SAW device with 1.5 mm aperture and gap height of a 65 μm (*top view*) (a) Before applying the RF power; (b) after application of a 20 W RF power and excitation frequency of 60 MHz, showing the heating and evaporation

Figure 8.9 shows the simulated streaming velocity profiles as a function of distance above the substrate for a range of gap heights and RF powers measured at the droplet centre through its height. Figure 8.10 shows the corresponding velocity vectors values at a gap height of 1,000 μm and measured at the centre of the droplet through its height. Figure 8.9(a), shows that when the gap height exceeds 500 μm at an excitation RF power of 5 mW, there is a gradual decrease in the streaming velocity. Below this value the velocity also reduces and when the gap height < 100 μm, the streaming velocity decreases to < 20 % of the peak value. For gap heights of 50 μm, the induced streaming is actually a creeping motion with a very low Reynolds number of Re ≤ 1. Figure 8.9(b) shows results for an RF power of 100mW, and similarly the streaming velocity is strongly suppressed as long as the gap height is < 100 μm (or H/l_{SAW} < 0.13), with a minor difference in velocity profiles for a gap height of 1,000 μm compared with Fig. 8.9 (a). This is mainly due to the significant increase in velocity at the top of the droplet, resulting from increasing the RF power from 5 mW to 100 mW. These can be clearly revealed from the differences in the velocity vectors illustrated in Fig. 8.10 for the two different RF powers. Besides, the results in Fig. 8.9 show that the flow symmetry along the gap height is broken (e.g., asymmetry velocity profile), for gap heights beyond H_{cr}, of a 500 μm.

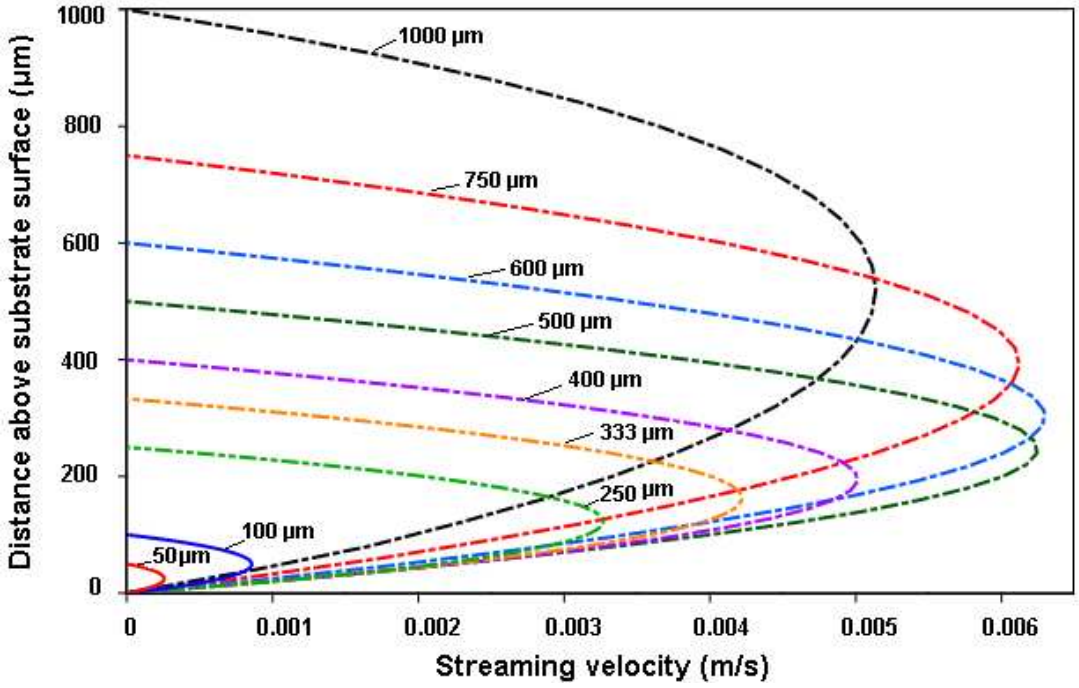

(a)

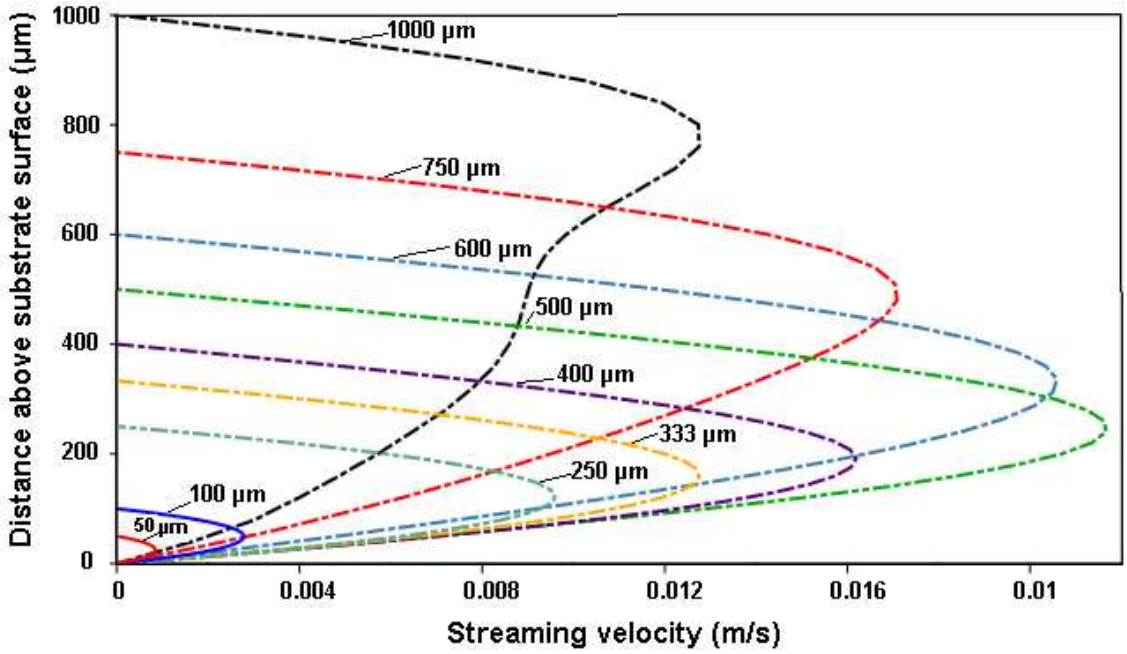

(b)

Figure 8.9 Numerical simulation results of the velocity profile for a 2 mm droplet diameter with different gap heights and measured at the droplet centre through its height, using a 128º YX-$LiNbO_3$ SAW device with a 1.5 mm aperture excited by a frequency of 60 MHz; (a) at an RF power of 5 mW; (b) at an RF power of 100 mW

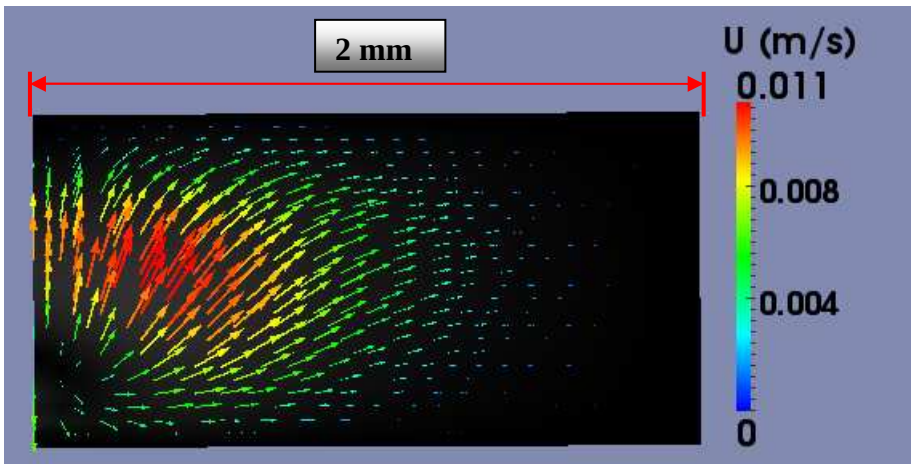

(a)

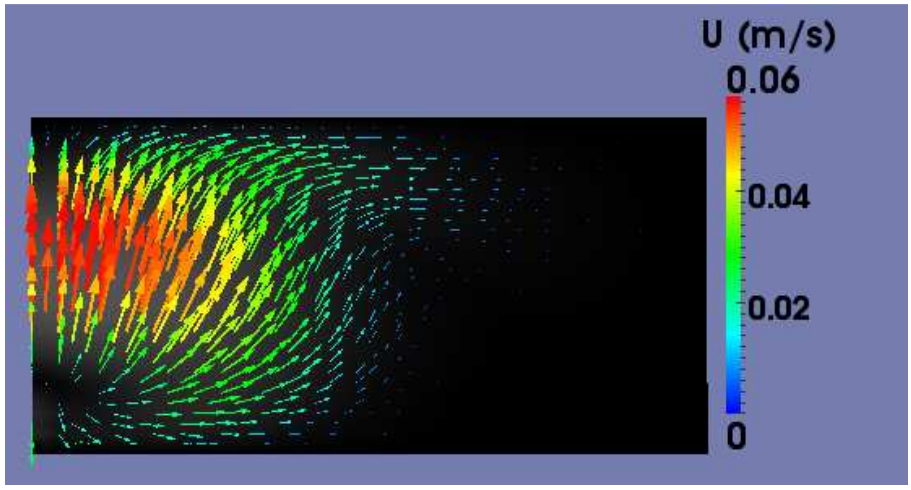

(b)

Figure 8.10 Cross-sectional numerical simulation results of velocity vectors values of 2mm droplet at gap height of 1,000 μm and measured at the centre of the droplet through its height; using a 128º YX-$LiNbO_3$ SAW device excited by a frequency of 60 MHz ; (a) at an RF power of 5 mW; (b) at an RF power of 100 mW. Coloured vectors show flow direction and velocity value

8.4 Summary

This study presents an experimental and numerical investigation for the scaling effects on the characteristic flow hydrodynamics in a confined microdroplet induced by SAW. The configuration of the study set-up includes a top glass slide and $LiNbO_3$ substrate on the propagation path of a SAW, between which a liquid microdroplet was placed. The microfluidic experiments were carried out using 128º YX-$LiNbO_3$ SAW devices excited with a frequency of 60 MHz. Analysis from both the experimental and numerical results showed that, compared with freestanding droplets, there is a significant scaling effect that influences the streaming behaviour of flow hydrodynamics in the microdroplets confined between the two plates. For example, if the gap height, *H*, is <

100 μm, the characteristic streaming velocity reduces considerably with a decrease in the gap height, and approaches zero at a gap height of 50 μm. Therefore, the ability of using the SAW momentum to drive the fluids into confined spaces or microchannels at smaller gap heights will be problematic, due to the increased wall shear gradient at smaller gap heights [11]. Furthermore, it has been observed that there is a critical value for the gap height, above which the streaming velocity decreases. This critical value have been characterised by a dimensionless ratio of the gap height, *H*, and the attenuation length of the Rayleigh SAW, l_{SAW} where the detailed experimental and numerical results have revealed this critical value to be $(H/l_{SAW})_{cr} \approx 0.7$.

Chapter 9

CONCLUSIONS AND FUTURE WORK

Microscale mixing and pumping are essential elements in a variety of microfluidic applications such as biochemical analysis and drug delivery [161-163]. However, effective mixing and pumping of liquids in microlitre volumes or smaller is extremely challenging due to the inherently low Reynolds number flow conditions [12, 164]. One approach to addressing this problem is to employ surface acoustic waves (SAW) as an efficient actuation technology for both micromixing and micropumping [165]. In this study, experimental and numerical investigations of an acoustic streaming generated in sessile microdroplets by the Rayleigh SAWs were conducted. The main conclusions deduced from this study are given below, followed by a recommendation for future work.

9.1 **Conclusions**

A 3D numerical model of SAW acoustic streaming in microfluidic applications has been developed. The acoustic streaming model has been calibrated using experimental results, where a good agreement between the two results was obtained. The 3D model which has been developed captures the physics behind the mechanism of different streaming phenomena, such as the concentration of suspended particles by placing the SAW driven microdroplet in an asymmetric position.

By introducing a new dimensionless acoustic force parameter of $F_{\mathrm{NA}} = \frac{F\lambda}{\sigma/R_d}$ in the current study analysis for the SAW-induced streaming inside sessile droplets (1-30µl), it has been possible for the first time to present qualitative and quantitative comparisons between the experimental data and numerical simulation results. The results provide a strong evidence of the existence of significant hydrodynamics nonlinearity in this system, over a range of the values of F_{NA}. The results suggest that when $F_{\mathrm{NA}} \geq 0.01$; the full 3D Navier-Stokes equations must be applied in order to avoid errors during the predictions of streaming velocities which could be as large as ~ 93%. Besides, droplet deformation or movement has been observed when $F_{\mathrm{NA}} \geq 0.45$. In brief, it has been demonstrated that the hydrodynamic nonlinearity plays a significant role in most noticeable SAW acoustic streaming of droplets actuation (e.g., Re ≥ 1).

The SAW attenuation length, l_{SAW}, (a factor directly related to the SAW excitation frequency and wavelength) has been identified as a parameter indicating the efficiency of SAW-inducing convective mixing. A fast and effective mixing process is induced until a SAW attenuation length, l_{SAW} reaches a critical value, beyond which a significant decrease in streaming velocity and mixing efficiency was observed. The magnitude of streaming velocity, mixing rate and efficiency were determined by the droplet size to be a highest when the ratio of the droplet radius to SAW attenuation length $R_d / l_{SAW} \leq 1.0$, even at small SAW powers, such as 0.05 mW. In contrast, inhomogeneous mixtures with slower mixing rates were obtained when $R_d / l_{SAW} >> 1.0$, due to the higher attenuation rate of acoustic energy and minimisation of energy reaching the droplet free surface. As a high power results in a significant heating effect, this means the critical ratio ($R_d / l_{SAW} \leq 1$) can be used as a guideline in the SAW device design for microfluidic applications that include temperature sensitive biological samples inside the microdroplet [141, 142].

Analysis from both the experimental and numerical results showed that, compared with freestanding droplets, there is a significant scaling effect that influences the streaming behaviour of flow hydrodynamics in the microdroplets confined between the two plates. For example, a considerable decrease in characteristic streaming velocity has been observed, when the gap height between the two plates, H, is < 100 μm. Thus, the ability of using the SAW momentum to drive the fluids into confined spaces or microchannels at smaller gap heights will be problematic, due to the increased wall shear gradient at smaller gap heights [11]. Furthermore, it has been also observed that further increase in the gab height above a higher critical value, will induce a decrease in the streaming velocity. This critical value has been characterised by a new dimensionless ratio between the gap height and penetration distance of the Rayleigh wave into the fluid, which has been identified to be $(H/l_{SAW})_{cr} \approx 0.7$.

9.2 **Future Work**

Although the acoustic streaming phenomena of sessile droplets at different design parameters have been fully explored, the present 3D model is limited to the low power regimes, where neither droplets deformation nor transportation by the actuation of the Rayleigh wave was induced. There is also heating effects unconsidered, and during the experiments it has been observed that the application of SAW at high power levels

induces heat generations and liquids evaporation. Therefore, future work should be aimed at extend the investigations carried out during this project in the following directions:

- In order to study the droplets dynamics and particle formation at high RF powers in 3D dimension, which has not been fully explored, a suitable two-phase model that can capture the interface tension and distortions must be implemented in the current streaming model, such as volume of fluid method (VOF) [166].

- Whereas, the current available studies on heating effects inside droplet generated by a Rayleigh wave are quite limited and based only on the experimental observations [141, 167-169]. Besides, a mechanism of which this phenomenon was generated has not been explored yet. Thus, the present 3D streaming model could be extended to understand the physics behind a heat generation and temperature increase inside the liquid droplet by a high power source of a Rayleigh wave.

- The devolved mixing model in this study was used successfully for the characterisation of SAW mixing performance of two different species. The mixing model could be extended to include the chemical reactions for LOC systems, where the influences of the SAW streaming on the characteristics of chemical species generation and reaction efficiency could be thoroughly investigated.

However, SAW-based Microfluidics has drawn much attention for lab-on-chip research, where many streaming phenomena are still under study and a 3D modeling has not been fully provided. Future work can also be extended to streaming phenomenon generated by the shear type surface acoustic wave [170], or that generated by a standing surface acoustic wave [77].

References

[1] K. Chono, N. Shimizu, Y. Matsui, J. Kondoh, S. Shiokawa, Development of novel atomization system based on SAW streaming, Jap. J. Appl. Phys, **43** (2004) 2987-2991.

[2] A. Sano, Y. Rlatsui, S. Shiokawa, A new manipulator based on surface acoustic wave streaming, in: Ultrasonics Symposium, 1997. Proceedings., 1997 IEEE, Toronto, Ont, 1997, pp. 467-470.

[3] A. Manz, N. Graber, H.M. Widmer, Miniaturized total chemical analysis systems: A novel concept for chemical sensing, Sensors and Actuators B: Chemical, **1** (1990) 244–248.

[4] F. Zhang, B. Liu, W. Liu, Q. Zhang, DNA computing model based on lab-on-a-chip and its application on solving the timetabling problem, Progress in Natural Science **18** (2008) 633-637.

[5] C. Zhang, D. Xing, Y. Li, Micropumps, microvalves, and micromixers within PCR microfluidic chips: Advances and trends, Biotechnology Advances, **25** (2007) 483-514.

[6] S. Haeberle, R. Zengerle, Microfluidic platforms for lab-on-a-chip applications, Lab on a chip, **7** (2007) 1094-1110.

[7] G.H.W. Sanders, A. Manz, Chip-based microsystems for genomic and proteomic analysis, TrAC Trends in Analytical Chemistry, **19** (2000) 364-378.

[8] B.H. Weigl, R.L. Bardell, C.R. Cabrera, Lab-on-a-chip for drug development, Advanced Drug Delivery Reviews, **55** (2003) 349-377.

[9] M.B. Elman, M. Sternheim, R. Rosen, S. Krylov, Y. Shacham, Towrds Toxity Detection Using Lab-on-Chip Based on the Integration of MEMS and Whole-Cell Sensors, Biosensors and Bioelectronics, **23** (2008).

[10] L.-J. Yang, T.-J. Yao, Y.-C. Tai, The marching velocity of the capillary meniscus in a microchannel, J. Micromech. Microeng. , **14** (2004) 220–225.

[11] K. Kang, L.J. Lee, K.W. Koelling, High shear microfluidics and its application in rheological measurement, Experiments in Fluids, **38** (2005) 222-232.

[12] K. Strobl, M.F. Schneider, A. Wixforth, Acoustic Mixing at Low Reynolds Number, Applied Physics Letters, **88** (2006) 054102.

[13] K.A. Shaikh, K.S. Ryu, E.D. Goluch, J.-M. Nam, J. Liu, C.S. Thaxton, A modular microfluidic architecture for integrated biochemical analysis, **102** (2005) 9745-9750.

[14] C.K. Fredrickson, Z.H. Fan, Macro-to-micro interfaces for microfluidic devices, Lab on a chip, **4** (2004) 526-533.

[15] Y. Li, Y.Q. Fu, S.D. Brodie, M. Alghane, A.J. Walton, Integrated microfluidics system using surface acoustic wave and electrowetting on dielectrics technology, Biomicrofluidics, **6** (2012) 012812-012819.

[16] A. Wixforth, Acoustically driven planar microfluidics, Superlattices and Microstructures, **33** (2003) 389–396.

[17] X.Y. Du, M.E. Swanwick, Y.Q. Fu, J.K. Luo, A.J. Flewitt, D.S. Lee, S. Maeng, W.I. Milne, Surface acoustic wave induced streaming and pumping in 128° Y-cut LiNbO3 for microfluidic applications Journal of Micromechanics and Microengineering **19** (2009) 035016.

[18] C.J. Strobl, A. Rathgeber, A. Wixforth, C. Gauer, J. Scriba, Planar microfluidic processors, in: Ultrasonics Symposium, 2002. Proceedings. 2002 IEEE, 2002, pp. 255-258 vol.251.

[19] X.Y. Du, Y.Q. Fu, J.K. Luo, A.J. Flewitt, W.I. Milne, Microfluidic pumps employing surface acoustic waves generated in ZnO thin films, Journal of Applied Physics, **105** (2009) 024508-024508-024507.

[20] M.K. Tan, J.R. Friend, L.Y. Yeo, Interfacial Jetting Phenomena Induced by Focused Surface Vibrations, Physical Review Letters, **103** (2009) 024501.

[21] A. Qi, L.Y. Yeo, J.R. Friend, Interfacial destabilization and atomization driven by surface acoustic waves, Physics of Fluids, **20** (2008) 074103-074114.

[22] R.J. Shilton, L.Y. Yeo, J.R. Friend, Quantification of surface acoustic wave induced chaotic mixing-flows in microfluidic wells, Sensors and Actuators B: Chemical, **160** (2011) 1565-1572.

[23] L. Yeo, J.R. Friend, Ultrafast microfluidics using surface acoustic waves, Biomicrofluidics, **3** (2009) 012002.

[24] P.R. Rogers, J.R. Friend, L.Y. Yeo, Exploitation of surface acoustic waves to drive size-dependent microparticle concentration within a droplet, Lab on a chip, **10** (2010) 2979-2985.

[25] T. Frommelt, T.D. Gogel, M. Kostur, P. Talkner, P. Hanggi, Flow patterns and transport in Rayleigh surface acoustic wave streaming, IEEE Transaction on Ultrasonics **55** (2008) 2298-2305.

[26] J.V. Atanasoff, P.J. Hart, Dynamical Determinitation of the Elastic Constants and Their Temperature Coefficients for Quartz, Physical Review, **59** (1941) 85-96.

[27] S. Datta, Surface Acoustic Wave Devices, A Division of Simimon and Schuster,Inc, New Jersy 1986

[28] M.J. Fernandez, J.L. Fotecha, I. Sayago, M. Aleixander, J. Lozano, Discrimination of Volatile Copmounds Through an Electric Nose Based on Zno SAW Sensors, Sensors and Actuators B, **127** (2007) 277-283.

[29] H. Li, J.R. Friend, L.Y. Yeo, A scaffold cell seeding method driven by surface acoustic waves, Biomaterials, **28** (2007) 4098-4104.

[30] S.C. Terry, J.H. Jerman, J.B. Angell, A gas chromatographic air analyzer fabricated on a silicon wafer, IEEE Transactions on Electron Devices, ED-26 (1979) 1880-1885.

[31] M.A. Burns, B.N. Johnson, S.N. Brahmasandra, K. Handique, J.R. Webster, M. Krishnan, T.S. Sammarco, P.M. Man, D. Jones, D. Heldsinger, C.H. Mastrangelo, D.T. Burke, An Integrated Nanoliter DNA Analysis Device, Science, **282** (1998) 484-487.

[32] George Karniadakis, Ali Beşkök, N.R. Aluru, Microflows And Nanoflows: Fundamentals And Simulation in: S.S. Antman, J.E. Marsden, L. Sirovich (Eds.), Springer Science+Business Media, Inc., New York, 2005.

[33] D.R. Reyes, D. Iossifidis, P.A. Auroux, A. Manz, Micro total analysis systems. 1. Introduction, theory, and technology, Anal Chem., **74** (2002) 2623-2636.

[34] M. Tan, J. Friend, L. Yeo, Surface Acoustic Wave Driven Microchannel Flow, in: Proc 16th Australasian Fluid Mech Conf, Gold Coast, Australia, 2007, pp. 790–793

[35] K. Sollier, C. Mandon, K. Heyries, L. Blum, C. Marquette, "Print-n-Shrink" technology for the rapid production of microfluidic chips and protein microarrays, Lab Chip, **9** (2009) 3489-3494.

[36] D.J. Laser, J.G. Santiago, A review of micropumps, Journal of Micromechanics and Microengineering, **14** (2004) R35.

[37] A.A. Oliner, Acoustic surface waves, in: Topics in applied physics Springer-Verlag, New York, 1978.

[38] D.S. Ballantine, R.M. White, S.J. Martin, A.J. Ricco, E.T. Zellers, G.C. Frye, H. Wohltjen, Acoustic Wave Sensors: Theory, Design, and Physico-Chemical Applications in: M. Levy, R. Stern (Eds.), Academic Press, 1997.

[39] D. Royer, E. Dieulesaint, Elastic Waves in Solids I: Free and Guided Propagation (Advanced Texts in Physics), Springer, 2000.

[40] J.W. Gardner, V.K. Varadan, O.O. Awadelkarim, Microsensors, MEMS and Smart Devices, John Wiley & Sons, Inc, New York, 2001.

[41] S. Shiokawa, Y. Matsui, T. Ueda, Study on acoustic streaming and its application to fluid devices, Japanese Journal of Applied Physics **29** (1990) 137-139.

[42] L. Rayleigh, On Waves Propagated along the Plane Surface of an Elastic Solid, Proceedings of the London Mathematical Society, s**1-17** (1885) 4-11.

[43] A. Müller, A. Darga, A. Wixforth, Surface Acoustic Wave Studies for Chemical and Biological Sensors
Nanoscale Devices - Fundamentals and Applications, in: R. Gross, A. Sidorenko, L. Tagirov (Eds.), Springer Netherlands, 2006, pp. 3-13.
[44] P.J. Feenstra, Modeling and control of surface acoustic wave motors, University of Twente [Host], Enschede, 2005.
[45] J. David, N. Cheeke, , Fundamentals and Applications of Ultrasonic Waves
CRC Press LLC., Florida, 2002.
[46] S.K.R.S. Sankaranarayanan, V.R. Bhethanabotla, Design of efficient focused surface acoustic wave devices for potential microfluidic applications, Journal of Applied Physics, **103** (2008) 064518-064518-064517.
[47] J. Berthier, Microdrops and Digital Microfluidic, William Andrew Inc., Norwich, USA, 2008.
[48] S.K.R.S. Sankaranarayanan, S. Cular, V.R. Bhethanabotla, B. Joseph, Flow induced by acoustic streaming on surface-acoustic-wave devices and its application in biofouling removal: A computational study and comparisons to experiment, Physical Review E, **77** (2008) 066308.
[49] J. Friend, L.Y. Yeo, Microscale acoustofluidics: Microfluidics driven via acoustics and ultrasonics, Reviews of Modern Physics, **83** (2011) 647-704.
[50] K. Dransfeld, E. Salzmann, Excitation, detection and attenuation of high-frequency elastic surface waves, in: W.P. Mason, R.N. Thurston (Eds.) Physical Acoustics, Academic press, New York, 1970, pp. 219-272.
[51] J.D.N. Cheeke, P. Morisseau, Attenuation of Rayleigh waves on a LiNbO3 crystal in contact with a liquid4He bath, J Low Temp Phys, **46** (1982) 319-330.
[52] S. Shiokawa, Y. Matsui, T. Moriizumi, Experimental Study on Liquid Streaming by SAW Jpn. J. Appl. Phys., **28** (1989) 126-128.
[53] R.M. Arzt, E. Salzmann, K. Dransfeld, ELASTIC SURFACE WAVES IN QUARTZ AT 316 MHz Appl. Phys. Lett., **10** (1967) 165-167.
[54] W.L. Nyborg, Acoustic streaming, in: e. W.P Mason (Ed.) Physical Acoustics, Academic press, 1965 pp. 265-331.
[55] J. Lighthill, Acoustic streaming J. Sound Vib, **61** (1978) 391-418.
[56] J. Lighthill, Internal waves in fluids, Cambridge University Press, Cambridge, 1978.
[57] M.k. Tan, J.R. Friend, L.Y. Yeo, Surface Acoustic Wave Driven Microchannel Flow, in, ScienceDirect, Crown Plaza,Gold Coast,Australi 2007.

[58] K. Sritharan, C.J. Strobl, M.F. Schneider, A. Wixforth, Z. Guttenberg, Acoustic mixing at low Reynold's numbers, Applied Physics Letters, **88** (2006) 054102-054103.
[59] T. Uchida, T. Suzukki, T. Shiokawa, Investigation of Acoustic Streaming Excited by Surface Acoustic Waves, IEEE Ultrasonic Symposium, **2** (1995) 1081-1084.
[60] S. Shiokawa, Y. Matsui, T. Ueda, Liquid streaming and droplet formation caused by leaky Rayleigh waves, Ultrasonics Symposium Proceedings, **1** (1989) 643-646.
[61] A. Renaudin, P. Tabourier, V. Zhang, J.C. Camart, C. Druon, SAW nanopump for handling droplets in view of biological applications, Sensors and Actuators B: Chemical, **113** (2006) 389-397.
[62] M. Alghane, Y.Q. Fu, B.X. Chen, Y. Li, M.P.Y. Desmulliez, A.J. Walton, Streaming phenomena in microdroplets induced by Rayleigh surface acoustic wave, Journal of Applied Physics, **109** (2011) 114901-114908.
[63] K. Kulkarni, J. Friend, L. Yeo, P. Perlmutter, Surface acoustic waves as an energy source for drop scale synthetic chemistry, Lab on a chip, **9** (2009) 754-755.
[64] T. Frommelt, M. Kostur, S. Wenzel, auml, M. fer, P. Talkner, auml, P. nggi, A. Wixforth, Microfluidic Mixing via Acoustically Driven Chaotic Advection, Physical Review Letters, **100** (2008) 034502.
[65] M. Maezawa, R. Kamada, T. Suda, T. Kamakura, Liquid Mixing using Streaming in Frequency-Modulated Ultrasonic Beams Radiated from SAW Devices, in: Proceedings of 20th International Congress on Acoustics, Sydney, Australia, 2010.
[66] W. Tseng, J. Lin, W. Sung, S. Chen, G. Lee, Active micro-mixers using surface acoustic waves on Y-cut 128 LiNbO3, J. Micromech. Microeng **16** (2006) 539-548.
[67] Q. Zeng, F. Guo, L. Yao, H.W. Zhu, L. Zheng, Z.X. Guo, W. Liu, Y. Chen, S.S. Guo, X.Z. Zhao, Milliseconds mixing in microfluidic channel using focused surface acoustic wave, Sensors and Actuators B: Chemical, **160** (2011) 1552-1556.
[68] H. Li, J. Friend, L. Yeo, Surface acoustic wave concentration of particle and bioparticle suspensions, Biomedical Microdevices, **9** (2007) 647-656.
[69] R. Shilton, M.K. Tan, L.Y. Yeo, J.R. Friend, Particle concentration and mixing in microdrops driven by focused surface acoustic waves, Journal of Applied Physics, **104** (2008) 014910-014911-014919.
[70] R. Raghavan, J. Friend, L. Yeo, Particle concentration via acoustically driven microcentrifugation: microPIV flow visualization and numerical modelling studies, Microfluidics and Nanofluidics, **8** (2010) 73-84.
[71] A. Zhang, W. Liu, Z. Jiang, J. Fei, Rapid concentration of particle and bioparticle suspension based on surface acoustic wave, Applied Acoustics, **70** (2009) 1137-1142.

[72] R. Wilson, J. Reboud, Y. Bourquin, S. Neale, Y. Zhang, J. Cooper, Phononic crystal structures for acoustically driven microfluidic manipulations, Lab on a chip, **11** (2011) 323-328.

[73] J. Shi, X. Mao, D. Ahmed, A. Colletti, T.J. Huang, Focusing microparticles in a microfluidic channel with standing surface acoustic waves (SSAW), Lab on a chip, **8** (2008) 221-223.

[74] T. Kamakura, K. Matsuda, Y. Kumamoto, M.A. Breazeale, Acoustic streaming induced in focused Gaussian beams, The Journal of the Acoustical Society of America, **97** (1995) 2740-2746.

[75] J. Shi, H. Huang, Z. Stratton, Y. Huang, T.J. Huang, Continuous particle separation in a microfluidic channel via standing surface acoustic waves (SSAW), Lab on a chip, **9** (2009) 3354-3359.

[76] J. Shi, D. Ahmed, X. Mao, S.-C.S. Lin, A. Lawit, T.J. Huang, Acoustic tweezers: patterning cells and microparticles using standing surface acoustic waves (SSAW), Lab on a chip, **9** (2009) 2890-2895.

[77] L. Meng, F. Cai, Z. Zhang, L. Niu, Q. Jin, F. Yan, J. Wu, Z. Wang, H. Zheng, Transportation of single cell and microbubbles by phase-shift introduced to standing leaky surface acoustic waves, Biomicrofluidics, **5** (2011) 44104-4410410.

[78] X. Ding, J. Shi, S.-C.S. Lin, S. Yazdi, B. Kiraly, T.J. Huang, Tunable patterning of microparticles and cells using standing surface acoustic waves, Lab on a chip, **12** (2012) 2491-2497.

[79] L. Meng, F. Cai, J. Chen, L. Niu, Y. Li, J. Wu, H. Zheng, Precise and programmable manipulation of microbubbles by two-dimensional standing surface acoustic waves, Applied Physics Letters, **100** (2012) 173701-173701-173704.

[80] D. Beyssen, L. Le Brizoual, O. Elmazria, P. Alnot, Microfluidic device based on surface acoustic wave, Sensors and Actuators B: Chemical, **118** (2006) 380-385.

[81] J.K. Luo, Y.Q. Fu, Y. Li, X.Y. Du, A.J. Flewitt, A. Walton, W.I. Milne, Moving-part-free microfluidic systems for lab-on-a-chip, Journal of Micromechanics and Microengineering, **19** (2009) 054001.

[82] S. Girardo, M. Cecchini, F. Beltram, R. Cingolani, D. Pisignano, Polydimethylsiloxane-LiNbO3 surface acoustic wave micropump devices for fluid control into microchannels, Lab on a chip, **8** (2008) 1557-1563.

[83] M. Cecchini, S. Girardo, D. Pisignano, R. Cingolani, F. Beltram, Acoustic-counterflow microfluidics by surface acoustic waves, Applied Physics Letters, **92** (2008) 104103-104103-104103.

[84] L. Masini, M. Cecchini, S. Girardo, R. Cingolani, D. Pisignano, F. Beltram, Surface-acoustic-wave counterflow micropumps for on-chip liquid motion control in two-dimensional microchannel arrays, Lab on a chip, **10** (2010) 1997-2000.

[85] S. Shiokawa, Y. Matsui, T. Ueda, Study on SAW Streaming and its Application to Fluid Devices, Jpn. J. Appl. Phys., **29**S1 (1990) 137-139.

[86] S. Shiokawa, Y. Matsui, T. Ueda, Liquid streaming and droplet formation caused by leaky Rayleigh waves, in: Ultrasonics Symposium, 1989. Proceedings., IEEE Montreal, Que, 1989, pp. 643-646

[87] J. Bennes, S. Alzuaga, S. Ballandras, F. Cherioux, F. Bastien, J.F. Manceau, Droplet ejector using surface acoustic waves, in: Ultrasonics Symposium, 2005 IEEE, 2005, pp. 823-826.

[88] M. Kurosawa, T. Watanabe, A. Futami, T. Higuchi, Surface acoustic wave atomizer, Sensors and Actuators A: Physical, **50** (1995) 69-74.

[89] J. Ju, Y. Yamagata, H. Ohmori, T. Higuchi, High-frequency surface acoustic wave atomizer, Sensors and Actuators A: Physical, 145–146 (2008) 437-441.

[90] M. Alvarez, J. Friend, L. Yeo, Surface vibration induced spatial ordering of periodic polymer patterns on a substrate, Langmuir, **24** (2008) 10629-10632.

[91] J. Friend, L. Yeo, D. Arifin, A. Mechler, Evaporative self-assembly assisted synthesis of polymeric nanoparticles by surface acoustic wave atomization, Nanotechnology, **19** (2008) 145301.

[92] A. Qi, L. Yeo, J. Friend, J. Ho, The extraction of liquid, protein molecules and yeast cells from paper through surface acoustic wave atomization, Lab on a chip, **10** (2010) 470-476.

[93] T.A. Franke, A. Wixforth Microfluidics for Miniaturized Laboratories on a Chip, ChemPhysChem, 9 (2008) 2140–2156.

[94] H. Antil, A. Gantner, R.H.W. Hoppe, D. K¨oster, K. Siebert, A. Wixforth, Modeling and Simulation of Piezoelectrically Agitated Acoustic Streaming of Microfluidic Biochips, Licture Notes in Computation Science, **60** (2008) 305-312.

[95] D. Köster, Numerical Simulation of Acoustic Streaming on Surface Acoustic Wave-driven Biochips SIAM J. on Scientific Computing, **29** (2007).

[96] R.G. Harbir Antil, Ronald H.W. Hoppe, Christopher Linsenmann, Tsorng-Whay Pan, Achim Wixforth, MODELING, SIMULATION, AND OPTIMIZATION OF SURFACE ACOUSTIC WAVE DRIVEN MICROFLUIDIC BIOCHIPS, Journal of Computational Mathematics, **28** (2010) 149-169.

[97] W.L. Nyborg, Acoustic streaming, in: M.F. Hamilton (Ed.) Nonlinear acoustics, Academic Press, New York, 1998, pp. 207-331.

[98] C.E. Bradley, Acoustic streaming field structure: The influence of the radiator, The Journal of the Acoustical Society of America, **100** (1996) 1399-1408.

[99] W.L. Nyborg, Acoustic Streaming due to Attenuated Plane Waves, The Journal of the Acoustical Society of America, **25** (1953) 68-75.

[100] W.L. Nyborg, Acoustic Streaming near a Boundary, The Journal of the Acoustical Society of America, **30** (1958) 329-339.

[101] M.K. Tan, L.Y. Yeo, J.R. Friend, Rapid fluid flow and mixing induced in microchannels using surface acoustic waves, EPL (Europhysics Letters), **87** (2009) 47003.

[102] M. Schindler, P. Talkner, M. Kostur, P. Hänggi, Accumulating particles at the boundaries of a laminar flow, Physica A: Statistical Mechanics and its Applications, **385** (2007) 46-58.

[103] S.K.R.S. Sankaranarayanan, R. Singh, V.R. Bhethanabotla, Acoustic streaming induced elimination of nonspecifically bound proteins from a surface acoustic wave biosensor: Mechanism prediction using fluid-structure interaction models, Journal of Applied Physics, **108** (2010) 104507-104511.

[104] M.K. Tan, J.R. Friend, O.K. Matar, L.Y. Yeo, Capillary wave motion excited by high frequency surface acoustic waves, Physics of Fluids, **22** (2010) 112112-112122.

[105] M. Schindler, P. Talkner, P. Hanggi, Computing stationary free-surface shapes in microfluidics, Physics of Fluids, **18** (2006) 103303-103316.

[106] D. Koster, Numerical Simulation of Acoustic Streaming on Surface Acoustic Wave-Driven Biochips, SIAM J SCI, **6** (2007) 2352-2380.

[107] A. Huerta, W.K. Liu, Viscous flow with large free surface motion, Computer Methods in Applied Mechanics and Engineering, **69** (1988) 277-324.

[108] ANSYS, [online] available at http://www.ansys.com/products/cfx.asp, (accessed on December 2008).

[109] ANSYS, online] available at http://www.fluent.com/software/fluent/index.htm, (accessed December 2008).

[110] ANSYS, *[online] availabe at http://www.ansys.com/products/multiphysics.asp*, (accessed December 2008).

[111] FLOW-3D, [online] available at http://www.flow3d.com/, (accessed January 2009).

[112] COMSOL, [online] availabe at http://www.euro.comsol.com/, (accessed January 2009).

[113] MFiX, [online] available at https://mfix.netl.doe.gov/index.php, (accessed January 2009).

[114] OpenFVM, [online] availabe at http://openfvm.sourceforge.net/, (accessed January 2009).

[115] Elmer, [online] available at http://www.ann.jussieu.fr/~lehyaric/stats/link.php?from=http:%2f%2fwww.ann.jussieu.fr%2ffree.htm&to=http:%2f%2fwww.csc.fi%2felmer%2f&subject=Elmer&version=070702 (accessed january 2009).

[116] OpenFOAM, [online] available at http://www.ann.jussieu.fr/~lehyaric/stats/link.php?from=http:%2f%2fwww.ann.jussieu.fr%2ffree.htm&to=http:%2f%2fwww.opencfd.co.uk%2fopenfoam%2f&subject=OpenFOAM&version=070702, (accessed January 2009).

[117] OOFEM, [online] available at http://www.oofem.org/en/oofem.html, (accessed January 2009).

[118] M.K. Kurosawa, State-of-the-art surface acoustic wave linear motor and its future applications, Ultrasonics **38** (2000) 15-19.

[119] M.K.B. M. I. Newton, T. K. H. Starke, S. M. Bowan, G. McHale, Sensor & Actuat, **76** (1999) 89.

[120] L. Rayleigh, On the Circulation of Air Observed in Kundt's Tubes, and on Some Allied Acoustical Problems, Philosophical Transactions of the Royal Society of London, **175** (1884) 1-21.

[121] OpenFOAM user guide, in, OpenCFD Ltd, 2008.

[122] H. Mitome, The mechanism of generation of acoustic streaming, Electronics and Communications in Japan (Part III: Fundamental Electronic Science), **81** (1998) 1-8.

[123] S.K.R.S. Sankaranarayanan, V.R. Bhethanabotla, Numerical analysis of wave generation and propagation in a focused surface acoustic wave device for potential microfluidics applications, IEEE Trans Ultrason Ferroelectr Freq Control., **56** (2009) 631-643.

[124] T. Uchida, T. Suzuki, S. Shiokawa, Investigation of acoustic streaming excited by surface acoustic wave, IEEE Ultrasonics Symposium **2** (1995) 1081-1084.

[125] T. Franke, A.R. Abate, D.A. Weizt, A. Wixforth, Surface acoustic wave (SAW) directed droplet flow in microfluidics for PDMS devices, Lab on a chip **9** (2009) 2625-2627.

[126] K. Matsuda, T. Kamakura , Y. Kumamoto, Acoustic streaming by a focused sound source, in: H. Hobxk (Ed.) Proceedings of the 13th International Symposium on Nonlinear Acoustics, World Scientific, Bergen, 1993, pp. 595–600.

[127] J.C. Campbell, W.R. Jones, A method for estimating optimal crystal cuts and propagation direction for excitation of piezoelectric surface waves, IEEE Transactions on sonic and ultrasonics **15** (1968) 209

[128] J.C. Campbell, W.R. Jones, propagation of surface waves at the boundary between a piezoelectric crystal and a fluid medium, IEEE Transactions on sonic and ultrasonics **17** (1970) 71-76.

[129] S.V. Patankar, Numerical heat transfer and fluid flow, Hemisphere Publishing Corporation, New York, 1980.

[130] H.K. Versteeg, W. Malalasekera, An Introduction to Computational Fluid Dynamics; The Finite Volume Method longman Group Ltd, London, 1995.

[131] S. Oberti, A. Neild, R. Quach, J. Dual, The use of acoustic radiation forces to position particles within fluid droplets, Ultrasonics, **49** (2009) 47-52.

[132] J. Friend, H. Li, L. Yeo, Surface Acoustic Wave Concentration of Microparticle and Nanoparticle Suspensions, in: Proc 16th Australasian Fluid Mech Conf., Gold Coast, Australia, 2008, pp. 1038–1041.

[133] G.K. Batchelor, NOTE ON A CLASS OF SOLUTIONS OF THE NAVIER-STOKES EQUATIONS REPRESENTING STEADY ROTATIONALLY-SYMMETRIC FLOW, in, Oxford University Press, 1951.

[134] L.Y. Yeo, J.R. Friend, D.R. Arifin, Electric tempest in a teacup: The tea leaf analogy to microfluidic blood plasma separation, Applied Physics Letters, **89** (2006) 103516-103513.

[135] D.R. Arifin, L.Y. Yeo, J.R. Friend, Microfluidic blood plasma separation via bulk electrohydrodynamic flows, Biomicrofluidics, **1** (2007) 014103-014113.

[136] A. Einstein, Die Ursache der Mäanderbildung der Flußläufe und des sogenannten Baerschen Gesetzes, Naturwissenschaften, **14** (1926) 223-224.

[137] A. Tandon, J. Marshall, Einstein's Tea Leaves and Pressure Systems in the Atmosphere, The Physics Teacher, **48** (2010) 292-295.

[138] R.M. Moroney, R.M. White, R.T. Howe, Microtransport induced by ultrasonic Lamb waves, Applied Physics Letters, **59** (1991) 774-776.

[139] M.W. Thompson, A.A. Atchley, M.J. Maccarone, Influences of a temperature gradient and fluid inertia on acoustic streaming in a standing wave, The Journal of the Acoustical Society of America, **117** (2005) 1839-1849.

[140] M. Alghane, B.X. Chen, Y.Q. Fu, Y. Li, J.K. Luo, A.J. Walton, Experimental and numerical investigation of acoustic streaming excited by using a surface acoustic wave device on a 128° YX-LiNbO 3 substrate, Journal of Micromechanics and Microengineering, **21** (2011) 015005.

[141] J. Kondoh, N. Shimizu, Y. Matsui, M. Sugimoto, S. Shiokawa, Temperature-control system for small droplet using surface acoustic wave device, in: Sensors, 2005 IEEE, Irvine, CA, 2005, pp. 4 pp.

[142] T.-D. Luong, V.-N. Phan, N.-T. Nguyen, High-throughput micromixers based on acoustic streaming induced by surface acoustic wave, Microfluidics and Nanofluidics, **10** (2011) 619-625.

[143] P. Brunet, M. Baudoin, O.B. Matar, F. Zoueshtiagh, Droplet displacements and oscillations induced by ultrasonic surface acoustic waves: A quantitative study, Physical Review E, **81** (2010) 036315.

[144] N.I. Newton, M.K. Banerjee, T.K.H. Starke, S.M. Bowan, G. McHale, Surface acoustic wave-liquid drop interactions, Sensors & Actuators, **76** (1999) 89-92.

[145] Y.Q. Fu, J.K. Luo, X. Du, A.J. Flewitt, Y. Li, A. Walton, W.I. Milne, Recent developments in ZnO films for acoustic wave based bio-sensing and microfluidic applications, Sens. Actuat. B., **143** (2010) 606-619.

[146] X.Y. Du, M.E. Swanwick, Y.Q. Fu, J.K. Luo, A.J. Flewitt, D.S. Lee, S. Maeng, W.I. Milne, Surface acoustic wave induced streaming and pumping in 128° Y-cut LiNbO 3 for microfluidic applications, Journal of Micromechanics and Microengineering, **19** (2009) 035016.

[147] A. Wixforth, Acoustically Driven Programmable Microfluidics for Biological and Chemical Applications, J. Assoc. Lab. Autom, **11** (2006) 399-405

[148] A. Wixforth, C. Strobl, C. Gaue, A. Toegl, C. Scriba, Z.V. Guttenberg, Acoustic Manipolation of Small Droplets, Anal. Bional. Chem., (2004) 982-991.

[149] R.M. Arzt, E. Salzmann, K. Dransfeld, ELASTIC SURFACE WAVES IN QUARTZ AT 316 MHz Appl. Phys. Lett. , **10** (1967) 165-167.

[150] M.K. Tan, L.L. Yeo, J.R. Friend, Inducing rapid fluid flows in microchannels with surface acoustic waves, in: Ultrasonics Symposium (IUS), 2009 IEEE International, 2009, pp. 609-612.

[151] M.K. Tan, L.Y. Yeo, J.R. Friend, Unique flow transitions and particle collection switching phenomena in a microchannel induced by surface acoustic waves, Applied Physics Letters, **97** (2010) 234106-234103.

[152] A. Gantner, R.H.W. Hoppe, D. Köster, K. Siebert, A. Wixforth, Numerical simulation of piezoelectrically agitated surface acoustic waves on microfluidic biochips, Comput. Vis. Sci., **10** (2007) 145-161.

[153] L. Schmid, A. Wixforth, D. Weitz, T. Franke, Novel surface acoustic wave (SAW)-driven closed PDMS flow chamber, Microfluidics and Nanofluidics, **12** (2011) 1-7.

[154] H.h. Gu, S.y. Zhang, L.p. Cheng, D. Ma, F.m. Zhou, Z.j. Chen, X.j. Shui, Study on non-contact linear motors driven by surface acoustic waves Sensors & Actuators: A, **155** (2009) 163-167.

[155] L. Tzong-Shyng, S. Horng-Jiann, New pumping mechanism by surface waves in a microchannel, in: Nano/Micro Engineered and Molecular Systems, 2009. NEMS 2009. 4th IEEE International Conference on, 2009, pp. 747-750.

[156] N. Nam-Trung, R.M. White, Acoustic streaming in micromachined flexural plate wave devices: numerical simulation and experimental verification, Ultrasonics, Ferroelectrics and Frequency Control, IEEE Transactions on, **47** (2000) 1463-1471.

[157] N.T. Nguyen, R.M. White, Design and optimization of an ultrasonic flexural plate wave micropump using numerical simulation, Sensors and Actuators A: Physical, 77 (1999) 229-236.

[158] T. Min-Chien, L. Tzong-Shyng, The Study of Flexible Plate Wave Device for Micro Pumping System, in: Nano/Micro Engineered and Molecular Systems, 2007. NEMS '07. 2nd IEEE International Conference on, 2007, pp. 452-457.

[159] H. Guo, H. Sun, P.-T. Sah, Theoretical study of acoustic streaming induced cooling effect in the microscale, IEEE International Ultrasonics Symposium Proceedings, (2008) 934-937.

[160] Q. Weilin, G. Mohiuddin Mala, L. Dongqing, Pressure-driven water flows in trapezoidal silicon microchannels, International Journal of Heat and Mass Transfer, **43** (2000) 353-364.

[161] W. Achim, Acoustically Driven Programmable Microfluidics for Biological and Chemical Applications, j.jala, **11** (2006) 399-405.

[162] F. Josse, F. Bender, R.W. Cernosek, Guided Shear Horizontal Surface Acoustic Wave Sensors for Chemical and Biochemical Detection in Liquids, Analytical Chemistry, **73** (2001) 5937-5944.

[163] J K Luo, Y Q Fu, Y Li, X Y Du, A J Flewitt, A J Walton, W.I. Milne, Moving-part-free microfluidic systems for lab-on-a-chip, J. Micromech. Microeng, **19** (2009) 054001.

[164] V. Singhal, S.V. Garimella, J.Y. Murthy, Low Reynolds number flow through nozzle-diffuser elements in valveless micropumps, Sensors and Actuators A: Physical, **113** (2004) 226-235.

[165] N.S. K. Chono, Y. Matsu, J. Kondoh, S. Shiokawa, Jap. J. Appl. Phys. **43** (2004) 2987.

[166] J.P. Wang, A.G.L. Borthwick, R.E. Taylor, Finite-volume-type VOF method on dynamically adaptive quadtree grids, International Journal for Numerical Methods in Fluids, **45** (2004) 485-508.

[167] J. Kondoh, N. Shimizu, Y. Matsui, M. Sugimoto, S. Shiokawa, Development of temperature-control system for liquid droplet using surface Acoustic wave devices, Sensors and Actuators A: Physical, **149** (2009) 292-297.

[168] D. Beyssen, L. Le Brizoual, O. Elmazria, P. Alnot, I. Perry, D. Maillet, 6I-2 Droplet Heating System Based on SAW/Liquid Interaction, in: Ultrasonics Symposium, 2006. IEEE, 2006, pp. 949-952.

[169] I. Shihoko, S. Mitsunori, M. Yoshikazu, K. Jun, Study of Surface Acoustic Wave Streaming Phenomenon Based on Temperature Measurement and Observation of Streaming in Liquids,Jpn. J. Appl. Phys., **46** (2007) 4718-4722.

[170] D.S. Brodie, Y.Q.F. Fu, Y. Li , M. Alghane , R.L. Reuben, A.J. Walton Shear horizontal surface acoustic wave induced microfluidic flow, Appl. Phys. Lett., **99** (2011) 153704